


國立交通大學

機械工程學系

碩士論文

狹窄水平雙套管中 R-410A 冷媒流量震盪與可變功率之週期

性流動沸騰研究



Time Periodic Flow Boiling of Refrigerant R-410A due to  
Refrigerant Flow Rate or Heat Flux Oscillations in a Horizontal  
Narrow Annular Duct

研 究 生：許書豪

指 導 老 師：林清發教授

中 華 民 國 九 十 九 年 六 月

狹窄水平雙套管中 R-410A 冷媒流量震盪與可變功率之週期性

流動沸騰研究

Time Periodic Flow Boiling of Refrigerant R-410A due to  
Refrigerant Flow Rate or Heat Flux Oscillations in a Horizontal  
Narrow Annular Duct

研 究 生：許書豪

Student: Shu -Hao Hsu

指 導 老 師：林清發

Advisor: Tsing-Fa Lin

國 立 交 通 大 學



Submitted to Department of Mechanical Engineering

College of Engineering

National Chiao Tung University

In Partial Fulfillment of the Requirements

For the Degree of

Master of Science

In Mechanical Engineering

June 2010

Hsinchu, Taiwan, Republic of China

中華民國 九十九 年 六 月

## 誌謝

兩年的研究生生活在今年年中終於劃下句點。這些年來遇到許多人相識的、不相識的；碰到許多事順意的、不如意的。如今在畢業口試後留在深深的記憶中。能有此機會完成論文真如陳之藩在謝天中所言得之於人者太多出之於己者太少，在這樣一個感恩的篇幅中，首先感謝指導教授林清發博士，在受於教林教授兩年的時光中，深刻感受到一位諄諄學者的風範，在每次實驗細節討論與論文指導潤筆中，所獲得的不僅是實驗結果物理意義深邃的闡釋，更是治學一絲不苟的呈現，這些都令我受益匪淺。

幕然回首兩年前的此時，對於離家到新竹交大求學的我而言，心中真是充滿了既期待又害怕的複雜心情。來到交大這充滿學術研究氣息的生活，讓我覺得在此讀書做研究是一種享受。然而，一想到即將要離開這可愛的校園，不禁令人懷念起在此的點點滴滴。要感謝實驗室許多臥虎藏龍的博士班：張文瑞、陳建安、汪書磊學長們的幫忙及指導。同學游象麟、熊宏嘉、陳俊州的互相砥礪幫忙，當然也少不了一群為實驗室注入活力、帶來歡樂的學弟們：房業勳及楊軒政的幫忙。得之於人者太多，在此一同向所有幫助過我的人致謝。

最後，僅以本文獻給我所關心的人和所有關心我的人。

許書豪

2010, 6 於新竹交大

# 狹窄水平雙套管中R-410A冷媒流量震盪與可變功率之週期性流動沸騰研究

研究生：許書豪

指導教授：林清發

國立交通大學機械工程學系

## 摘要

本研究以實驗方式探討R-410A新冷媒在水平狹窄雙套管中流動沸騰熱傳(含次冷及飽和流動沸騰)及相關氣泡特徵之影響。流道之間隙為 2.0 mm。我們探討了冷媒質通量或熱功率振盪、周期、飽和溫度、以及熱通量對熱傳係數及氣泡特徵的影響。氣泡特徵包含氣泡脫離直徑和頻率以及成核密度可由流場觀測得之。在實驗中，冷媒平均質通量從 300 到 500 kg/m<sup>2</sup>s，振幅為 10,20 和 30%，熱震盪振幅為 10,30 和 50%，周期都分別為 20、60、120s，平均冷媒飽和溫度為 5, 10 和 15°C。

在第一部份探討流量震盪的影響。流量在振盪過程中，在相對應的瞬時壁溫、熱傳遞係數、氣泡脫離直徑、脫離頻率和成核址密度也會有振盪的現象發生，但是當流量振盪的振幅和週期經過時間平均化之後的飽和態流動的暫態流動沸騰熱傳特徵沒有明顯的影響，類似穩態的流動沸騰。然後我們定義單相沸騰、漸歇性沸騰、完全沸騰。除此之外，在高振盪振幅、長週期的情況下對其壁溫會造成更強烈的振盪情況發生。冷媒的飽和溫度和質通量對壁溫的振盪並無比較大的影響。壁溫氣泡脫離直徑、脫離頻率和成核址密度震盪頻率和流量相同。在流量震盪的時候，隨流量減少時振幅所造成成核址密度振盪遠大於氣泡脫離直徑和脫離頻率所以使的壁溫降低、熱傳變好。

在第二部份探討熱功率震盪的影響。熱量在震盪過程中，壁溫、熱傳遞係數、氣泡脫離直徑、脫離頻率和成核址密度也會有振盪的現象發生，但是會有相當明顯的壁溫落後其熱量變化的時間，也就是熱量最高時，壁溫會在過一小段時間才到達最高。另外當熱量振盪的振幅和週期經過時間平均化之後的飽和態流動的暫態流動沸騰熱傳特徵沒有明顯的影響，類似穩態的流動沸騰。在高振盪振幅、長週期的情況下對其壁溫氣泡脫離直徑、脫離頻率和成核址密度會造成更強烈的振盪情況發生。



**Time Periodic Flow Boiling of Refrigerant R-410A due to Refrigerant Flow  
Rate or Heat Flux Oscillations in a Horizontal Narrow Annular Duct**

**Student: Shu -Hao Hsu**

**Advisor: Prof. Tsing-Fa Lin**

**Department of Mechanical Engineering**

**National Chiao Tung University**

**ABSTRACT**

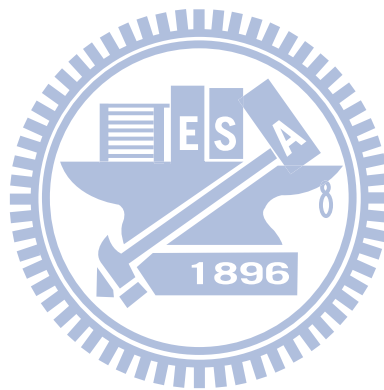
An experiment is carried out here to investigate the heat transfer and associated bubble characteristics in time periodic flow boiling of refrigerant R-410A in a horizontal narrow annular duct subject to a time periodic mass flux or heat flux oscillation. Both the imposed mass flux and heat flux oscillations are in the form of triangular waves. Effects of the refrigerant mass flux oscillation, heat flux oscillation, and refrigerant saturated temperature on the temporal flow boiling heat transfer and bubble characteristics are examined. The bubble characteristics at the middle axial location of the duct are obtained from the flow visualization of the boiling flow, including the time variations of the bubble departure diameter and frequency and active nucleation site density. The present experiment is conducted for the mean refrigerant mass flux  $\bar{G}$  varied from 300 to 500 kg/m<sup>2</sup>s, the amplitude of the mass flux oscillation  $\Delta G$  is fixed at 10, 20 and 30% and the amplitude of the heat flux oscillation  $\Delta q$  is fixed at 10, 30 and 50% of their respective mean levels  $\bar{G}$  and  $\bar{q}$ , and the period of the G or q oscillation is fixed at 20, 60 and 120 seconds. The mean refrigerant saturation temperature  $\bar{T}_{\text{sat}}$  is set at 5, 10 and 15 °C. The gap of the duct is fixed at 2.0 mm. The measured boiling heat transfer data are expressed in terms of the boiling curves and boiling heat transfer coefficients along with the time variations of the heated wall temperature.

In the first part of the present study the measured heat transfer data for the R-410A flow boiling for a constant coolant mass flux are first compared with the time-average data for the flow subject to a time periodic mass flux oscillation. This comparison shows that the mass flux oscillation exerts negligible influences on the time-average boiling heat transfer coefficients. Then, we present the data to elucidate the effects of the experimental parameters on the amplitude of  $T_w$  oscillation over a wide range of the imposed heat flux

covering the single-phase, intermittent and persistent boiling flow regimes. The results indicate that the  $T_w$  oscillation is stronger for a higher amplitude and a longer period of the mass flux oscillation. However, the mean saturated temperature of the refrigerant exhibits much weaker effects on the  $T_w$  oscillation and the mean refrigerant mass flux exerts nonmonotonic effects on the amplitude of the  $T_w$  oscillation. Moreover, the heated wall temperature, bubble departure diameter and frequency, and active nucleation site density are found to oscillate periodically in time and at the same frequency as the mass flux oscillation. Furthermore, the oscillations of  $d_p$ ,  $f$  and  $n_{ac}$  are somewhat like triangular waves. In the first half of the cycle in which the mass flux decreases linear increases in  $d_p$  and  $n_{ac}$  and linear decrease in  $f$  are found. The effect of  $\Delta G/\bar{G}$  on  $n_{ac}$  oscillation is much stronger than on  $d_p$  and  $f$  oscillation causing the heated wall temperature to decrease and heat transfer coefficient to increase at reducing  $G$  in the flow boiling opposed to that in the single-phase flow. But they are only slightly affected by the period of the mass flux oscillation. Besides, a small time lag in the  $T_w$  oscillation is also noted.

In the second part of the present study the measured heat transfer data for the R-410A flow boiling for a constant heat flux are also first compared with the time-average data for a time periodic heat flux oscillation. This comparison shows that the time-average heat transfer coefficients are not affected by the time periodic heat flux oscillation to a significant degree. Then, we present the data to elucidate the effects of the experimental parameters on the amplitude of  $T_w$  oscillation over a wide range of the mean imposed heat flux covering the single-phase, intermittent and persistent boiling flow regimes. The results indicate that the  $T_w$  oscillation gets stronger for a higher amplitude and a longer period of the imposed heat flux oscillation and for a higher mean imposed heat flux. Moreover, a significant time lag in the heated surface temperature oscillation is also noted, which apparently results from the thermal inertia of the copper inner pipe. The effects of the heat flux oscillation at extremely short and long periods have been explored. Due to the existence of the thermal inertia of the heated copper duct, the resulting heated surface temperature does not oscillate with time at an extremely short period of the imposed heat flux oscillation. When the mean imposed heat flux is close to the heat flux corresponding to that for the onset of stable flow boiling, intermittent flow boiling appears. A flow regime map and an empirical correlation are given to delineate the boundaries separating different boiling flow regimes in the annular duct subject to imposed heat flux oscillation. Furthermore, the bubble departure diameter and frequency, and active nucleation site

density also oscillate periodically in time and at the same frequency as the heat flux oscillation. The results also show that the oscillations in  $d_p$ ,  $f$  and  $n_{ac}$  get larger for a long period and a larger amplitude of the imposed heat flux oscillation and for a higher mean imposed heat flux. Furthermore, the bubbles become smaller and more dispersed after the time lag when the imposed heat flux decreases with time. The opposite processes take place at increasing heat flux.



# CONTENTS

<b>ABSTRACT(CHINESE)</b>	<b>i</b>
<b>ABSTRACT(ENGLISH)</b>	<b>ii</b>
<b>CONTENTS</b>	<b>v</b>
<b>LIST OF TABLES</b>	<b>vi</b>
<b>LIST OF FIGURES</b>	<b>viii</b>
<b>NOMENCLATURE</b>	<b>xiv</b>
<b>CHAPTER 1 INTRODUCTION</b>	<b>1</b>
1.1 Motivation	1
1.2 Literature Review	2
1.2.1 Stable Flow Boiling Heat Transfer	2
1.2.2 Time Periodic Flow Boiling Heat Transfer	4
1.2.3 Flow Patterns and Bubble Characteristics	6
1.2.4 Correlation Equations for Flow Boiling Heat Transfer	7
1.3 Objective of the Present Study	8
<b>CHAPTER 2 EXPERIMENTAL APPARATUS AND PROCEDURES</b>	<b>13</b>
2.1 Refrigerant Flow Loop	13
2.2 Test Section	14
2.3 Water Loop for Preheater	15
2.4 Water-Glycol Loop	15
2.5 DC Power Supply	16
2.6 Photographic System	16
2.7 Data Acquisition	17
2.8 Experimental Procedures	17
2.9 Experimental Parameters	18

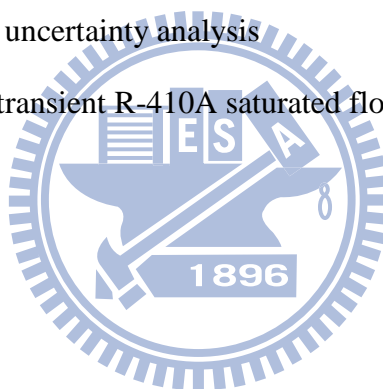
<b>CHAPTER 3</b>	<b>DATA REDUCTION</b>	<b>27</b>
3.1	Flow Boiling Heat Transfer Coefficient	27
3.2	Flow Boiling Bubble Characteristics	29
3.3	Uncertainty Analysis	30
<b>CHAPTER 4</b>	<b>TIME PERIODIC SATURATED FLOW BOILING OF R-410A IN NARROW ANNULAR DUCT DUE TO MASS FLUX OSCILLATION</b>	<b>33</b>
4.1	Single-phase Heat Transfer	33
4.2	Stable and Time-average Saturated Flow Boiling Curves and Heat Transfer Coefficients	34
4.3	Time periodic flow boiling heat transfer characteristics	35
4.4	Intermittent Boiling	38
4.5	Time Periodic Bubble Characteristics in Saturated Flow Boiling	39
<b>CHAPTER 5</b>	<b>TIME PERIODIC SATURATED FLOW BOILING OF R-410A IN A NARROW ANNULAR DUCT DUE TO HEAT FLUX OSCILLATION</b>	<b>101</b>
5.1	Time-average Saturated Flow Boiling Curves and Heat Transfer Coefficients	102
5.2	Time Periodic Flow Boiling Heat Transfer Characteristics	102
5.3	Intermittent Boiling	103
5.4	Effect of Heat Flux Oscillation at Extremely Short and Long Periods	104
5.5	Effect of Heat Flux Oscillation Amplitude	105
5.6	Time Periodic Bubble Characteristics in Saturated Flow Boiling	105
<b>CHAPTER 6</b>	<b>Comparison of Flow Boiling in R-410A and R-134a</b>	<b>161</b>
6.1	Comparison of Saturated Flow Boiling in R-410A and R-134a	161
6.2	Comparison of Time Periodic Flow Boiling in R-410A and R-134a Due to Mass Flux Oscillation	161
6.3	Comparison of Time Periodic Flow Boiling in R-410A and R-134a Due to Heat Flux Oscillation	162

<b>CHAPTER 7 CONCLUDING REMARKS</b>	<b>177</b>
-------------------------------------	------------

REFERENCES	179
------------	-----

## LIST OF TABLES

Table 1.1	Table 1.1 Comparison of some properties of three HFCs refrigerants for air-conditioning and refrigeration applications	9
Table 1.2	Heat transfer correlations for two-phase flow boiling in small channels	10
Table 2.1	List of conditions of the experimental parameters for R-410A (flow rate oscillation)	19
Table 2.2	List of conditions of the experimental parameters for R-410A (heat flux oscillation)	19
Table 2.3	Thermophysical properties of refrigerant R-410A	20
Table 3.1	Summary of the uncertainty analysis	31
Table 5.1	Time scales for transient R-410A saturated flow boiling ( $d=2\text{mm}$ )	109



## LIST OF FIGURES

Fig. 2.1	Schematic of experimental system for the annular duct	21
Fig. 2.2	Schematic of mass flux control loop	22
Fig. 2.3	The detailed arrangement of the test section for the annular duct	23
Fig. 2.4	The cross-sectional view of the annular duct showing the heater and locations of the thermocouples	24
Fig. 2.5	Schematic of heat flux control loop	25
Fig. 4.1	Comparison of the preset single-phase liquid convection heat transfer data with the correlations of Gnielinski and Dittus-Boelter.	43
Fig. 4.2	Stable saturated flow boiling curves for R-410A for various refrigerant mass fluxes at $T_{\text{sat}}=10^{\circ}\text{C}$ and $\delta = 2.0\text{mm}$ .	44
Fig. 4.3	Stable saturated flow boiling curves for R-410A for various refrigerant saturated temperatures at $G = 400\text{ kg/m}^2\text{s}$ and $\delta = 2.0\text{ mm}$ .	45
Fig. 4.4	Time-average flow boiling curves for R-410A for (a) various amplitudes of refrigerant mass flux oscillation at $\bar{T}_{\text{sat}}=10^{\circ}\text{C}$ , $\delta = 2.0\text{ mm}$ , $\bar{G}=400\text{kg/m}^2$ and $t_p = 60\text{ sec.}$ and (b) various periods of refrigerant mass flux oscillation at $\bar{T}_{\text{sat}}=10^{\circ}\text{C}$ , $\delta = 2.0\text{ mm}$ , $\bar{G}=400\text{kg/m}^2$ and $\Delta G/\bar{G}=20\%$ .	46
Fig. 4.5	Stable saturated flow boiling heat transfer coefficient for R-410A for various refrigerant mass fluxes at $\bar{T}_{\text{sat}}=10^{\circ}\text{C}$ .	47
Fig. 4.6	Stable saturated flow boiling heat transfer coefficient for R-410A for various refrigerant saturated temperatures at $G = 400\text{ kg/m}^2\text{s}$ and $\delta = 2.0\text{ mm}$ .	48
Fig. 4.7	Time-average heat transfer coefficients for R-410A for (a) various $\Delta G/\bar{G}$ at $\bar{T}_{\text{sat}}=10^{\circ}\text{C}$ , $\bar{G} = 400\text{ kg/m}^2\text{s}$ , $\delta = 2.0\text{ mm}$ and $t_p = 60\text{ sec.}$ and (b) various $t_p$ at $\bar{T}_{\text{sat}}=10^{\circ}\text{C}$ , $\bar{G} = 400\text{ kg/m}^2\text{s}$ , $\delta = 2.0\text{ mm}$ and $\Delta G/\bar{G}=20\%$	49
Fig. 4.8	Time variations of the measured heated surface temperature for the stable saturated flow boiling of R-410A for various imposed heat fluxes at (a) $\bar{G} = 300\text{ kg/m}^2\text{s}$ and (b) $\bar{G} = 400\text{ kg/m}^2\text{s}$ .	50
Fig. 4.9	Time variations of oscillating refrigerant mass flux and measured wall	

temperature in time periodic saturated flow boiling of R-410A for various imposed heat fluxes at  $\bar{T}_{\text{sat}}=10^{\circ}\text{C}$ ,  $\delta = 2.0\text{mm}$ ,  $t_p = 60$  sec and  $\bar{G} = 400$   $\text{kg/m}^2\text{s}$  with  $\Delta G/\bar{G}=10\%$ . 51

Fig. 4.10 Time variations of oscillating refrigerant mass flux and measured wall temperature in time periodic saturated flow boiling of R-410A for various imposed heat fluxes at  $\bar{T}_{\text{sat}}=10^{\circ}\text{C}$ ,  $\delta = 2.0\text{mm}$ ,  $t_p = 60$  sec and  $\bar{G} = 400\text{kg/m}^2\text{s}$  with  $\Delta G/\bar{G}=20\%$ . 52

Fig. 4.11 Time variations of oscillating refrigerant mass flux and measured wall temperature in time periodic saturated flow boiling of R-410A for various imposed heat fluxes at  $\bar{T}_{\text{sat}}=10^{\circ}\text{C}$ ,  $\delta = 2.0\text{mm}$ ,  $t_p = 60$  sec and  $\bar{G} = 400$   $\text{kg/m}^2\text{s}$  with  $\Delta G/\bar{G}=30\%$ . 53

Fig. 4.12 Time variations of oscillating refrigerant mass flux and measured wall temperature in time periodic saturated flow boiling of R-410A for various imposed heat flux at  $\bar{T}_{\text{sat}}=10^{\circ}\text{C}$ ,  $\delta = 2.0\text{mm}$ ,  $t_p = 20$  sec and  $\bar{G} = 400$   $\text{kg/m}^2\text{s}$  with  $\Delta G/\bar{G}=20\%$ . 54

Fig. 4.13 Time variations of oscillating refrigerant mass flux and measured wall temperature in time periodic saturated flow boiling of R-410A for various imposed heat flux at  $\bar{T}_{\text{sat}}=10^{\circ}\text{C}$ ,  $\delta = 2.0\text{mm}$ ,  $t_p = 120$  sec and  $\bar{G} = 400$   $\text{kg/m}^2\text{s}$  with  $\Delta G/\bar{G}=20\%$ . 55

Fig. 4.14 Time variations of oscillating refrigerant mass flux and measured wall temperature in time periodic saturated flow boiling of R-410A for various imposed heat flux at  $\bar{T}_{\text{sat}}=10^{\circ}\text{C}$ ,  $\delta = 2.0\text{mm}$ ,  $t_p = 60$  sec and  $\bar{G} = 300$   $\text{kg/m}^2\text{s}$  with  $\Delta G/\bar{G}=20\%$ . 56

Fig. 4.15 Time variations of oscillating refrigerant mass flux and measured wall temperature in time periodic saturated flow boiling of R-410A for various imposed heat flux at  $\bar{T}_{\text{sat}}=10^{\circ}\text{C}$ ,  $\delta = 2.0\text{mm}$ ,  $t_p = 60$  sec and  $\bar{G} = 500$   $\text{kg/m}^2\text{s}$  with  $\Delta G/\bar{G}=20\%$ . 57

Fig. 4.16 Time variations of oscillating refrigerant mass flux and measured wall temperature in time periodic saturated flow boiling of R-410A for various imposed heat flux at  $\bar{T}_{\text{sat}}=5^{\circ}\text{C}$ ,  $\delta = 2.0\text{mm}$ ,  $t_p = 60$  sec and  $\bar{G} = 400$   $\text{kg/m}^2\text{s}$  with  $\Delta G/\bar{G}=20\%$ . 58

Fig. 4.17 Time variations of oscillating refrigerant mass flux and measured wall temperature in time periodic saturated flow boiling of R-410A for various imposed heat flux at  $\bar{T}_{\text{sat}}=15^{\circ}\text{C}$ ,  $\delta = 2.0\text{mm}$ ,  $t_p = 60$  sec and  $\bar{G} = 400$



kg/m<sup>2</sup>s with  $\Delta G/\bar{G}=20\%$  . 59

Fig. 4.18 Time variations of flow boiling heat transfer coefficients in time periodic saturated flow boiling of R-410A for various imposed heat fluxes at  $\bar{T}_{\text{sat}}=10^{\circ}\text{C}$  ,  $\delta = 2.0\text{mm}$ ,  $t_p = 60 \text{ sec}$  and  $\bar{G} = 400 \text{ kg/m}^2\text{s}$  with  $\Delta G/\bar{G}=10\%$  . 60

Fig. 4.19 Time variations of flow boiling heat transfer coefficients in time periodic saturated flow boiling of R-410A for various imposed heat fluxes at  $\bar{T}_{\text{sat}}=10^{\circ}\text{C}$  ,  $\delta = 2.0\text{mm}$ ,  $t_p = 60 \text{ sec}$  and  $\bar{G} = 400 \text{ kg/m}^2\text{s}$  with  $\Delta G/\bar{G}=20\%$  . 61

Fig. 4.20 Time variations of flow boiling heat transfer coefficients in time periodic saturated flow boiling of R-410A for various imposed heat fluxes at  $\bar{T}_{\text{sat}}=10^{\circ}\text{C}$  ,  $\delta = 2.0\text{mm}$ ,  $t_p = 60 \text{ sec}$  and  $\bar{G} = 400 \text{ kg/m}^2\text{s}$  with  $\Delta G/\bar{G}=30\%$  . 62

Fig. 4.21 Time variations of flow boiling heat transfer coefficients in time periodic saturated flow boiling of R-410A for various imposed heat fluxes at  $\bar{T}_{\text{sat}}=10^{\circ}\text{C}$  ,  $\delta=2.0\text{mm}$ ,  $t_p = 20 \text{ sec}$  and  $\bar{G} = 400 \text{ kg/m}^2\text{s}$  with  $\Delta G/\bar{G}=20\%$  . 63

Fig. 4.22 Time variations of flow boiling heat transfer coefficients in time periodic saturated flow boiling of R-410A for various imposed heat fluxes at  $\bar{T}_{\text{sat}}=10^{\circ}\text{C}$  ,  $\delta=2.0\text{mm}$ ,  $t_p = 120 \text{ sec}$  and  $\bar{G} = 400 \text{ kg/m}^2\text{s}$  with  $\Delta G/\bar{G}=20\%$  . 64

Fig. 4.23 Time variations of flow boiling heat transfer coefficients in time periodic saturated flow boiling of R-410A for various imposed heat fluxes at  $\bar{T}_{\text{sat}}=10^{\circ}\text{C}$  ,  $\delta=2.0\text{mm}$ ,  $t_p = 60 \text{ sec}$  and  $\bar{G} = 300 \text{ kg/m}^2\text{s}$  with  $\Delta G/\bar{G}=20\%$  . 65

Fig. 4.24 Time variations of flow boiling heat transfer coefficients in time periodic saturated flow boiling of R-410A for various imposed heat fluxes at  $\bar{T}_{\text{sat}}=10^{\circ}\text{C}$  ,  $\delta=2.0\text{mm}$ ,  $t_p = 60 \text{ sec}$  and  $\bar{G} = 500 \text{ kg/m}^2\text{s}$  with  $\Delta G/\bar{G}=20\%$  . 66

Fig. 4.25 Time variations of flow boiling heat transfer coefficients in time periodic saturated flow boiling of R-410A for various imposed heat fluxes at  $\bar{T}_{\text{sat}}=5^{\circ}\text{C}$  ,  $\delta=2.0\text{mm}$ ,  $t_p = 60 \text{ sec}$  and  $\bar{G} = 400 \text{ kg/m}^2\text{s}$  with  $\Delta G/\bar{G}=20\%$  . 67

Fig. 4.26 Time variations of flow boiling heat transfer coefficients in time periodic

saturated flow boiling of R-410A for various imposed heat fluxes at  $\bar{T}_{\text{sat}}=15^{\circ}\text{C}$ ,  $\delta=2.0\text{mm}$ ,  $t_p=60\text{sec}$  and  $\bar{G}=400\text{kg/m}^2\text{s}$  with  $\Delta\bar{G}/\bar{G}=20\%$ .

68

Fig. 4.27 Effects of imposed heat flux on amplitudes of wall temperature oscillation in time periodic saturated flow boiling of R-410A for various amplitudes of mass flux oscillation (a), periods of mass flux oscillation (b), mean mass fluxes (c), and refrigerant saturated temperatures (d).

69

Fig. 4.28 Flow regime map for some periodic R410A flow boiling regimes at  $\delta=2\text{mm}$ , and  $t_p=60\text{sec}$  for various saturated temperatures and mean mass fluxes.

71

Fig. 4.29 Photos of boiling flow in stable saturated flow boiling of R-410A for various imposed heat flux at  $\delta=2.0\text{mm}$ ,  $t_p=60\text{sec}$ ,  $\bar{G}=400\text{kg/m}^2\text{s}$  and  $\bar{T}_{\text{sat}}=10^{\circ}\text{C}$  &  $\bar{T}_{\text{sat}}=15^{\circ}\text{C}$ .

72

Fig. 4.30 Photos of boiling flow in stable saturated flow boiling of R-410A for various imposed heat flux at  $\delta=2.0\text{mm}$ ,  $t_p=60\text{sec}$ ,  $\bar{T}_{\text{sat}}=10^{\circ}\text{C}$ ,  $\bar{G}=300\text{kg/m}^2\text{s}$  and  $500\text{kg/m}^2\text{s}$ .

73

Fig. 4.31 Photos of intermittent saturated flow boiling flow of R-410A at selected time instants in a typical periodic cycle for  $q=4\text{kW/m}^2$  at  $\bar{G}=400\text{kg/m}^2\text{s}$ ,  $\Delta\bar{G}/\bar{G}=10\%$ ,  $\bar{T}_{\text{sat}}=10^{\circ}\text{C}$ ,  $\delta=2.0\text{mm}$  and  $t_p=60\text{sec}$ .

74

Fig. 4.32 Photos of intermittent saturated flow boiling flow of R-410A at selected time instants in a typical periodic cycle for  $q=4\text{kW/m}^2$  at  $\bar{G}=400\text{kg/m}^2\text{s}$ ,  $\Delta\bar{G}/\bar{G}=20\%$ ,  $\bar{T}_{\text{sat}}=10^{\circ}\text{C}$ ,  $\delta=2.0\text{mm}$  and  $t_p=60\text{sec}$ .

75

Fig. 4.33 Photos of intermittent saturated flow boiling flow of R-410A at selected time instants in a typical periodic cycle for  $q=4\text{kW/m}^2$  at  $\bar{G}=400\text{kg/m}^2\text{s}$ ,  $\Delta\bar{G}/\bar{G}=30\%$ ,  $\bar{T}_{\text{sat}}=10^{\circ}\text{C}$ ,  $\delta=2.0\text{mm}$  and  $t_p=60\text{sec}$ .

76

Fig. 4.34 Photos of intermittent saturated flow boiling flow of R-410A at selected time instants in a typical periodic cycle for  $q=4\text{kW/m}^2$  at  $\bar{G}=400\text{kg/m}^2\text{s}$ ,  $\Delta\bar{G}/\bar{G}=20\%$ ,  $\bar{T}_{\text{sat}}=10^{\circ}\text{C}$ ,  $\delta=2.0\text{mm}$  and  $t_p=20\text{sec}$ .

77

Fig. 4.35 Photos of intermittent saturated flow boiling flow of R-410A at selected time instants in a typical periodic cycle for  $q=4\text{kW/m}^2$  at  $\bar{G}=400\text{kg/m}^2\text{s}$ ,  $\Delta\bar{G}/\bar{G}=20\%$ ,  $\bar{T}_{\text{sat}}=10^{\circ}\text{C}$ ,  $\delta=2.0\text{mm}$  and  $t_p=120\text{sec}$ .

78

Fig. 4.36 Photos of intermittent saturated flow boiling flow of R-410A at selected time instants in a typical periodic cycle for  $q=3\text{kW/m}^2$  at  $\bar{G}=300$

kg/m<sup>2</sup>s,  $\Delta G/\bar{G} = 20\%$  ,  $\bar{T}_{\text{sat}} = 10^{\circ}\text{C}$  ,  $\delta = 2.0\text{mm}$  and  $t_p = 60\text{sec}$ . 79

Fig. 4.37 Photos of intermittent saturated flow boiling flow of R-410A at selected time instants in a typical periodic cycle for  $q = 5\text{ kW/m}^2$  at  $\bar{G} = 500\text{ kg/m}^2\text{s}$ ,  $\Delta G/\bar{G} = 20\%$  ,  $\bar{T}_{\text{sat}} = 10^{\circ}\text{C}$  ,  $\delta = 2.0\text{mm}$  and  $t_p = 60\text{sec}$ . 80

Fig. 4.38 Photos of intermittent saturated flow boiling flow of R-410A at selected time instants in a typical periodic cycle for  $q = 4\text{ kW/m}^2$  at  $\bar{G} = 400\text{ kg/m}^2\text{s}$ ,  $\Delta G/\bar{G} = 20\%$  ,  $\bar{T}_{\text{sat}} = 5^{\circ}\text{C}$  ,  $\delta = 2.0\text{mm}$  and  $t_p = 60\text{sec}$ . 81

Fig. 4.39 Photos of intermittent saturated flow boiling flow of R-410A at selected time instants in a typical periodic cycle for  $q = 4\text{ kW/m}^2$  at  $\bar{G} = 400\text{ kg/m}^2\text{s}$ ,  $\Delta G/\bar{G} = 20\%$  ,  $\bar{T}_{\text{sat}} = 15^{\circ}\text{C}$  ,  $\delta = 2.0\text{mm}$  and  $t_p = 60\text{sec}$ . 82

Fig. 4.40 Photos of time periodic saturated flow boiling flow of R-410A at selected time instants in a typical periodic cycle for  $q = 10\text{ kW/m}^2$  at  $\bar{G} = 400\text{ kg/m}^2\text{s}$ ,  $\Delta G/\bar{G} = 10\%$  ,  $\bar{T}_{\text{sat}} = 10^{\circ}\text{C}$  ,  $\delta = 2.0\text{mm}$  and  $t_p = 60\text{sec}$ . 83

Fig. 4.41 Photos of time periodic saturated flow boiling flow of R-410A at selected time instants in a typical periodic cycle for  $q = 10\text{ kW/m}^2$  at  $\bar{G} = 400\text{ kg/m}^2\text{s}$ ,  $\Delta G/\bar{G} = 20\%$  ,  $\bar{T}_{\text{sat}} = 10^{\circ}\text{C}$  ,  $\delta = 2.0\text{mm}$  and  $t_p = 60\text{sec}$ . 84

Fig. 4.42 Photos of time periodic saturated flow boiling flow of R-410A at selected time instants in a typical periodic cycle for  $q = 10\text{ kW/m}^2$  at  $\bar{G} = 400\text{ kg/m}^2\text{s}$ ,  $\Delta G/\bar{G} = 30\%$  ,  $\bar{T}_{\text{sat}} = 10^{\circ}\text{C}$  ,  $\delta = 2.0\text{mm}$  and  $t_p = 60\text{sec}$ . 85

Fig. 4.43 Photos of time periodic saturated flow boiling flow of R-410A at selected time instants in a typical periodic cycle for  $q = 10\text{ kW/m}^2$  at  $\bar{G} = 400\text{ kg/m}^2\text{s}$ ,  $\Delta G/\bar{G} = 20\%$  ,  $\bar{T}_{\text{sat}} = 10^{\circ}\text{C}$  ,  $\delta = 2.0\text{mm}$  and  $t_p = 20\text{sec}$ . 86

Fig. 4.44 Photos of time periodic saturated flow boiling flow of R-410A at selected time instants in a typical periodic cycle for  $q = 10\text{ kW/m}^2$  at  $\bar{G} = 400\text{ kg/m}^2\text{s}$ ,  $\Delta G/\bar{G} = 20\%$  ,  $\bar{T}_{\text{sat}} = 10^{\circ}\text{C}$  ,  $\delta = 2.0\text{mm}$  and  $t_p = 120\text{sec}$ . 87

Fig. 4.45 Photos of time periodic saturated flow boiling flow of R-410A at selected time instants in a typical periodic cycle for  $q = 10\text{ kW/m}^2$  at  $\bar{G} = 300\text{ kg/m}^2\text{s}$ ,  $\Delta G/\bar{G} = 20\%$  ,  $\bar{T}_{\text{sat}} = 10^{\circ}\text{C}$  ,  $\delta = 2.0\text{mm}$  and  $t_p = 60\text{sec}$ . 88

Fig. 4.46 Photos of time periodic saturated flow boiling flow of R-410A at selected time instants in a typical periodic cycle for  $q = 10\text{ kW/m}^2$  at  $\bar{G} = 500\text{ kg/m}^2\text{s}$ ,  $\Delta G/\bar{G} = 20\%$  ,  $\bar{T}_{\text{sat}} = 10^{\circ}\text{C}$  ,  $\delta = 2.0\text{mm}$  and  $t_p = 60\text{sec}$ . 89

Fig. 4.47 Photos of time periodic saturated flow boiling flow of R-410A at selected

time instants in a typical periodic cycle for  $q= 10 \text{ kW/m}^2$  at  $\bar{G}=500 \text{ kg/m}^2\text{s}$ ,  $\Delta\bar{G}/\bar{G} = 20\%$ ,  $\bar{T}_{\text{sat}}=5^\circ\text{C}$ ,  $\delta=2.0\text{mm}$  and  $t_p= 60\text{sec}$ . 90

Fig. 4.48 Photos of time periodic saturated flow boiling of R-410A at selected time instants in a typical periodic cycle for  $q= 10 \text{ kW/m}^2$  at  $\bar{G}=500 \text{ kg/m}^2\text{s}$ ,  $\Delta\bar{G}/\bar{G} = 20\%$ ,  $\bar{T}_{\text{sat}}=15^\circ\text{C}$ ,  $\delta=2.0\text{mm}$  and  $t_p= 60\text{sec}$ . 91

Fig. 4.49 Time variations of mean bubble departure diameter in time periodic saturated flow boiling for  $q= 10 \text{ kW/m}^2$  at  $\bar{T}_{\text{sat}}=10^\circ\text{C}$ ,  $\bar{G}=400 \text{ kg/m}^2\text{s}$ ,  $\delta=2.0\text{mm}$  (a) for various oscillation amplitudes of  $G$  at  $t_p= 60\text{sec}$ , and (b) for various periods of  $G$  oscillation at  $\Delta\bar{G}/\bar{G} = 20\%$ . 92

Fig. 4.50 Time variations of mean bubble departure diameter in time periodic saturated flow boiling of R-410A for  $q= 10 \text{ kW/m}^2$  at  $\bar{T}_{\text{sat}}=10^\circ\text{C}$ ,  $\bar{G}=400 \text{ kg/m}^2\text{s}$ ,  $\delta=2.0\text{mm}$  (a) for various mean mass fluxes at  $\bar{T}_{\text{sat}}=10^\circ\text{C}$ , and (b) for various mean saturated temperatures at  $\bar{G}=400\text{kg/m}^2\text{s}$ . 93

Fig. 4.51 Time variations of mean bubble departure frequency in time periodic saturated flow boiling of R-410A for  $q= 10 \text{ kW/m}^2$  at  $\bar{T}_{\text{sat}}=10^\circ\text{C}$ ,  $\bar{G}=400 \text{ kg/m}^2\text{s}$ ,  $\delta=2.0\text{mm}$  (a) for various oscillation amplitudes of  $G$  at  $t_p=60\text{sec}$ , and (b) for various periods of  $G$  oscillation at  $\Delta\bar{G}/\bar{G} = 20\%$ . 94

Fig. 4.52 Time variations of mean bubble departure frequency in time periodic saturated flow boiling of R-410A for  $q= 10 \text{ kW/m}^2$  at  $\delta=2.0\text{mm}$ ,  $\bar{G}=400 \text{ kg/m}^2\text{s}$ ,  $\Delta\bar{G}/\bar{G} = 20\%$ ,  $t_p=60\text{sec}$ , and (a) for various mean fluxes at  $\bar{T}_{\text{sat}}=10^\circ\text{C}$ , and (b) for various mean saturated temperatures at  $\bar{G} = 400\text{kg/m}^2\text{s}$ . 95

Fig. 4.53 Time variations of mean active nucleation site density in time periodic saturated flow boiling of R-410A for  $q= 10 \text{ kW/m}^2$  at  $\delta=2.0\text{mm}$ ,  $\bar{G}=400 \text{ kg/m}^2\text{s}$ ,  $\Delta\bar{G}/\bar{G} = 20\%$ ,  $t_p=60\text{sec}$ , and (a) for various oscillation amplitudes of  $G$  at  $t_p=60\text{sec}$ , and (b) for various periods of  $G$  oscillation at  $\Delta\bar{G}/\bar{G} = 20\%$ . 96

Fig. 4.54 Time variations of mean active nucleation site density in time periodic saturated flow boiling of R-410A for  $q= 10 \text{ kW/m}^2$  at  $\delta=2.0\text{mm}$ ,  $\bar{G}=400 \text{ kg/m}^2\text{s}$ ,  $\Delta\bar{G}/\bar{G} = 20\%$ ,  $t_p=60\text{sec}$ , and (a) for various mean fluxes at  $\bar{T}_{\text{sat}}=10^\circ\text{C}$ , and (b) for various mean saturated temperatures at  $\bar{G} = 400\text{kg/m}^2\text{s}$ . 97

- Fig. 4.55 Variations of bubble departure diameter (a), departure frequency (b), and active nucleation site density (c) with R-410A mass flux for time-periodic saturated flow boiling of R-410A. 98
- Fig. 5.1 Time-average flow boiling curves for R-410A for (a) various amplitudes of imposed heat flux oscillation at  $T_{\text{sat}}=10^{\circ}\text{C}$ ,  $\delta = 2.0$  mm,  $G=400\text{kg/m}^2$  and  $t_p = 60$  sec. and (b) various periods of heat flux oscillation at  $T_{\text{sat}} = 10^{\circ}\text{C}$ ,  $\delta = 2.0$  mm,  $G=400\text{kg/m}^2$  and  $\Delta q/\bar{q}=30\%$ . 110
- Fig. 5.2 Time-average flow boiling heat transfer coefficients for R-410A for (a) various amplitudes of imposed heat flux oscillation at  $T_{\text{sat}} = 10^{\circ}\text{C}$ ,  $\delta = 2.0$  mm,  $G=400\text{kg/m}^2$  and  $t_p = 60$  sec. and (b) various periods of heat flux oscillation at  $T_{\text{sat}}=10^{\circ}\text{C}$ ,  $\delta = 2.0$  mm,  $G=400\text{kg/m}^2$  and  $\Delta q/\bar{q}=30\%$ . 111
- Fig. 5.3 Time variations of imposed heat flux and measured wall temperature in time periodic saturated flow boiling of R-410A at  $T_{\text{sat}} = 10^{\circ}\text{C}$ ,  $\delta = 2.0\text{mm}$ ,  $t_p = 60$  sec and  $G = 400\text{kg/m}^2\text{s}$  with  $\Delta q/\bar{q}=10\%$ . 112
- Fig. 5.4 Time variations of imposed heat flux and measured wall temperature in time periodic saturated flow boiling of R-410A at  $T_{\text{sat}} = 10^{\circ}\text{C}$ ,  $\delta = 2.0\text{mm}$ ,  $t_p = 60$  sec and  $G = 400\text{kg/m}^2\text{s}$  with  $\Delta q/\bar{q}=30\%$ . 113
- Fig. 5.5 Time variations of imposed heat flux and measured wall temperature in time periodic saturated flow boiling of R-410A at  $T_{\text{sat}} = 10^{\circ}\text{C}$ ,  $\delta = 2.0\text{mm}$ ,  $t_p = 60$  sec and  $G = 400\text{kg/m}^2\text{s}$  with  $\Delta q/\bar{q} = 50\%$ . 114
- Fig. 5.6 Time variations of imposed heat flux and measured wall temperature in time periodic saturated flow boiling of R-410A at  $T_{\text{sat}} = 10^{\circ}\text{C}$ ,  $\delta = 2.0\text{mm}$ ,  $t_p = 20$  sec and  $G = 400\text{kg/m}^2\text{s}$  with  $\Delta q/\bar{q} = 30\%$ . 115
- Fig. 5.7 Time variations of imposed heat flux and measured wall temperature in time periodic saturated flow boiling of R-410A at  $T_{\text{sat}} = 10^{\circ}\text{C}$ ,  $\delta = 2.0\text{mm}$ ,  $t_p = 120$  sec and  $G = 400\text{kg/m}^2\text{s}$  with  $\Delta q/\bar{q} = 30\%$ . 116
- Fig. 5.8 Time variations of imposed heat flux and measured wall temperature in time periodic saturated flow boiling of R-410A at  $T_{\text{sat}} = 10^{\circ}\text{C}$ ,  $\delta = 2.0\text{mm}$ ,  $t_p = 60$  sec and  $G = 300\text{kg/m}^2\text{s}$  with  $\Delta q/\bar{q} = 30\%$ . 117
- Fig. 5.9 Time variations of imposed heat flux and heat transfer coefficient in time periodic saturated flow boiling of R-410A at  $T_{\text{sat}} = 10^{\circ}\text{C}$ ,  $\delta = 2.0\text{mm}$ ,  $t_p = 60$  sec and  $G = 500\text{kg/m}^2\text{s}$  with  $\Delta q/\bar{q} = 30\%$ . 118
- Fig. 5.10 Time variations of imposed heat flux and heat transfer coefficient in time

- periodic saturated flow boiling of R-410A at  $T_{\text{sat}} = 15^{\circ}\text{C}$ ,  $\delta = 2.0\text{mm}$ ,  $t_p = 60\text{ sec}$  and  $G = 400\text{kg/m}^2\text{s}$  with  $\Delta q/\bar{q} = 30\%$ . 119
- Fig. 5.11 Time variations of imposed heat flux and heat transfer coefficient in time periodic saturated flow boiling of R-410A at  $T_{\text{sat}} = 5^{\circ}\text{C}$ ,  $\delta = 2.0\text{mm}$ ,  $t_p = 60\text{ sec}$  and  $G = 400\text{kg/m}^2\text{s}$  with  $\Delta q/\bar{q} = 30\%$ . 120
- Fig. 5.12 Time variations of imposed heat flux and heat transfer coefficient in time periodic saturated flow boiling of R-410A at  $T_{\text{sat}} = 10^{\circ}\text{C}$ ,  $\delta = 2.0\text{mm}$ ,  $t_p = 60\text{ sec}$  and  $G = 400\text{kg/m}^2\text{s}$  with  $\Delta q/\bar{q} = 10\%$ . 121
- Fig. 5.13 Time variations of imposed heat flux and heat transfer coefficient in time periodic saturated flow boiling of R-410A at  $T_{\text{sat}} = 10^{\circ}\text{C}$ ,  $\delta = 2.0\text{mm}$ ,  $t_p = 60\text{ sec}$  and  $G = 400\text{kg/m}^2\text{s}$  with  $\Delta q/\bar{q} = 30\%$ . 122
- Fig. 5.14 Time variations of imposed heat flux and heat transfer coefficient in time periodic saturated flow boiling of R-410A at  $T_{\text{sat}} = 10^{\circ}\text{C}$ ,  $\delta = 2.0\text{mm}$ ,  $t_p = 60\text{ sec}$  and  $G = 400\text{kg/m}^2\text{s}$  with  $\Delta q/\bar{q} = 50\%$ . 123
- Fig. 5.15 Time variations of imposed heat flux and heat transfer coefficient in time periodic saturated flow boiling of R-410A at  $T_{\text{sat}} = 10^{\circ}\text{C}$ ,  $\delta = 2.0\text{mm}$ ,  $t_p = 20\text{ sec}$  and  $G = 400\text{kg/m}^2\text{s}$  with  $\Delta q/\bar{q} = 30\%$ . 124
- Fig. 5.16 Time variations of imposed heat flux and heat transfer coefficient in time periodic saturated flow boiling of R-410A at  $T_{\text{sat}} = 10^{\circ}\text{C}$ ,  $\delta = 2.0\text{mm}$ ,  $t_p = 120\text{ sec}$  and  $G = 400\text{kg/m}^2\text{s}$  with  $\Delta q/\bar{q} = 30\%$ . 125
- Fig. 5.17 Time variations of imposed heat flux and heat transfer coefficient in time periodic saturated flow boiling of R-410A at  $T_{\text{sat}} = 10^{\circ}\text{C}$ ,  $\delta = 2.0\text{mm}$ ,  $t_p = 60\text{ sec}$  and  $G = 300\text{kg/m}^2\text{s}$  with  $\Delta q/\bar{q} = 30\%$ . 126
- Fig. 5.18 Time variations of imposed heat flux and heat transfer coefficient in time periodic saturated flow boiling of R-410A at  $T_{\text{sat}} = 10^{\circ}\text{C}$ ,  $\delta = 2.0\text{mm}$ ,  $t_p = 60\text{ sec}$  and  $G = 500\text{kg/m}^2\text{s}$  with  $\Delta q/\bar{q} = 30\%$ . 127
- Fig. 5.19 Time variations of imposed heat flux and heat transfer coefficient in time periodic saturated flow boiling of R-410A at  $T_{\text{sat}} = 15^{\circ}\text{C}$ ,  $\delta = 2.0\text{mm}$ ,  $t_p = 60\text{ sec}$  and  $G = 400\text{kg/m}^2\text{s}$  with  $\Delta q/\bar{q} = 30\%$ . 128
- Fig. 5.20 Time variations of imposed heat flux and heat transfer coefficient in time periodic saturated flow boiling of R-410A at  $T_{\text{sat}} = 5^{\circ}\text{C}$ ,  $\delta = 2.0\text{mm}$ ,  $t_p = 60\text{ sec}$  and  $G = 400\text{kg/m}^2\text{s}$  with  $\Delta q/\bar{q} = 30\%$ . 129

- Fig. 5.21 Flow regime map for time periodic R-410A flow boiling regimes at  $\delta = 2\text{mm}$  and  $t_p = 60\text{ sec}$  for various saturated temperatures and mass fluxes. 130
- Fig. 5.22 Time variations of imposed heat flux and wall temperature at  $z = 80\text{ mm}$  for  $t_p = 2\text{ sec}$ . 131
- Fig. 5.23 Time variations of imposed heat flux and wall temperature at  $z = 80\text{ mm}$  for  $t_p = 120\text{ sec}$ . 132
- Fig. 5.24 Time variations of imposed heat flux and wall temperature at  $z = 80\text{ mm}$  for  $t_p = 600\text{ sec}$ . 133
- Fig. 5.25 Time variations of imposed heat flux and wall temperature at  $z = 80\text{ mm}$  for various  $\Delta q/\bar{q}$ . 134
- Fig. 5.26 Photos of time periodic intermittent flow boiling of R-410A at selected time instants in a typical periodic cycle at  $T_{\text{sat}} = 10^\circ\text{C}$ ,  $G = 400\text{ kg/m}^2\text{s}$ ,  $\delta = 2.0\text{mm}$  and  $t_p = 60\text{ sec}$  for  $\bar{q} = 4\text{kW/m}^2$ ,  $\Delta q/\bar{q} = 10\%$ . 135
- Fig. 5.27 Photos of time periodic intermittent flow boiling of R-410A at selected time instants in a typical periodic cycle at  $T_{\text{sat}} = 10^\circ\text{C}$ ,  $G = 400\text{ kg/m}^2\text{s}$ ,  $\delta = 2.0\text{mm}$  and  $t_p = 60\text{ sec}$  for  $\bar{q} = 4\text{kW/m}^2$ ,  $\Delta q/\bar{q} = 30\%$ . 136
- Fig. 5.28 Photos of time periodic intermittent flow boiling of R-410A at selected time instants in a typical periodic cycle at  $T_{\text{sat}} = 10^\circ\text{C}$ ,  $G = 400\text{ kg/m}^2\text{s}$ ,  $\delta = 2.0\text{mm}$  and  $t_p = 60\text{ sec}$  for  $\bar{q} = 4\text{kW/m}^2$ ,  $\Delta q/\bar{q} = 50\%$  137
- Fig. 5.29 Photos of time periodic intermittent flow boiling of R-410A at selected time instants in a typical periodic cycle at  $T_{\text{sat}} = 10^\circ\text{C}$ ,  $G = 400\text{ kg/m}^2\text{s}$ ,  $\delta = 2.0\text{mm}$  and  $t_p = 20\text{ sec}$  for  $\bar{q} = 4\text{kW/m}^2$ ,  $\Delta q/\bar{q} = 10\%$ . 138
- Fig. 5.30 Photos of time periodic intermittent flow boiling of R-410A at selected time instants in a typical periodic cycle at  $T_{\text{sat}} = 10^\circ\text{C}$ ,  $G = 400\text{ kg/m}^2\text{s}$ ,  $\delta = 2.0\text{mm}$  and  $t_p = 120\text{ sec}$  for  $\bar{q} = 4\text{kW/m}^2$ ,  $\Delta q/\bar{q} = 30\%$ . 139
- Fig. 5.31 Photos of time periodic intermittent flow boiling of R-410A at selected time instants in a typical periodic cycle at  $T_{\text{sat}} = 10^\circ\text{C}$ ,  $G = 400\text{ kg/m}^2\text{s}$ ,  $\delta = 2.0\text{mm}$  and  $t_p = 60\text{ sec}$  for  $\bar{q} = 3\text{kW/m}^2$ ,  $\Delta q/\bar{q} = 30\%$ . 140
- Fig. 5.32 Photos of time periodic intermittent flow boiling of R-410A at selected time instants in a typical periodic cycle at  $T_{\text{sat}} = 10^\circ\text{C}$ ,  $G = 400\text{ kg/m}^2\text{s}$ ,  $\delta = 2.0\text{mm}$  and  $t_p = 60\text{ sec}$  for  $\bar{q} = 5\text{kW/m}^2$ ,  $\Delta q/\bar{q} = 30\%$ . 141



- Fig. 5.33 Photos of time periodic intermittent flow boiling of R-410A at selected time instants in a typical periodic cycle at  $T_{\text{sat}} = 5^{\circ}\text{C}$ ,  $G = 400 \text{ kg/m}^2\text{s}$ ,  $\delta = 2.0\text{mm}$  and  $t_p = 60 \text{ sec}$  for  $\bar{q} = 5\text{kW/m}^2$ ,  $\Delta q/\bar{q} = 30\%$ . 142
- Fig. 5.34 Photos of time periodic intermittent flow boiling of R-410A at selected time instants in a typical periodic cycle at  $T_{\text{sat}} = 15^{\circ}\text{C}$ ,  $G = 400 \text{ kg/m}^2\text{s}$ ,  $\delta = 2.0\text{mm}$  and  $t_p = 60 \text{ sec}$  for  $\bar{q} = 4\text{kW/m}^2$ ,  $\Delta q/\bar{q} = 30\%$ . 143
- Fig. 5.35 Photos of time periodic saturated flow boiling of R-410A at selected time instants in a typical periodic cycle at  $T_{\text{sat}} = 10^{\circ}\text{C}$ ,  $G = 400 \text{ kg/m}^2\text{s}$ ,  $\delta = 2.0\text{mm}$  and  $t_p = 60 \text{ sec}$  for  $\bar{q} = 10\text{kW/m}^2$ ,  $\Delta q/\bar{q} = 10\%$  144
- Fig. 5.36 Photos of time periodic saturated flow boiling of R-410A at selected time instants in a typical periodic cycle at  $T_{\text{sat}} = 10^{\circ}\text{C}$ ,  $G = 400 \text{ kg/m}^2\text{s}$ ,  $\delta = 2.0\text{mm}$  and  $t_p = 60 \text{ sec}$  for  $\bar{q} = 10\text{kW/m}^2$ ,  $\Delta q/\bar{q} = 30\%$ . 145
- Fig. 5.37 Photos of time periodic saturated flow boiling of R-410A at selected time instants in a typical periodic cycle at  $T_{\text{sat}} = 10^{\circ}\text{C}$ ,  $G = 400 \text{ kg/m}^2\text{s}$ ,  $\delta = 2.0\text{mm}$  and  $t_p = 60 \text{ sec}$  for  $\bar{q} = 10\text{kW/m}^2$ ,  $\Delta q/\bar{q} = 30\%$ . 146
- Fig. 5.38 Photos of time periodic saturated flow boiling of R-410A at selected time instants in a typical periodic cycle at  $T_{\text{sat}} = 10^{\circ}\text{C}$ ,  $G = 400 \text{ kg/m}^2\text{s}$ ,  $\delta = 2.0\text{mm}$  and  $t_p = 20 \text{ sec}$  for  $\bar{q} = 10\text{kW/m}^2$ ,  $\Delta q/\bar{q} = 30\%$ . 147
- Fig. 5.39 Photos of time periodic saturated flow boiling of R-410A at selected time instants in a typical periodic cycle at  $T_{\text{sat}} = 10^{\circ}\text{C}$ ,  $G = 400 \text{ kg/m}^2\text{s}$ ,  $\delta = 2.0\text{mm}$  and  $t_p = 120 \text{ sec}$  for  $\bar{q} = 10\text{kW/m}^2$ ,  $\Delta q/\bar{q} = 30\%$ . 148
- Fig. 5.40 Photos of time periodic saturated flow boiling of R-410A at selected time instants in a typical periodic cycle at  $T_{\text{sat}} = 10^{\circ}\text{C}$ ,  $G = 300 \text{ kg/m}^2\text{s}$ ,  $\delta = 2.0\text{mm}$  and  $t_p = 60\text{sec}$  for  $\bar{q} = 10\text{kW/m}^2$ ,  $\Delta q/\bar{q} = 30\%$ . 149
- Fig. 5.41 Photos of time periodic saturated flow boiling of R-410A at selected time instants in a typical periodic cycle at  $T_{\text{sat}} = 10^{\circ}\text{C}$ ,  $G = 500 \text{ kg/m}^2\text{s}$ ,  $\delta = 2.0\text{mm}$  and  $t_p = 60\text{sec}$  for  $\bar{q} = 10\text{kW/m}^2$ ,  $\Delta q/\bar{q} = 30\%$ . 150
- Fig. 5.42 Photos of time periodic saturated flow boiling of R-410A at selected time instants in a typical periodic cycle at  $T_{\text{sat}} = 5^{\circ}\text{C}$ ,  $G = 400 \text{ kg/m}^2\text{s}$ ,  $\delta = 2.0\text{mm}$  and  $t_p = 60\text{sec}$  for  $\bar{q} = 10\text{kW/m}^2$ ,  $\Delta q/\bar{q} = 30\%$ . 151
- Fig. 5.43 Photos of time periodic saturated flow boiling of R-410A at selected time instants in a typical periodic cycle at  $T_{\text{sat}} = 15^{\circ}\text{C}$ ,  $G = 400 \text{ kg/m}^2\text{s}$ ,  $\delta = 2.0\text{mm}$  and  $t_p = 60\text{sec}$  for  $\bar{q} = 10\text{kW/m}^2$ ,  $\Delta q/\bar{q} = 30\%$ . 152



- Fig. 5.44 Time variations of mean bubble departure diameter in time periodic saturated flow boiling of R-410A for  $\bar{q} = 10 \text{ kW/m}^2$  at  $T_{\text{sat}} = 10^\circ\text{C}$ ,  $G = 400 \text{ kg/m}^2\text{s}$  and  $\delta = 2.0 \text{ mm}$  for (a) various  $\Delta q/\bar{q}$  at  $t_p = 60 \text{ sec}$  and (b) various  $t_p$  at  $\Delta q/\bar{q} = 30\%$ . 153
- Fig. 5.45 Time variations of mean bubble departure diameter in time periodic saturated flow boiling of R-410A for  $\bar{q} = 10 \text{ kW/m}^2$  at  $\Delta q/\bar{q} = 30\%$ ,  $t_p = 60 \text{ sec}$  and  $\delta = 2.0 \text{ mm}$  for (a) various  $G$  at  $T_{\text{sat}} = 10^\circ\text{C}$  and (b) various  $T_{\text{sat}}$  at  $G = 400 \text{ kg/m}^2\text{s}$ . 154
- Fig. 5.46 Time variations of mean bubble departure frequency in time periodic saturated flow boiling of R-410A for  $\bar{q} = 10 \text{ kW/m}^2$  at  $T_{\text{sat}} = 10^\circ\text{C}$ ,  $G = 400 \text{ kg/m}^2\text{s}$  and  $\delta = 2.0 \text{ mm}$  for (a) various  $\Delta q/\bar{q}$  at  $t_p = 60 \text{ sec}$  and (b) various  $t_p$  at  $\Delta q/\bar{q} = 30\%$  155
- Fig. 5.47 Time variations of mean bubble departure frequency in time periodic saturated flow boiling of R-410A for  $\bar{q} = 10 \text{ kW/m}^2$  at  $\Delta q/\bar{q} = 30\%$ ,  $t_p = 60 \text{ sec}$  and  $\delta = 2.0 \text{ mm}$  for (a) various  $G$  at  $T_{\text{sat}} = 10^\circ\text{C}$  and (b) various  $T_{\text{sat}}$  at  $G = 400 \text{ kg/m}^2\text{s}$ . 156
- Fig. 5.48 Time variations of mean active nucleation site density in time periodic saturated flow boiling of R-410A for  $\bar{q} = 10 \text{ kW/m}^2$  at  $T_{\text{sat}} = 10^\circ\text{C}$ ,  $G = 400 \text{ kg/m}^2\text{s}$  and  $\delta = 2.0 \text{ mm}$  for (a) various  $\Delta q/\bar{q}$  at  $t_p = 60 \text{ sec}$  and (b) various  $t_p$  at  $\Delta q/\bar{q} = 30\%$  157
- Fig. 5.49 Time variations of mean bubble departure frequency in time periodic saturated flow boiling of R-410A for  $\bar{q} = 10 \text{ kW/m}^2$  at  $\Delta q/\bar{q} = 30\%$ ,  $t_p = 60 \text{ sec}$  and  $\delta = 2.0 \text{ mm}$  for (a) various  $G$  at  $T_{\text{sat}} = 10^\circ\text{C}$  and (b) various  $T_{\text{sat}}$  at  $G = 400 \text{ kg/m}^2\text{s}$ . 158
- Fig. 5.50 Variations of bubble departure diameter (a), departure frequency (b), and active nucleation site density (c) with heat flux for time-periodic saturated flow boiling of R-410A. 159
- Fig. 6.1 Stable saturated flow boiling curves(a) and heat transfer coefficients for various refrigerant at  $T_{\text{sat}} = 10^\circ\text{C}$ ,  $G = 400 \text{ kg/m}^2\text{s}$  and  $\delta = 2.0 \text{ mm}$ . 163
- Fig. 6.2 Time variations of oscillating refrigerant mass flux and measured heated wall temperature in time periodic saturated flow boiling of R-410A (a) and R-134a (b) for various imposed heat fluxes at  $\bar{T}_{\text{sat}} = 10^\circ\text{C}$ ,  $\delta = 2.0 \text{ mm}$ ,  $t_p = 60 \text{ sec}$  and  $\bar{G} = 400 \text{ kg/m}^2\text{s}$  with  $\Delta G/\bar{G} = 20\%$ . 164

- Fig. 6.3 Time variations of flow boiling heat transfer coefficients in time periodic saturated flow boiling of R-410A (a) and R-134a (b) for various imposed heat fluxes at  $\bar{T}_{\text{sat}}=10^{\circ}\text{C}$ ,  $\delta = 2.0\text{mm}$ ,  $t_p = 60 \text{ sec}$  and  $\bar{G} = 400 \text{ kg/m}^2\text{s}$  with  $\Delta G/\bar{G}=20\%$ . 165
- Fig. 6.4 Variations of amplitudes of heated wall temperature with imposed heat flux for various refrigerants R-410A & R-134a. 166
- Fig. 6.5 Photos of time periodic saturated flow boiling of R-134a at selected time instants in a typical periodic cycle for  $q= 10 \text{ kW/m}^2$  at  $\bar{G}=400 \text{ kg/m}^2\text{s}$ ,  $\Delta G/\bar{G} = 20\%$ ,  $T_{\text{sat}} = 10^{\circ}\text{C}$ ,  $\delta=2.0\text{mm}$  and  $t_p= 60\text{sec}$ . 167
- Fig. 6.6 Photos of time periodic saturated flow boiling of R-410A at selected time instants in a typical periodic cycle for  $q= 10 \text{ kW/m}^2$  at  $\bar{G}=400 \text{ kg/m}^2\text{s}$ ,  $\Delta G/\bar{G} = 20\%$ ,  $T_{\text{sat}} = 10^{\circ}\text{C}$ ,  $\delta=2.0\text{mm}$  and  $t_p= 60\text{sec}$ . 168
- Fig. 6.7 Time variations of mean bubble departure diameter (a), bubble departure frequency(b), and active nucleation site density(c) in time periodic saturated flow boiling of R-410A & R-134a. 169
- Fig. 6.8 Time variations of imposed heat flux and measured wall temperature in time periodic saturated flow boiling of R-410A (a) and R-134a (b) for various imposed heat fluxes at  $T_{\text{sat}} = 10^{\circ}\text{C}$ ,  $\delta = 2.0\text{mm}$ ,  $t_p = 60 \text{ sec}$  and  $G = 400\text{kg/m}^2\text{s}$  with  $\Delta q/\bar{q} = 30\%$ . 171
- Fig. 6.9 Time variations of imposed heat flux and heat transfer coefficients in time periodic saturated flow boiling of R-410A (a) and R-134a (b) at  $T_{\text{sat}} = 10^{\circ}\text{C}$ ,  $\delta = 2.0\text{mm}$ ,  $t_p = 60 \text{ sec}$  and  $G = 400\text{kg/m}^2\text{s}$  with  $\Delta q/\bar{q} = 30\%$ . 172
- Fig. 6.10 Photos of time periodic saturated flow boiling of R-134a at selected time instants in a typical periodic cycle for  $q= 10 \text{ kW/m}^2$  at  $T_{\text{sat}} = 10^{\circ}\text{C}$ ,  $\delta = 2.0\text{mm}$ ,  $t_p = 60 \text{ sec}$  and  $G = 400\text{kg/m}^2\text{s}$  with  $\Delta q/\bar{q} = 30\%$ . 173
- Fig. 6.11 Photos of time periodic saturated flow boiling of R-410A at selected time instants in a typical periodic cycle for  $q= 10 \text{ kW/m}^2$  at  $T_{\text{sat}} = 10^{\circ}\text{C}$ ,  $\delta = 2.0\text{mm}$ ,  $t_p = 60 \text{ sec}$  and  $G = 400\text{kg/m}^2\text{s}$  with  $\Delta q/\bar{q} = 30\%$ . 174
- Fig. 6.12 Time variations of mean bubble departure diameter (a), bubble departure frequency (b), and active nucleation site density(c) in time periodic saturated flow boiling of R-410A & R-134a. 175

## NOMENCLATURE

A	heat transfer area of the annular duct, m <sup>2</sup>
Bo	Boiling number, $Bo = \frac{q}{G \cdot i_{fg}}$ , dimensionless
c <sub>p</sub>	specific heat, J/kg°C
D	diameter of duct, m
D <sub>h</sub>	hydraulic diameter, m, $D_h = 4A_c/P = (D_o - D_i)$
d <sub>p</sub>	bubble departure diameter, m
f	bubble generation frequency
f <sub>f</sub>	friction factor
F <sub>f</sub>	fluid-dependent parameter
Fr	Froude number, $Fr = \frac{G^2}{\rho_l^2 \cdot g \cdot D_h}$ , dimensionless
g	acceleration due to gravity, m/s <sup>2</sup>
G	mass flux, kg/m <sup>2</sup> s
$\bar{G}$	mean mass flux, kg/m <sup>2</sup> s
h	heat transfer coefficient, W/m <sup>2</sup> °C
i <sub>fg</sub>	enthalpy of vaporization, J/kg
I	measured current from DC power supply, A
Ja <sub>1</sub>	Jakob number based on $\Delta T_{sat}$ , $Ja_1 = \frac{\rho_l \cdot C_p \cdot \Delta T_{sat}}{\rho_g \cdot i_{fg}}$ , dimensionless
Ja <sub>2</sub>	Jakob number based on $\Delta T_{sub}$ , $Ja_2 = \frac{\rho_l \cdot C_p \cdot \Delta T_{sub}}{\rho_g \cdot i_{fg}}$ , dimensionless
k	thermal conductivity, W/m°C
L	heating length of the annular duct, m
N <sub>ac</sub>	active nucleation site density, n/m <sup>2</sup>

$N_{\text{conf}}$	Confinement number, $N_{\text{conf}} = \frac{(\sigma/(g\Delta\rho))^{0.5}}{D_h}$ , dimensionless
$Nu$	Nusselt number, $Nu = \frac{hD_h}{k}$ , dimensionless
$P$	system pressure, kpa
$Pr$	Prandtl number, $Pr = \frac{\mu \cdot C_p}{k}$ , dimensionless
$q$	average imposed heat flux, $W/m^2$
$Q$	heat transfer rate, W
$Ra$	Rayleigh number, $g\beta\Delta TH^3/\alpha\nu$
$Re$	$Re = \frac{GD_h}{\mu_l}$
$Re_l$	Reynolds number of liquid in two-phase flow, $Re_l = \frac{GD_h(1-x)}{\mu_l}$ , dimensionless
$t_p$	period of mass flux oscillation, sec
$T$	temperature, °C
$T_{\text{sat}}$	saturated temperature of the refrigerant, °C
$V$	measured voltage from DC power supply, V
$We_l$	Weber number based on liquid, $We_l = \frac{G^2 \cdot D}{\rho_l \cdot \sigma}$ , dimensionless
$X_{tt}$	Martnelli parameter
$x$	vapor quality
$z$	coordinate (downstream coordinate for annular duct flow), mm

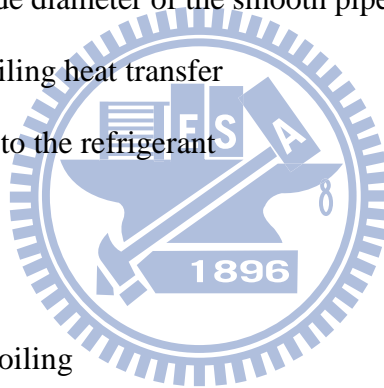
### Greek Symbols

$\Delta G$	amplitude of mass flux oscillation, $kg/m^2s$
$\Delta T$	temperature difference, °C
$\delta$	gap size, mm
$\mu$	viscosity, $N \cdot s/m^2$
$\rho$	density, $kg/m^3$

$\Delta\rho$	density difference, $\Delta\rho = \rho_l - \rho_g$ , $\text{kg/m}^3$
$\sigma$	surface tension, N/m
$\varepsilon$	mean absolute error, $\varepsilon = \frac{1}{N} \sum_1^N \left  \frac{\text{predicted value} - \text{experimental value}}{\text{experimental value}} \right $ , %
$\lambda$	fraction of data predicted to within $\pm 30\%$ , %

### Subscripts

ave	average
exp	experimental value
fg	difference between liquid phase and vapor phase
g	vapor
i, o	inside and outside diameter of the smooth pipe
l	all-liquid nonboiling heat transfer
n	net power input to the refrigerant
r	refrigerant side
s	heater surface
sat	saturated flow boiling
sub	subcooled flow boiling
tp	two-phase
w	duct wall



# CHAPTER 1

## INTRODUCTION

### 1.1 Motivation

It is well known that refrigerant R-22 is one of the most widely used working fluids in air-conditioning systems. However, the use of the chlorofluorocarbons refrigerants (CFCs) such as CFC-11, CFC-12, CFC-113, CFC-114, CFC-115 and the hydrochlorofluorocarbons refrigerants (HCFCs) such as R-22 have resulted in the destruction of the ozone layer in the arctic area and the global warming. Thus the Montreal Protocol signed in 1987 only allowed the use of the CFCs up to 1996 and the HCFCs are going to be phased out in 2020. Therefore, the substitution of CFCs and HCFCs becomes urgent. The hydrofluorocarbons refrigerants (HFCs) such as R-134a, R-407C, R-410A, R-410b and R-507 have been considered to be suitable and some are currently in use.

Refrigerant R-410A has zero ozone depletion potential and is recognized as the main replacement to R-22. It is a high pressure and near-azeotropic binary mixture refrigerant consisting of 50 wt% of R-32 and 50 wt% of R-125. This near-azeotropic mixture has a very small temperature glide (0.1 °C) and behaves like a single component refrigerant. The operating conditions of refrigerants R-410A, R-407C and R-134a are compared in Table 1.1.

In the past, the use of variable frequency compressors in air-conditioning and refrigeration systems to meet the changing heat load is found to significantly improve their energy efficiencies. It is important to note that the two-phase flow in these systems is subject to time varying refrigerant flow rate and heat flux. The use of compact heat exchangers to promote the thermal performance of these systems is beneficial because of their low thermal resistance, very high ratio of surface area to volume, and lower total mass of working fluids.

Additionally, it is also well known that the IC junction temperature must be kept under 85°C to avoid being damaged and to maintain its normal operation. The use of the direct liquid cooling accompanying with phase change can greatly increase the heat

removal rate, but the power dissipation in IC chips are often time dependent in practical operation. Therefore, the transient oscillatory flow boiling resulting from varying heat load needs to be explored.

In view of the possible enhancement of heat transfer in small channels, we require to develop smaller and more compact evaporators and condensers. Despite the great effort has been paid to the investigation of single- and two-phase flow and heat transfer in small channels from the heat transfer research community, the detailed heat transfer mechanisms in the small-channel flow boiling remain controversial. A detailed understanding of the phase-change processes in-small channel flow subject to time varying coolant flow rate or imposed heat flux is essential in thermal design for electronics cooling and air-conditioning and refrigeration systems. Although considerable research has been carried out in the past for the two-phase flow and heat transfer under the condition of fixed flow rate and imposed heat flux, the corresponding research for the transient oscillatory flow rate or imposed heat flux remains largely unexplored. In the present study an initial attempt is made to unravel how the characteristics of flow boiling and associated heat transfer and bubble motion in a narrow annular channel are affected by given time periodic refrigerant flow rate or imposed heat flux oscillation.

## 1.2 Literature Review

In sizing the small channels, Kandlikar and Grande [1] proposed that  $D_h > 3\text{mm}$  for the conventional channels,  $200\mu\text{m} < D_h < 3\text{mm}$  for the mini-channels,  $10\mu\text{m} < D_h < 200\mu\text{m}$  for the micro-channels,  $0.1\mu\text{m} < D_h < 10\mu\text{m}$  for the transitional channels,  $1\mu\text{m} < D_h < 10\mu\text{m}$  for the transitional micro-channels,  $0.1\mu\text{m} < D_h < 1\mu\text{m}$  for the transitional nano-channels, and  $D_h \leq 0.1\mu\text{m}$  for the molecular nano-channels. On the other hand, Kew and Cornwell [2]

introduced a dimensionless group named as the Confinement number,  $N_{\text{conf}} = \frac{(\sigma/(g\Delta\rho))^{0.5}}{D_h}$ ,

which represents the importance of the restriction of the flow by the small size of the channel. They showed that when  $N_{\text{conf}} > 0.5$ , the effects of the channel size become very important.

### 1.2.1 Stable Flow Boiling Heat Transfer

The literature on stable flow boiling heat transfer is reviewed at first. Here the stable flow boiling denotes the boiling subject to constant imposed flow rate and heat flux. It is

well known that boiling heat transfer for flow inside channels can be regarded as a combination of convective heat transfer from the wall to the liquid and nucleate boiling at the wall. In convection-dominated flow boiling, the heat transfer coefficient is independent of the wall heat flux but increases with increasing mass flux and vapor quality. On the contrary, in nucleation-dominated flow boiling the boiling heat transfer coefficient is independent of the mass flux and vapor quality. However, it increases with the heat flux and is sensitive to the refrigerant saturation pressure level.

Hsieh et al. [3] examined the stable flow boiling heat transfer and associated bubble characteristics of R-410A in a horizontal annular duct. They showed that raising the imposed heat flux can increase the boiling heat transfer coefficient. Wang et al. [4] compared the two-phase heat transfer characteristics of refrigerants R-22 and R-410A. Their results indicate that the evaporative heat transfer coefficients for R-410A are about 10-20% higher than that for R-22. Ebisu and Torikoshi [5] examined the evaporative heat transfer for R-410A, R-407C and R-22. They showed that evaporative heat transfer coefficient of R-410A was about 20% higher than that of R-22 up to the vapor quality of 0.4, while the heat transfer coefficients of R-410A and R-22 became almost the same at the quality of 0.6.

Fujita et al. [6] studied flow boiling heat transfer and pressure drop for refrigerant R-123 in a horizontal small-diameter tube ( $D_h=1.12$  mm). They showed that the flow boiling was dominated by bubble nucleation in the small tube rather than the forced convective evaporation because of very weak influences of the mass velocity and vapor quality. Hsieh et al. [7] investigate the effect of the channel size on R-407C saturated flow boiling heat transfer in a narrow annular duct. The gap of the duct is fixed at 1.0 mm and 2.0 mm. They reported that the saturated flow boiling heat transfer coefficient increased with a decrease in the duct gap. Besides, Lie & Lin [8,9] examined the flow boiling heat transfer and associated bubble characteristics of R-134a in the same duct ( $D_h = 2&4$  mm). The effects of the refrigerant mass flux and saturated temperature on the boiling heat transfer coefficient were found to be small.

Flow boiling of refrigerants R-11 and R-123 in a small horizontal copper tube ( $D_h=1.95$  mm) investigated by Bao et al. [10] showed that the heat transfer coefficients were independent of the refrigerant mass flux and vapor quality, but were a strong function of the heat flux. Nucleate boiling was noted to be the dominant mechanism over a wide



range of flow conditions. A similar study from Tran et al. [11] examined flow boiling of refrigerant R-12 in small circular and rectangular channels ( $D_h=2.46, 2.4$  mm). Two distinct two-phase flow regions were noted, convective boiling dominant region at lower wall superheat ( $< 2.75K$ ) and nucleate boiling dominant region at higher wall superheat ( $> 2.75K$ ). Kandlikar and Steinke [12] noted that for a high liquid-vapor density ratio ( $\rho_l/\rho_g$ ), the convective effects dominated as the vapor quality increased. This led to an increasing trend in the boiling heat transfer coefficient at increasing vapor quality. A high Boiling number results in a higher nucleate boiling contribution, which tends to decrease as the vapor quality increases. This leads to a decreasing trend in heat transfer coefficient with increasing vapor quality. Oh et al. [13] examined flow boiling heat transfer characteristics of R-134a in a capillary tube heat exchanger ( $D_h=2, 1, 0.75$  mm). Their data showed that the heat transfer in the forced convection dominated region was more influenced by the mass flux than by the Boiling number and the heat transfer coefficient was controlled by the Reynolds number.

Yin et al. [14] investigated the subcooled flow boiling heat transfer for refrigerant R-134a flowing in a horizontal annular duct. The gap of duct is 5.16 mm. They found that boiling heat transfer is insignificantly affected by the mass flux, imposed heat flux and refrigerant saturation temperature. But a decrease in the inlet subcooling results in much better heat transfer. Chen et al. [15] investigate how the channel size affects the subcooled flow boiling heat transfer of refrigerant R-407C in a horizontal narrow annular duct ( $D_h = 1.0$  and  $2.0$  mm). They indicated that the temperature overshoot at ONB is relatively significant. Besides, the subcooled flow boiling heat transfer coefficient increases with a reduction in the duct gap, but decreases with an increase in the inlet liquid subcooling.

### **1.2.2 Time Dependent Flow Boiling Heat Transfer**

In examining two-phase flow instabilities in a circular channel ( $D_h=9.525$ mm), Comakli et al [16] found that the periods and amplitudes of the pressure drop and density wave type oscillations decreased with decreasing mass flow rate and increased with decreasing inlet temperature. Recently, some detailed characteristics associated with these intrinsic instabilities were investigated through experimental measurement and theoretical modeling. An experimental investigation of thermal instabilities in forced convection boiling of R-11 in a vertical annular channel ( $D_h =17$  mm) was conducted by Kakac et al. [17]. Two-phase homogeneous model along with the thermodynamic equilibrium

assumption were used to predict the condition leading to the thermal oscillation. And their predicted periods and amplitudes of the oscillations were in a good agreement with their measured data. In a continuing study for R-11 in a horizontal tube of 106 cm long, Ding et al. [18] examined the dependence of the oscillation amplitude and period on the system parameters and located the boundaries of various types of oscillations on the steady-state pressure-drop versus mass flux characteristic curves.

Wang et al. [19] noted that the boiling onset in a upward flow of subcooled water in a vertical tube of 7.8-m long connected with a liquid surge tank could cause substantial flow pressure and density-wave oscillations. These boiling onset oscillations were attributed to a sudden increase of pressure-drop across the channel and a large fluctuation in the water flow rate at the onset of nucleate boiling. This in turn results from the feedback of the pressure-drop and flow rate by the system, causing the location of the boiling onset to move in and out of the channel. Experimental investigation on the critical heat flux was conducted under the forced flow oscillation condition by Ozawa et al. [20]. They found that the reduction of the CHF from the steady state value was larger for increases in the amplitude and period of the flow oscillation.

Kotaoka et al. [21] investigated transient flow boiling of water over a platinum wire subject to an exponentially increasing heat input. The wire diameter and length respectively vary from 0.8 to 1.5 mm and from 3.93 to 10.4 cm. Two types of transient boiling were observed. In A-type (heating period is 20 ms, 50 ms or 10 s) boiling, the transient maximum critical heat flux increases with decreasing heating period at constant flow velocity. Whereas in the B-type (heating period is 5ms, 10ms, or 14ms) boiling, the transient maximum critical heat flux decreases first with the period and then increases. Two-phase flow and heat transfer in a small tube of 1 mm in the internal diameter using R-141b as the working fluid were studied by Lin et al. [22]. At a low heat flux input, a relatively constant wall temperature was obtained. Besides, forced convection evaporation occurs towards the outlet end of the tube and the fluctuations in the wall temperature are small. With a high heat flux input, however, significant fluctuation in the wall temperature can appear. This is caused by a combination of time varying heat transfer coefficient and time varying local pressure and fluid saturation temperature.

The dynamic behavior for a horizontal boiling channel connected with a surge tank for liquid supply has also received some attention. Mawasha and Gross [23] used a

constitutive model containing a cubic nonlinearity combined with a homogeneous two-phase flow model to simulate the pressure-drop oscillation. Their prediction is matched with the measured data. Later, the channel wall heat capacity effects were included [24] to allow the wall temperature and heat transfer coefficient to vary with time.

### 1.2.3 Flow Patterns and Bubble Characteristics

To elucidate the flow boiling heat transfer mechanisms in small channels, we require to delineate the prevailing flow regimes. Cornwell and Kew [25] examined various flow regimes for boiling of refrigerant R-113 in a vertical rectangular multi-channel with  $D_h = 1.03$  and  $1.64$  mm. Based on visualization of the flow and measurement of the heat transfer, three flow regimes have been suggested, namely, the isolated bubble, confined bubble and annular-slug bubble flows. In the isolated bubble regime, heat transfer coefficient depends on the heat flux and hydraulic diameter. In the confined bubble regime, heat transfer coefficient depends on the heat flux, mass flux, vapor quality and hydraulic diameter. While in the annular-slug bubble regime, heat transfer coefficient depends on the mass flux, vapor quality and hydraulic diameter.

However, bubble characteristics such as bubble departure frequency, growth, sliding and departure size are known to play an important role in flow boiling heat transfer. Visualization of subcooled flow boiling of upward water flow in a vertical annular channel ( $D_h=19$  mm) by Situ et al. [26] suggested that generally the bubble departure frequency increased as the heat flux increased. The averaged bubble growth rate drops sharply after lift-off. An experimental analysis was carried out by Thorncroft et al. [27] to investigate the vapor bubble growth and departure in vertical upflow and downflow boiling of FC-87. They found that the bubble growth rate and bubble departure diameter increased with the Jacob number (increasing  $\Delta T_{sat}$ ) and decreased at increasing mass flux in both the upflow and downflow. Hsieh et al. [3] examined saturated flow boiling heat transfer and associated bubble characteristics of R-410A in a horizontal annular duct. They concluded that a higher refrigerant mass flux results in a smaller bubble departing size and a higher bubble departure frequency.

Kandlikar [28] examined the subcooled flow boiling of water in a rectangular horizontal channel. They noted that the bubble growth was slow at high subcooling and the departure diameter decreased as the flow rate increased. The influence of the heat flux on

the waiting time between two cycles is much weaker. Chang et al. [29] studied the near-wall bubble behavior for water in a vertical rectangular channel with one-side heated ( $D_h=4.44$  mm). They showed that the size of coalesced bubbles decreased for an increase in the mass flux and the mass flux only exhibited a strong effect on the bubble size. Del Balle and Kenning [30] examined the subcooled flow boiling for water in a rectangular vertical channel and found that the maximum bubble diameter was independent of the heat flux. Yin et al. [14] examined the bubble characteristics associated with subcooled flow boiling of refrigerant R-134a in a horizontal annular duct ( $D_h=10.31$  mm). They noted that the bubble departure frequency was suppressed by raising the mass flux and subcooling of R-134a, and only the subcooling showed a strong effect on the bubble size. The study of water boiling in a horizontal rectangular channel with one side heated ( $D_h=40$  mm) conducted by Maurus et al. [31] found that the waiting time between two bubble cycles decreased significantly at increasing mass flux. An experimental study on bubble rise path after the departure from a nucleation site for water in a vertical upward tube ( $D_h=20$  mm) by Okawa et al. [32] suggested that the inertia force significantly influenced the onset of bubble detachment and the shear force induced a lift force to detach the bubble from the wall.

#### **1.2.4 Correlation Equations for Flow Boiling Heat Transfer**

An early general correlation model for the flow boiling in channels was proposed by Chen [33]. He divided the boiling heat transfer coefficient into two parts: a microconvective (nucleate boiling) contribution estimated by the pool boiling correlations and a macroconvective (non-boiling forced convection) contribution estimated by the single-phase correlation such as the Dittus-Boelter equation [34]. In order to account for the diminished contribution of nucleate boiling, as the convective boiling effects increased at a higher vapor quality he introduced the enhanced factor  $E$  and suppression factor  $S$  to respectively accommodate the forced convective and nucleate boiling contributions. Gungor and Winterton [35] modified the Chen's correlation and proposed the correlations for the enhanced and suppression factors. A new correlation from Liu and Winterton [36] introduced an asymptotic function to predict the heat transfer coefficient for vertical and horizontal flows in tubes and annuli. Zhang et al. [37] modified the Chen's correlation to predict the heat transfer in mini channels. Besides, Tran et al. [11] modified the heat transfer correlation of Lazarek and Black [38] with the Reynolds number of the flow

replaced by the Weber number to eliminate viscous effects in favor of the surface tension. Similar correlations were proposed by Fujita et al. [6].

Kandlikar [39] proposed a general correlation for saturated flow boiling heat transfer inside horizontal and vertical tubes. The correlation was based on a model utilizing the contributions due to nucleate boiling and convective mechanisms. In a following study [40,41], he developed correlations to predict transition, laminar and deep laminar flows in minichannels and microchannels. A new correlation for boiling heat transfer in small diameter channels was proposed by Kew and Cornwell [2]. The correlation was divided by three flow regimes based on the values of the Confinement number. Some empirical correlation equations proposed in the literature for flow boiling heat transfer coefficients in the small channels were summarized in Table 1.2.

### **1.3 Objective of the Present Study**

The above literature review clearly indicates that the dynamic instabilities in the flow boiling of refrigerant in a channel subject to constant inlet flow rate and uniform heating has received considerable attention. However, the unstable characteristics of flow boiling heat transfer and associated bubble behavior in a channel subject to imposed time varying refrigerant flow rate or time varying heat flux remain largely unexplored. In this study, an experimental study will be carried out to investigate how an imposed time periodic inlet flow rate oscillation affects the time dependent saturated R-410A flow boiling heat transfer and associated bubble characteristics in a horizontal narrow annular duct with a constant imposed heat flux. On the other hand, another experimental study will be conducted to examine how a time periodic imposed heat flux oscillation affects the time dependent saturated R-410A flow boiling heat transfer and associated bubble characteristics in the same horizontal narrow annular duct with a constant inlet flow rate. Effects of the period and amplitude of the imposed flow rate or heat flux oscillation on the boiling characteristics will be examined in detail for various average refrigerant mass fluxes, imposed heat fluxes, and refrigerant saturated temperatures of R-410A.

**Table 1.1 Comparison of some properties of three HFCs refrigerants for air-conditioning and refrigeration applications**

Refrigerant	R-410A	R-134a	R-407C
Component	HFC-32/125	HFC-134a	HFC-32/125/134a
Wt %	50/50%	100 %	23/25/52%
Comparison with R-22	<ol style="list-style-type: none"> <li>1. near-azeotropic refrigerant.</li> <li>2. the working pressure is five times than R-22.</li> <li>3. the friction pressure drop is smaller.</li> </ol>	<ol style="list-style-type: none"> <li>1. the lower working pressure.</li> <li>2. the friction pressure drop is larger in the same capability of freezing.</li> </ol>	<ol style="list-style-type: none"> <li>1. zeotropic refrigerant, and the components charge easy.</li> <li>2. the working pressure is same with R-22.</li> </ol>
The energy efficiency ratio relative to R-22	94~100	72~90	90~97
Molecule quality	72.6	102.3	85.62
Remark	<ol style="list-style-type: none"> <li>1. the design of system must to consider the strong and optimum elements.</li> </ol>	<ol style="list-style-type: none"> <li>1. the volume of operating system becomes larger.</li> <li>2. the air-out volume of compress is larger.</li> </ol>	<ol style="list-style-type: none"> <li>1. the solutions of variation of R-407C components.</li> </ol>
Green-house effect (100 years)	1725	1300	1526
Toxicity limit (kg/m <sup>3</sup> )	0.44	0.25	0.31
Boiling point (°C)	-52.7 R32 (-51.8°C) / R125 (-48.5°C)	-26.2	-43.6 R32 (-51.8°C) / R125 (-48.5°C) / R134a (-26.2°C)
Temperature glides	< 1 °F	—	10 °F

**Table 1.2 Heat transfer correlations for flow boiling in small channels**

Reference	Fluid	Heat Transfer Coefficient Correlations	Application Range
Lazarek and Black [38]	R-113	$h_p = 30 \text{Re}_l^{0.857} \text{Bo}^{0.714} (k_l / D)$	$D: 3.1\text{mm}$ $G: 125 - 750 \text{kg}/\text{m}^2\text{s}$ $q: 14 - 380 \text{kW}/\text{m}^2$ $\text{Re}: 860 - 5500$ $\text{Bo}: 2.3 \times 10^{-4} - 76 \times 10^{-4}$ $P: 1.3 - 4.1 \text{bar}$
Y. Fujita et al. [6]	R-123	$h_p = 0.884 G^{0.143} q^{0.714}$	$D: 1.12\text{mm}$ $G: 50 - 400 \text{kg}/\text{m}^2\text{s}$ $q: 5 - 20 \text{kW}/\text{m}^2$ $\text{Re}: 135 - 1070$ $P: 1.1 - 1.2 \text{bar}$ $x: -0.2 - 0.9$ $\text{Bo}: 3 \times 10^{-4} - 8.9 \times 10^{-4}$
Z.Y. Bao et al. [10]	R-11, R-123	$h_p/h_l = 1 + 3000 \text{Bo}^{0.86} + 1.12(x/(1-x))^{0.75} (\rho_l/\rho_g)^{0.41}$	$D: 1.95\text{mm}$ $G: 50 - 1800 \text{kg}/\text{m}^2\text{s}$ $q: 50 - 200 \text{kW}/\text{m}^2$ $\text{Re}: 860 - 5500$ $P: 2 - 5 \text{bar}$ $x: -0.3 - 0.9$ $\Delta T_{sat}: 5 - 15^\circ\text{C}$
T.N. Tran et al. [11]	R-12, R113	$h_p = (8.4 \times 10^{-5}) (\text{Bo}^2 \text{We}_l)^{0.3} \left( \frac{\rho_l}{\rho_g} \right)^{-0.4}$ for $\Delta T > 2.75^\circ\text{C}$	$D: 2.46\text{mm}, 2.92\text{mm}; D_h = 2.4\text{mm}$ $G: 44 - 832 \text{kg}/\text{m}^2\text{s}$ $q: 7.5 - 129 \text{kW}/\text{m}^2$ $P_r: 0.045 - 0.2$ $\text{Bo}: 2 \times 10^{-4} - 23 \times 10^{-4}$ $\Delta T_{sat}: 2.8 - 18.2^\circ\text{C}$

Table 1.2 Continued

Reference	Fluid	Heat Transfer Coefficient Correlations	Application Range
Z. Liu and R.H.S. Winterton [36]		$h_{ip}^2 = (Fh_l)^2 + (Sh_{pool})^2$ $h_l = 0.023(k_l/D) \text{Re}_l^{0.8} \text{Pr}_l^{0.4}$ $h_{pool} = 55P_r^{0.12} (-\ln P_r)^{-0.55} M^{-0.5} q$ $F = (1 + x \text{Pr}_l (\rho_l / \rho_g - 1))^{0.35}$ $S = (1 + 0.55F^{0.1} \text{Re}_l^{0.16})^{-1}$	$D : 2.95 - 32 \text{ mm} \quad G : 12.4 - 8179.3 \text{ kg/m}^2 \text{ s}$ $q : 0.35 - 2620 \text{ kW/m}^2 \quad \text{Re} : 568.9 - 87500$ $P_r : 0.0023 - 0.895 \quad x : 0 - 0.948$ $Fr : 2.66 \times 10^{-4} - 2240 \quad \text{Pr}_l : 0.83 - 9.1$
W. Zhang et al. [37]	R-11, R-123	$h_{ip} = S \cdot h_{pool} + F \cdot h_l$ $S = 1 / (1 + 2.53 \times 10^{-6} \text{Re}_l^{1.17})$ $h_{pool} = 0.00122 \left( \frac{k_l^{0.79} c_{pl}^{0.45} \rho_l^{0.49}}{\sigma^{0.5} \mu_l^{0.29} i_{fg}^{0.24} \rho_g^{0.24}} \right) (T_w - T_{sat})^{0.24} \Delta P_{sat}^{0.75}$ $F = \text{Max} \left( 0.64 \left( 1 + \frac{C}{X_{tt}} + \frac{1}{X_{tt}^2} \right)^{0.5}, 1 \right)$	$D_h = 0.78 - 6 \text{ mm} \quad G = 23.4 - 2939 \text{ kg/m}^2 \text{ s}$ $q = 2.95 - 2511 \text{ kW/m}^2 \quad P = 0.101 - 1.21 \text{ MPa}$



**Table 1.2 Continued**

Reference	Fluid	Heat Transfer Coefficient Correlations	Application Range
S.G. Kandlikar [40]		$h_p/h_l = \text{maximun of } \begin{cases} [h_p/h_l]_{NBD} \\ [h_p/h_l]_{CBD} \end{cases}$ <p>Nucleate boiling dominant region</p> $[h_p/h_l]_{NBD} = 0.6683(\rho_l/\rho_g)^{0.1} x^{0.16} (1-x)^{0.64} f(Fr_l) + 1058Bo^{0.7} F_f (1-x)^{0.8}$ <p>Convection boiling dominant region</p> $[h_p/h_l]_{CBD} = 1.1360(\rho_l/\rho_g)^{0.45} x^{0.72} (1-x)^{0.08} f_2(Fr_l) + 667.2Bo^{0.7} F_f (1-x)^{0.8}$ $f(Fr_l) = \begin{cases} (25Fr_l)^{0.3} & \text{for } Fr_l < 0.04 \text{ for H.-tube} \\ 1 & \text{for } Fr_l > 0.04 \text{ for H. \& V.-tube} \end{cases}$	$D: 8.1 - 20mm$ $G: 123 - 1523 kg/m^2s$ $q: 0.8 - 82.1 kW/m^2$ $P: 1.6 - 14.8 bar$ $x: 0 - 0.868$ $Bo: 0.035 \times 10^{-4} - 24.02 \times 10^{-4}$

## CHAPTER 2

### EXPERIMENTAL APPARATUS AND PROCEDURES

The experimental apparatus used in the present study to investigate the time periodic flow boiling heat transfer and associated bubble characteristics of refrigerant R-410A in a horizontal narrow annular duct is schematically shown in Fig. 2.1. The apparatus consists of three main loops, namely, a refrigerant loop, a water-glycol loop and a hot-water loop for preheater, along with a data acquisition system and a 100V-50A DC power supply. Refrigerant R-410A is circulated in the refrigerant loop. We need to control the temperature and flow rate in the water-glycol loop to obtain enough cooling capacity for condensing the refrigerant vapor and for maintaining the refrigerant liquid at a preset temperature. The liquid refrigerant in the narrow duct is heated by passing a DC current through the inner pipe in the test section from the DC power supply. To unravel the bubble characteristics in the boiling of the refrigerant on the heating surface, a high-speed movie camera connected to a photographic microscope is set up beside the test section to observe the boiling flow.

#### 2.1 Refrigerant Flow Loop

The main components in the refrigerant loop include an oil-free variable-speed refrigerant pump, an accumulator, a mass flow meter, a test section, a condenser, a sub-cooler, a receiver, a filter/dryer, and four sight glasses. An AC motor is used to control the refrigerant mass flow rate through the change of the inverter frequency. Figure 2.2 schematically show the control loop for the mass flux oscillation. Specifically, the temporal oscillation of the coolant flow rate can be implemented by an optional external control of the inverter through a programmable DC current or voltage signal sequence. The time-average refrigerant flow rate can also be adjusted by regulating a by-pass valve installed in the by-pass flow path. The refrigerant at the outlet of the refrigerant pump is kept subcooled to avoid any vapor flow through the mass flow meter. The flow meter has an accuracy of  $\pm 1\%$ . The preheater is used to heat the refrigerant to a specified state before entering the test section. The vapor generated in the test section is reliquefied in an oversized condenser/subcooler in the cold water-glycol loop. Leaving the subcooler, the

liquid refrigerant flows back to the receiver at the bottom of the system. An accumulator is connected to a high-pressure nitrogen tank to dampen the high frequency random fluctuations of the flow rate and pressure. The filter/dryer is used to filter the impurities and noncondensable gas possibly existing in the loop. Varying the temperature and flow rate of the water-glycol mixture flowing through the condenser and subcooler allows us to control the time-average pressure of the refrigerant loop. Two absolute pressure transducers are respectively installed at the inlet and exit of the test section with a resolution up to  $\pm 2\text{kPa}$ . All the refrigerant and water temperatures are measured by copper-constantan thermocouples (T-type) with a calibrated accuracy of  $\pm 0.2^\circ\text{C}$ . The test section is thermally insulated with a polyethylene insulation layer of 19.5 mm thick so that heat loss from it can be reduced significantly.

## 2.2 Test Section

Boiling of refrigerant R-410A flow in an annular duct with a small clearance between the inner and outer pipes is explored here. As schematically shown in Fig. 2.3, the test section of the experimental apparatus is a horizontal annular duct with the outer pipe made of Pyrex glass to permit the visualization of boiling processes in the refrigerant flow. The outer Pyrex glass pipe is 160 mm long and 4 mm thick with the inside diameter of 20 mm. Both ends of the pipe are connected with a copper tube of the same size by means of flanges and are sealed by O-rings. The inner smooth copper pipe has 16.0 mm nominal outside diameter (the pipe wall thickness is 1.5 mm) and is 0.41 m long, so that the hydraulic diameter of the annular duct  $D_h$  is 4.0 mm (corresponding to the gap size of 2.0 mm for the duct). In order to insure the gap between the ducts being uniform, we first measure the average outside diameter of the inner pipe and the mean inside diameter of the Pyrex glass pipe by digital calipers having a resolution of 0.001 mm. The absolute accuracy of the measurement is in the range of 0.01 mm. Then we photo the top and side view pictures of the annular ducts and measure the average distance between the inside surface of the Pyrex glass pipe and the outside surface of the inner tube, with an absolute accuracy also in the range of 0.01 mm. From the above procedures the duct gap is ascertained and its absolute uncertainty is estimated to be 0.019 mm. An electric cartridge heater of 160 mm in length and 12.5 mm in diameter with a maximum power output of 800W is inserted into the inner pipe. Furthermore, the pipe has an inactive heating zone of 10-mm long at each

end and is thermally insulated with Teflon blocks and non-conducting epoxy to minimize heat loss from it. Thermal contact between the heater and the inner pipe is improved by coating a thin layer of heat-sink compound on the heater surface before the installation of the heater. Then, 8 T-type calibrated thermocouples are electrically insulated by covering their beads with the electrically non-conducting thermal bond before they are fixed on the inside surface of the inner pipe so that the voltage signals from the thermocouples are not interfered by the DC current passing through the cartridge heater. The thermocouples are positioned at three axial stations along the smooth pipe. At each axial station, two to four thermocouples are placed at top, bottom, or two sides of the pipe circumference with  $180^\circ$  or  $90^\circ$  apart. The outside surface temperature  $T_w$  of the inner pipe is then derived from the measured inside surface temperature by taking the radial heat conduction through the pipe wall into account. Figure 2.4 shows the detailed thermocouple locations at each axial station and the arrangement of the cartridge heater.

### **2.3 Water Loop for Preheater**

In order to maintain the preset refrigerant temperature at the test section inlet, a water loop is used to preheat the refrigerant before it arrives at the inlet. The water loop for the preheater system includes a double-tube heat exchanger, having a heat transfer area of  $0.12 \text{ m}^2$ , a 125-liter hot water container with three 2.0-kW heaters in it, and a 0.5-hp water pump which can deliver the hot water at specified temperature and flow rate to the preheater. In the preheater the hot water passes through the outer pipe while the liquid refrigerant flows in the inner pipe. The water flow rate is controlled by an AC motor through the change of the inverter frequency and by a by-pass valve. The connecting pipe between the preheater and test section is thermally insulated with a 5-cm thick polyethylene layer to reduce the heat loss from the pipe.

### **2.4 Water-Glycol Loop**

The water-glycol loop is designed for condensing the refrigerant vapor and for subcooling the liquid refrigerant. The water-glycol loop is cooled by a water cooled R-22 refrigeration system. The cooling capacity is 3.5-kW for the water-glycol mixture at  $-20^\circ\text{C}$ . The cold water-glycol mixture at a specified flow rate is driven by a 0.5-hp pump to the condenser as well as to the subcooler. A by-pass loop is provided to adjust the flow rate. By

adjusting the mixture temperature and flow rate, the bulk temperature of the refrigerant in the subcooler can be controlled at a preset level.

## 2.5 DC Power Supply

As described above, the inner pipe in the test section is heated by a 800-W cartridge heater. A 100V-50A programmable DC power supply (model 62012P-100-50 ) delivers the required electric current to the cartridge heater. A Yokogawa(WT210) digital power meter is used to measure the DC current through the cartridge heater and the voltage drop across the heater with an accuracy of  $\pm 1\%$ . Thus the power input to the heater can be calculated. Figure 2.5 schematically shows the detailed control loop for the heat flux oscillation. Specifically, the temporal oscillation of the imposed heat flux to the refrigerant in the test section can be implemented by an optional external control of the inverter through a programmable DC current or voltage signal sequence.

## 2.6 Photographic System

The photographic apparatus established in the present study to record the bubble characteristics in the saturated flow boiling in the annular duct consists of an IDT X-Stream™ VISION XS-4 high speed CMOS digital camera, a Mitutoyo micro lens set, a 3D positioning mechanism, a personal computer, and a Nikon digital camera. The high-speed digital camera can take photographs up to 143,307 frames/s with an image resolution of 512×16. Here, a recording rate of 10,000 frames/s with the highest image resolution of 512×256 is adopted to obtain the images of the bubble ebullition processes in the flow boiling. The digital camera shutter speed can be as short as 1/4000 second in taking the overview of the flow boiling in the duct. The data for some bubble characteristics are collected in the regions around the middle axial location ( $z = 80$  mm). Note that the symbol  $z$  denotes the axial coordinate measuring from the inlet of the heated test section. After the experimental system reaches a statistical state, we start recording the boiling activity. The high-speed digital camera can store the images which are later downloaded to the personal computer. Then, the time variations of the space-average bubble departure diameter and frequency and active nucleation site density in a periodic cycle are calculated by viewing more than 1000 frames at each time instant. The bubble departure frequency is measured by counting the total number of bubbles that emerge from

the heating surface during a selected time interval of one second.

## 2.7 Data Acquisition

The data acquisition system includes a recorder (Yokogawa MX-100), a 24V-3A power supply, and a controller. The water flowmeter and differential pressure transducer need the power supply as a driver to output an electric current of 4 to 20 mA. The data signals are collected and converted by a hybrid recorder (Micro Motion RFT9739). The converted signals are then transmitted to a host computer through a GPIB interface for further calculation.

The system automatically monitors all the T-Type thermocouples, pressure transducers, differential pressure transducer and mass flowmeters. The thermodynamic and transport properties of the refrigerants are obtained by a manual from AlliedSignal Co. Ltd. and by the ASHRAE handbook.

## 2.8 Experimental Procedures

Before a test is started, the temperature of R-410A in the test section is compared with its saturation temperature corresponding to the measured saturation pressure and the allowable difference is kept in the range of 0.2-0.3K. Otherwise, the system is re-evacuated and then re-charged to remove the air existing in the refrigerant loop. A vacuum pump is used to evacuate non-condensable gases in the system to a low pressure of 0.067 pa in the loop. In the test the liquid refrigerant R-410A at the inlet of the test section is first maintained at a specified temperature by adjusting the water-glycol temperature and flow rate. In addition, we adjust the thermostat temperature in the water loop to stabilize the refrigerant temperature at the test section inlet. Then, we regulate the refrigerant pressure at the test section inlet by adjusting the opening of the gate valve locating right after the exit of the test section. Meanwhile, by changing the current of the AC motor connecting to the refrigerant pump, the refrigerant flow rate can be varied to procure the preset mean level and the chosen period and amplitude of the mass flux oscillation (Fig.2.2). More specifically, due to the flow inertia the actual refrigerant flow rate instead varies like a triangular wave. The heat flux to the coolant in the test section is provided by the programmable DC power supply. The programmable power supply allows us to impose the required temporal heat flux oscillation (Fig. 2.5) also chosen to be in the form of triangular

waves. By measuring the current delivered to and voltage drop across the heater and by photographing the bubble activity, we can calculate the heat transfer rate to the refrigerant and obtain the bubble characteristics. All tests are run at statistical state conditions after the initial transients have die out. The whole system is considered to be at a statistical state when the variations of the time-average system pressure and imposed heat flux are respectively within  $\pm 1\%$  and  $\pm 4\%$ , and the variations of the time-average heated wall temperature are less than  $\pm 0.2^\circ\text{C}$  for a period of 100 minutes. Then all the data channels are scanned every 0.05 second for a period of 360 seconds.

## 2.9 Experimental Parameters

The ranges of the experimental parameters and the corresponding dimensionless groups to be covered in the present study are listed in Tables 2.1 and 2.2. Moreover, some thermophysical properties of refrigerant R-410A are given in Table 2.3.

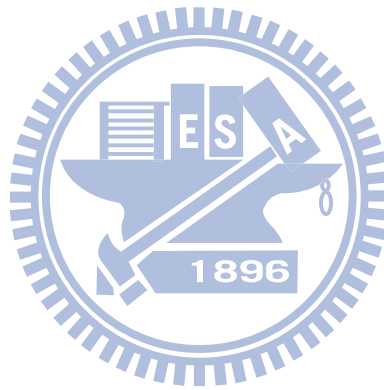


**Table 2.1 List of conditions of the experimental parameters for R-410A (flow rate oscillation)**

refrigerant	$\delta$	$\bar{G}$	$\frac{\Delta G}{G}$	$t_p$	$\bar{q}$	$\bar{T}_{sat}$	$Re_1$	$N_{conf}$
	(mm)	(kg/m <sup>2</sup> s)	%	sec	(kW/m <sup>2</sup> )	(°C)		
R-410A	2	300,400,500	10,20,30	20,60,120	0-45	5,10,15	6,584-16,460	0.2

**Table 2.2 List of conditions of the experimental parameters for R-410A (heat flux oscillation)**

refrigerant	$\delta$	$\bar{q}$	$\frac{\Delta q}{q}$	$t_p$	$G$	$\bar{T}_{sat}$	$Re_1$	$N_{conf}$
	(mm)	(kW/m <sup>2</sup> )	%	sec	(kg/m <sup>2</sup> s)	(°C)		
R-410A	2	0-45	10,30,50	20,60,120	300,400,500	5,10,15	8,230-13,717	0.2



**Table 2.3 Thermophysical properties of refrigerant R-410A**

Thermophysical properties		R-410A		
Temperature (°C) (Saturated Pressure)		<b>5.56</b> (950kpa)	<b>10.46</b> (1100 kPa)	<b>14.88</b> (1250 kPa)
Viscosity $\mu$ ( $\mu\text{N}\cdot\text{s}/\text{m}^2$ )	Liquid $\mu_l$	154.9	145.8	137.9
	$\Delta\mu = \mu_l - \mu_g$	<b>142.26</b>	<b>132.86</b>	<b>124.67</b>
	Vapor $\mu_g$	12.64	12.94	13.23
Density $\rho$ ( $\text{kg}/\text{m}^3$ )	Liquid $\rho_l$	1149	1128	1109
	$\Delta\rho = \rho_l - \rho_g$	<b>1112.52</b>	<b>1085.53</b>	<b>1165.93</b>
	Vapor $\rho_g$	36.48	42.47	48.61
Enthalpy $i$ (kJ/kg)	Liquid $i_f$	208.5	216.1	223
	$\Delta i = i_g - i_f$	<b>214.1</b>	<b>207.7</b>	<b>201.7</b>
	Vapor $i_g$	422.6	423.8	424.7
Conductivity $k$ (W/m·K)	Liquid $k_l$	<b>0.1105</b>	0.1074	<b>0.1046</b>
	Vapor $k_g$	0.01234	0.01295	0.01359
Surface Tension $\sigma$ (N/m)	Liquid	<b>0.00782</b>	<b>0.00709</b>	<b>0.00644</b>

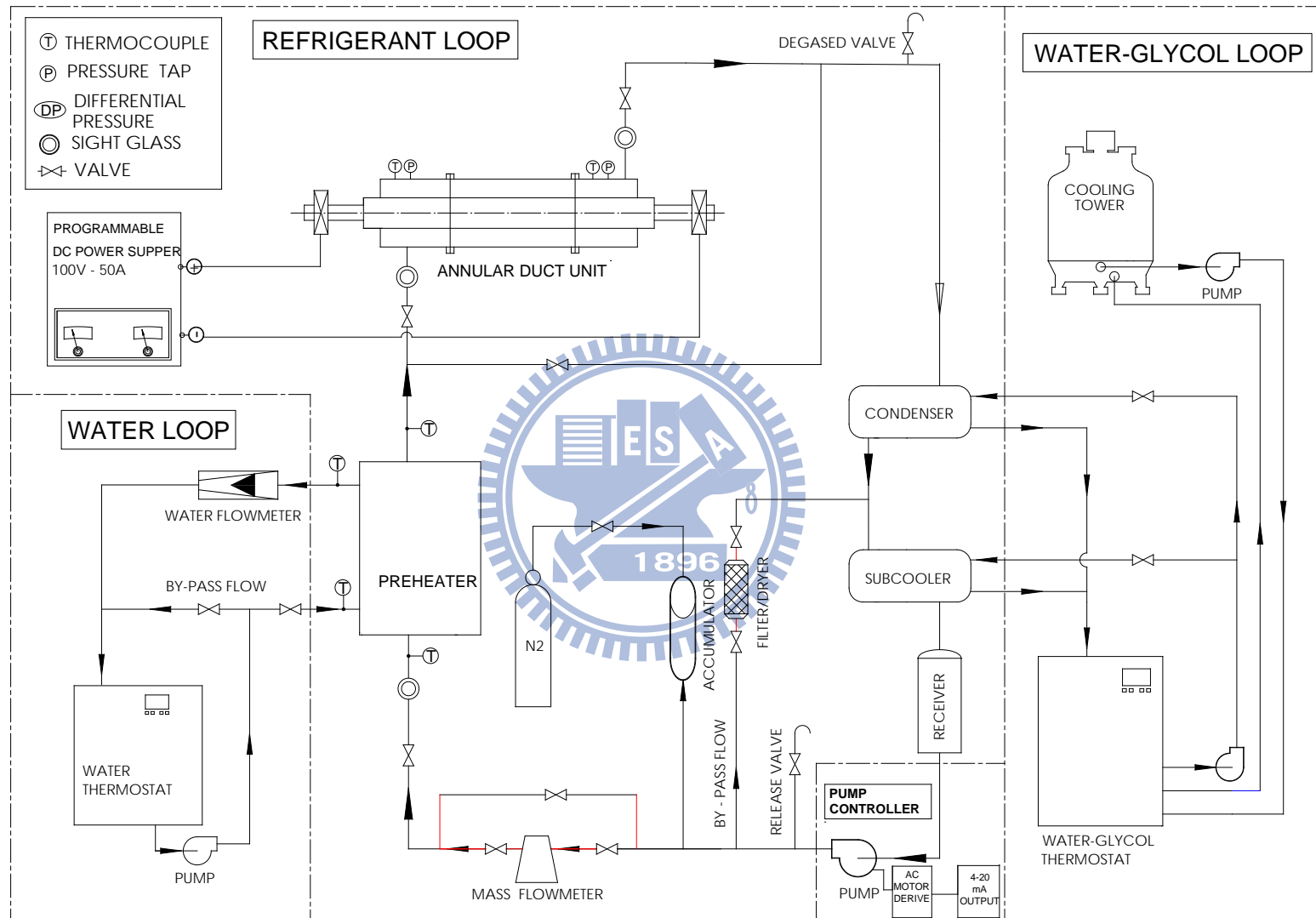


Fig. 2.1 Schematic of experimental system for the annular duct

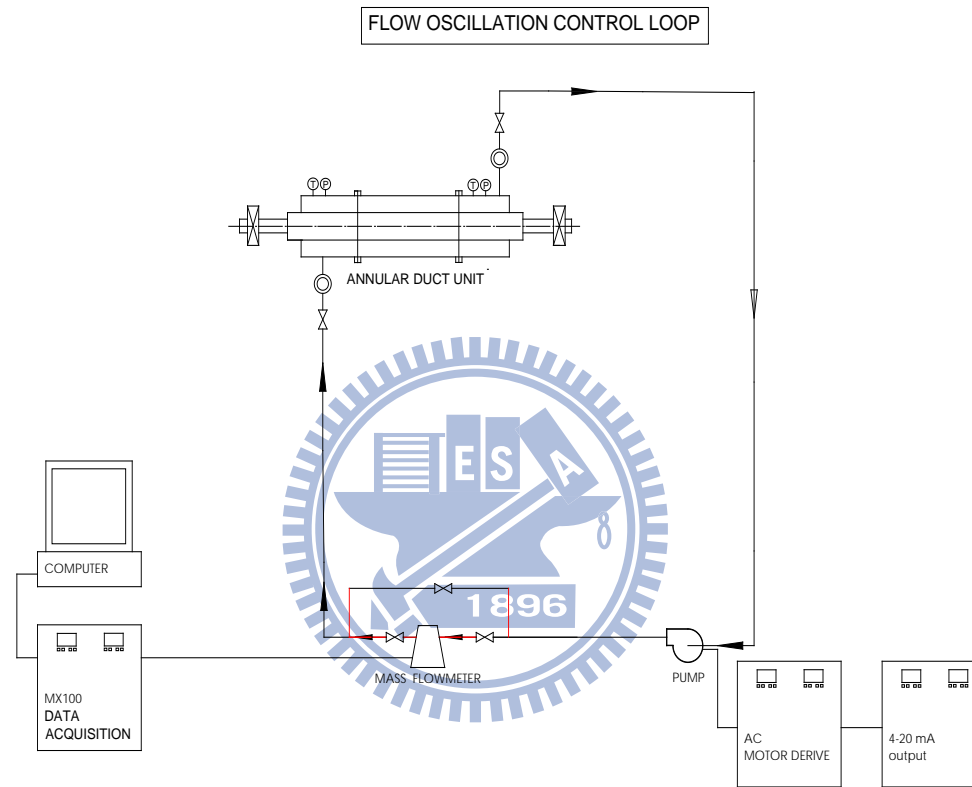


Fig. 2.2 Schematic of mass flux control loop

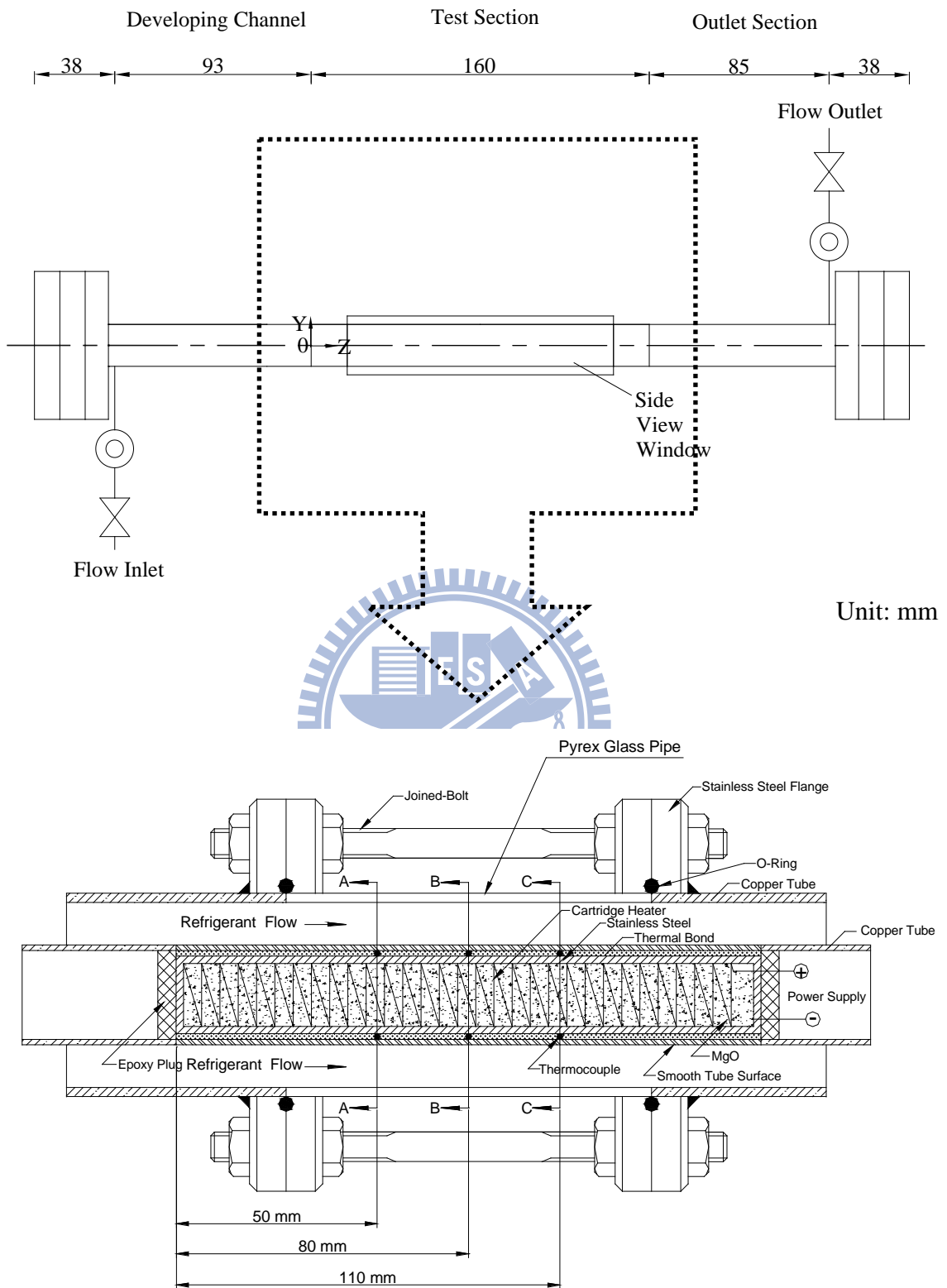


Fig. 2.3 The detailed arrangement of the test section for the annular duct

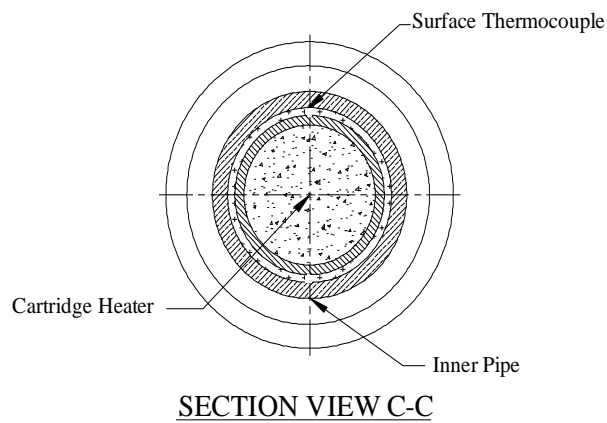
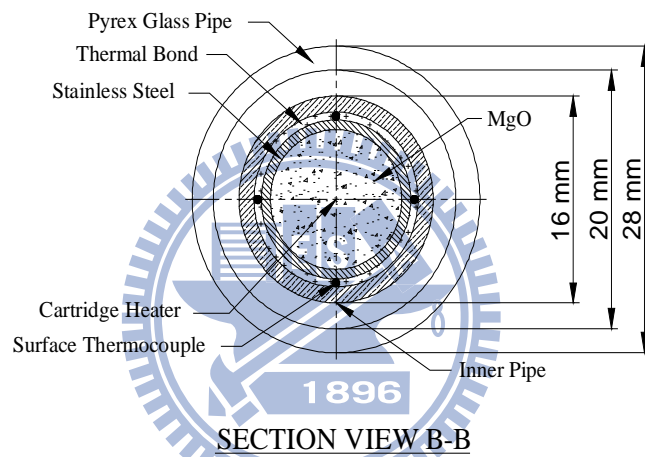
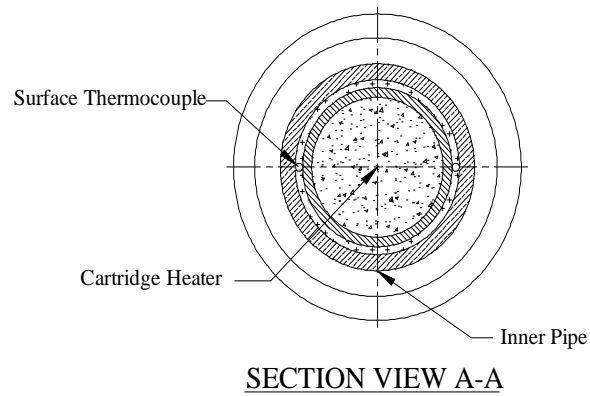


Fig. 2.4 The cross-sectional view of the annular duct showing the heater and locations of the thermocouples.

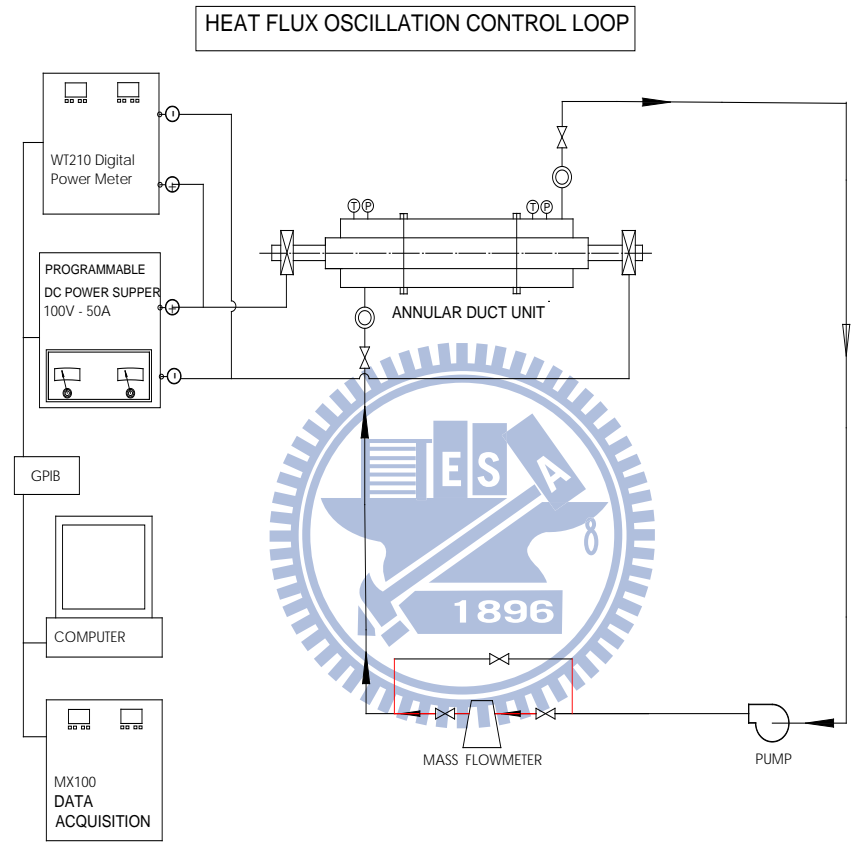


Fig. 2.5 Schematic of heat flux control loop



## CHAPTER 3

### DATA REDUCTION

In the present study of heat transfer and bubble characteristics in the time periodic flow boiling of R-410A in a narrow annular duct, the gap between the inner and outer circular pipes is fixed at 2.0 mm with the time-average refrigerant saturated temperature  $\bar{T}_{\text{sat}}$  set at 5°C, 10°C and 15°C. The mean refrigerant mass flux  $\bar{G}$  ranges from 300 kg/m<sup>2</sup>s to 500 kg/m<sup>2</sup>s, the imposed heat flux from 0 to 45KW/ m<sup>2</sup>. Besides, the amplitude of the mass flux oscillation or heat flux oscillation  $\Delta G$  or  $\Delta q$  is chosen to vary from 10% to 30% of their respective mean level  $\bar{G}$  or  $\bar{q}$  and the period of the  $G$  or  $q$  oscillation is fixed at 20, 60, 120 seconds. A data reduction analysis is needed to calculate the flow boiling heat transfer coefficient from the raw data measured in the horizontal narrow annular duct.

#### 3.1 Flow Boiling Heat Transfer Coefficient

The imposed heat flux to the refrigerant flow in the annular duct is calculated on the basis of the total power input  $Q_t$  and the total outside heat transfer area of the inner pipe of the annular duct  $A_s$ . The total power input is computed from the product of the measured voltage drop across the cartridge heater and the electric current passing through it. Hence the net power input to the test section  $Q_n$  is equal to  $(Q_t - Q_{\text{loss}})$ . The imposed heat flux at the outside surface of the inner pipe is then evaluated from the relation

$$q = Q_n / A_s \quad (3.1)$$

The total heat loss from the test section  $Q_{\text{loss}}$  is evaluated from the correlation for natural convection around a circular cylinder by Churchill and Chu [42]. The correlation is

$$Nu_a = \left\{ 0.6 + \frac{0.387 Ra_D^{1/6}}{\left[ 1 + (0.559/Pr)^{9/16} \right]^{8/27}} \right\}^2 \quad (3.2)$$

where



$$Ra_D = g\beta(\overline{T}_{ins} - T_a)D_{os}^3/\alpha\nu \quad (3.3)$$

To reduce the heat loss from the test section, we cover the test section with a polyethylene insulation layer. We measured the mean temperature of the outside surface of the insulation layer  $\overline{T}_{ins}$  and ambient temperature  $T_a$ . Hence  $Q_{loss} = h_N \cdot (\overline{T}_{ins} - T_a) \cdot A_{os}$  where  $A_{os}$  is the outside surface area of the insulation layer and  $h_N = Nu_a \cdot \frac{D_{os}}{k_a}$ . Note that  $D_{os}$  is the outside diameter of the insulation layer. The results from this heat loss test indicate that the heat loss from the test section is generally less than 1% of the total power input no matter when time dependent single-phase flow or two-phase boiling flow is in the duct.

The average single-phase convection heat transfer coefficient for the refrigerant flow over the entire heated surface in the annular duct is defined as

$$h_l = \frac{Q_n}{A_s \cdot (\overline{T}_w - T_{r,ave})} \quad (3.4)$$

and

$$T_{r,ave} = \frac{T_{r,i} + T_{r,o}}{2} \quad (3.5)$$

where  $Q_n$  is the net power input to the liquid refrigerant flow in the annular duct and  $T_{r,ave}$  is the average of the measured inlet and outlet temperatures of the refrigerant flow through the test section, which is taken as the average bulk liquid refrigerant temperature. Note that  $\overline{T}_w$  denotes the average outside surface temperature of the inner pipe measured at the selected thermocouple locations. The outside surface temperature at each thermocouple location is deduced from the measured inside surface temperature of the inner pipe by subtracting the radial temperature drop due to the radial heat conduction in the pipe wall. Thus we have

$$T_w = T_{w,i} - Q_n \frac{\ln(D_o/D_i)}{2\pi k_w L} \quad (3.6)$$

The local and time average saturated flow boiling heat transfer coefficient at a given axial location is defined as

$$h_{r,\text{sat}} = \frac{Q_n / A_s}{(T_w - \bar{T}_{\text{sat}})} \quad (3.7)$$

and

$$\bar{h}_{r,\text{sat}} = \frac{Q_n / A_s}{(\bar{T}_w(z) - \bar{T}_{\text{sat}})} \quad (3.8)$$

### 3.2 Flow Boiling Bubble Characteristics

To explore the bubble characteristics, we move further to estimate the space-average bubble departure diameter and frequency and the average active bubble nucleation site density on the heating surface for the cases dominated by the bubbly flow. Specifically, for a given case the average bubble departure diameter is determined by measuring the diameters of the departing bubbles on a small heated surface area and it is defined as

$$d_p = \frac{\sum d_p}{N_1} \quad (3.9)$$

where  $N_1$  is the number of measured bubbles. In this determination of  $d_p$ ,  $N_1$  is not less than 3. Similarly, the space-average bubble departure frequency is estimated by averaging the number of bubbles departing from the heated surface  $n_b$  over a certain period of time  $t_b$  at a few bubble departing sites  $N_2$ . Thus  $f_b$  is defined as

$$f_b = \frac{\sum f_b}{N_2} = \frac{\sum n_b / t_b}{N_2} \quad (3.10)$$

where  $N_2$  is also greater than 3 and  $t_b$  is chosen to be much shorter than  $t_p$ . The space-average active nucleation site density is estimated by counting the number of bubble nucleation sites  $n_s$  over a small heated surface area  $A_s'$ , and it is defined as

$$n_{\text{ac}} = n_s / A_s' \quad (3.1)$$

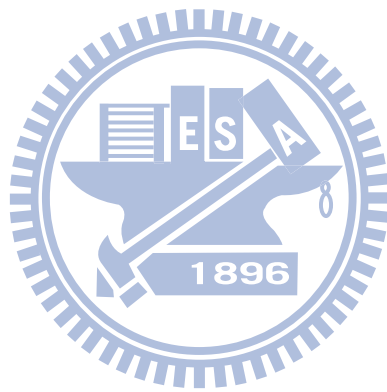
### 3.3 Uncertainty Analysis

Uncertainties of the heat transfer coefficients are estimated according to the procedures proposed by Kline and McClintock for the propagation of errors in physical measurement [43]. The results from this uncertainty analysis are summarized in Table 3.1.



**Table 3.1 Summary of results from uncertainty analysis**

<b>Parameter</b>	<b>Uncertainty</b>
<b>Annular duct geometry</b>	
Length, width and thickness (%)	±1.0%
Gap size (%)	±5.0%
Area (%)	±2.0%
<b>Parameter measurement</b>	
Temperature, T (°C)	±0.2
Temperature difference, $\Delta T$ (°C)	±0.28
Mean system pressure, P (MPa)	±0.002
Amplitude of mass flux oscillation, $\Delta G / \bar{G}$ (%)	±3.3
Period of mass flux oscillation, $t_p$ (sec.)	±0.3
Average mass flux of refrigerant, $\bar{G}$ (%)	±2.0
Average departure diameter, $\bar{d}_p$ (%)	±3.0
Average departure frequency, $\bar{f}$ (%)	±3.6
Average active nucleation site density, $1/\bar{n}_{ac}$ (%)	±5.0
Amplitude of mass flux oscillation, $\Delta q / \bar{q}$ (%)	±0.2
Period of mass flux oscillation, $t_p$ (sec.)	±0.25
Average mass flux of refrigerant, $\bar{q}$ (%)	±2.1
<b>Single-phase heat transfer</b>	
Imposed heat flux, q (%)	±4.5
Heat transfer coefficient, $h_{r,l}$ (%)	±12.5
<b>Saturated flow boiling heat transfer</b>	
Imposed heat flux, q (%)	±4.5
Heat transfer coefficient, $h_{r,sat}$ (%)	±14.5



## CHAPTER 4

### TIME PERIODIC SATURATED FLOW BOILING OF R-410A IN A NARROW ANNULAR DUCT DUE TO MASS FLUX OSCILLATION

The results obtained in the first part of the present study for the time periodic saturated flow boiling of R-410A in the duct due to the imposed mass flux oscillation are examined in this chapter. In a flow with an imposed temporal mass flux oscillation the refrigerant pressure at the duct inlet also varies with time, so does the refrigerant saturated temperature. In this part of the study the temperature of the refrigerant at the duct inlet is controlled at the time-average value of the instantaneous saturated temperature of the refrigerant corresponding to the refrigerant pressure. Besides, the refrigerant vapor quality at the inlet is set at zero. This is designated as "saturated flow boiling" here. The mass flux oscillation is in the form of triangular waves, as mentioned earlier. The present experiments are conducted for the mean refrigerant mass flux  $\bar{G}$  varied from 300 to 500 kg/m<sup>2</sup>s and the amplitude of the mass flux oscillation  $\Delta G/\bar{G}$  fixed at 10, 20, 30% of  $\bar{G}$  with the period of the mass flux oscillation  $t_p$  fixed at 20, 60 and 120 seconds. The time-average refrigerant saturation temperature  $\bar{T}_{sat}$  is set at 5, 10 and 15°C for the imposed heat flux varied from 0 to 45 kW/m<sup>2</sup>. The gap between the inner and outer pipes  $\delta$  is fixed at 2.0 mm. The measured boiling heat transfer data are expressed in terms of the boiling curves and boiling heat transfer coefficients along with the time variations of the heated surface temperature. Besides, the close view flow photos taken from the duct side at a small region around the middle axial station  $z = 80$  mm are presented to illustrate the bubble characteristics in the time periodic boiling flow. Then, comparison between the time periodic R-410A saturated flow boiling data due to the mass flux oscillation with that of stable boiling is made. Moreover, the quantitative bubble characteristics in the time periodic flow boiling will be examined.

#### 4.1 Single-phase Heat Transfer

Before beginning the time periodic flow boiling experiments, the steady single-phase convective heat transfer experiments are conducted for liquid R-410A. The measured

single-phase convection heat transfer coefficients are compared with the correlations proposed by Dittus-Boelter [34] and Gnielinski [44]. In the steady single-phase heat transfer tests the refrigerant mass flux is varied from 200 to 600 kg/m<sup>2</sup>s for the annular gap of the duct  $\delta = 2.0$  mm (corresponding to the Reynolds number of the refrigerant flow varied from 5,746 to 19,179) for the refrigerant saturated temperature  $T_{\text{sat}}=15^{\circ}\text{C}$  and inlet liquid subcooling  $\Delta T_{\text{sub}}=3^{\circ}\text{C}$ . Selected data from these tests are plotted in Figure 4.1.

The Dittus-Boelter correlation is

$$Nu_l = 0.023 \cdot Re^{0.8} \cdot Pr^{0.4} \quad \text{for } Re > 10^4 \quad (4.1)$$

and the Gnielinski correlation is

$$Nu_l = \frac{(f_f/8)(Re-1000)Pr}{1+12.7\sqrt{f_f/8}(Pr^{2/3}-1)} \quad \text{for } 2,300 < Re < 10^6 \quad (4.2)$$

$$\text{where } f_f = (1.82 \times \log_{10} Re - 1.64)^{-2} \quad (4.3)$$

The results in Figure 4.1 manifest that the present data for  $h_l$  are in good agreement with the Gnielinski correlation with a mean absolute error of 3.6%. Because of the lack of the unsteady turbulent forced convection heat transfer data in the open literature, direct validation of the present time periodic liquid heat transfer data is impossible.

## 4.2 Stable and Time-average Saturated Flow Boiling Curves and Heat Transfer Coefficients

To illustrate the effects of the mass flux oscillation on the flow boiling characteristics, data for the R-410A saturated flow boiling for a constant refrigerant mass flux measured at the middle axial location are shown in Figs. 4.2 and 4.3 and are first compared with the time-average data for the cases with the time periodic refrigerant mass flux oscillation in Fig. 4.4 by presenting the boiling curves for various mean mass fluxes and amplitudes and periods of the mass flux oscillation. Note that at a low  $q$  for each stable or time-average boiling curve the temperature of the heated wall at the middle axial location increases gradually with the imposed heat flux from the time-average saturated temperature of the

refrigerant to a certain value just slightly higher than  $\bar{T}_{\text{sat}}$  and no bubble nucleation is observed. The heat transfer in this region is completely due to the single-phase forced convection. With the continuing increase in the surface heat flux, bubbles begin to appear on the surface and the boiling curve is characterized by a sharp increase in the surface heat flux for a small rise in the temperature of the heated surface. We have onset of nucleate boiling (ONB) in the flow. The reason causing the sharp increase in the slope of the boiling curve is due to a significant increase in the surface heat transfer by the boiling processes when ONB occurs. For the cases with oscillating refrigerant mass fluxes the ONB locations marked in these plots are the time-average values. Besides, at a higher  $G$  the required heat flux for ONB is higher and this implies that more energy is needed for the vapor to nucleate from the wall since the residence time of the refrigerant on the heated surface is shorter and the refrigerant is at a lower temperature. It can be concluded from the results in Fig. 4.4 that the time-average boiling curves are not affected by the amplitude and period of the refrigerant mass flux oscillation.

We move further to explore how the time-average saturated flow boiling heat transfer coefficients  $h_r$  is affected by the R-410A mass flux oscillation. The results for the variations of the time-average  $h_r$  with the imposed surface heat flux at the middle axial location presented in Figs. 4.5-4.7 reveal that the amplitudes and periods of the refrigerant mass flux oscillation have negligible influences on the time-average boiling heat transfer coefficients. However, for a given refrigerant mass flux the time-average boiling heat transfer coefficient increases substantially with the imposed heat flux.

### 4.3 Time Periodic Flow Boiling Heat Transfer Characteristics

The time varying saturated flow boiling heat transfer characteristics of R-410A in the annular duct resulting from the imposed temporal refrigerant mass flux oscillation are illustrated by presenting the time variations of the space-average heated surface temperature  $T_w$  and boiling heat transfer coefficient  $h_r$  at the middle axial location in the statistical state. For the limiting case of stable flow boiling ( $\Delta G/\bar{G}=0$ ) the measured heated surface temperature at  $z=80$  mm for various  $q$  are essentially steady (Fig. 4.8). Data for various  $\bar{T}_{\text{sat}}$ ,  $\Delta G/\bar{G}$ ,  $t_p$  are shown in Figs. 4.9-4.17 for various imposed heat fluxes and mean mass fluxes. The results presented here and from the flow visualization indicate that at low imposed heat flux the single-phase liquid flow prevails in the duct and the heated



surface temperature oscillates significantly with time for a large  $\Delta G/\bar{G}$ . At a high imposed heat flux persistent boiling dominates. But, the heated surface temperature oscillation does not become stronger at increasing heat flux. For the in-between intermediate imposed heat flux we observe boiling activity only in a certain fraction of the periodic cycle. Otherwise, the flow is in single-phase state. Thus at this intermediate heat flux we have intermittent boiling in the flow. A close inspection of these data reveals that in the single-phase flow in the first half of the periodic cycle the heated surface temperature increases with time as the imposed mass flux decreases with time. But an opposite trend is noted in the flow dominated by the persistent boiling in which the heated surface temperature decreases as the imposed mass flux is lowered. This phenomenon is somewhat unusual and will be examined in detail later when the quantitative data for the bubble characteristics are analyzed. Note that the temporal oscillation of the heated surface temperature is also periodic in time and is at the same frequency as the mass flux oscillation. The saturation temperature of the refrigerant exhibits relatively weak effects on the  $T_w$  oscillation. Moreover, the  $T_w$  oscillation lags slightly behind the mass flux oscillation due to the thermal inertia of the heated pipe wall.

The appearance of the intermittent boiling in the flow needs to be examined closely. Based on the detailed flow observation, we note that at the imposed heat flux around that for the onset of stable flow boiling bubbles start to nucleate from the heated surface when the refrigerant mass flux is lowered to a certain level in the first half of the periodic cycle and more bubbles nucleate from the surface for a further reduction in the refrigerant mass flux. As a result of that, the heated surface temperature becomes lower. This trend is reversed when the mass flux increases in the second half of the periodic cycle. Specifically, at a certain high level of the mass flux the bubble nucleation stops and the flow is in single-phase state. Obviously, the single-phase flow prevails for a continuing rise in the mass flux. The above processes repeatedly occur forming the intermittent boiling. For the imposed heat flux well below and well above the onset heat flux of stable flow boiling, apparently the duct is dominated respectively by the single-phase liquid flow and persistent boiling. The time instants for the start and stop of the bubble nucleation are marked on the  $T_w$  curves for the cases with the intermittent boiling.

The corresponding time variations of the space-average flow boiling heat transfer coefficient at the middle axial location affected by the refrigerant mass flux oscillation are

shown in Figs. 4.18 – 4.26. The results manifest that the flow boiling heat transfer coefficients also oscillate periodically in time and at the same frequency as the  $G$  oscillation. For a longer period and larger amplitude of the mass flux oscillation, the boiling heat transfer coefficients oscillate stronger. For some increase in the imposed heat flux nucleate boiling persists over the entire period of the cycle and we have persistent flow boiling in the duct. It is of interest to note that at this higher  $q$  in the first half of the cycle in which  $G$  decrease with time,  $T_w$  also decrease with time, suggesting that the flow boiling heat transfer over the heated surface is better at a lower  $G$ . This trend is opposite to that for the single-phase convection. The results also show that the amplitude of  $h_r$  oscillation is not affected by the imposed heat flux in the persistent boiling to a noticeable degree. Moreover, the oscillation in  $h_r$  also lags slightly behind the mass flux oscillation. It is further noted that in the persistent boiling the amplitude of the  $h_r$  oscillation is only slightly affected by the heat flux for given  $\bar{G}$ ,  $\Delta G/\bar{G}$ ,  $t_p$  and  $\bar{T}_{sat}$ .

Finally, we move further to present the data in Fig. 4.27 to elucidate the effects of the experimental parameters on the amplitude of the  $T_w$  oscillation over a wide range of the imposed heat flux covering the single-phase, intermittent and persistent boiling flow regimes. The results in Figs. 4.27(a) and (b) indicate that for all boiling flow regimes the  $T_w$  oscillation is stronger for a higher amplitude and a longer period of the mass flux oscillation. Particularly, the  $T_w$  oscillation becomes much stronger for  $t_p$  raised from 20 seconds to 60 seconds. At the low  $t_p$  of 20 seconds, which is only slightly longer than the time constant of the present system, the  $T_w$  oscillation is rather weak (Fig. 4.27(b)), reflecting that the heated wall is unable to respond instantly to the fast mass flux oscillation for a  $t_p$  of 20 seconds. But the mean refrigerant mass flux exhibits a nonmonotonic effect on the amplitude of the  $T_w$  oscillation, as evident from the data in Fig. 4.27(c). The data given in Fig. 4.27(c) also indicate that in the single-phase flow the oscillation amplitude of  $T_w$  increases with the imposed heat flux for a given  $\Delta G/\bar{G}$ . Note that when the intermittent boiling appears the  $T_w$  oscillation starts to weaken substantially with the increase in the imposed heat flux. At a certain higher  $q$  but still in the intermittent boiling regime the  $T_w$  oscillation decays to a minimum point and then a further increase in  $q$  causes  $T_w$  to oscillate in a larger amplitude. We note that as the bubble nucleation starts to appear in the single-phase flow the  $T_w$  oscillation is weakened, and this trend continues until the effect of the boiling flow dominates over the single-phase flow for a rise in  $q$  to a certain level.

Then, the  $T_w$  oscillation gets stronger for a higher  $q$ . For a certain higher  $q$  the  $T_w$  oscillation decays at increasing imposed heat flux for lower mean mass fluxes and higher saturated temperatures (Figs. 4.27(c) and (d)). Specifically, at intermediate imposed heat flux for  $q$  ranging from 12 to 45 kW/m<sup>2</sup> in the intermittent and persistent boiling  $T_w$  oscillates in a smaller amplitude at a lower  $\bar{G}$ . However, the saturated temperature of the refrigerant exhibits weaker effects on the  $T_w$  oscillation shown in Fig. 4.27(d).

#### 4.4 Intermittent Boiling

It is of interest to note in the visualization of the boiling flow over the heated inner pipe in the annular duct that for the imposed heat flux close to that needed for the ONB of the stable boiling, intermittent boiling appears, as already mentioned earlier. More specifically, in a typical periodic cycle for a given such heat flux and for given amplitude and period of the mass flux oscillation bubble nucleation in the heated annular duct is first seen at a certain time instant after the mass flux decreases to a certain low level and the pipe wall temperature rises to exceed the wall superheat required for the onset of nucleate boiling. We have a start of boiling in the flow and the boiling process continues since then. However, after some period of time following the increase of the mass flux to a certain high level, bubble nucleation disappears and the boiling stops. The above process of intermittent boiling is repeatedly seen on the heated surface. To be more clearer, we indicate the time instants at which boiling starts and stops in Figs. 4.9 – 4.17 for the cases with the presence of the intermittent boiling. Note that at a lower mean refrigerant mass flux and a higher imposed heat flux the onset of boiling is earlier and the termination of boiling is later. A flow regime map to delineate the boundaries separating different flow boiling regimes in terms of the Boiling number versus the relative amplitude of the mass flux oscillation is given in Fig. 4.28. The results show that the intermittent boiling prevails over a significantly wider range of the Boiling number for a higher amplitude of the mass flux oscillation, a higher mean saturated temperature of the refrigerant, and a lower mean refrigerant mass flux. Based on the present data, the conditions leading to the appearance of the intermittent boiling can be empirically correlated as

$$\left(3.2 \times 10^{-5} + 5 \times 10^{-7} \overline{\text{Re}}^{0.5}\right) \leq \frac{\overline{\text{Bo}}^{-1.2}}{(\Delta G / \bar{G})^{2.5}} \leq \left(3.25 \times 10^{-3} - 7.85 \times 10^{-6} \overline{\text{Re}}^{0.5}\right) \quad (4.4)$$

where  $\overline{Bo} = \frac{q}{G \cdot i_{fg}}$ . More than 94% of the present data falls within the above correlation.

## 4.5 Time Periodic Bubble Characteristics in Saturated Flow Boiling

To elucidate the time-periodic saturated flow boiling heat transfer characteristics, the data for the bubble characteristics of R-410A flow boiling obtained from the present flow visualization are examined in the following. The side views of the boiling flow in a small region around the middle axial location of the duct for various refrigerant mass fluxes and imposed heat fluxes are shown in Figs. 4.31-4.48 for the time periodic saturated flow boiling. At first, the bubble characteristics for the limiting cases of constant mass fluxes are illustrated by the photos in Fig. 4.29 & 4.30. It is noted from the flow visualization and the results in Fig. 4.29 & 4.30 that the vapor bubbles begin to appear as the heated surface temperature exceeds the boiling incipient superheat. In the beginning, tiny bubbles are observed in the active nucleation sites. The bubbles grow and then detach from the heated surface with certain mean bubble departure diameter. As the imposed heat flux increases, more bubbles are generated on more active nucleation sites and more bubbles detach from the heated surface. Besides, the detached bubbles tend to merge into larger bubbles. Note that the large bubbles become distorted and elongated as they slide on the heating surface. Moreover, at a higher mass flux the bubbles are smaller and the bubble coalescence is less significant. Next, the bubble characteristics in the time periodic flow boiling are shown by presenting the photos of the boiling flow at eight selected time instants in a typical periodic cycle in Figs. 4.31–4.48. In these figures the symbol “  $t=t_0$  ” signifies the time instant at which the instantaneous mass flux is at the highest level and starts to decrease with time. The results for the persistent flow boiling (Figs. 4.40-4.48) indicate that for a given imposed heat flux and fixed mean level, amplitude and period of the mass flux oscillation the bubbles get smaller and become more dispersed in the period of the time in which the instantaneous mass flux increases. The opposite processes take place when the instantaneous mass flux decreases with time. These changes of the bubble characteristics with the instantaneous mass flux become more significant for an increase in the amplitude of the mass flux oscillation.

Then, the bubble behavior in the intermittent flow boiling for the intermediate imposed heat fluxes is shown in Figs. 4.31 – 4.39. The results clearly indicate that initially

in the beginning of the cycle the instantaneous mass flux decreases with time but is still well above  $\bar{G}$  no bubble nucleates from the heated surface. The flow is in single-phase state. Note that for the case shown in Fig. 4.31 the bubbles start to nucleate from the heated surface at a certain instant after  $t_0+t_p/8$  at which the instantaneous mass flux already decreases to a certain level. Note that the number and size of the bubbles increase noticeably with time in second quarter of the periodic cycle for the continuing decrease of the mass flux. Then in the third quarter of the periodic cycle the number and size of the bubbles diminish noticeably with time due to the increase of the mass flux with time. The bubbles cease to nucleate from the heated surface at a certain time instant after  $t_0+6t_p/8$  when the mass flux slightly exceeds  $\bar{G}$  and bubble nucleation stops completely. Single-phase flow again dominates. We have to wait until about the end of the first quarter of the next cycle to see the bubble nucleation appearing on the heated surface. The above processes repeat in each cycle. The precise instants of time at which the onset and termination of nucleate boiling vary with the flow condition. Similar bubble behavior is noted for other cases shown in Figs. 4.32-4.39.

To be more quantitative the bubble characteristics, the measured data for the time variations of the space-average bubble departure diameter and frequency and active nucleation site density on the heating surface in a typical periodic cycle are given in Figs. 4.49– 4.54 to illustrate the effects of the experimental parameters on  $d_p$ ,  $f$  and  $n_{ac}$ . The results in Figs. 4.49 and 4.50 indicate that as the refrigerant mass flux oscillates time periodically, the bubble departure diameter also varies time periodically and to some degree like a triangular wave as the mass flux oscillation. The case shown in Fig. 4.49(a) for the mass flux oscillation at low amplitude of 10% the bubble departure diameter varies mildly with time. More specifically, the size of the departing bubbles increases almost linearly in the first half of the periodic cycle in which the mass flux decreases with time. While in the second half of the cycle an opposite process is noted since the mass flux increases with time. Similar trend is noted in Fig. 4.49(a) for higher  $\Delta G/\bar{G}$  of 20% and 30%. The results in Fig. 4.49(a) further manifest that at the larger amplitude of the mass flux oscillation the time variation of the bubble departure diameter is noticeably stronger. Moreover, an increase in the period of the mass flux oscillation exhibits a relatively slight effect on the variation of the bubble departure diameter with time (Fig. 4.49(b)). Furthermore, an increase in the mean refrigerant mass flux and saturation temperature

cause the departing bubbles to become smaller but do not significantly change the form of the  $d_p$  variation with time (Figs. 4.50(a) and (b)).

Next, the data for the time variations of the space-average bubble departure frequency for various cases are shown in Figs. 4.51 & 4.52. Note that the bubble departure frequency also varies like a triangular wave. The increase of  $f$  with  $G$  is ascribed to the higher drag on the bubbles attaching to the heated surface by the liquid refrigerant moving at a higher speed for a higher  $G$ . This in turn, causes an earlier departure of the bubbles from the surface, resulting in a higher departure frequency. For an oscillation mass flux the bubbles depart from the heated surface at a decreasing rate in the first half of the periodic cycle in which the mass flux decreases with time. Apparently, in the second half of the cycle in which the mass flux increases with time the bubble departing rate increases. It should be pointed out that the time variations of the bubble departure frequency are stronger for the higher amplitude of the mass flux oscillation (Fig. 4.51(a)). But the effects of the period of the mass flux oscillation on the time variation of the bubble departure frequency are relatively small (Fig. 4.51(b)). Figure 4.52 shows that increasing  $\bar{G}$  and  $\bar{T}_{sat}$  mainly results in a higher mean level of the bubble departure frequency.

Finally, the time variation of the space-average active nucleation site density on the heated surface affected by the mass flux oscillation is illustrated in Figs. 4.53 & 4.54. Note that in the time periodic flow boiling the active nucleation site density increases with time in the first half of the periodic cycle in which the mass flux decreases with time. The reverse process appears in the second half of the cycle in which the mass flux increases with time. At the higher amplitude of the mass flux oscillation the time variation of  $n_{ac}$  is stronger (Fig. 4.53(a)). The effects of the period of the mass flux oscillation on the time variation of  $n_{ac}$  are also relatively small (Fig. 4.53(b)). Besides, the results in Fig. 4.54 show that a lower mean refrigerant mass flux and a higher mean refrigerant saturation temperature mainly cause higher mean levels of  $n_{ac}$ . It is due to the lower surface tension for R-410A at a higher saturated temperature which in turn facilitates the bubble nucleation.

Based on the present data, the dependence of the quantitative bubble characteristics on the mass flux oscillation can be approximately expressed as  $d_p \propto G^{-a}$ ,  $f \propto G^b$  and  $n_{ac} \propto G^c$  in Fig. 4.55, when the short time lag in the  $T_w$  oscillation is neglected. Here the exponents  $a$ ,  $b$  and  $c$  range respectively from 0.415 to 0.375, 1.11 to 1.2 and 1.25 to 1.15. Note that the latent heat transfer resulting from bubble nucleation in the persistent boiling

$q_b$  is proportional to  $d_p^3$ ,  $f$  and  $n_{ac}$ , as discussed in the previous study [8]. Thus  $q_b \propto G^{-d}$ , here  $d$  varies from 1.385 to 1.075. This result clearly indicates that the flow boiling heat transfer gets better at decreasing refrigerant mass flux since  $q_b$  prevails in the boiling heat transfer. This in turn causes the heated wall temperature to decrease at decreasing refrigerant mass flux in the time periodic flow boiling.



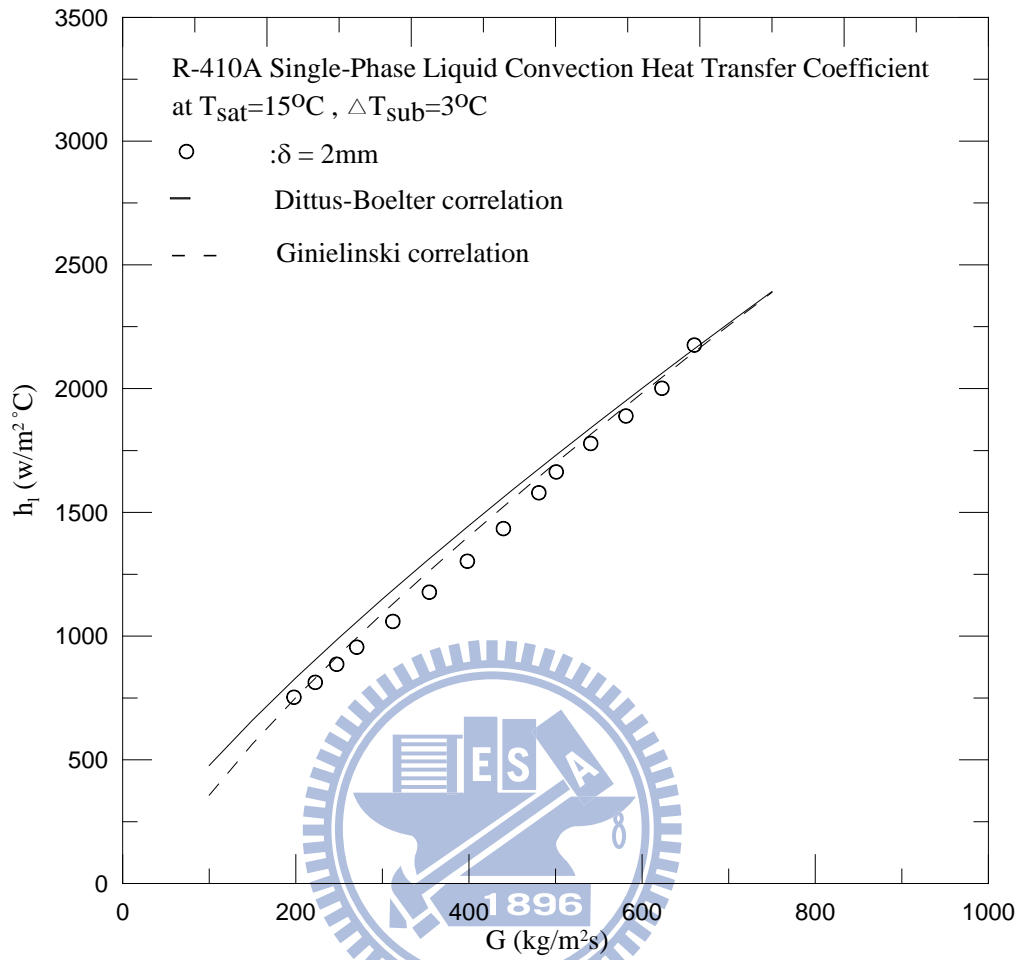


Fig. 4.1 Comparison of the preset single-phase liquid convection heat transfer data with the correlations of Gnielinski and Dittus-Boelter.



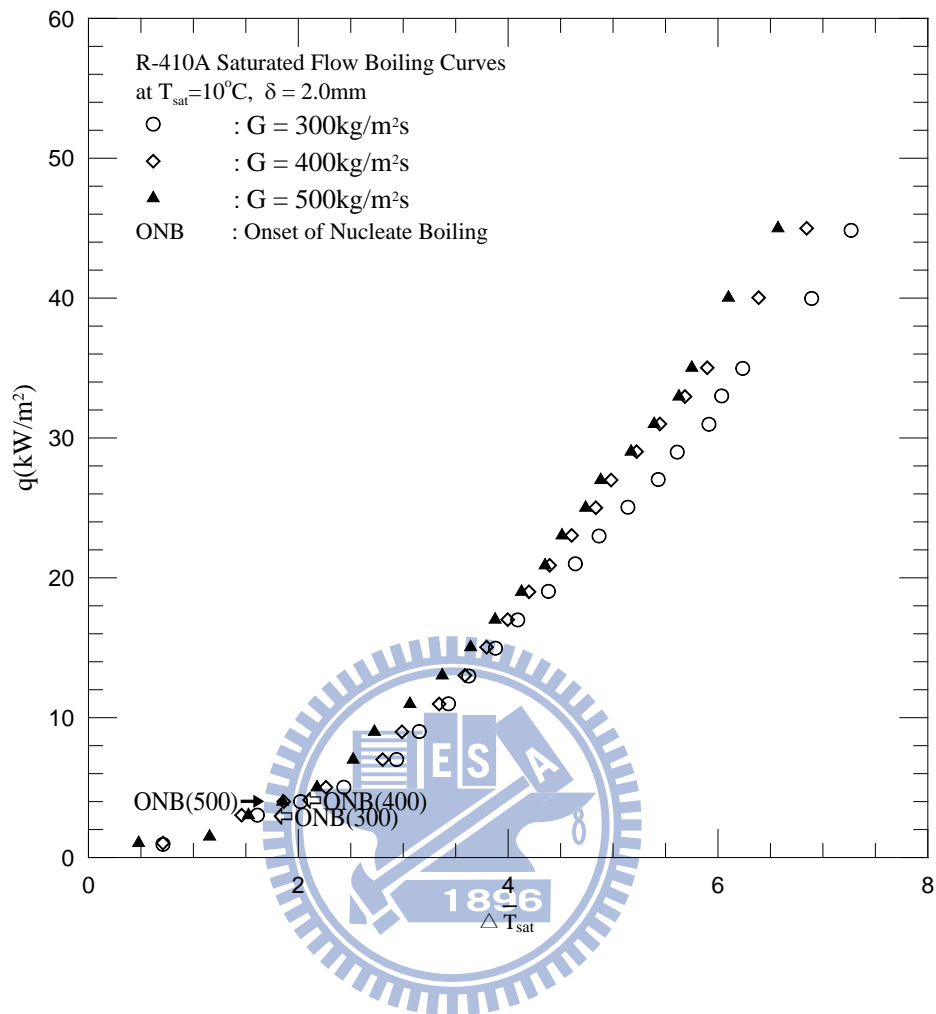


Fig. 4.2 Stable saturated flow boiling curves for R-410A for various refrigerant mass fluxes at  $T_{\text{sat}} = 10^\circ\text{C}$  and  $\delta = 2.0\text{mm}$ .

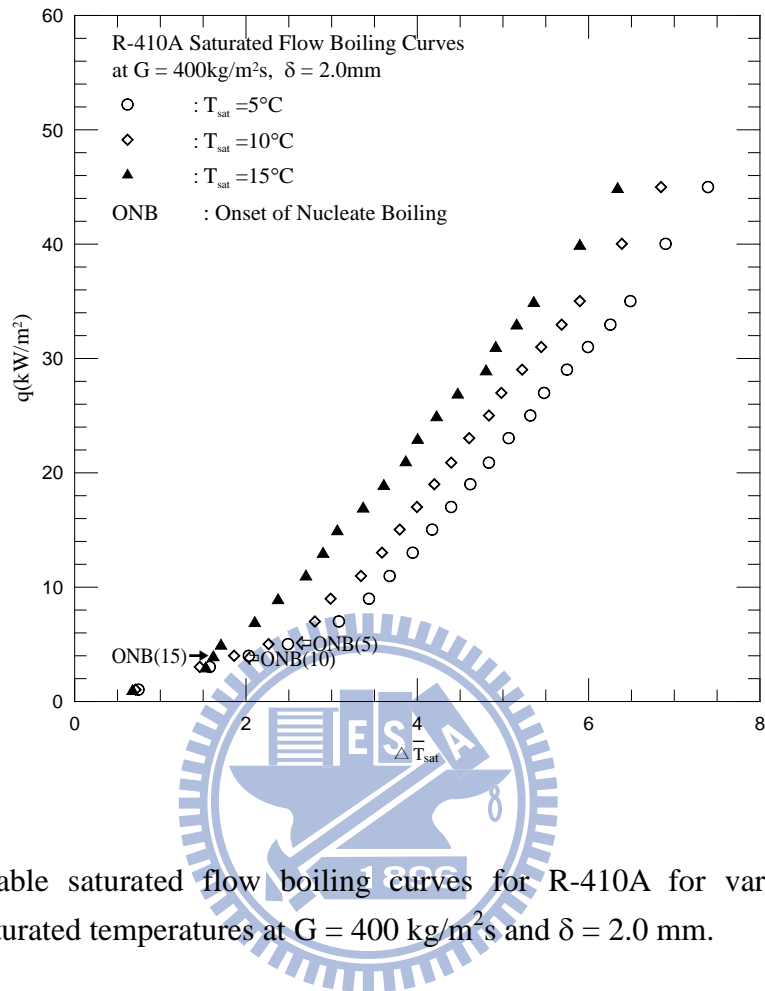


Fig. 4.3 Stable saturated flow boiling curves for R-410A for various refrigerant saturated temperatures at  $G = 400 \text{ kg/m}^2\text{s}$  and  $\delta = 2.0 \text{ mm}$ .

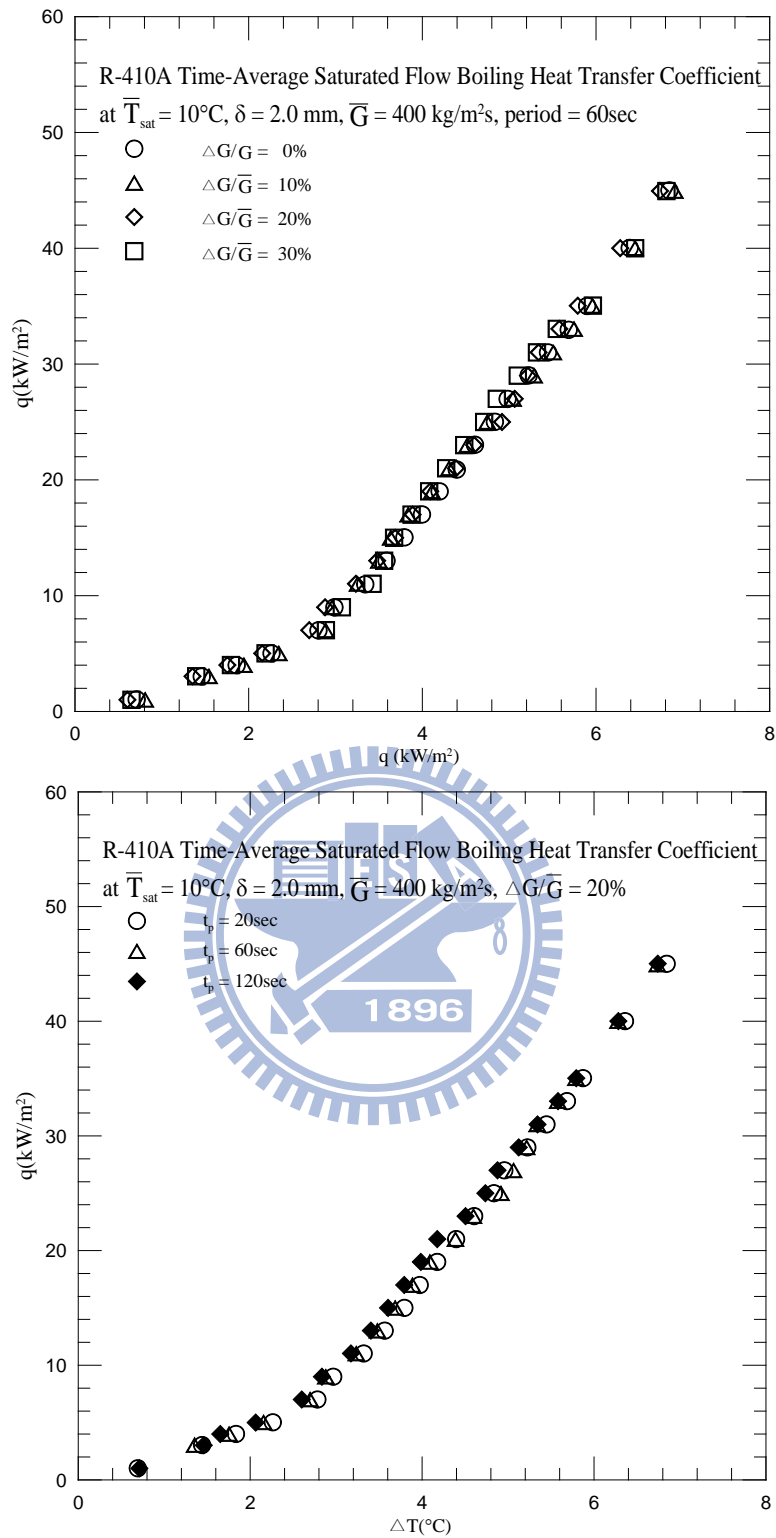


Fig. 4.4 Time-average flow boiling curves for R-410A for (a) various amplitudes of refrigerant mass flux oscillation at  $\bar{T}_{\text{sat}}=10^\circ\text{C}$ ,  $\delta = 2.0 \text{ mm}$ ,  $\bar{G}=400\text{kg/m}^2$  and  $t_p = 60 \text{ sec}$ . and (b) various periods of refrigerant mass flux oscillation at  $\bar{T}_{\text{sat}}=10^\circ\text{C}$ ,  $\delta = 2.0 \text{ mm}$ ,  $\bar{G}=400\text{kg/m}^2$  and  $\Delta G/\bar{G}=20\%$ .

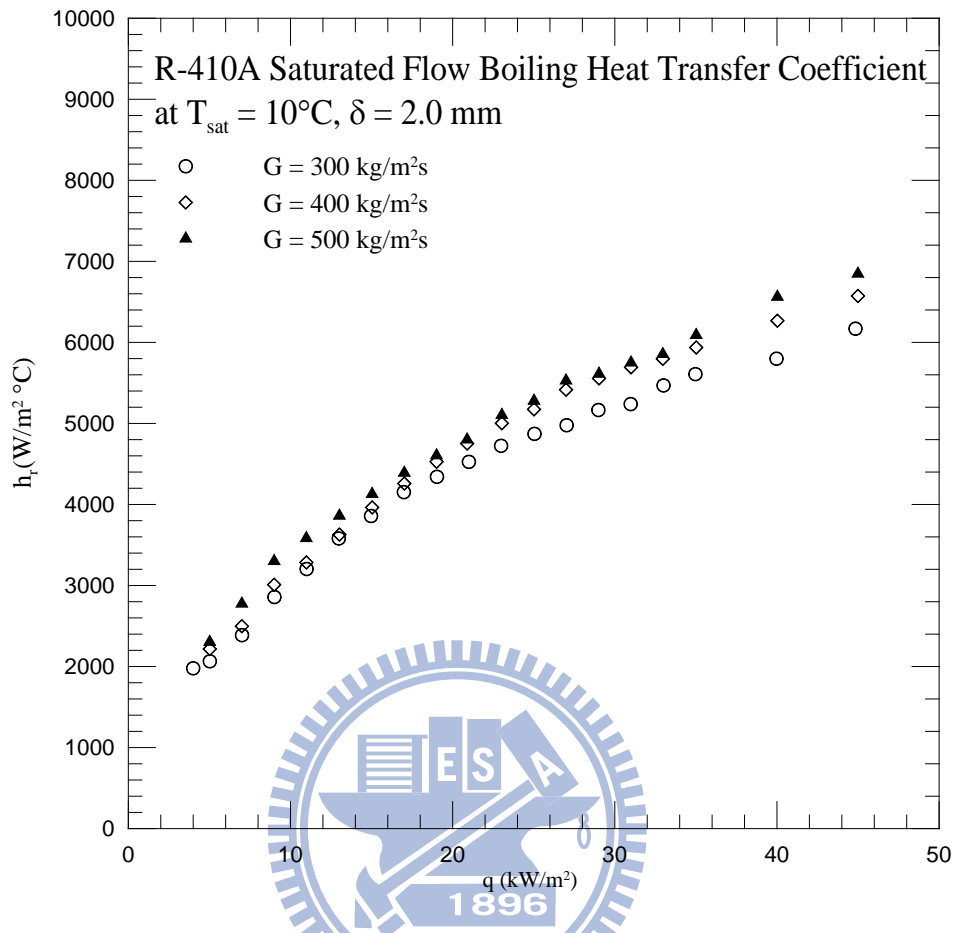


Fig. 4.5 Stable saturated flow boiling heat transfer coefficient for R-410A for various refrigerant mass fluxes at  $T_{\text{sat}} = 10^{\circ}\text{C}$ .

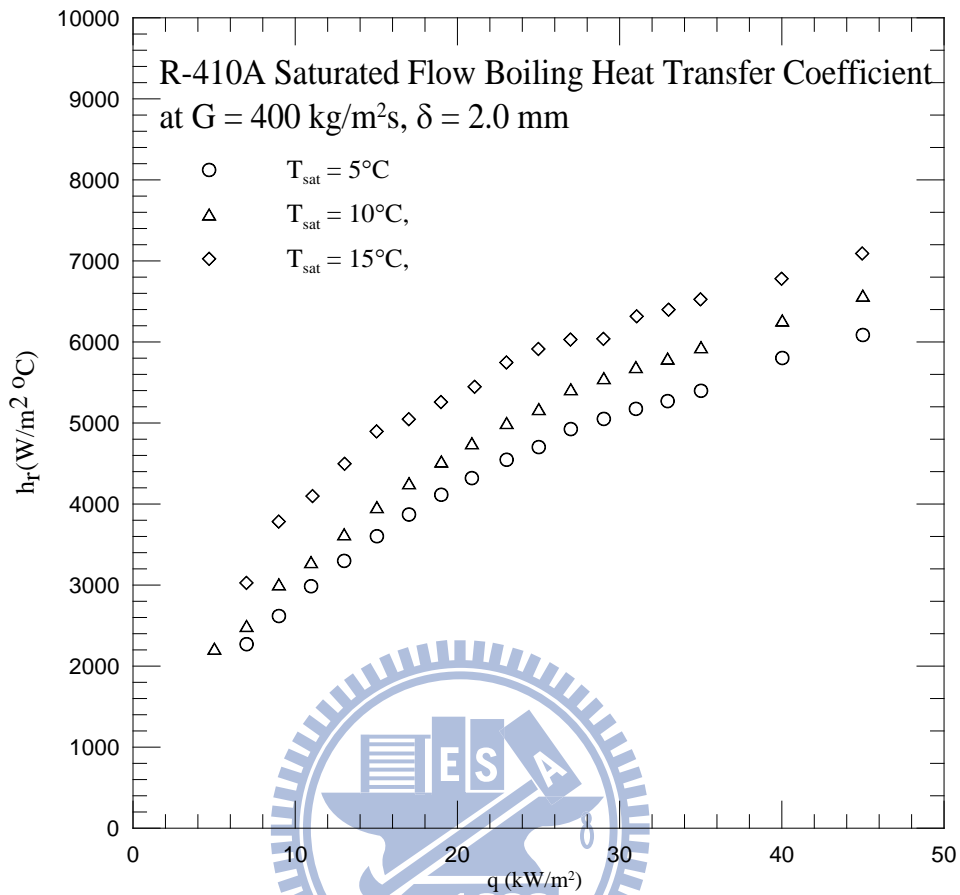


Fig. 4.6 Stable saturated flow boiling heat transfer coefficient for R-410A for various refrigerant saturated temperatures at  $G = 400 \text{ kg/m}^2\text{s}$  and  $\delta = 2.0 \text{ mm}$ .

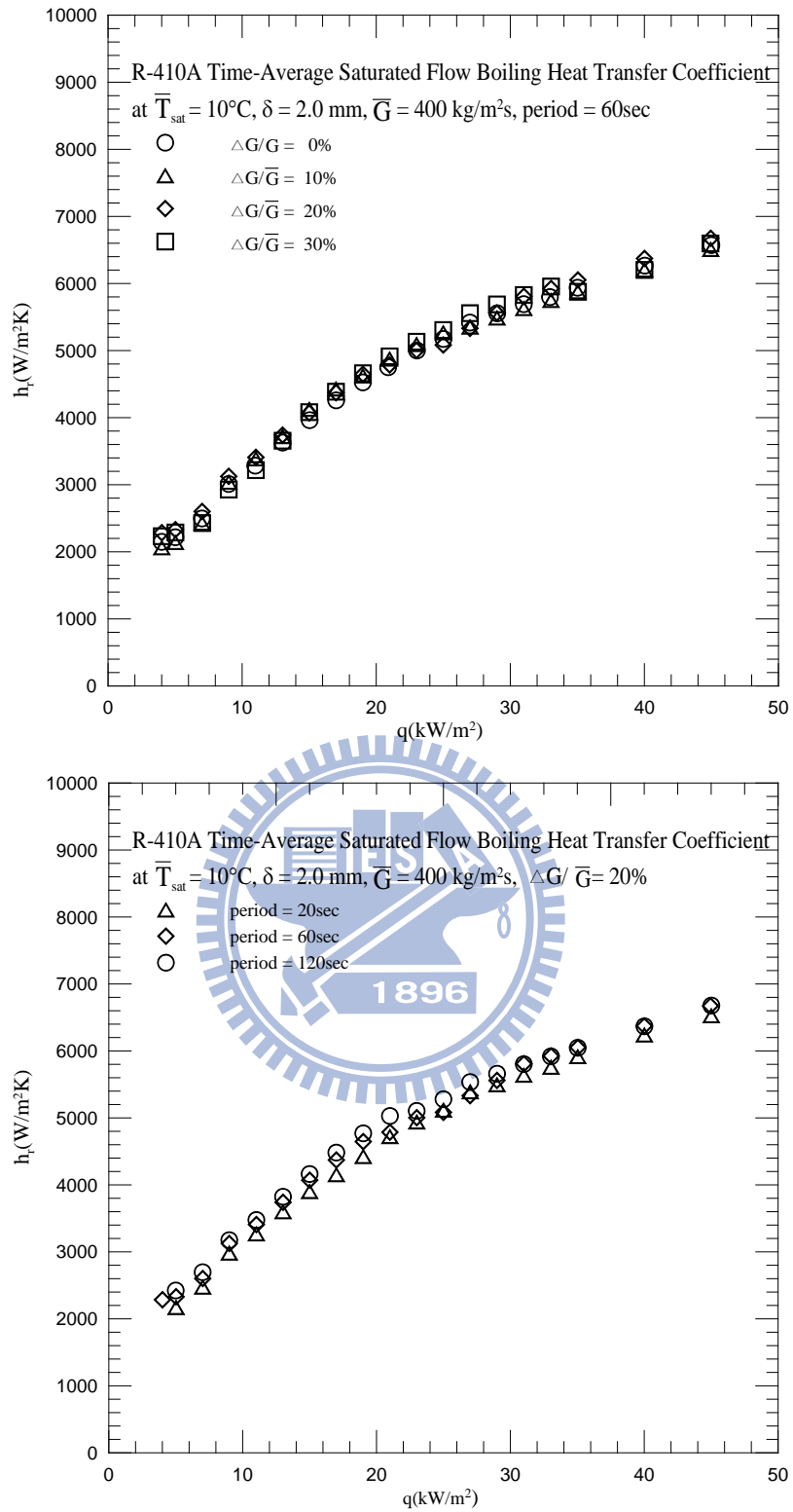


Fig. 4.7 Time-average heat transfer coefficients for R-410A for (a) various  $\Delta G/\bar{G}$  at  $\bar{T}_{\text{sat}} = 10^\circ\text{C}$ ,  $\bar{G} = 400 \text{ kg/m}^2\text{s}$ ,  $\delta = 2.0 \text{ mm}$  and  $t_p = 60 \text{ sec}$ . and (b) various  $t_p$  at  $\bar{T}_{\text{sat}} = 10^\circ\text{C}$ ,  $\bar{G} = 400 \text{ kg/m}^2\text{s}$ ,  $\delta = 2.0 \text{ mm}$  and  $\Delta G/\bar{G} = 20\%$ .

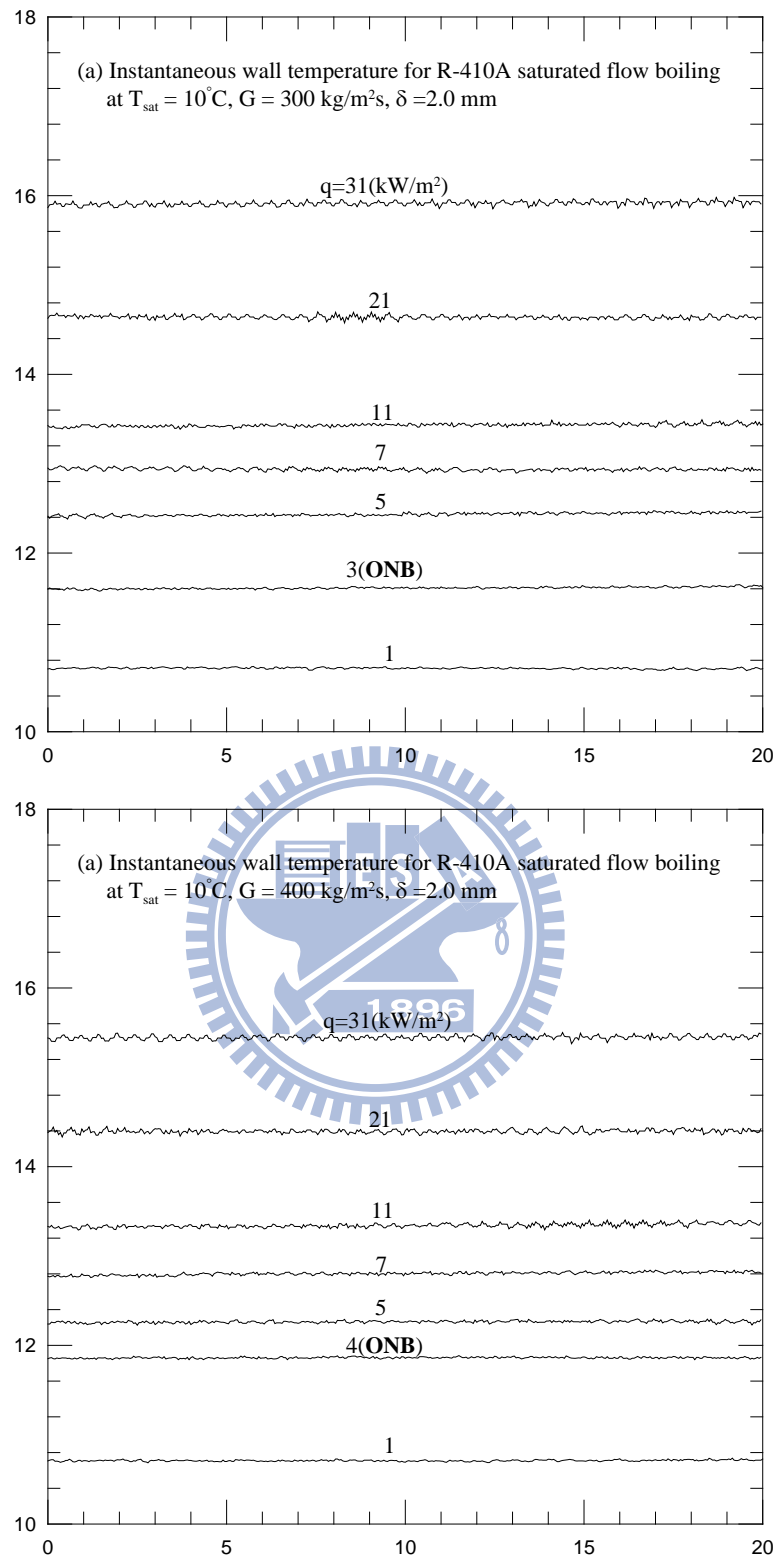


Fig. 4.8 Time variations of measured heated surface temperature for the stable saturated flow boiling of R-410A for various imposed heat fluxes at (a)  $\bar{G} = 300 \text{ kg/m}^2\text{s}$  and (b)  $\bar{G} = 400 \text{ kg/m}^2\text{s}$  at  $T_{\text{sat}} = 10^\circ\text{C}$ .

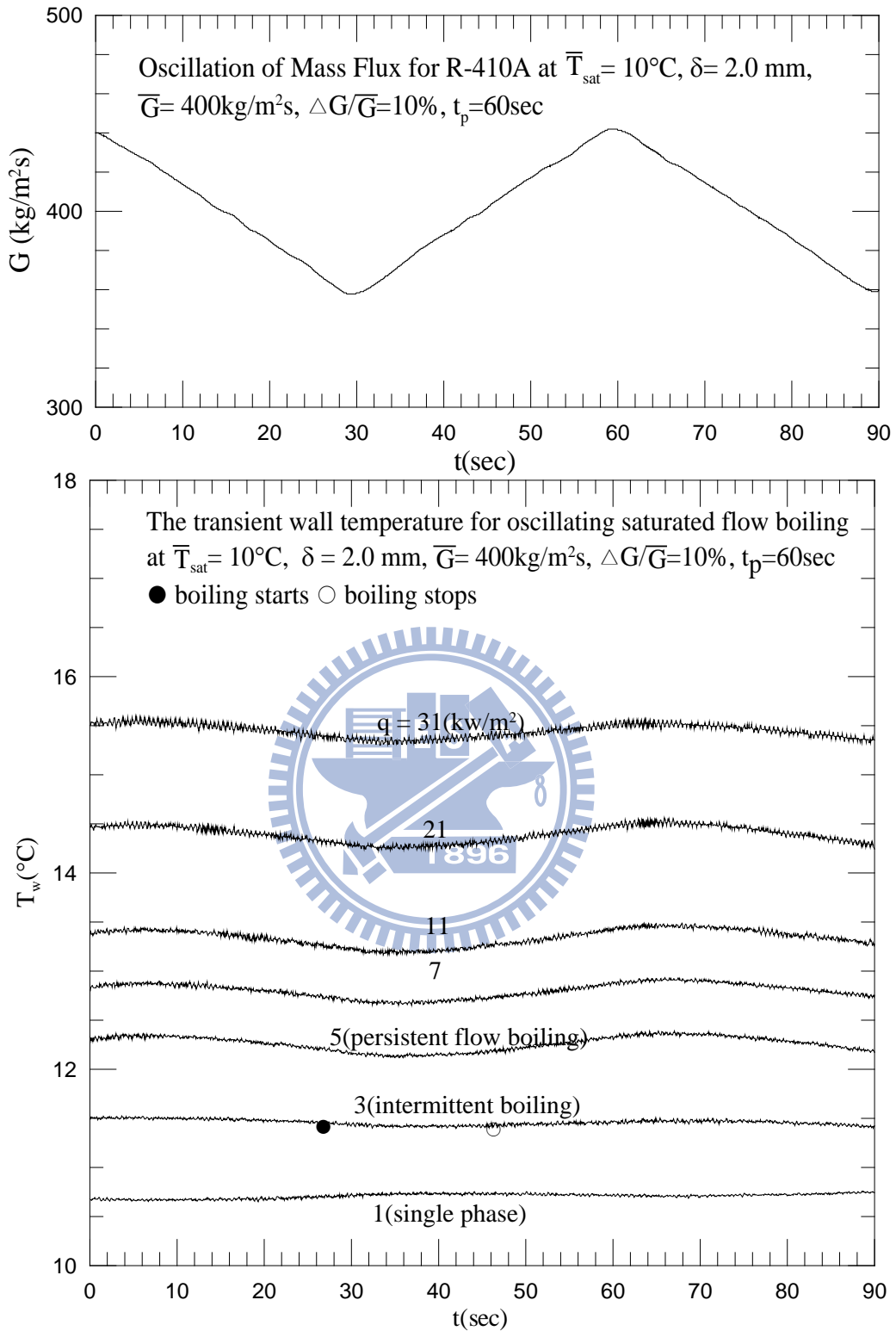


Fig. 4.9 Time variations of oscillating refrigerant mass flux and measured heated wall temperature in time periodic saturated flow boiling of R-410A for various imposed heat fluxes at  $\bar{T}_{\text{sat}} = 10^\circ\text{C}$ ,  $\delta = 2.0 \text{ mm}$ ,  $t_p = 60 \text{ sec}$  and  $\bar{G} = 400 \text{ kg/m}^2\text{s}$  with  $\Delta G/\bar{G} = 10\%$ .



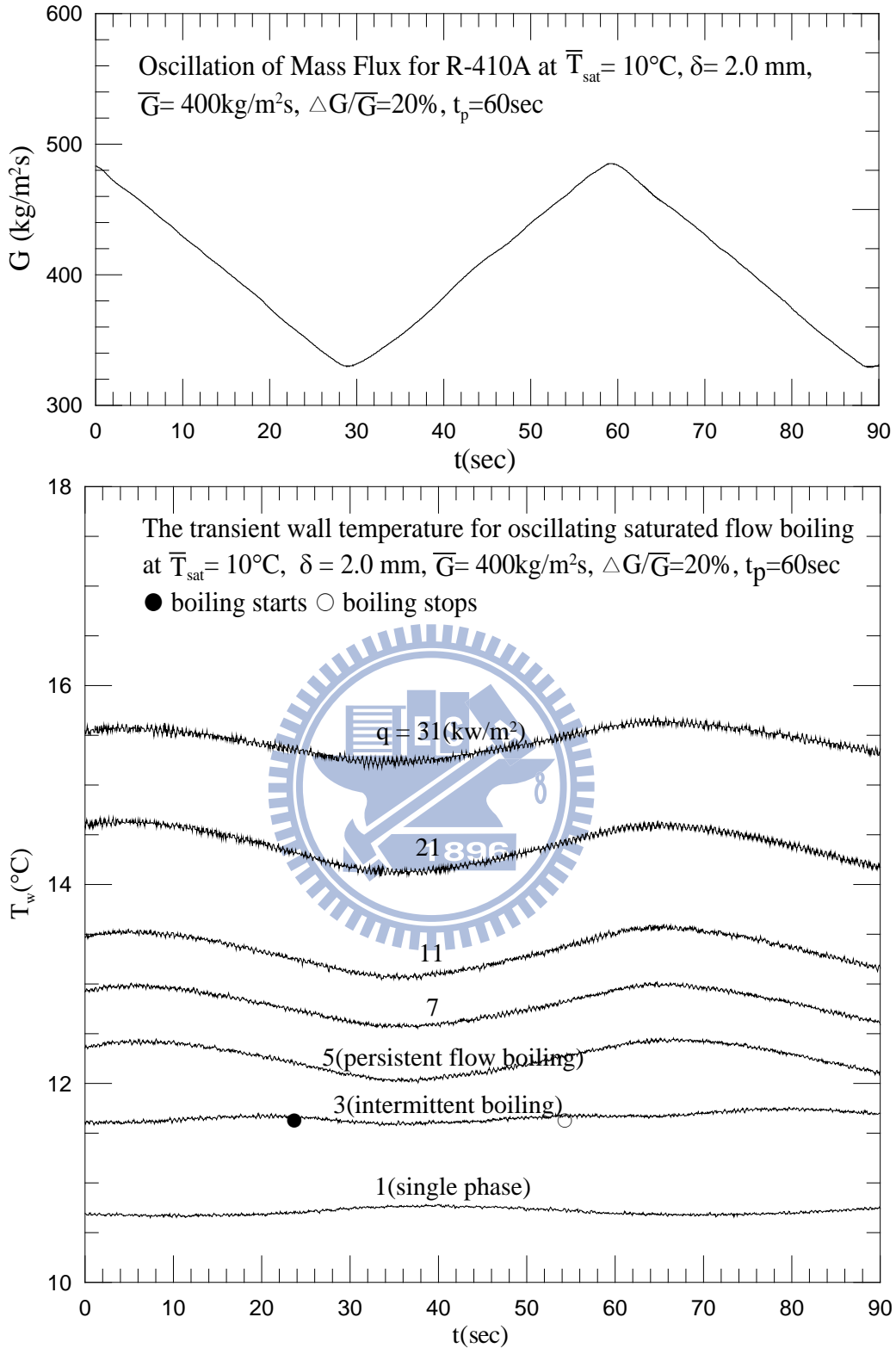


Fig. 4.10 Time variations of oscillating refrigerant mass flux and measured heated wall temperature in time periodic saturated flow boiling of R-410A for various imposed heat fluxes at  $\bar{T}_{\text{sat}} = 10^\circ\text{C}$ ,  $\delta = 2.0 \text{ mm}$ ,  $t_p = 60 \text{ sec}$  and  $\bar{G} = 400 \text{ kg/m}^2\text{s}$  with  $\Delta G/\bar{G} = 20\%$ .

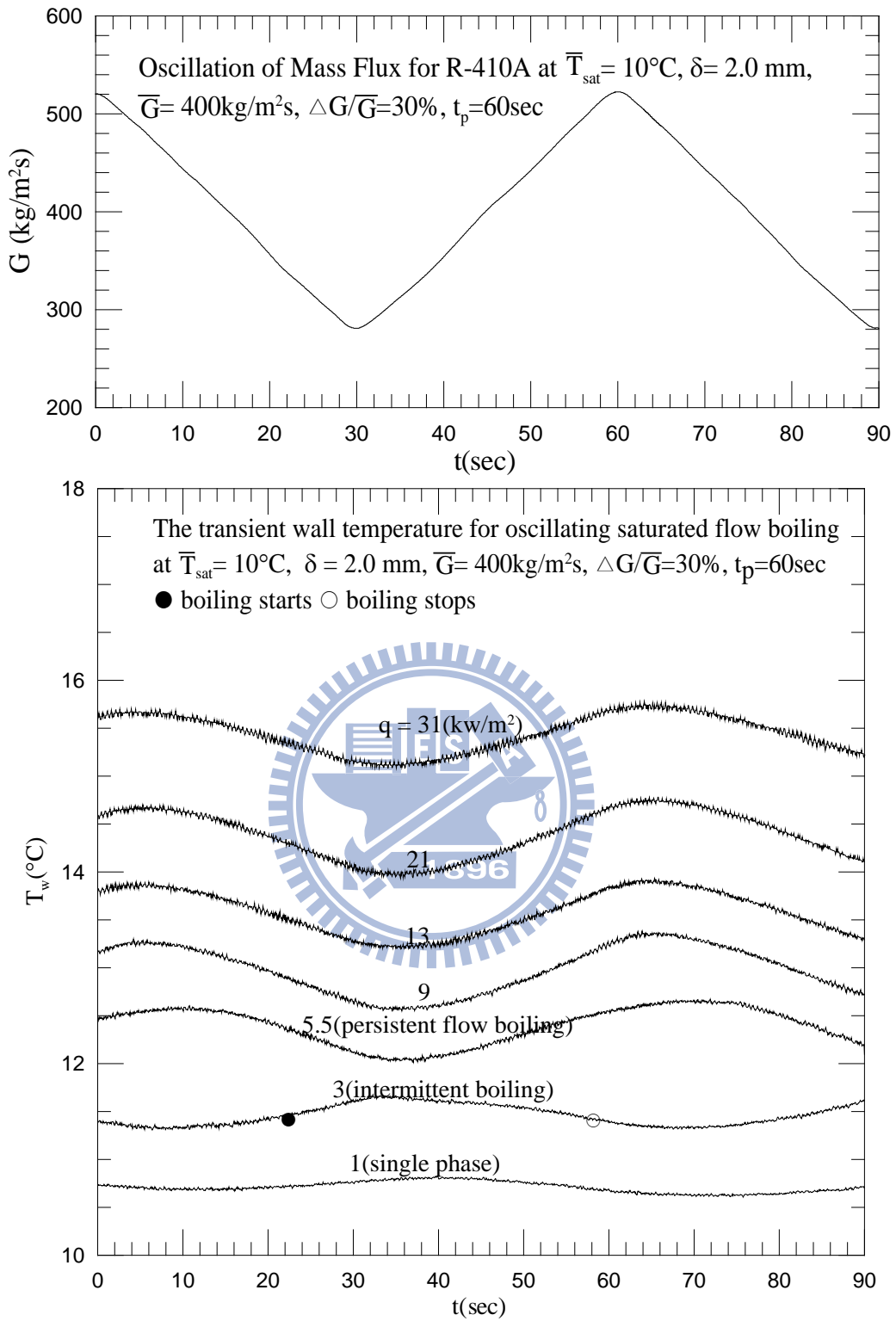


Fig. 4.11 Time variations of oscillating refrigerant mass flux and measured heated wall temperature in time periodic saturated flow boiling of R-410A for various imposed heat fluxes at  $\bar{T}_{\text{sat}} = 10^\circ\text{C}$ ,  $\delta = 2.0 \text{ mm}$ ,  $t_p = 60 \text{ sec}$  and  $\bar{G} = 400 \text{ kg/m}^2\text{s}$  with  $\Delta G/\bar{G} = 30\%$ .

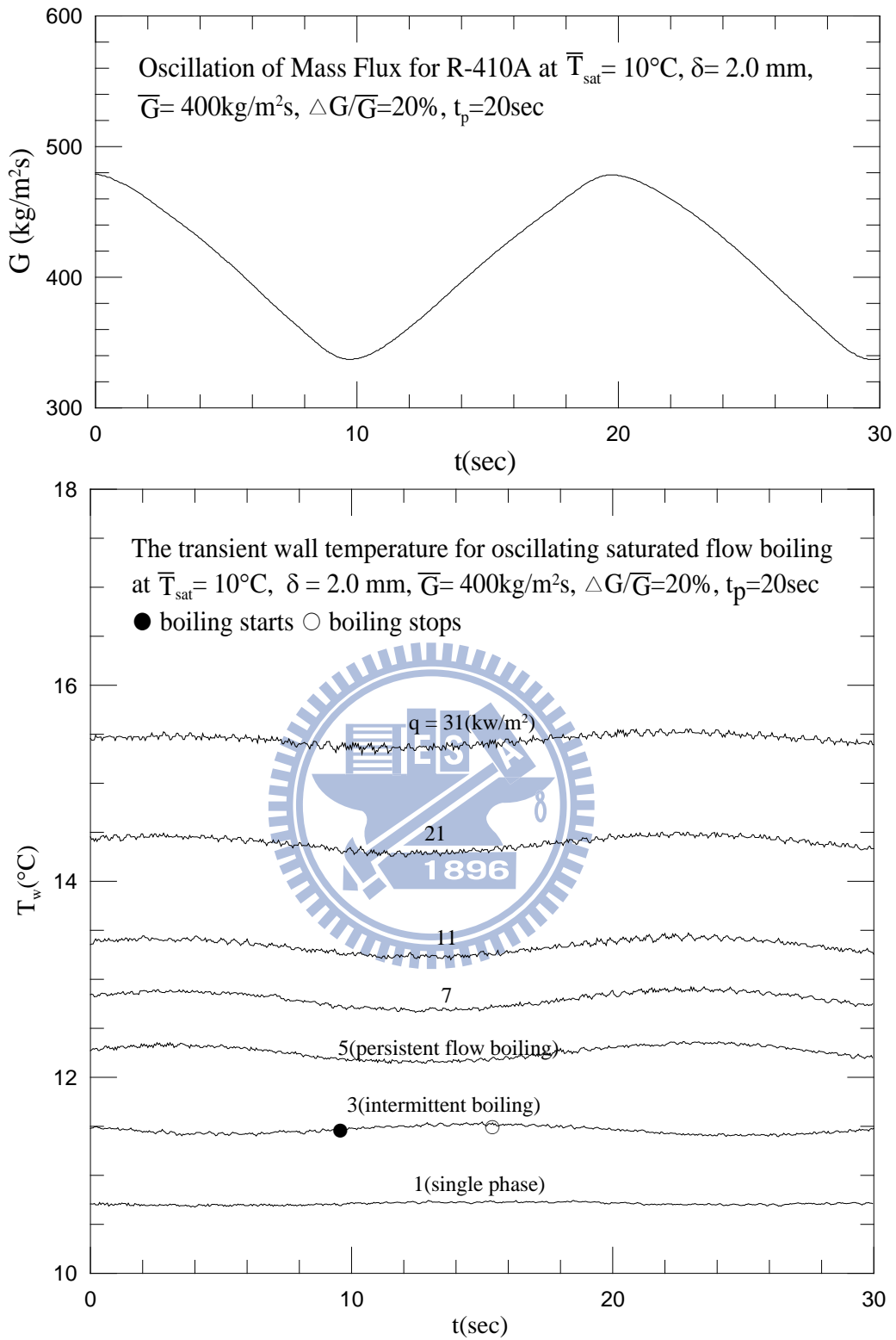


Fig. 4.12 Time variations of oscillating refrigerant mass flux and measured heated wall temperature in time periodic saturated flow boiling of R-410A for various imposed heat flux at  $\bar{T}_{sat} = 10^\circ\text{C}$ ,  $\delta = 2.0 \text{ mm}$ ,  $t_p = 20 \text{ sec}$  and  $\bar{G} = 400 \text{ kg/m}^2\text{s}$  with  $\Delta G/\bar{G} = 20\%$ .

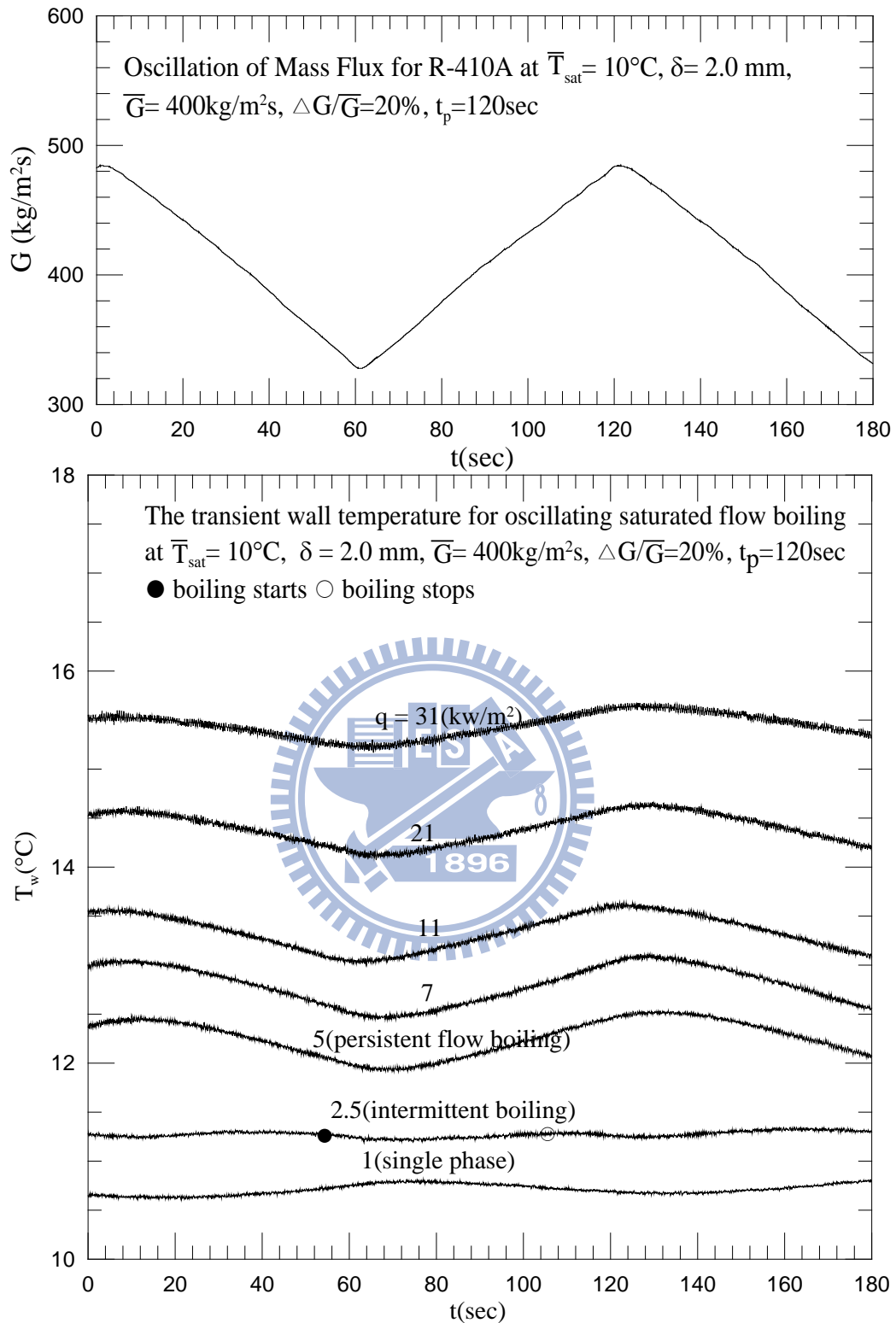


Fig. 4.13 Time variations of oscillating refrigerant mass flux and measured heated wall temperature in time periodic saturated flow boiling of R-410A for various imposed heat flux at  $\bar{T}_{\text{sat}}=10^\circ\text{C}$ ,  $\delta = 2.0\text{mm}$ ,  $t_p = 120 \text{ sec}$  and  $\bar{G} = 400 \text{ kg/m}^2\text{s}$  with  $\Delta G/\bar{G}=20\%$ .

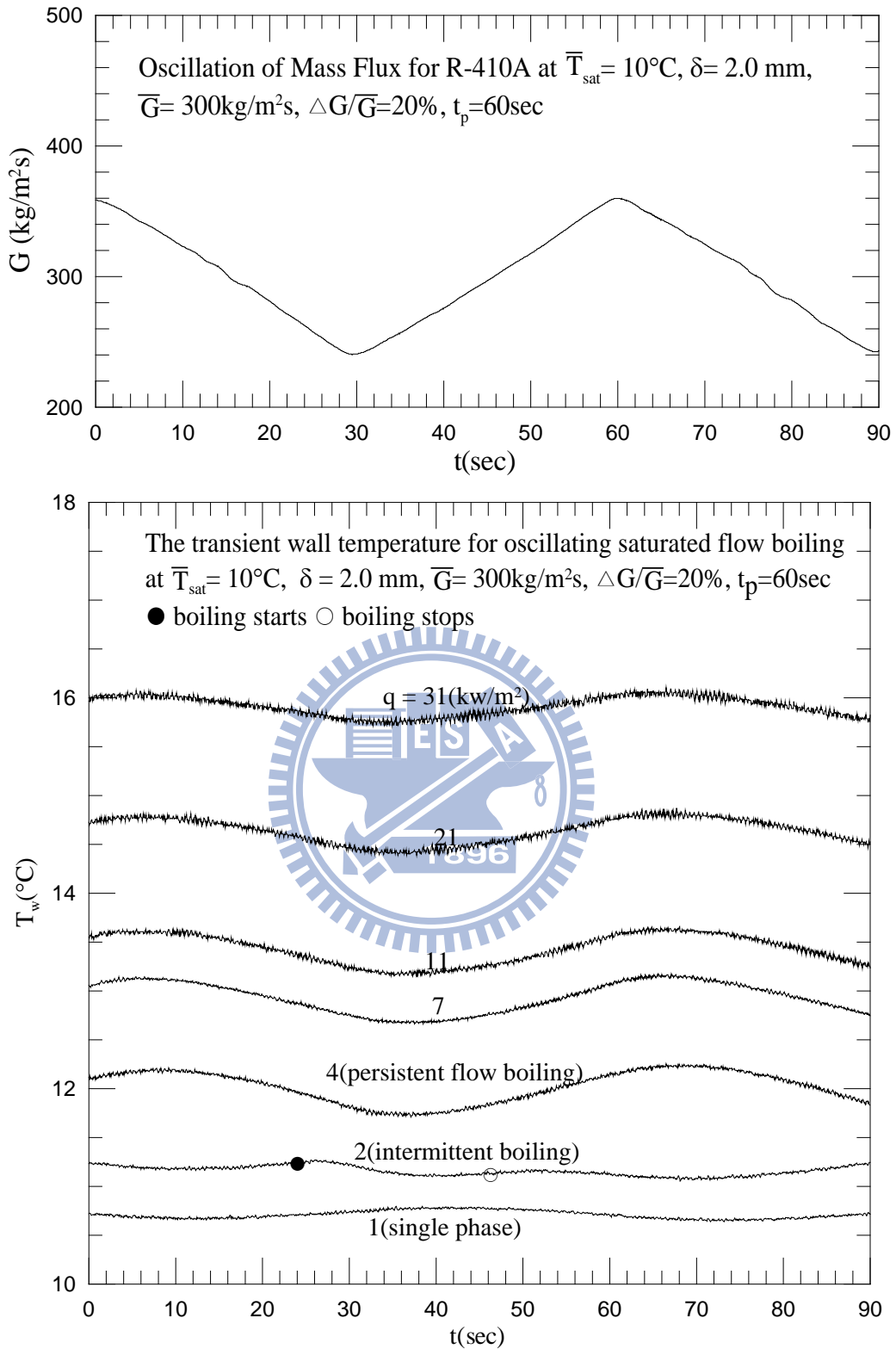


Fig. 4.14 Time variations of oscillating refrigerant mass flux and measured heated wall temperature in time periodic saturated flow boiling of R-410A for various imposed heat flux at  $\bar{T}_{\text{sat}} = 10^\circ\text{C}$ ,  $\delta = 2.0 \text{ mm}$ ,  $t_p = 60 \text{ sec}$  and  $\bar{G} = 300 \text{ kg/m}^2\text{s}$  with  $\Delta G/\bar{G} = 20\%$ .

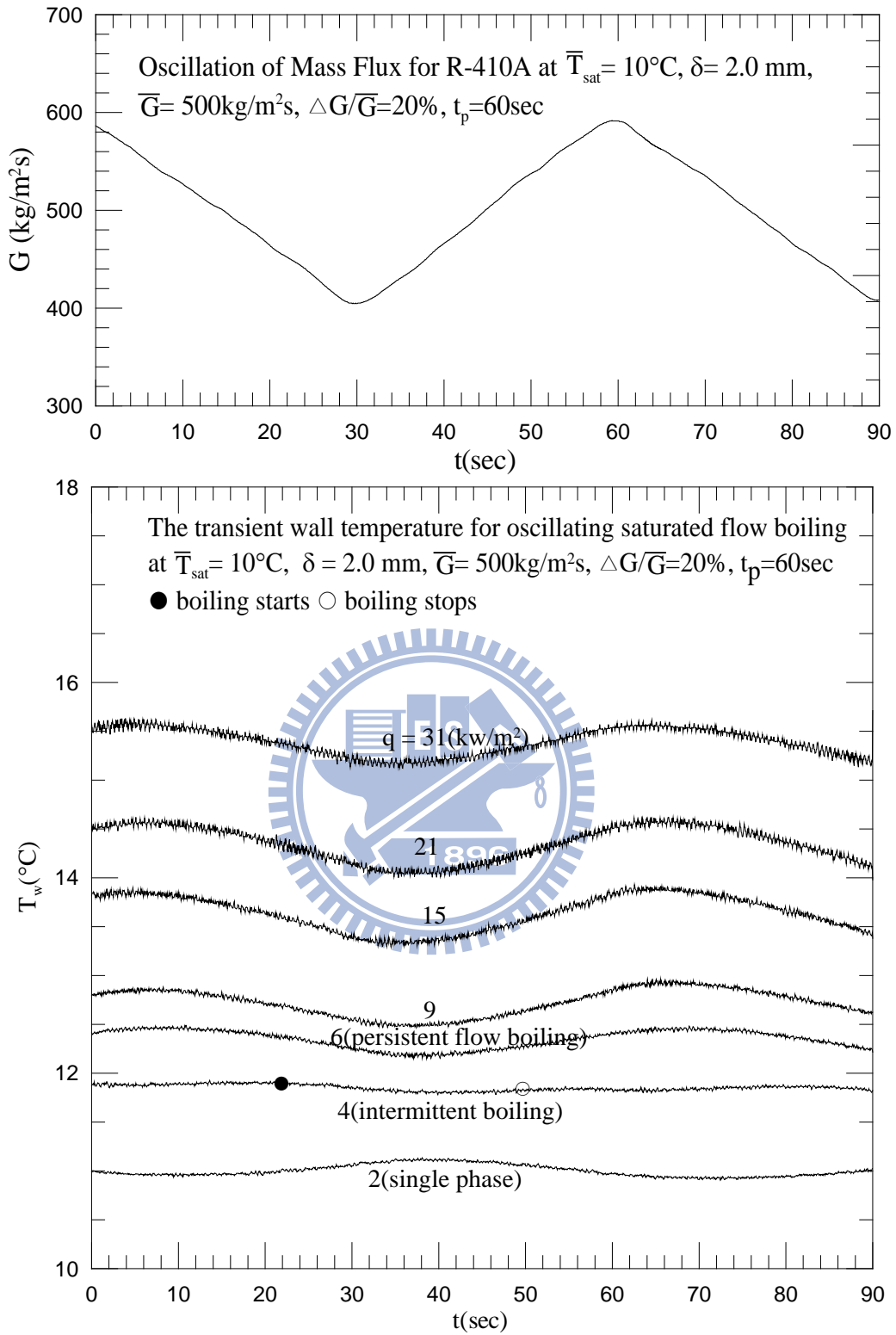


Fig. 4.15 Time variations of oscillating refrigerant mass flux and measured heated wall temperature in time periodic saturated flow boiling of R-410A for various imposed heat flux at  $\bar{T}_{sat} = 10^\circ\text{C}$ ,  $\delta = 2.0\text{ mm}$ ,  $t_p = 60\text{ sec}$  and  $\bar{G} = 500\text{ kg/m}^2\text{ s}$  with  $\Delta G/\bar{G} = 20\%$ .

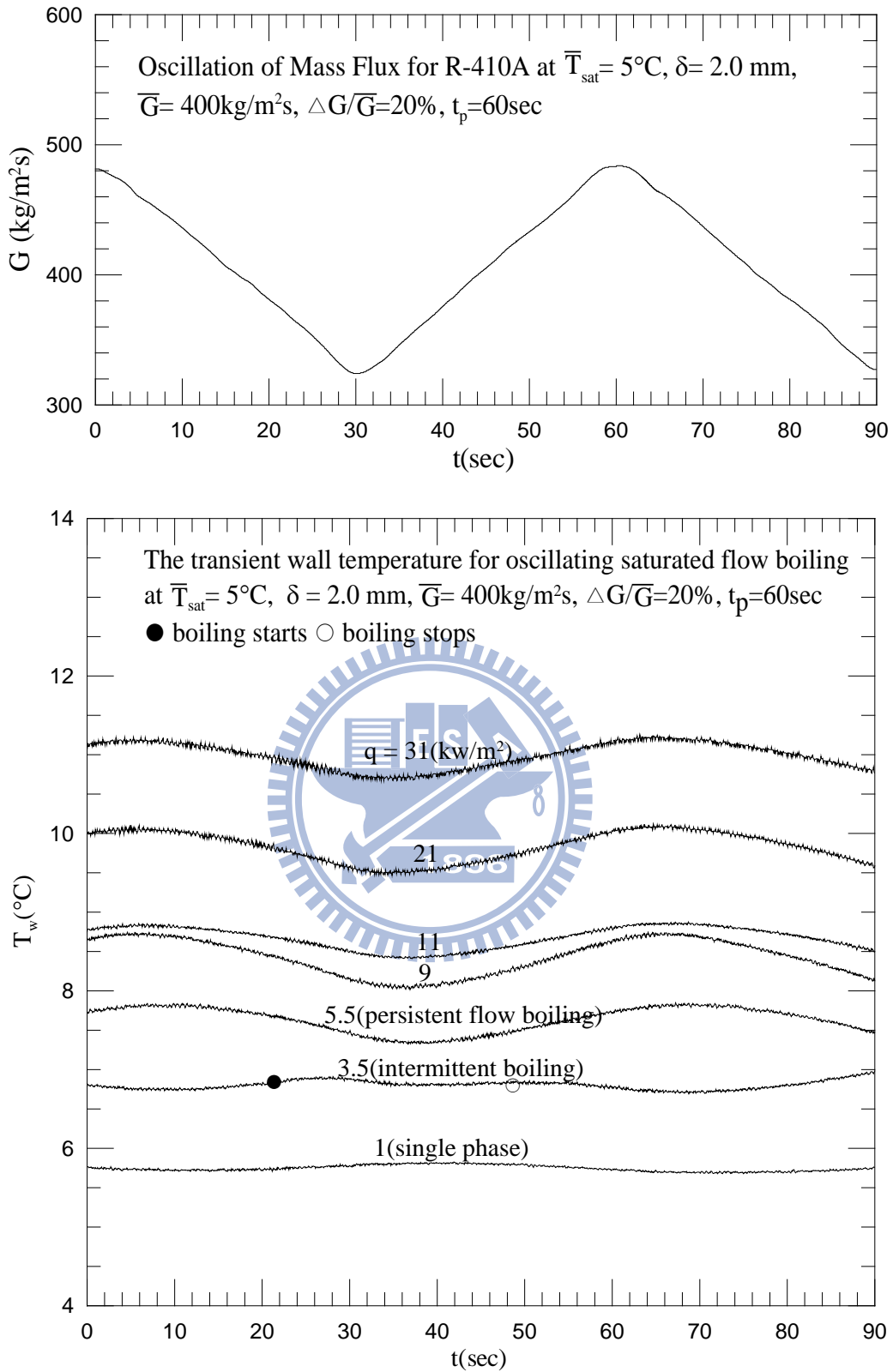


Fig. 4.16 Time variations of oscillating refrigerant mass flux and measured heated wall temperature in time periodic saturated flow boiling of R-410A for various imposed heat flux at  $\bar{T}_{sat} = 5^\circ\text{C}$ ,  $\delta = 2.0\text{ mm}$ ,  $t_p = 60\text{ sec}$  and  $\bar{G} = 400\text{ kg/m}^2\text{s}$  with  $\Delta G/\bar{G} = 20\%$ .

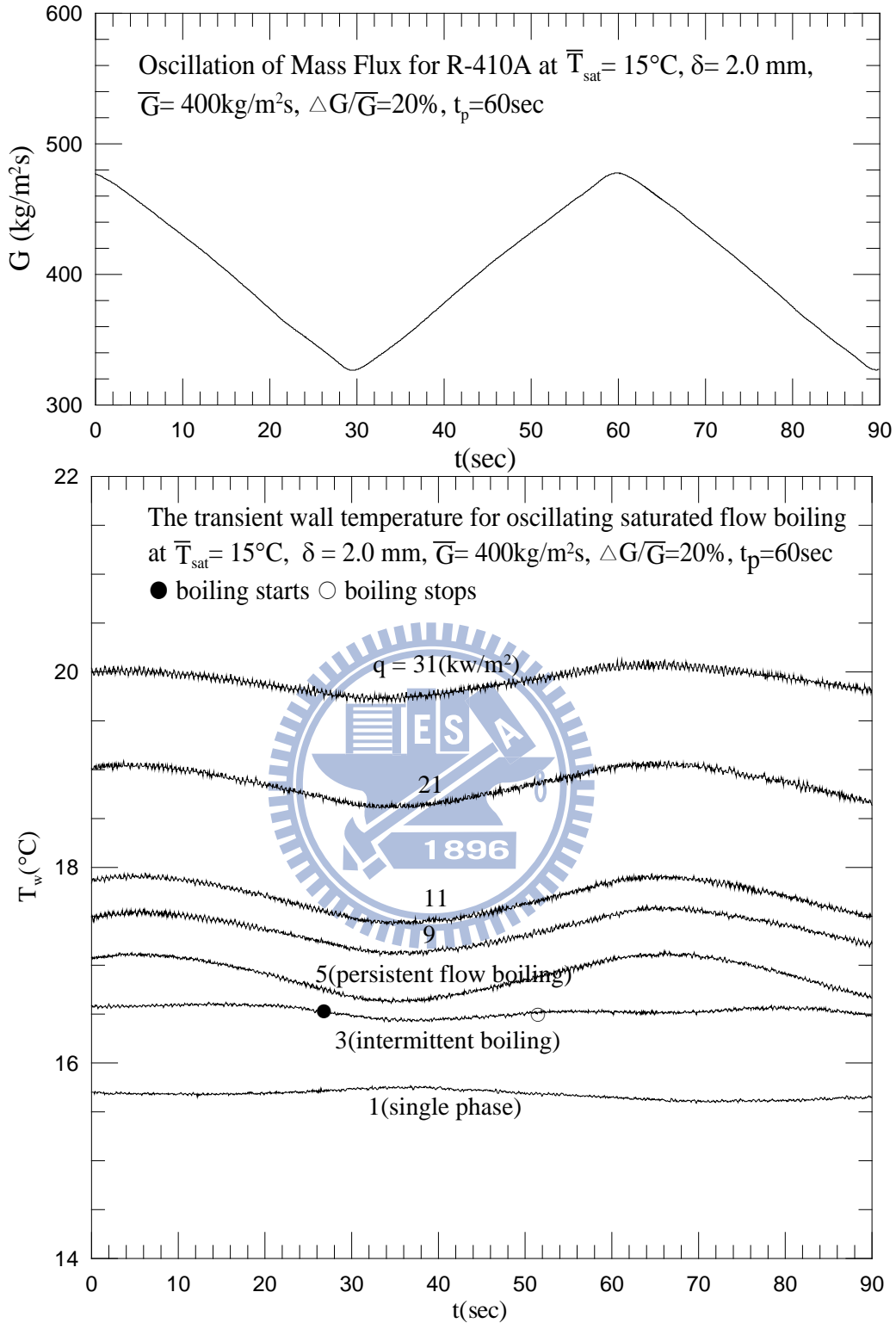


Fig. 4.17 Time variations of oscillating refrigerant mass flux and measured heated wall temperature in time periodic saturated flow boiling of R-410A for various imposed heat flux at  $\bar{T}_{\text{sat}} = 15^\circ\text{C}$ ,  $\delta = 2.0 \text{ mm}$ ,  $t_p = 60 \text{ sec}$  and  $\bar{G} = 400 \text{ kg/m}^2\text{s}$  with  $\Delta G/\bar{G} = 20\%$ .



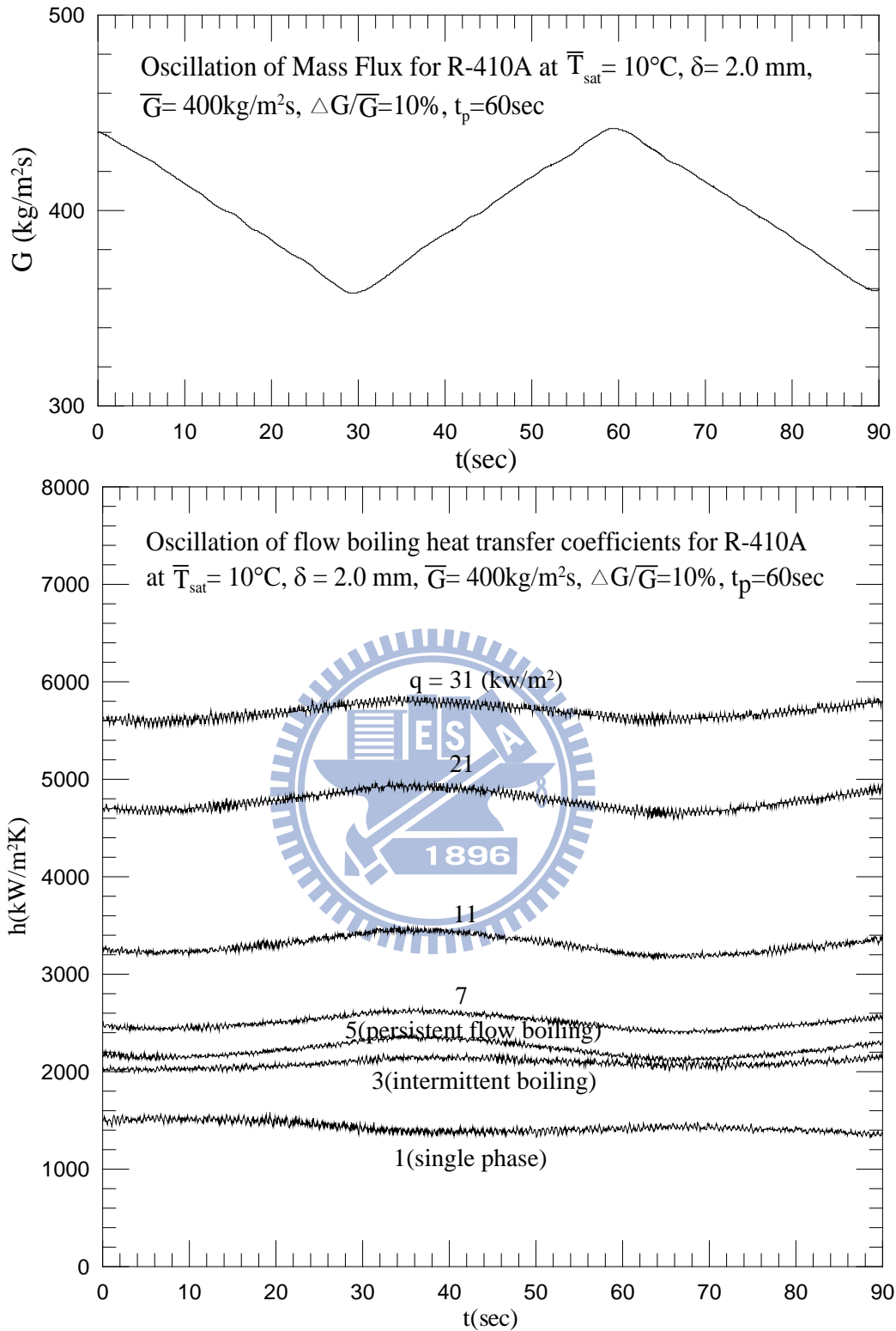


Fig. 4.18 Time variations of flow boiling heat transfer coefficients in time periodic saturated flow boiling of R-410A for various imposed heat fluxes at  $\bar{T}_{\text{sat}} = 10^\circ\text{C}$ ,  $\delta = 2.0 \text{ mm}$ ,  $t_p = 60 \text{ sec}$  and  $\bar{G} = 400 \text{ kg/m}^2\text{s}$  with  $\Delta G/\bar{G} = 10\%$ .

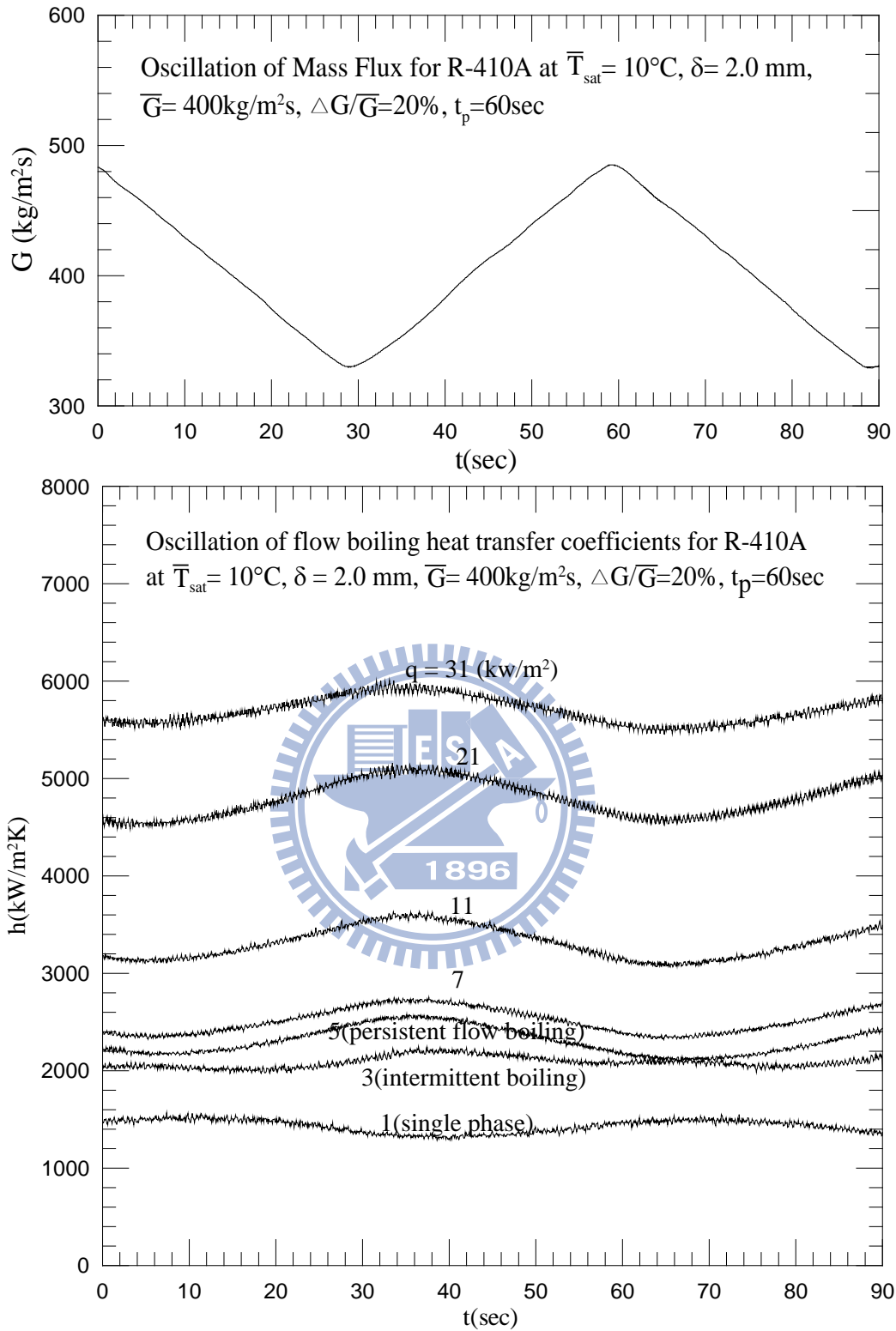


Fig. 4.19 Time variations of flow boiling heat transfer coefficients in time periodic saturated flow boiling of R-410A for various imposed heat fluxes at  $\bar{T}_{\text{sat}} = 10^\circ\text{C}$ ,  $\delta = 2.0 \text{ mm}$ ,  $t_p = 60 \text{ sec}$  and  $\bar{G} = 400 \text{ kg/m}^2\text{s}$  with  $\Delta G/\bar{G} = 20\%$ .

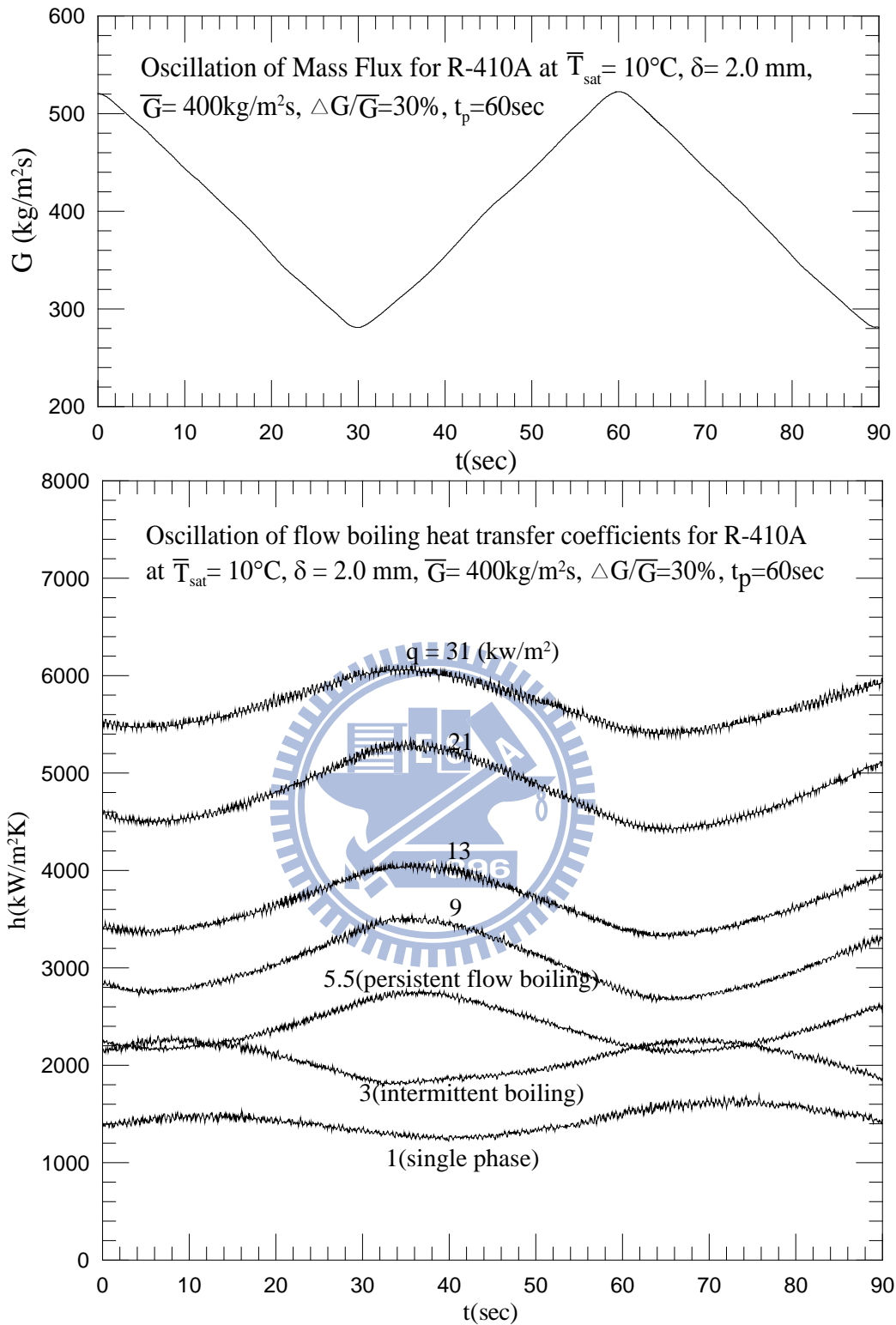


Fig. 4.20 Time variations of flow boiling heat transfer coefficients in time periodic saturated flow boiling of R-410A for various imposed heat fluxes at  $\bar{T}_{\text{sat}} = 10^\circ\text{C}$ ,  $\delta = 2.0 \text{ mm}$ ,  $t_p = 60 \text{ sec}$  and  $\bar{G} = 400 \text{ kg/m}^2\text{s}$  with  $\Delta G/\bar{G} = 30\%$ .

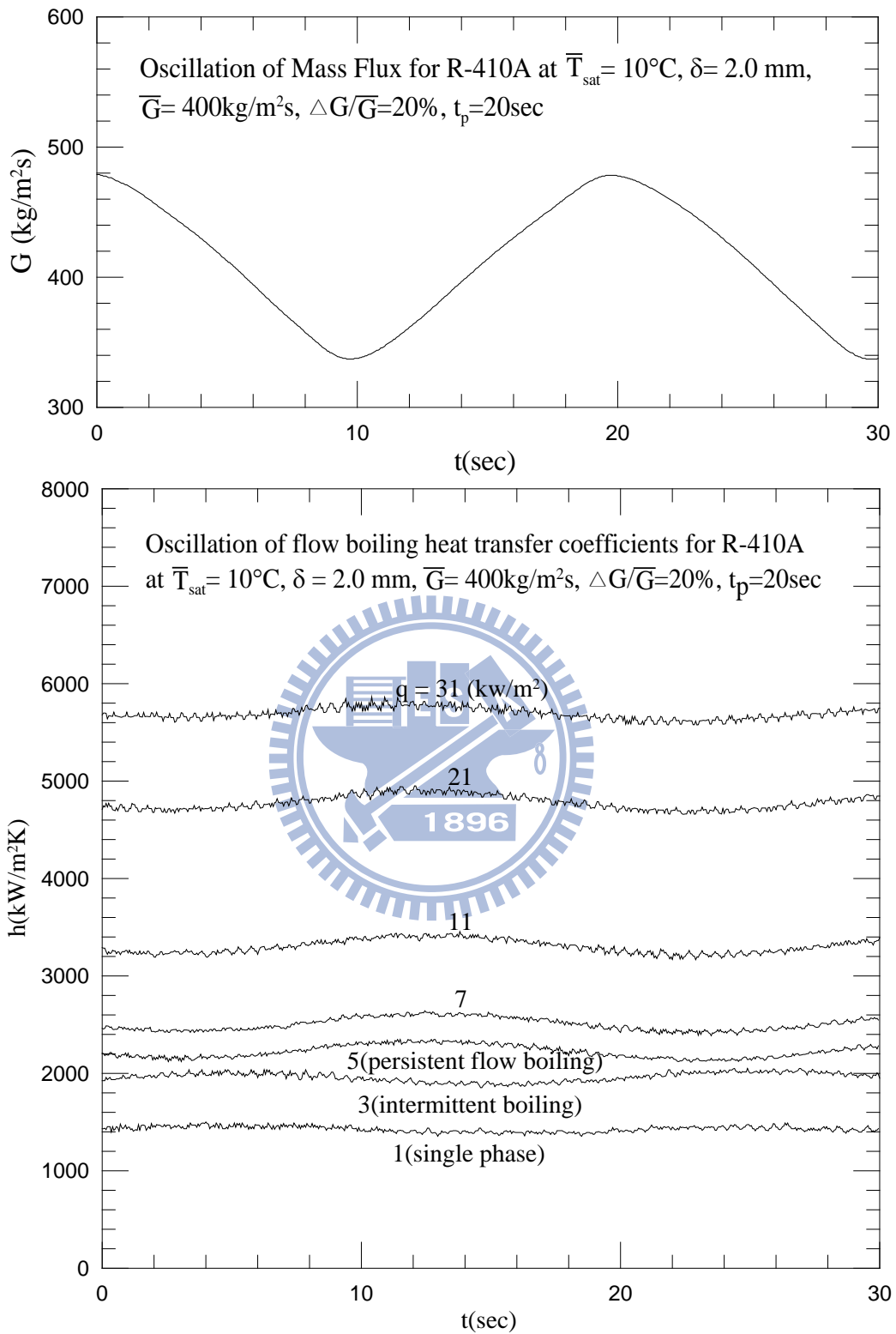


Fig. 4.21 Time variations of flow boiling heat transfer coefficients in time periodic saturated flow boiling of R-410A for various imposed heat fluxes at  $\bar{T}_{\text{sat}} = 10^\circ\text{C}$ ,  $\delta = 2.0 \text{ mm}$ ,  $t_p = 20 \text{ sec}$  and  $\bar{G} = 400 \text{ kg/m}^2\text{s}$  with  $\Delta G/\bar{G} = 20\%$  .

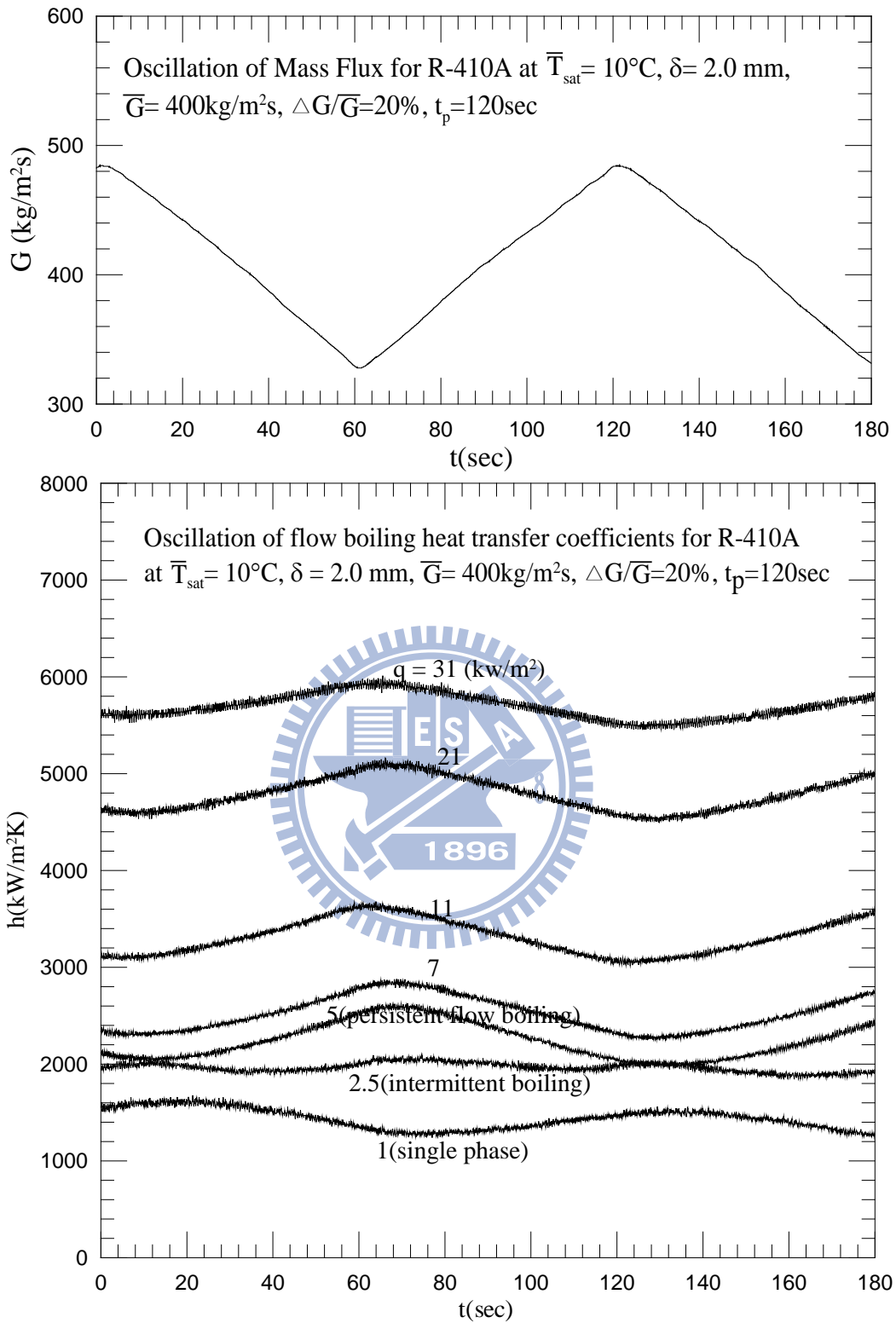


Fig. 4.22 Time variations of flow boiling heat transfer coefficients in time periodic saturated flow boiling of R-410A for various imposed heat fluxes at  $\bar{T}_{\text{sat}} = 10^\circ\text{C}$ ,  $\delta = 2.0\text{mm}$ ,  $t_p = 120$  sec and  $\bar{G} = 400$  kg/m<sup>2</sup>s with  $\Delta G/\bar{G} = 20\%$ .

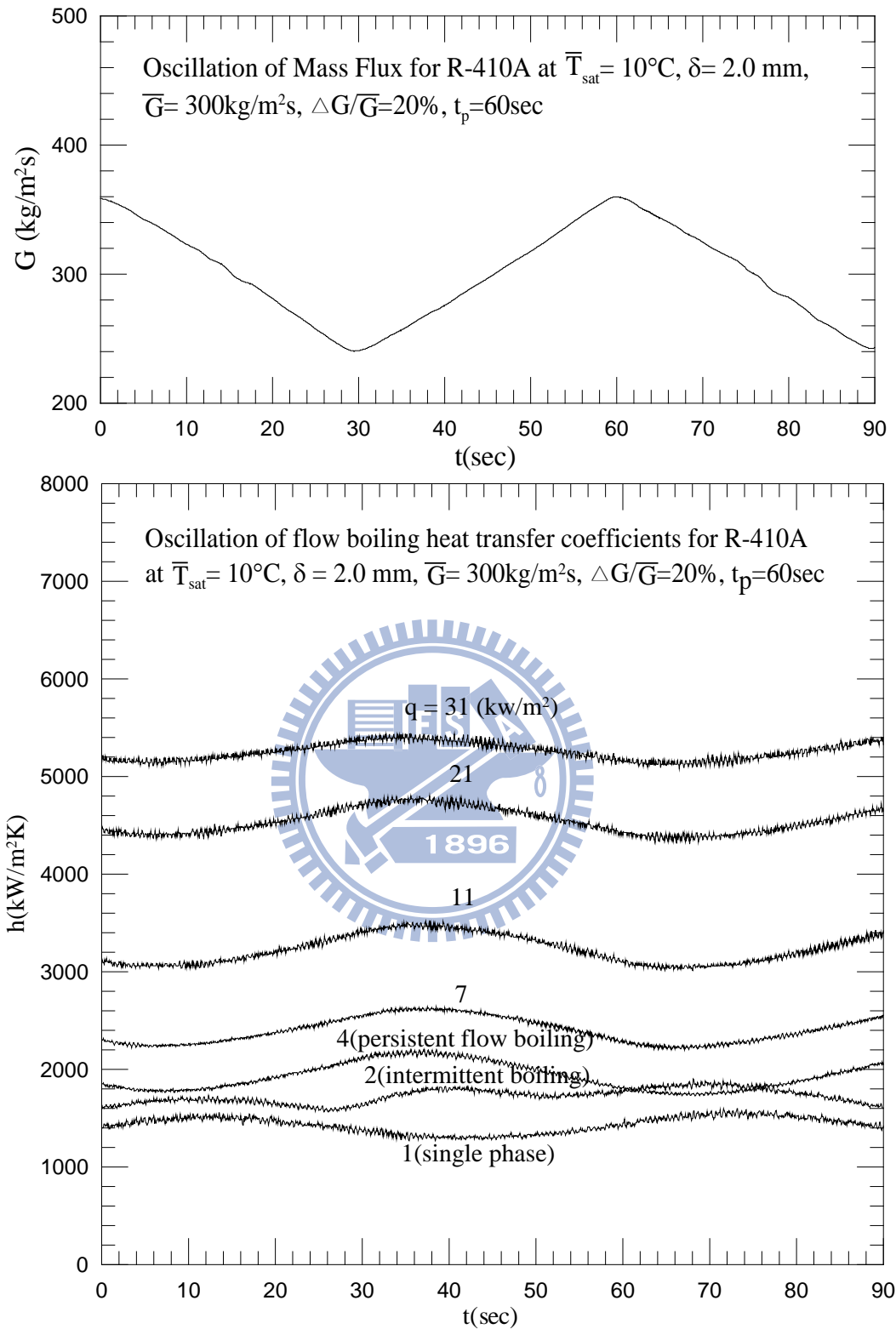


Fig. 4.23 Time variations of flow boiling heat transfer coefficients in time periodic saturated flow boiling of R-410A for various imposed heat fluxes at  $\bar{T}_{\text{sat}} = 10^\circ\text{C}$ ,  $\delta = 2.0 \text{ mm}$ ,  $t_p = 60 \text{ sec}$  and  $\bar{G} = 300 \text{ kg/m}^2\text{s}$  with  $\Delta G/\bar{G} = 20\%$ .

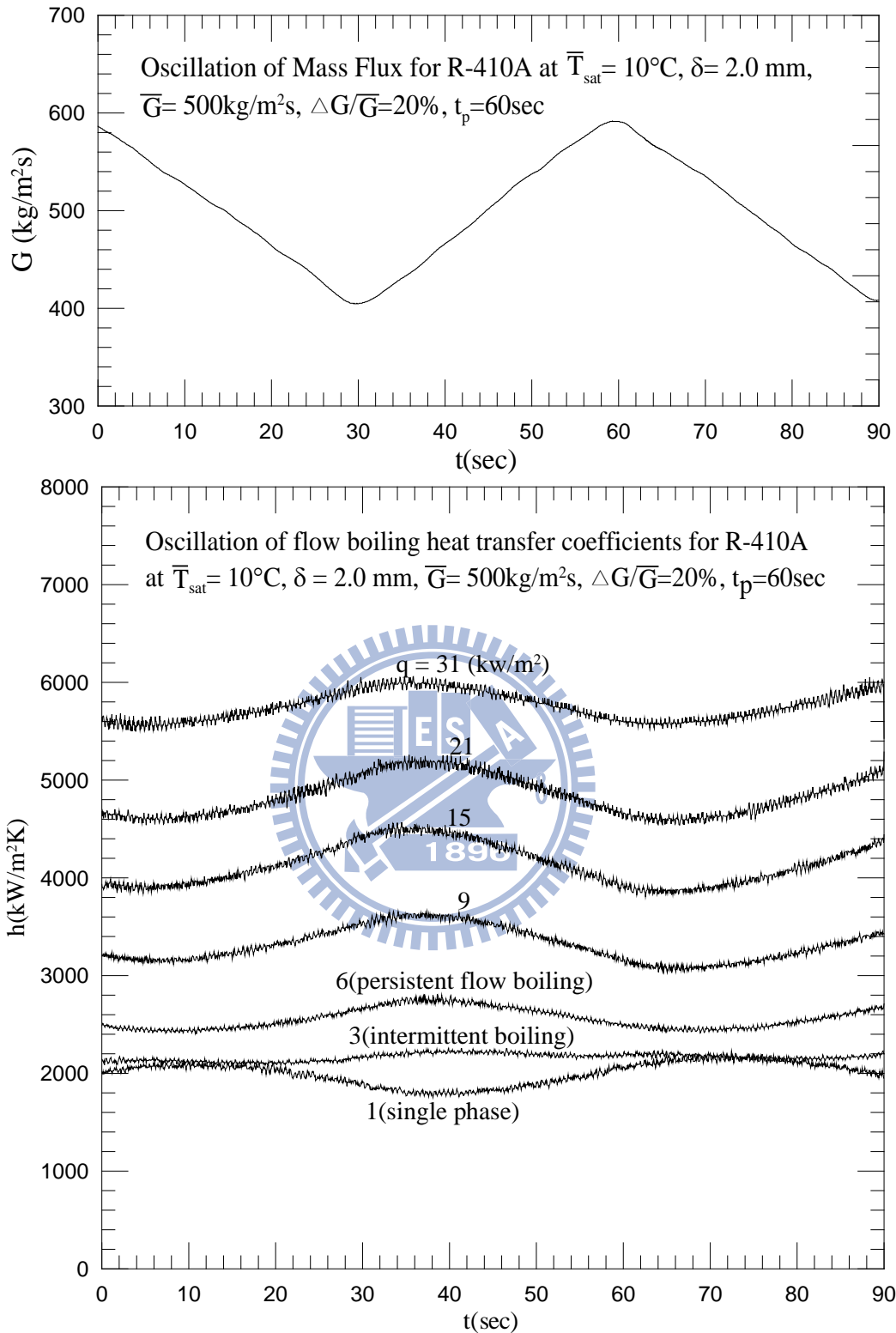


Fig. 4.24 Time variations of flow boiling heat transfer coefficients in time periodic saturated flow boiling of R-410A for various imposed heat fluxes at  $\bar{T}_{\text{sat}} = 10^\circ\text{C}$ ,  $\delta = 2.0 \text{ mm}$ ,  $t_p = 60 \text{ sec}$  and  $\bar{G} = 500 \text{ kg/m}^2\text{s}$  with  $\Delta G/\bar{G} = 20\%$ .

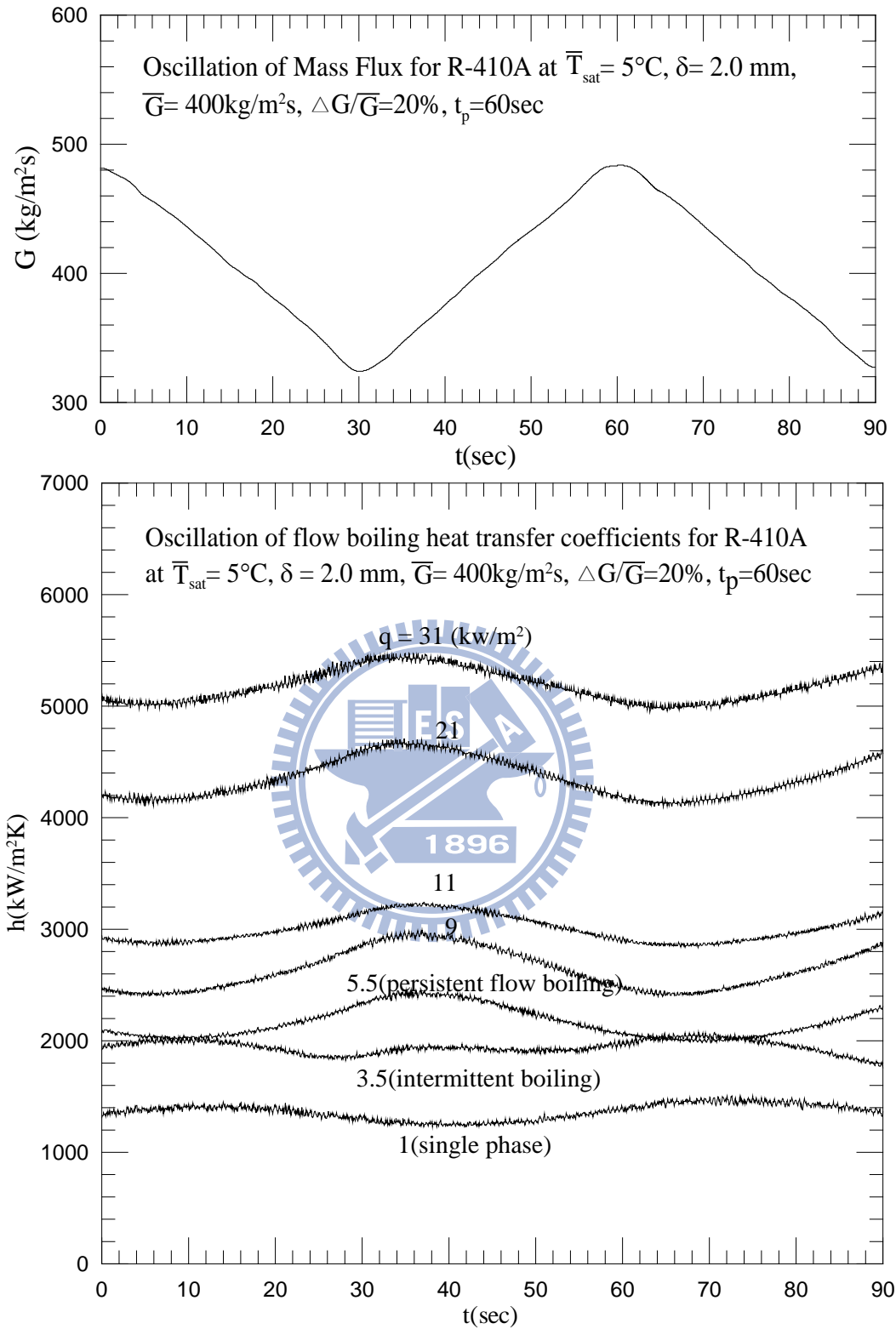


Fig. 4.25 Time variations of flow boiling heat transfer coefficients in time periodic saturated flow boiling of R-410A for various imposed heat fluxes at  $\bar{T}_{\text{sat}} = 5^\circ\text{C}$ ,  $\delta = 2.0 \text{ mm}$ ,  $t_p = 60 \text{ sec}$  and  $\bar{G} = 400 \text{ kg/m}^2\text{s}$  with  $\Delta G/\bar{G} = 20\%$ .



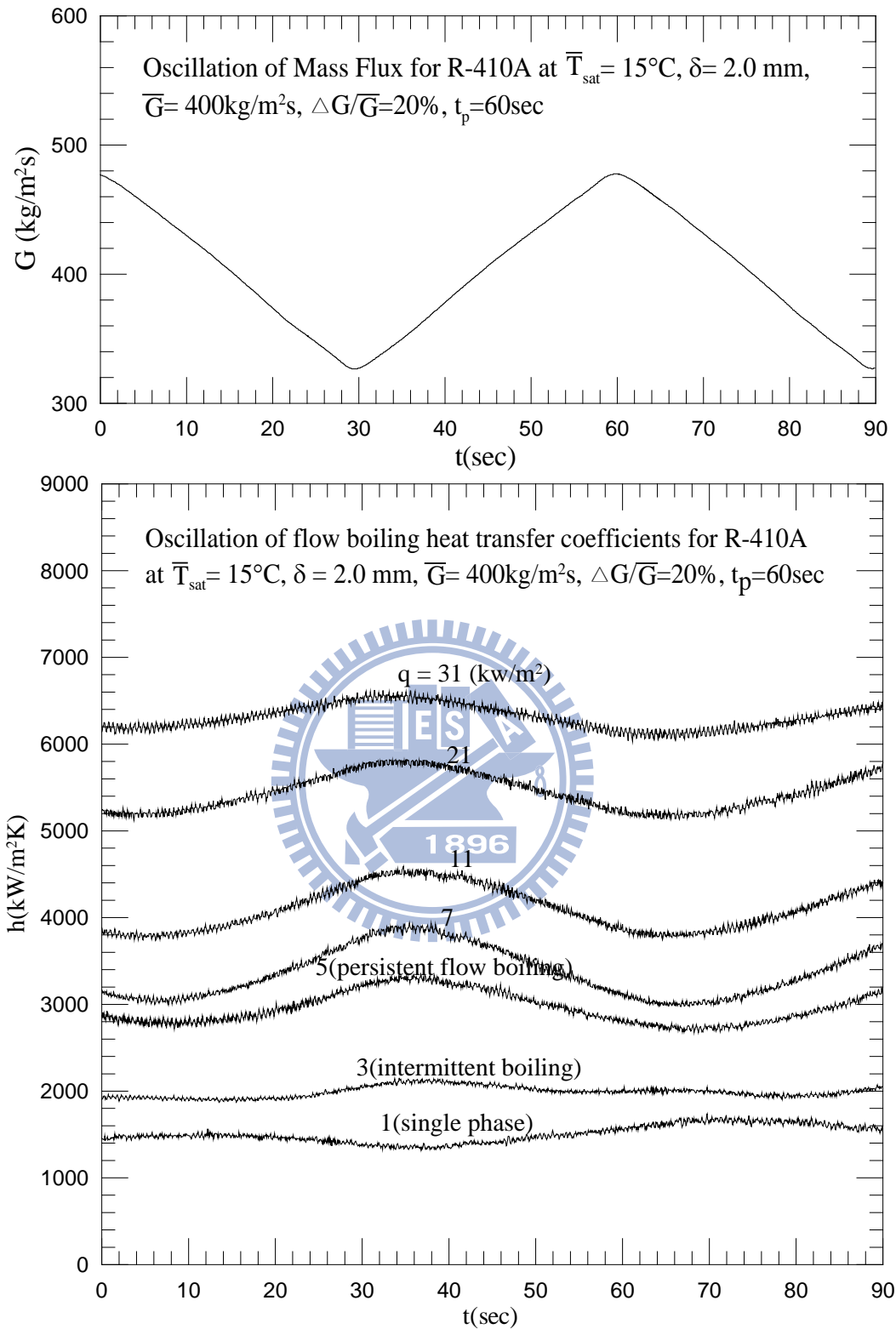


Fig. 4.26 Time variations of flow boiling heat transfer coefficients in time periodic saturated flow boiling of R-410A for various imposed heat fluxes at  $\bar{T}_{\text{sat}} = 15^\circ\text{C}$ ,  $\delta = 2.0 \text{ mm}$ ,  $t_p = 60 \text{ sec}$  and  $\bar{G} = 400 \text{ kg/m}^2\text{s}$  with  $\Delta G/\bar{G} = 20\%$ .

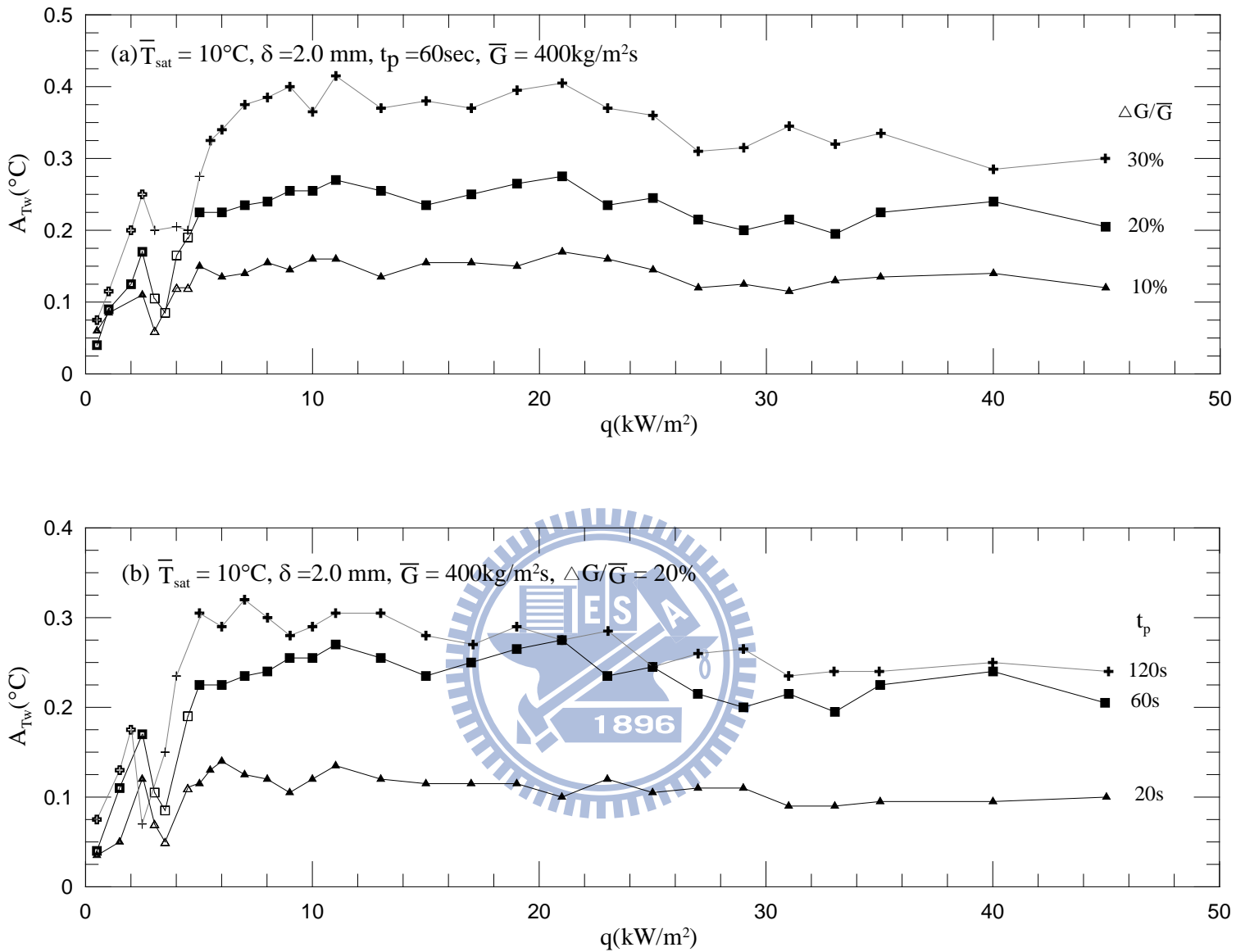


Fig. 4.27 Effects of imposed heat flux on amplitudes of wall temperature oscillation in time periodic saturated flow boiling of R-410A for various amplitudes of mass flux oscillation (a), periods of mass flux oscillation (b), mean mass fluxes (c), and refrigerant saturated temperatures (d). ( $\oplus, \square, \triangle$  Single Phase;  $+, \blacksquare, \blacktriangle$  Intermittent Boiling;  $+, \blacksquare, \blacktriangle$  Persistent Flow Boiling).

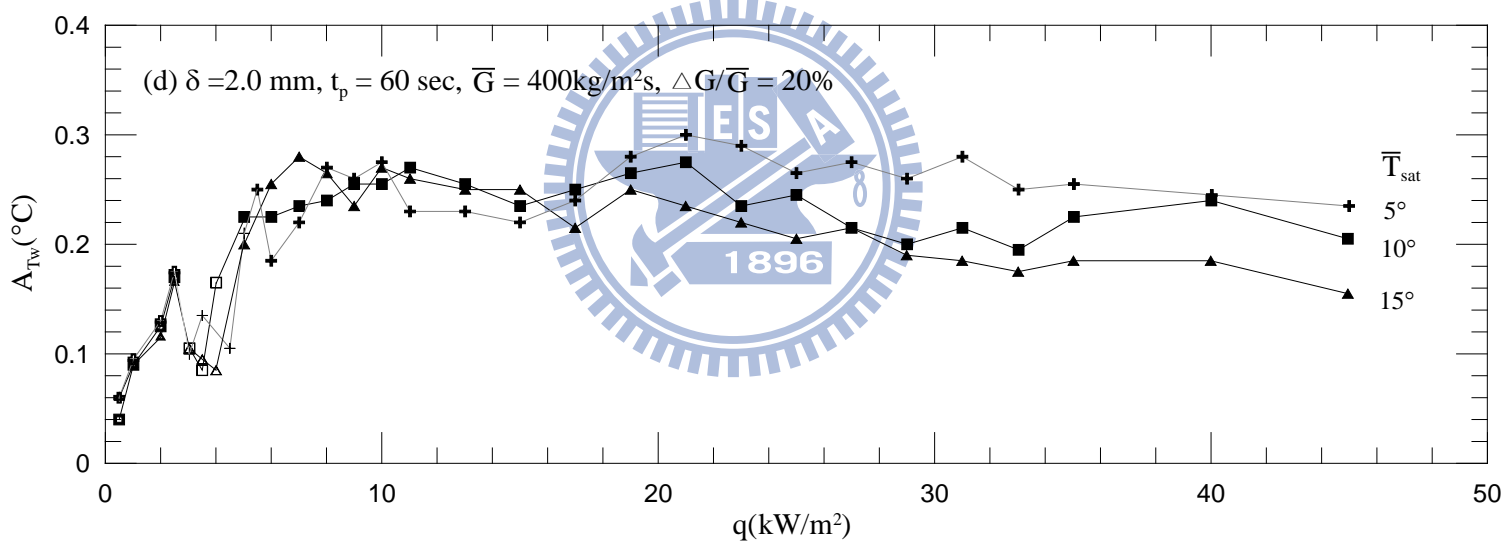
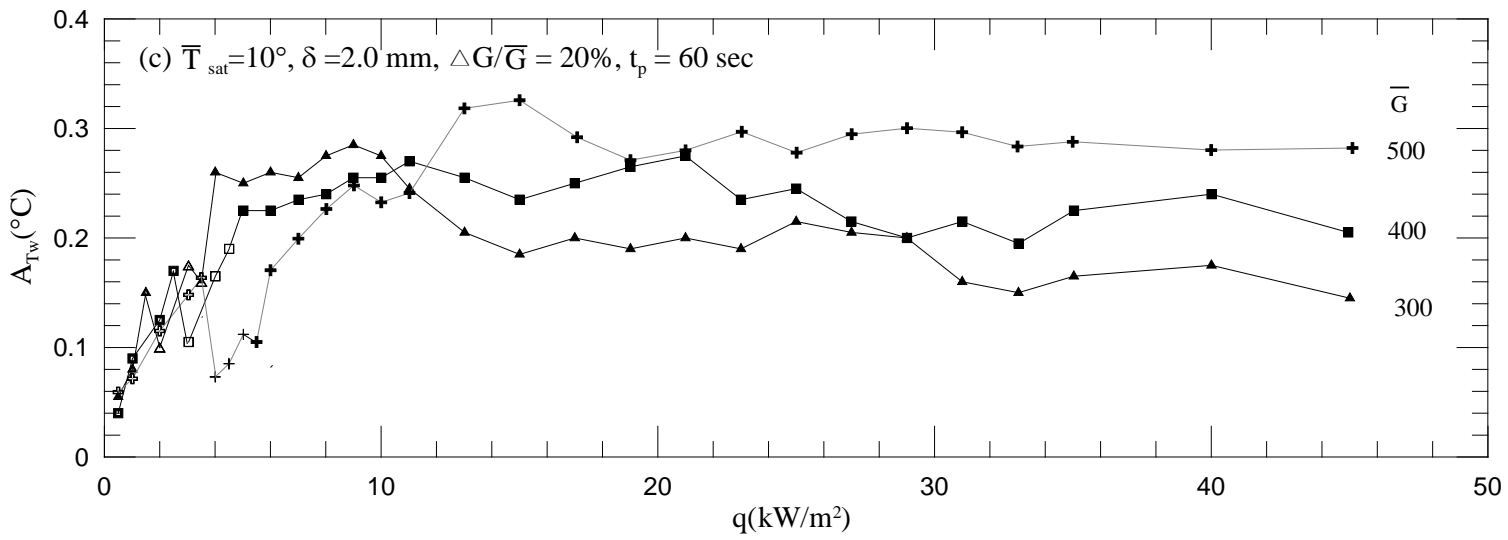


Fig. 4.27 continues

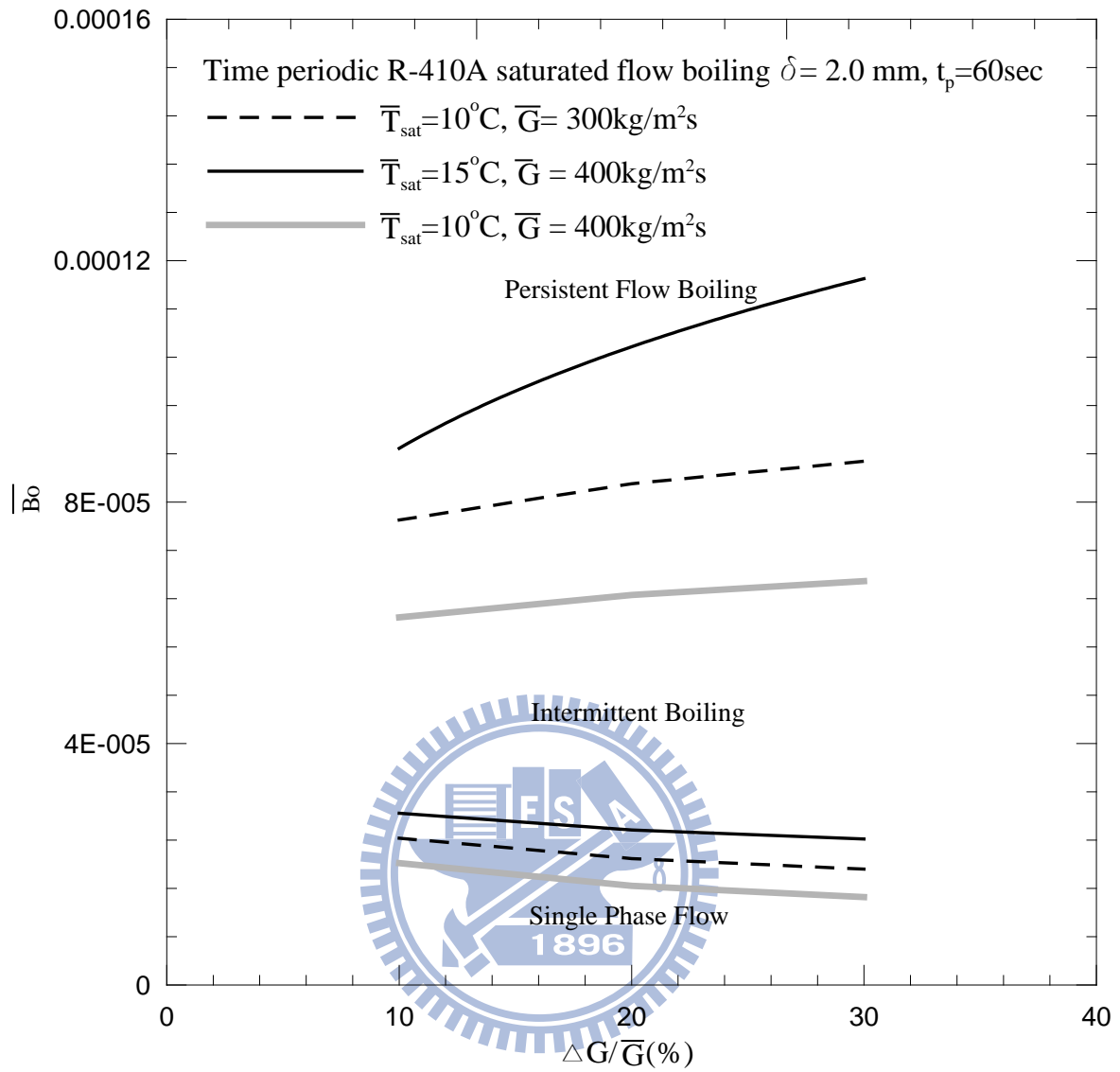


Fig. 4.28 Flow regime map for time periodic R-410A flow boiling at  $\delta = 2.0$  mm and  $t_p = 60$  sec for various mean saturated temperatures and mean mass fluxes.

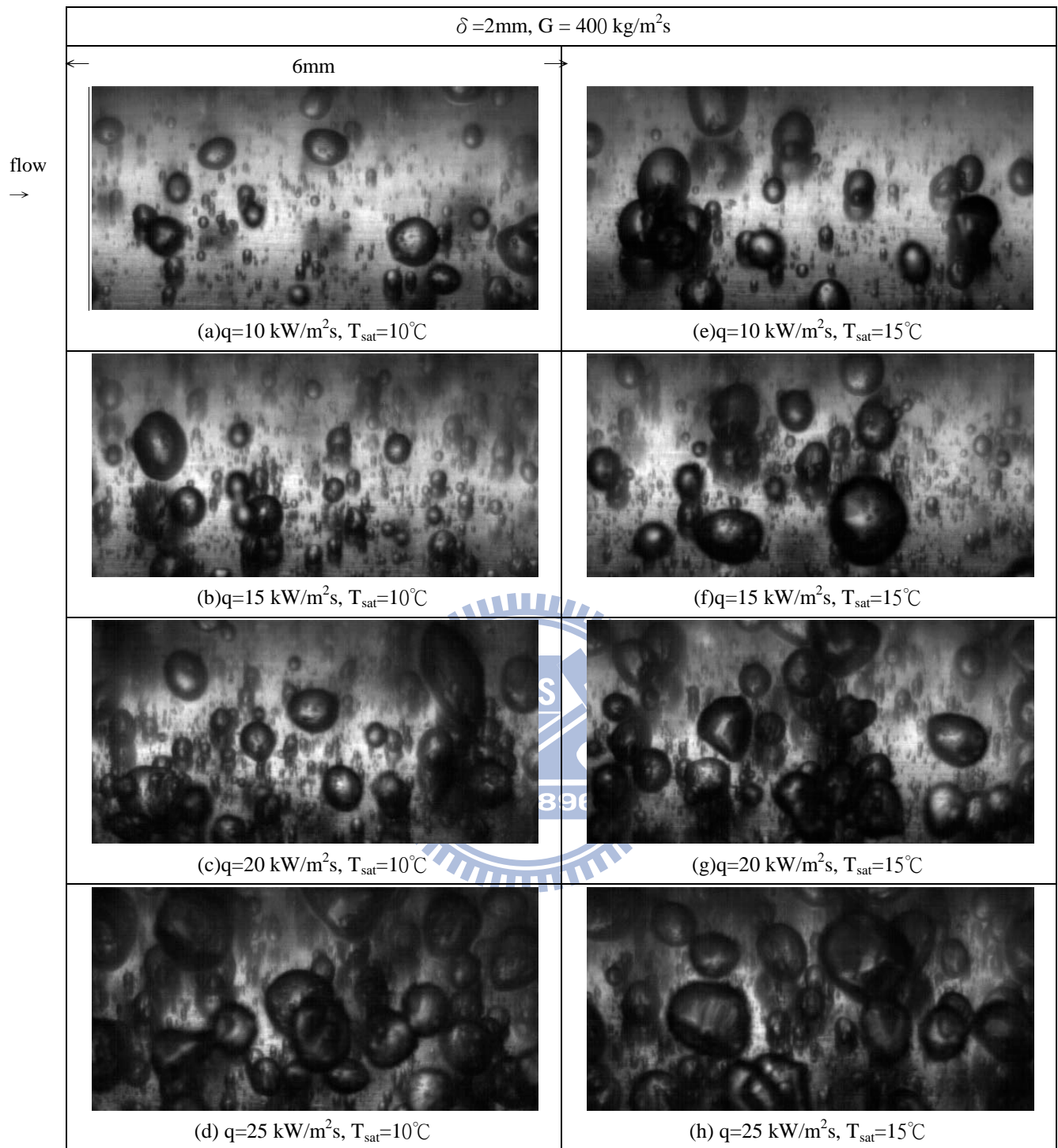


Fig. 4.29 Photos of boiling flow in stable saturated flow boiling of R-410A for various imposed heat fluxes at  $\delta = 2.0\text{mm}$ ,  $G = 400 \text{ kg/m}^2\text{s}$  and  $T_{\text{sat}} = 10^\circ\text{C}$  &  $15^\circ\text{C}$ .

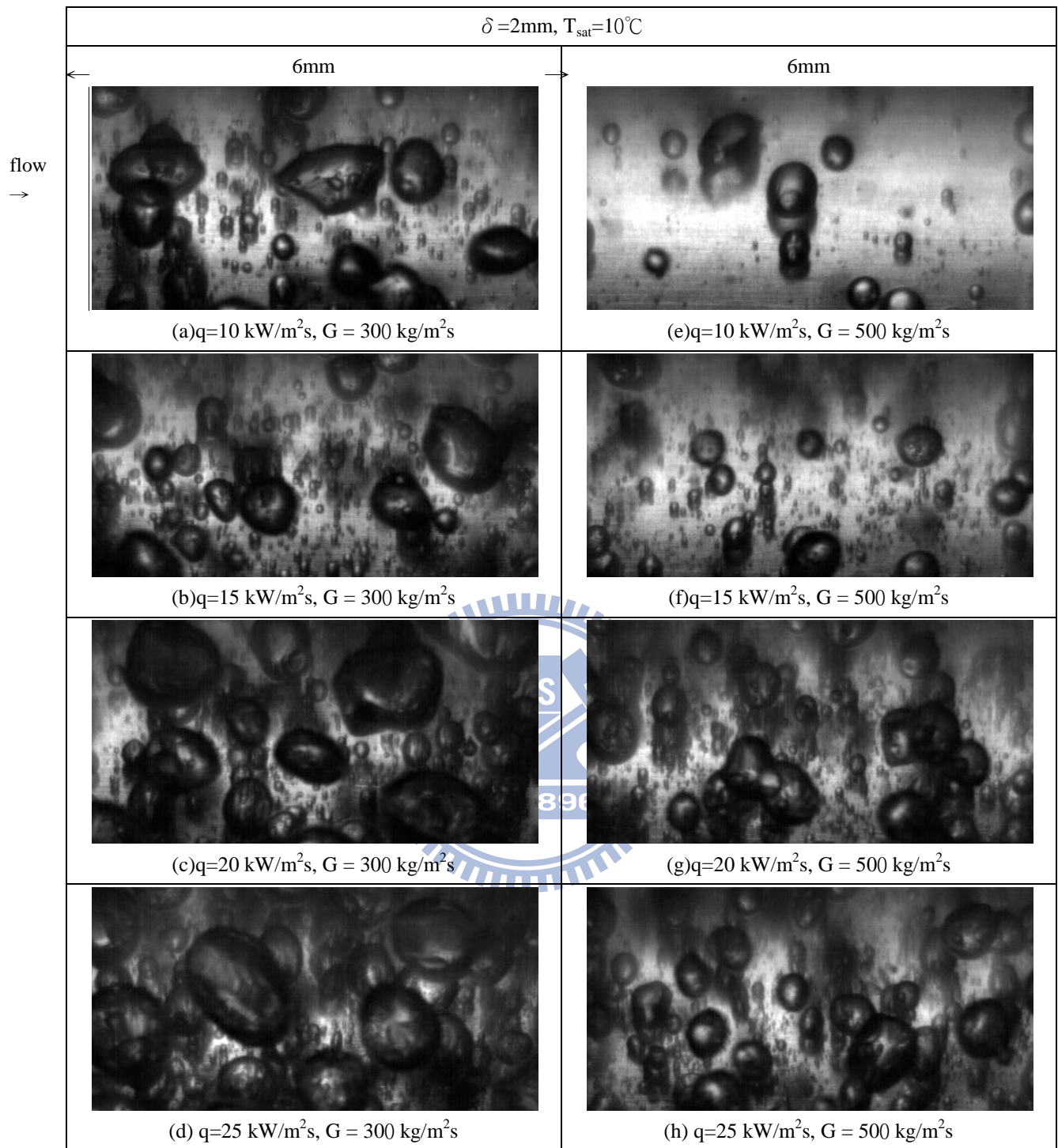


Fig. 4.30 Photos of boiling flow in stable saturated flow boiling of R-410A for various imposed heat fluxes at  $\delta = 2.0\text{mm}$ ,  $T_{\text{sat}} = 10^\circ\text{C}$ ,  $G = 300\text{kg/m}^2\text{s}$  and  $500 \text{ kg/m}^2\text{s}$ .



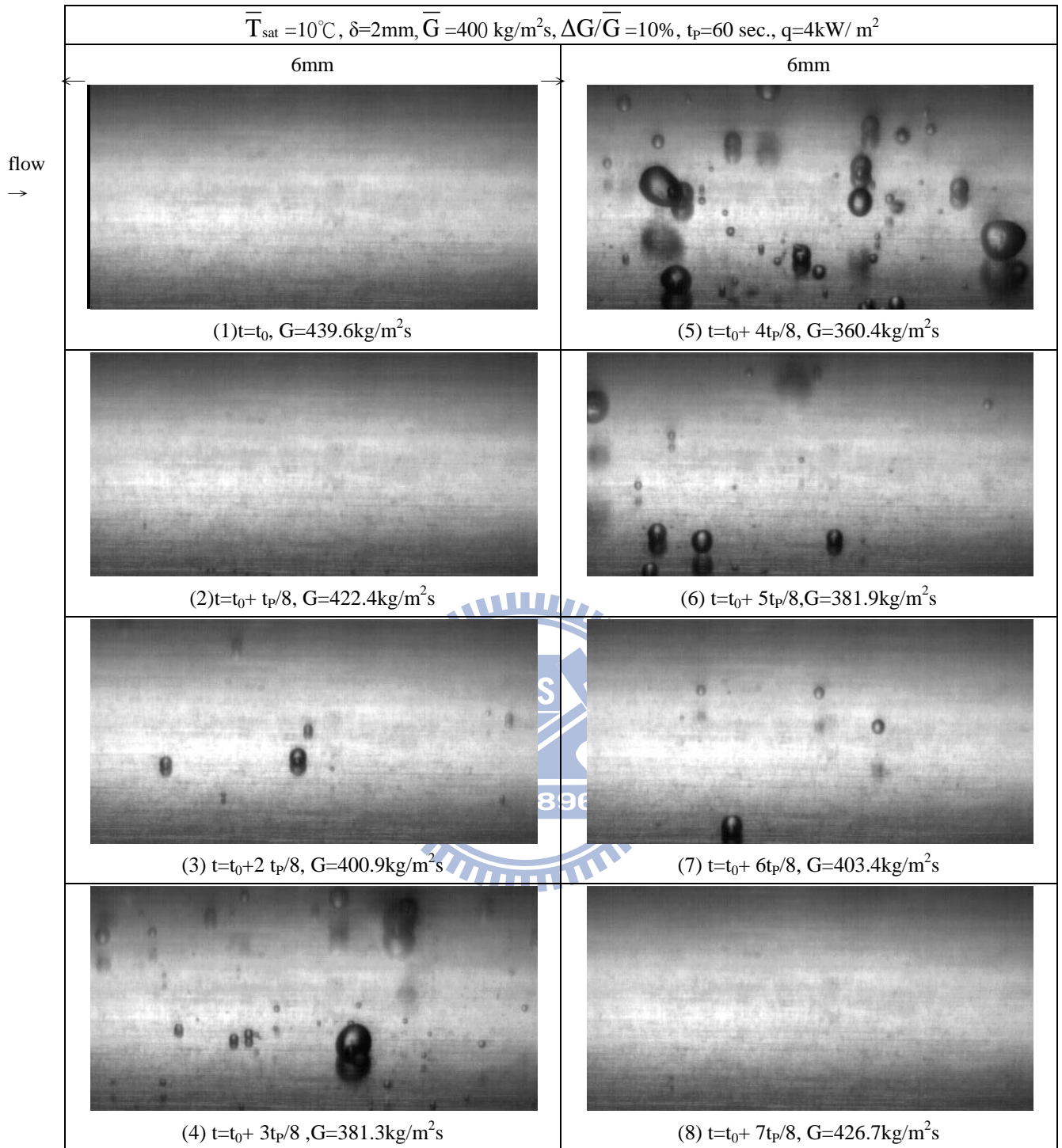


Fig. 4.31 Photos of intermittent saturated flow boiling of R-410A at selected time instants in a typical periodic cycle for  $q = 4 \text{ kW/m}^2$  at  $\bar{G} = 400 \text{ kg/m}^2\text{s}$ ,  $\Delta G/\bar{G} = 10\%$ ,  $\bar{T}_{\text{sat}} = 10^\circ\text{C}$ ,  $\delta = 2.0\text{mm}$  and  $t_p = 60\text{sec.}$

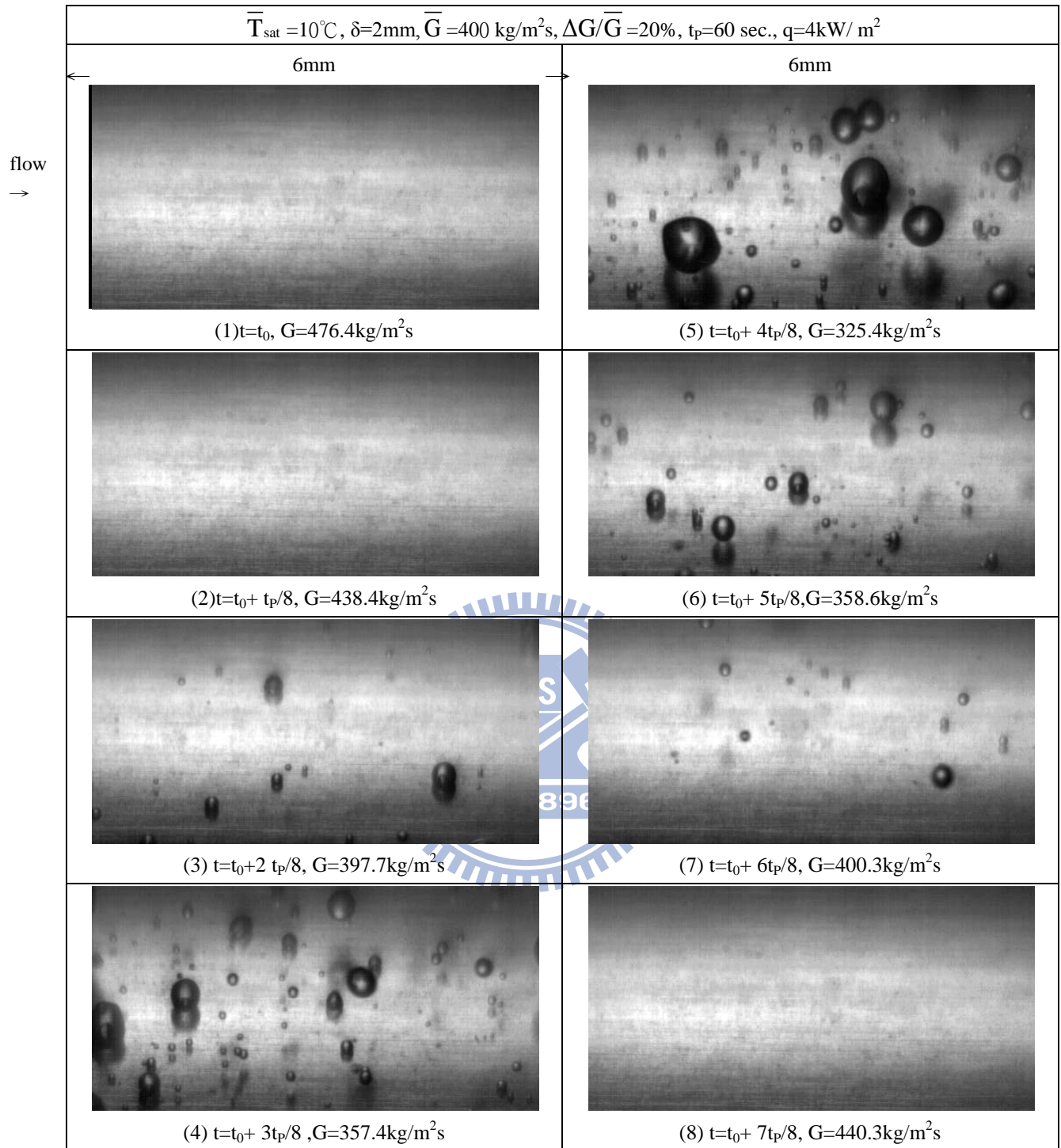


Fig. 4.32 Photos of intermittent saturated flow boiling of R-410A at selected time instants in a typical periodic cycle for  $q = 4 \text{ kW/m}^2$  at  $\bar{G} = 400 \text{ kg/m}^2\text{s}$ ,  $\Delta\bar{G}/\bar{G} = 20\%$ ,  $\bar{T}_{\text{sat}} = 10^\circ\text{C}$ ,  $\delta = 2.0\text{mm}$  and  $t_p = 60\text{sec}$ .



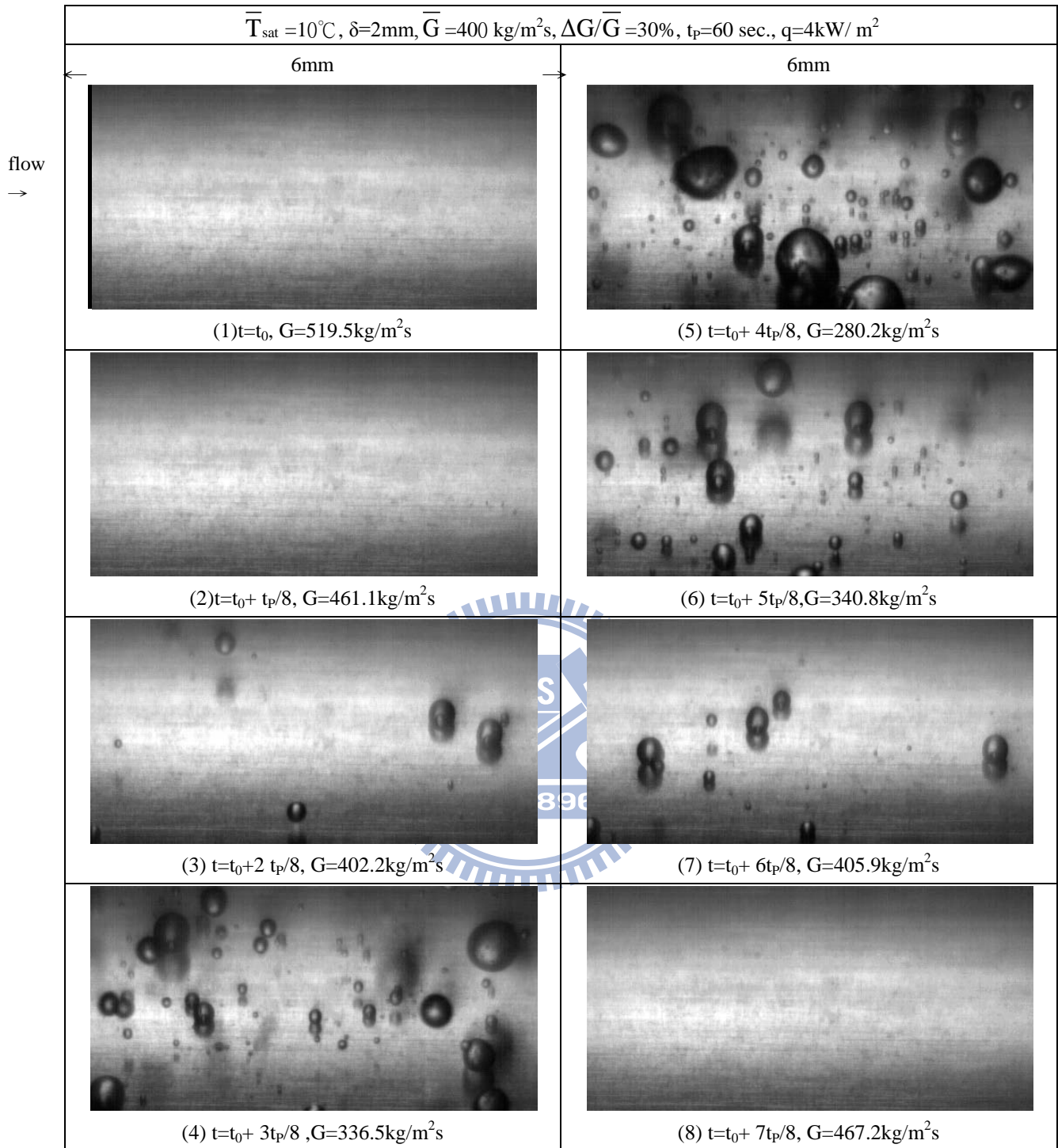


Fig. 4.33 Photos of intermittent saturated flow boiling of R-410A at selected time instants in a typical periodic cycle for  $q = 4 \text{ kW/m}^2$  at  $\bar{G} = 400 \text{ kg/m}^2\text{s}$ ,  $\Delta G/\bar{G} = 30\%$ ,  $\bar{T}_{\text{sat}} = 10^\circ\text{C}$ ,  $\delta = 2.0\text{mm}$  and  $t_p = 60\text{sec}$ .

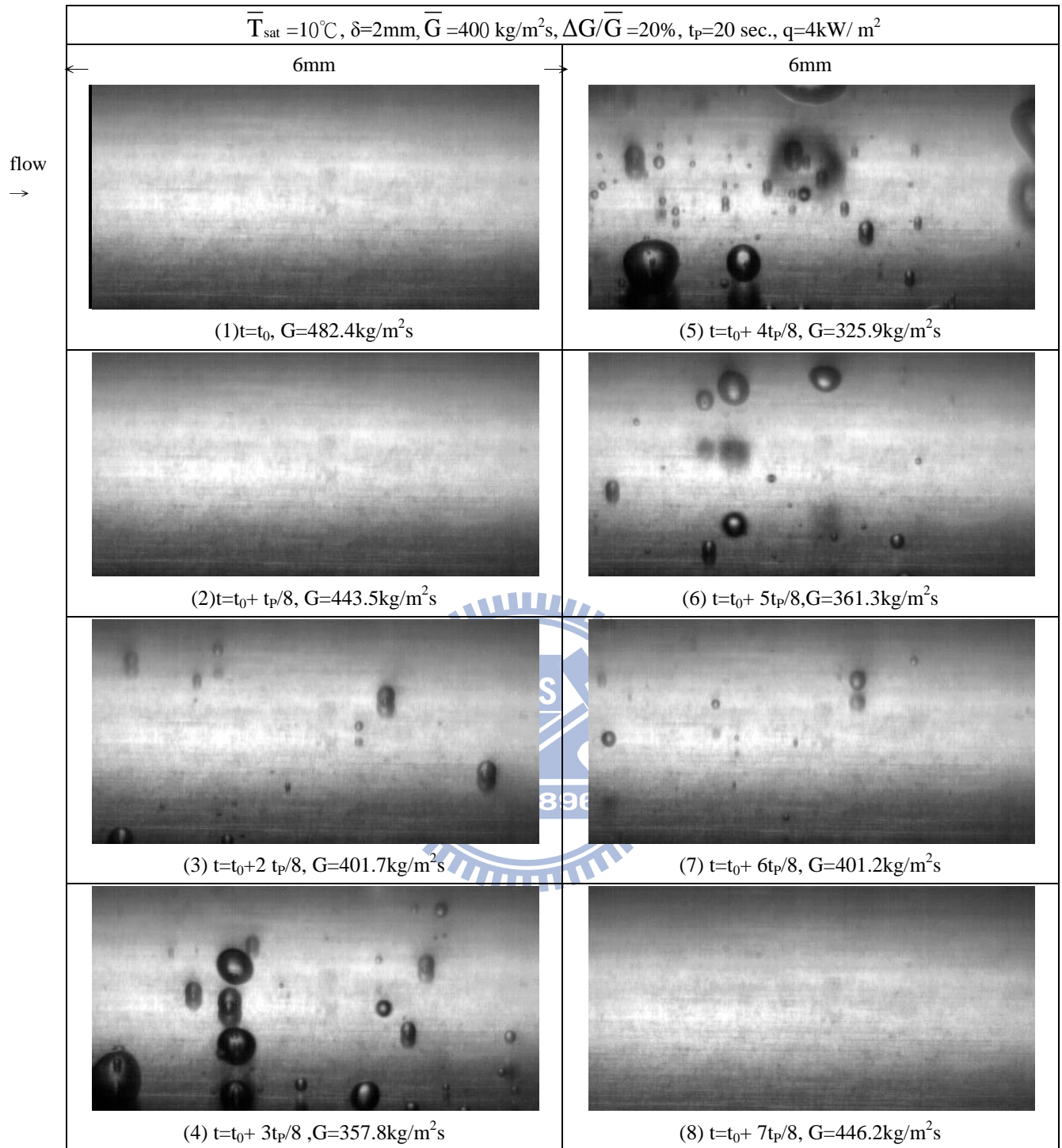


Fig. 4.34 Photos of intermittent saturated flow boiling of R-410A at selected time instants in a typical periodic cycle for  $q = 4 \text{ kW/m}^2$  at  $\bar{G} = 400 \text{ kg/m}^2\text{s}$ ,  $\Delta G/\bar{G} = 20\%$ ,  $\bar{T}_{\text{sat}} = 10^\circ\text{C}$ ,  $\delta = 2.0\text{mm}$  and  $t_p = 20\text{sec}$ .

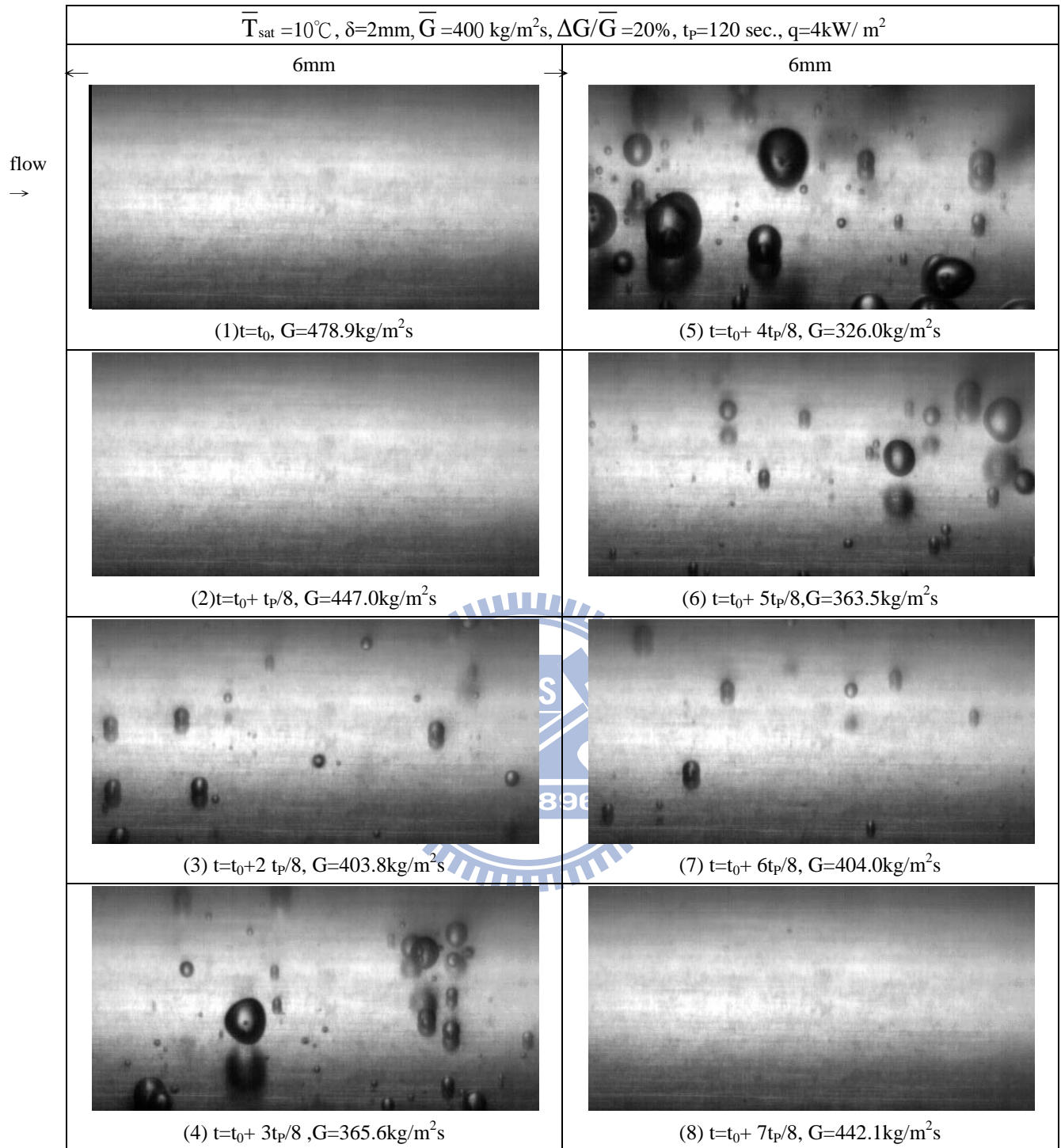


Fig. 4.35 Photos of intermittent saturated flow boiling of R-410A at selected time instants in a typical periodic cycle for  $q = 4 \text{ kW/m}^2$  at  $\bar{G} = 400 \text{ kg/m}^2\text{s}$ ,  $\Delta G/\bar{G} = 20\%$ ,  $\bar{T}_{\text{sat}} = 10^\circ\text{C}$ ,  $\delta = 2.0\text{mm}$  and  $t_p = 120\text{sec.}$



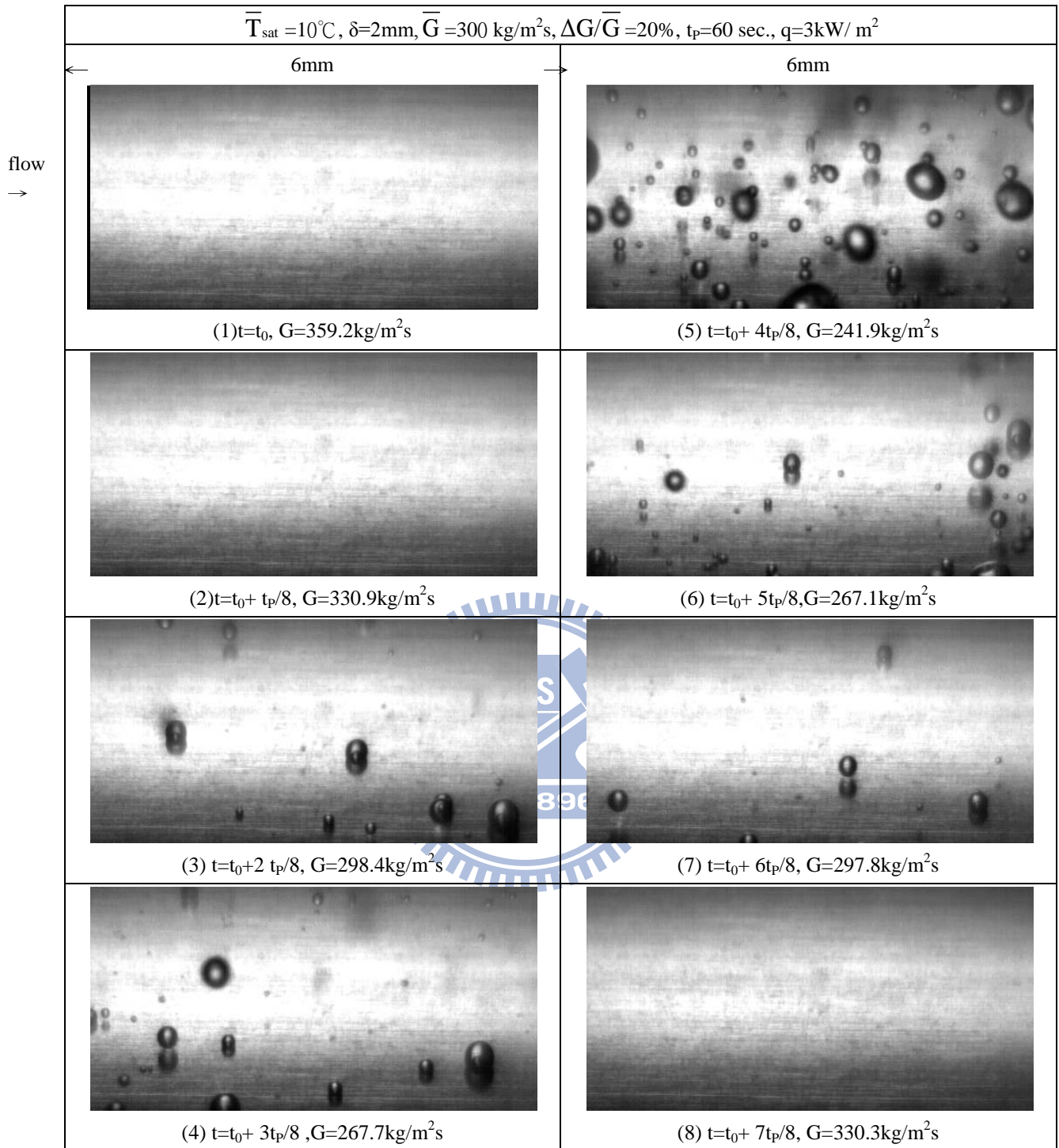


Fig. 4.36 Photos of intermittent saturated flow boiling of R-410A at selected time instants in a typical periodic cycle for  $q = 3 \text{ kW/m}^2$  at  $\bar{G} = 300 \text{ kg/m}^2\text{s}$ ,  $\Delta G/\bar{G} = 20\%$ ,  $\bar{T}_{\text{sat}} = 10^\circ\text{C}$ ,  $\delta = 2.0\text{mm}$  and  $t_p = 60\text{sec}$ .

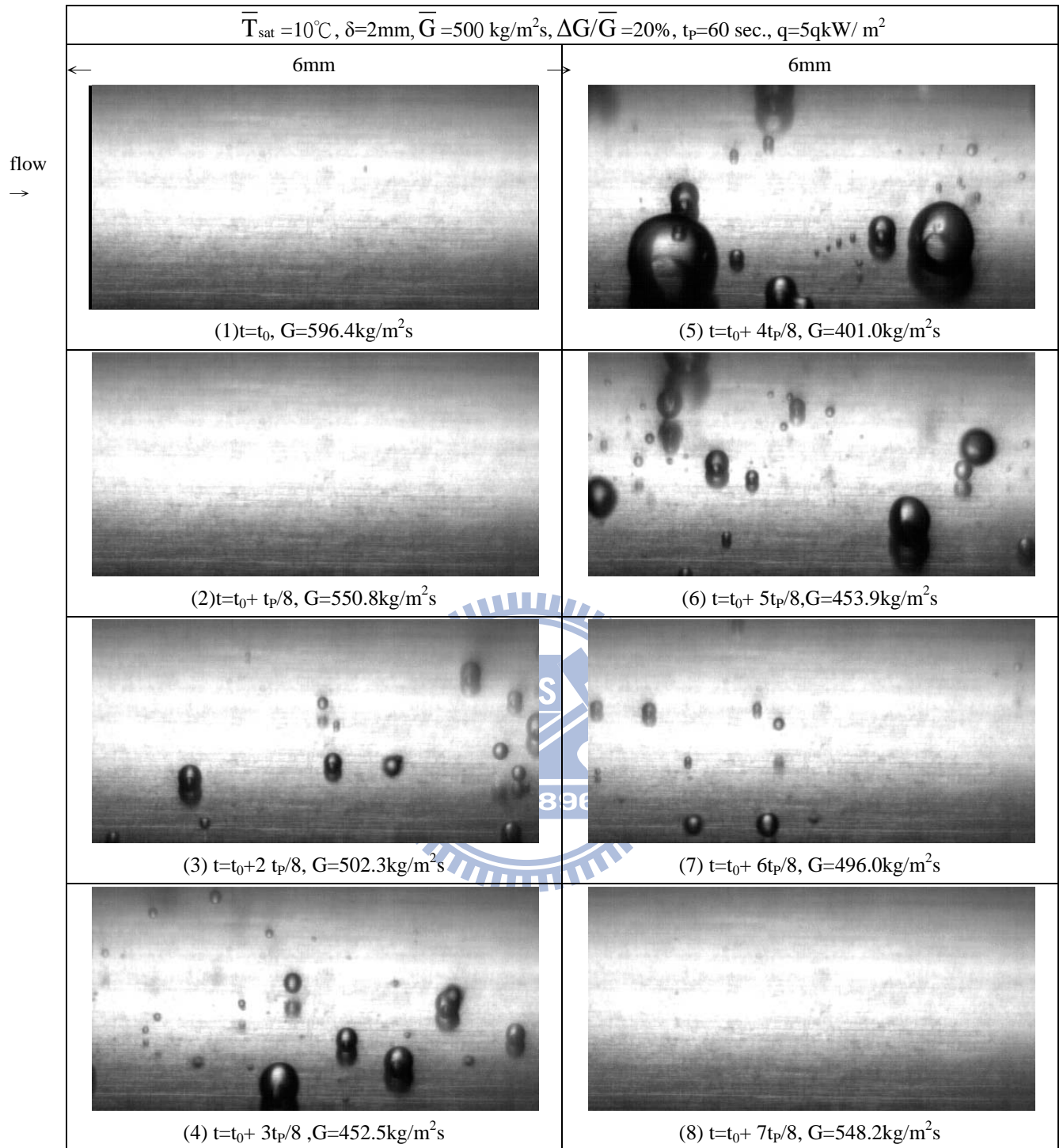


Fig. 4.37 Photos of intermittent saturated flow boiling of R-410A at selected time instants in a typical periodic cycle for  $q = 5 \text{ kW/m}^2$  at  $\bar{G} = 500 \text{ kg/m}^2\text{s}$ ,  $\Delta G/\bar{G} = 20\%$ ,  $\bar{T}_{\text{sat}} = 10^\circ\text{C}$ ,  $\delta = 2.0\text{mm}$  and  $t_p = 60\text{sec.}$

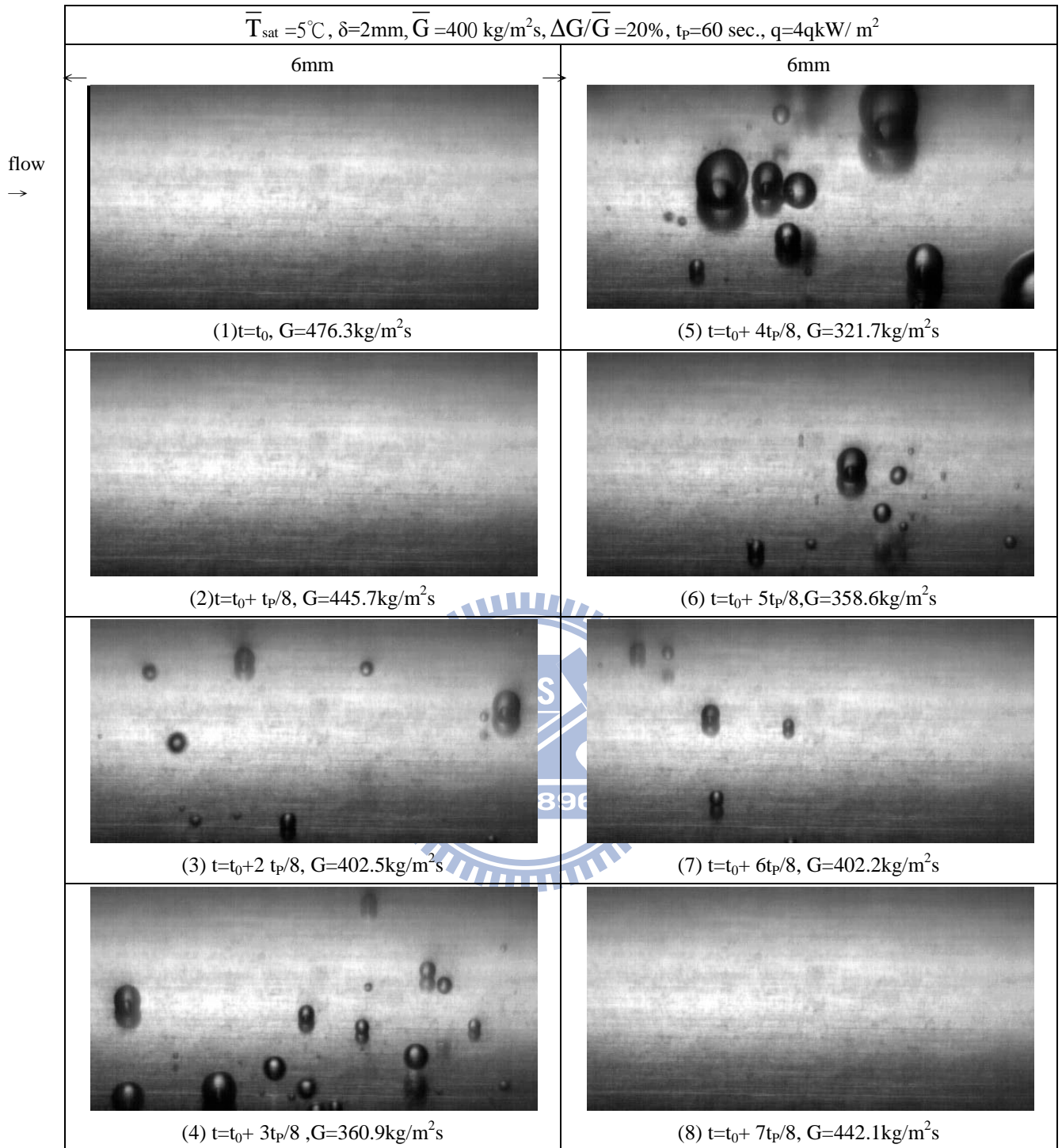


Fig. 4.38 Photos of intermittent saturated flow boiling of R-410A at selected time instants in a typical periodic cycle for  $q = 4 \text{ kW/m}^2$  at  $\bar{G} = 400 \text{ kg/m}^2\text{s}$ ,  $\Delta G/\bar{G} = 20\%$ ,  $\bar{T}_{\text{sat}} = 5^\circ\text{C}$ ,  $\delta = 2.0\text{mm}$  and  $t_p = 60\text{sec.}$



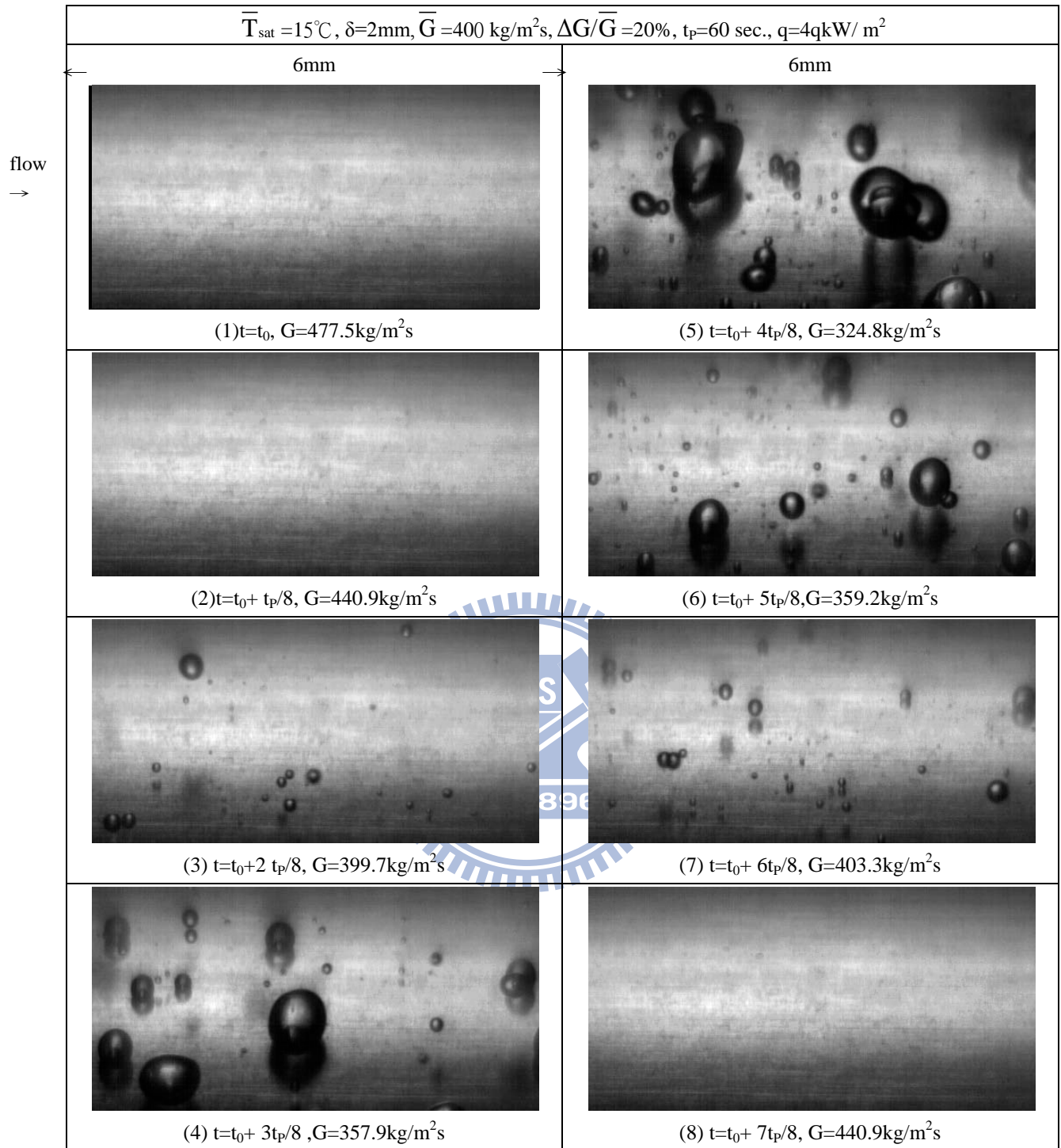


Fig. 4.39 Photos of intermittent saturated flow boiling of R-410A at selected time instants in a typical periodic cycle for  $q = 4 \text{ kW/m}^2$  at  $\bar{G} = 400 \text{ kg/m}^2\text{s}$ ,  $\Delta\bar{G}/\bar{G} = 20\%$ ,  $\bar{T}_{\text{sat}} = 15^\circ\text{C}$ ,  $\delta = 2.0\text{mm}$  and  $t_p = 60\text{sec.}$

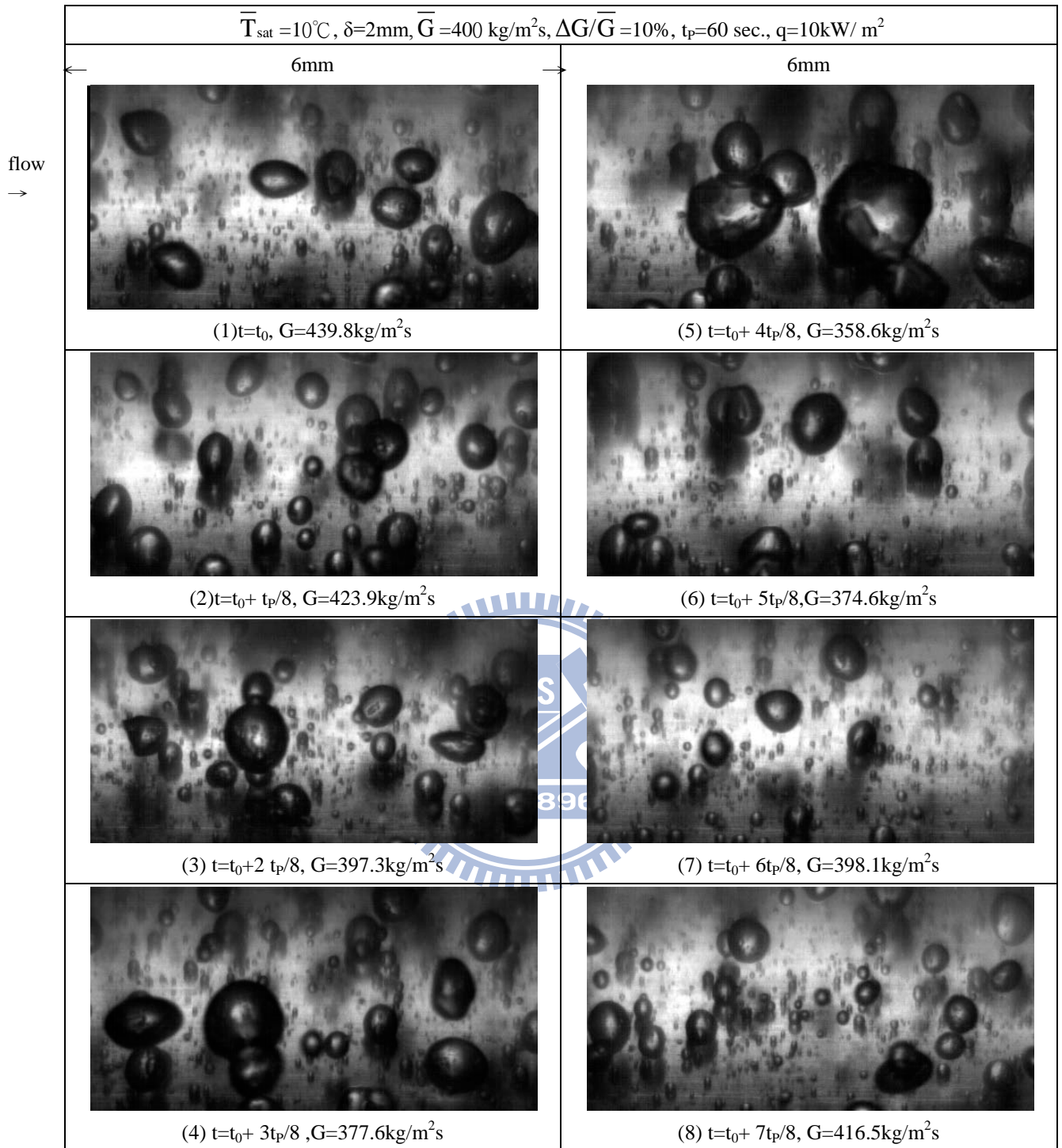


Fig. 4.40 Photos of time periodic saturated flow boiling of R-410A at selected time instants in a typical periodic cycle for  $q = 10 \text{ kW/m}^2$  at  $\bar{G} = 400 \text{ kg/m}^2\text{s}$ ,  $\Delta\bar{G}/\bar{G} = 10\%$ ,  $\bar{T}_{\text{sat}} = 10^\circ\text{C}$ ,  $\delta = 2.0\text{mm}$  and  $t_p = 60\text{sec}$ .



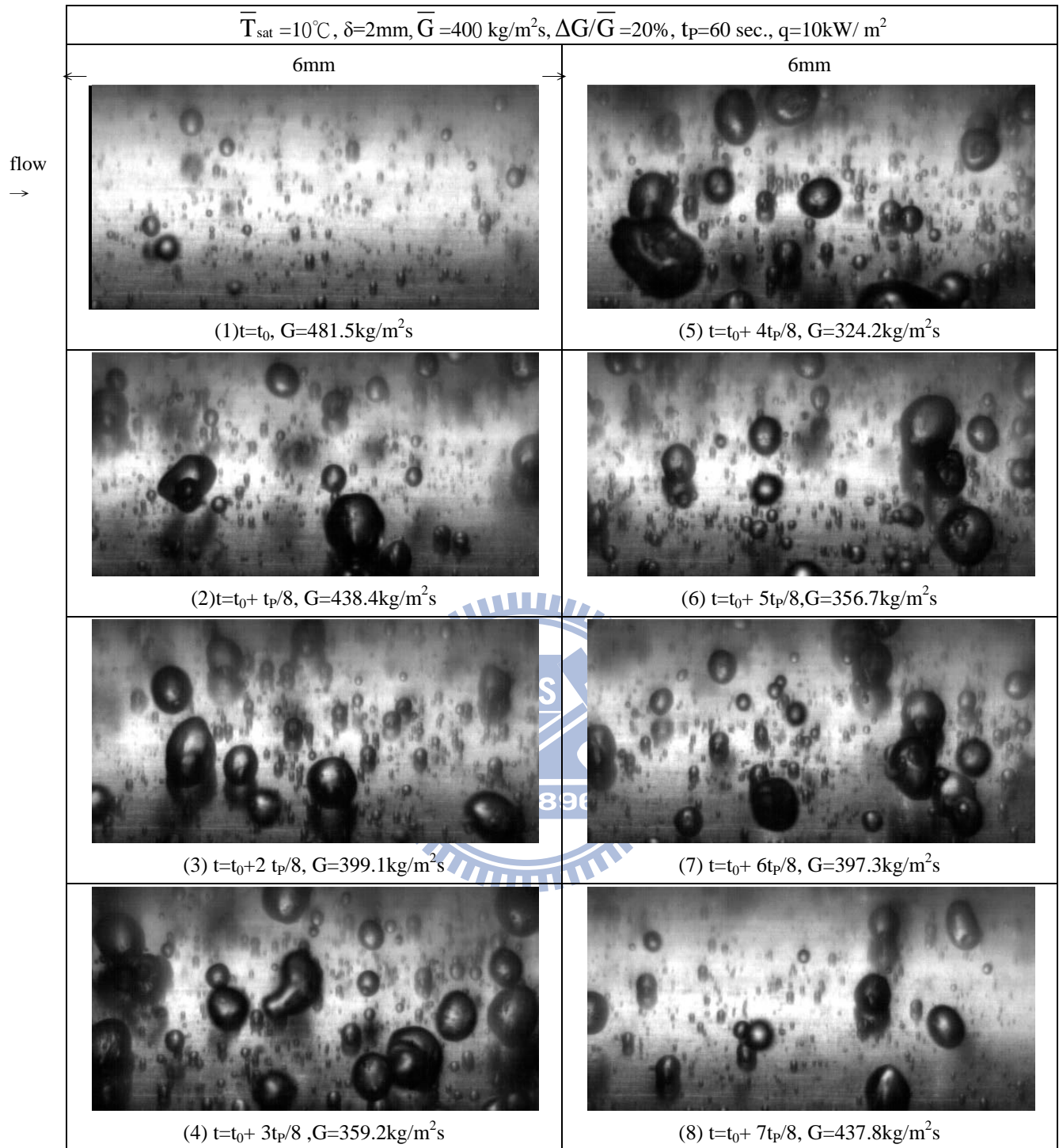


Fig. 4.41 Photos of time periodic saturated flow boiling of R-410A at selected time instants in a typical periodic cycle for  $q = 10 \text{ kW/m}^2$  at  $\bar{G} = 400 \text{ kg/m}^2\text{s}$ ,  $\Delta G/\bar{G} = 20\%$ ,  $\bar{T}_{\text{sat}} = 10^\circ\text{C}$ ,  $\delta = 2.0\text{mm}$  and  $t_p = 60\text{sec}$ .

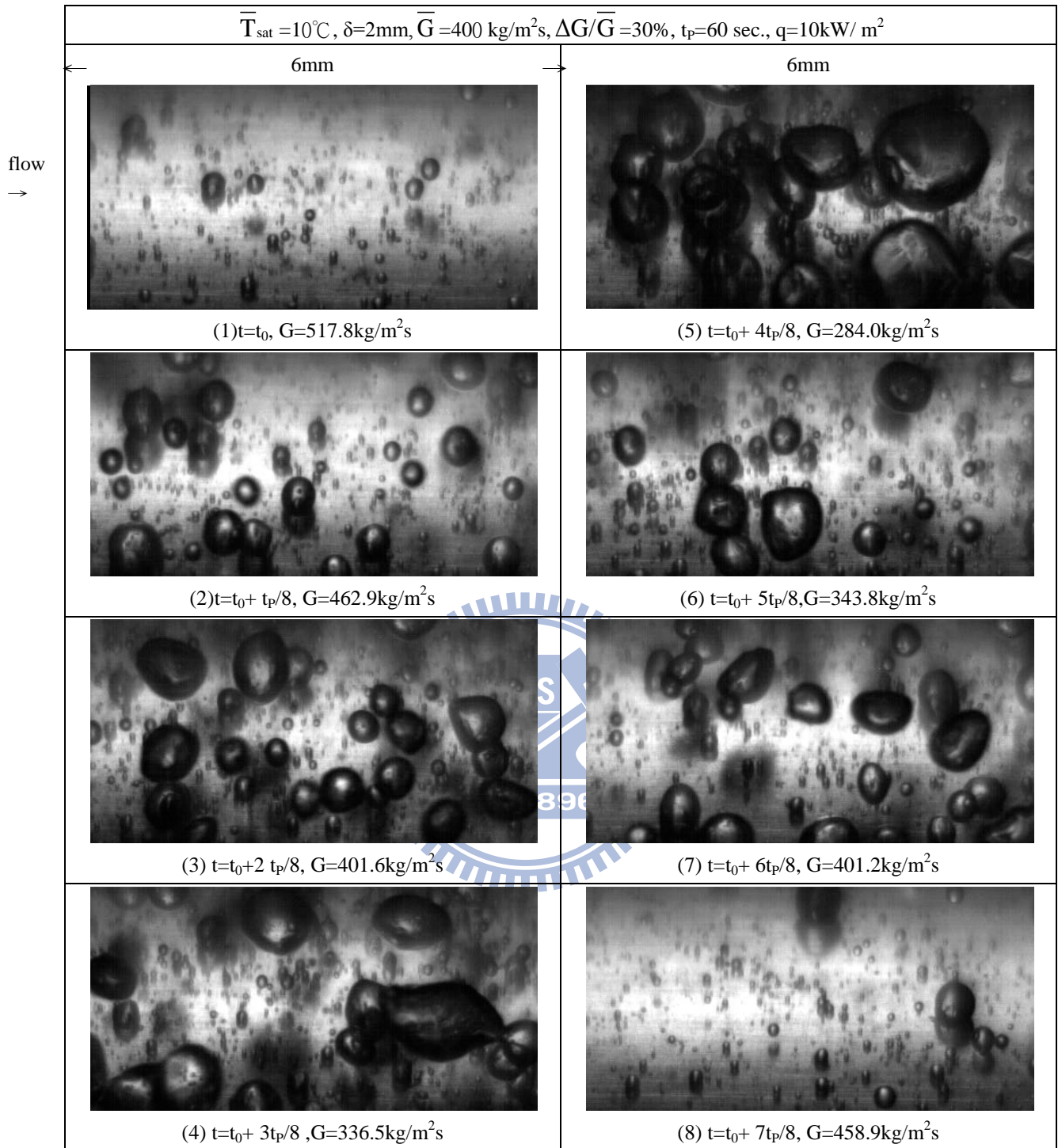


Fig. 4.42 Photos of time periodic saturated flow boiling of R-410A at selected time instants in a typical periodic cycle for  $q = 10 \text{ kW/m}^2$  at  $\bar{G} = 400 \text{ kg/m}^2\text{s}$ ,  $\Delta\bar{G}/\bar{G} = 30\%$ ,  $\bar{T}_{\text{sat}} = 10^\circ\text{C}$ ,  $\delta = 2.0\text{mm}$  and  $t_p = 60\text{sec.}$

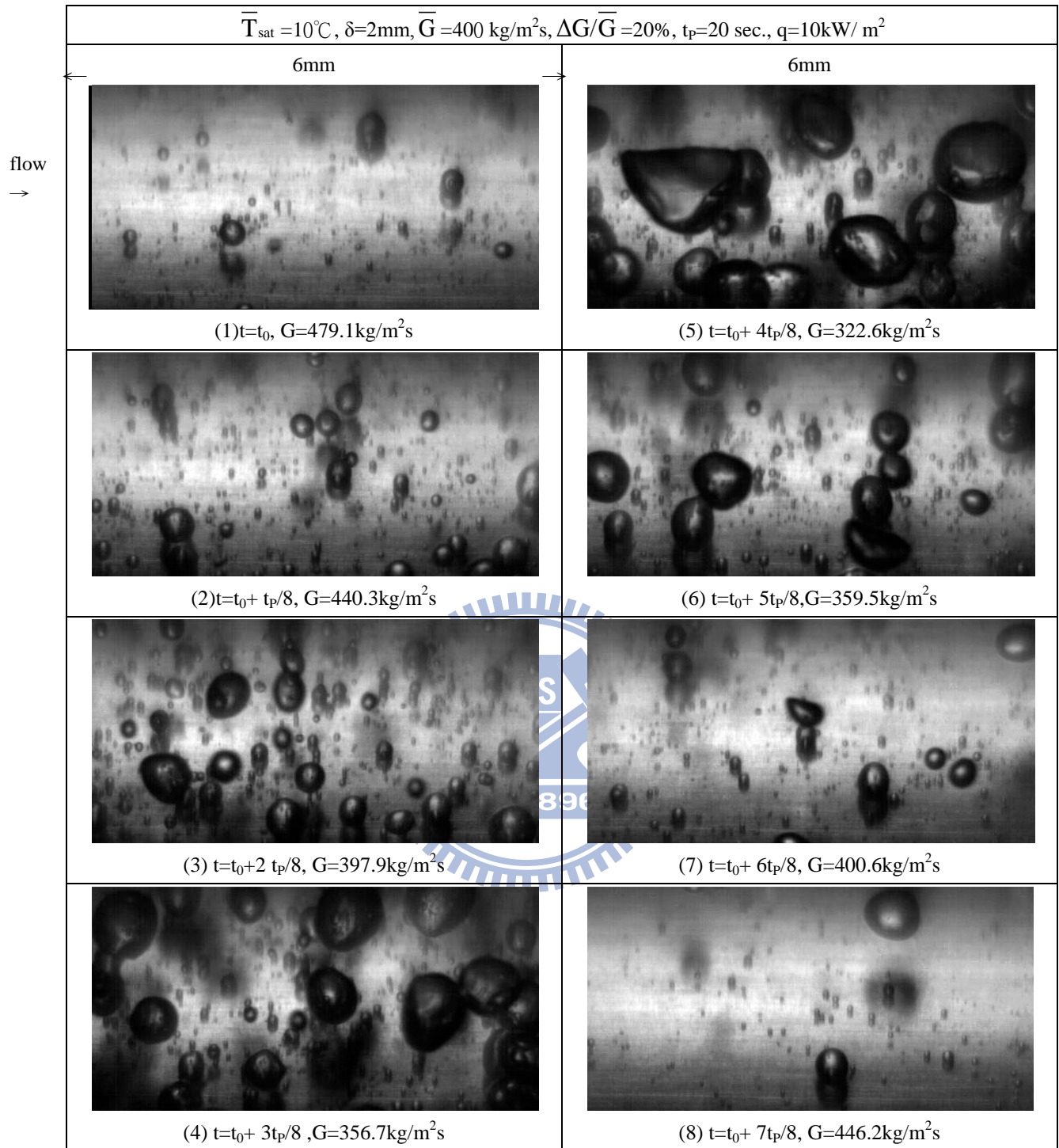


Fig. 4.43 Photos of time periodic saturated flow boiling of R-410A at selected time instants in a typical periodic cycle for  $q = 10 \text{ kW/m}^2$  at  $\bar{G} = 400 \text{ kg/m}^2\text{s}$ ,  $\Delta G/\bar{G} = 20\%$ ,  $\bar{T}_{\text{sat}} = 10^\circ\text{C}$ ,  $\delta = 2.0\text{mm}$  and  $t_p = 20\text{sec.}$



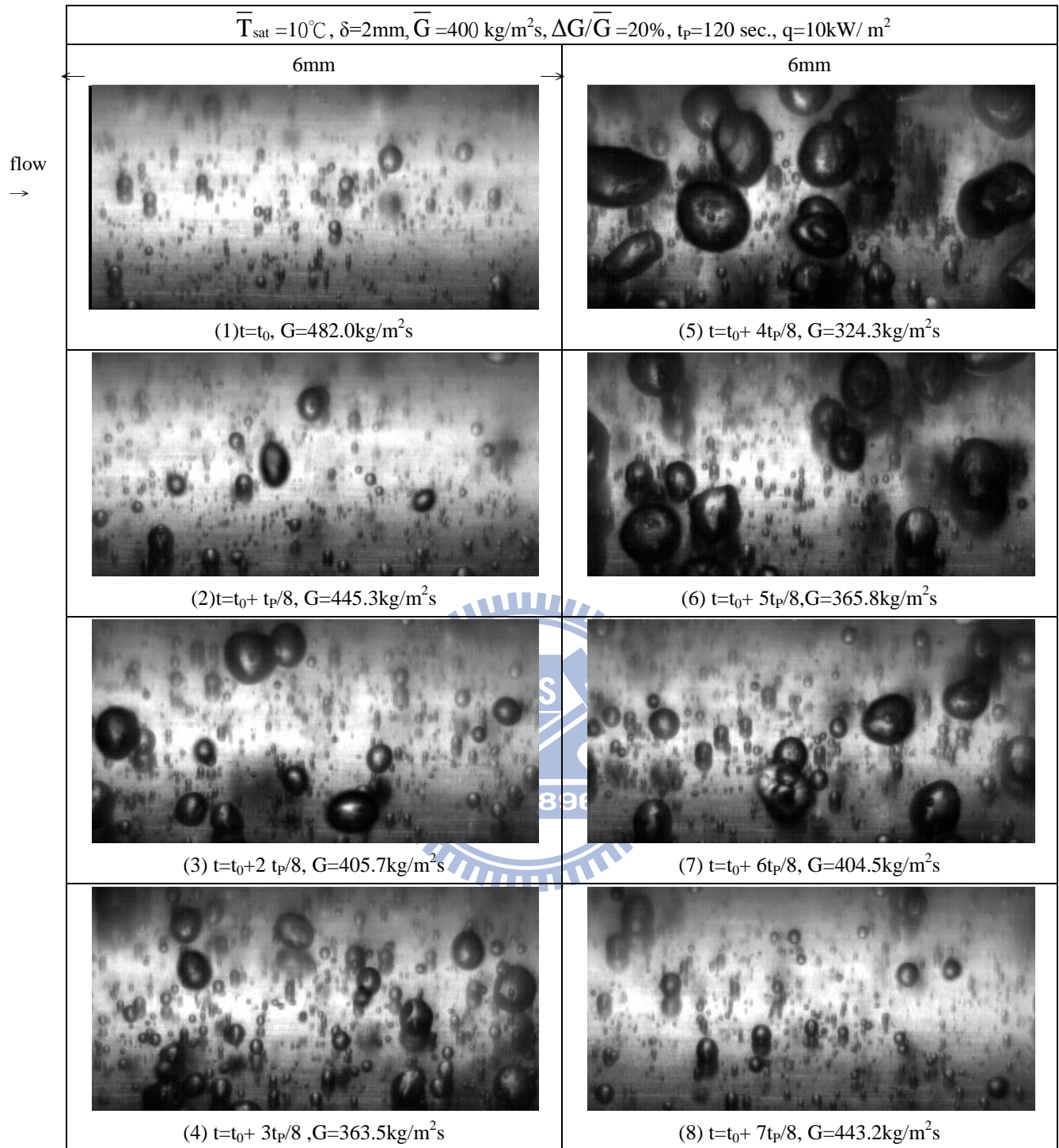


Fig. 4.44 Photos of time periodic saturated flow boiling of R-410A at selected time instants in a typical periodic cycle for  $q = 10 \text{ kW/m}^2$  at  $\bar{G} = 400 \text{ kg/m}^2\text{s}$ ,  $\Delta\bar{G}/\bar{G} = 20\%$ ,  $\bar{T}_{\text{sat}} = 10^\circ\text{C}$ ,  $\delta = 2.0\text{mm}$  and  $t_p = 120\text{sec.}$

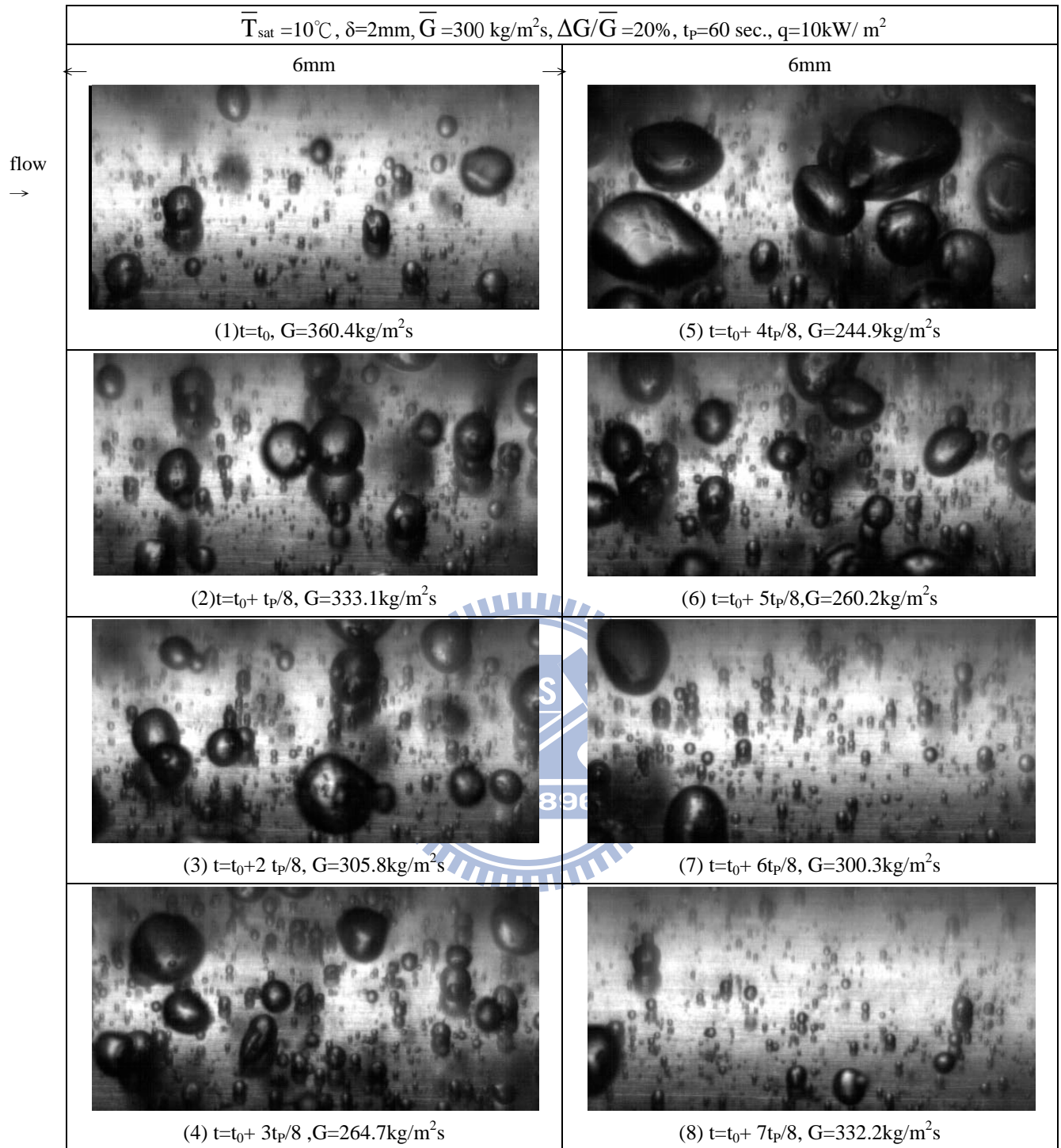


Fig. 4.45 Photos of time periodic saturated flow boiling of R-410A at selected time instants in a typical periodic cycle for  $q = 10 \text{ kW/m}^2$  at  $\bar{G} = 300 \text{ kg/m}^2\text{s}$ ,  $\Delta\bar{G}/\bar{G} = 20\%$ ,  $\bar{T}_{\text{sat}} = 10^\circ\text{C}$ ,  $\delta = 2.0\text{mm}$  and  $t_p = 60\text{sec.}$

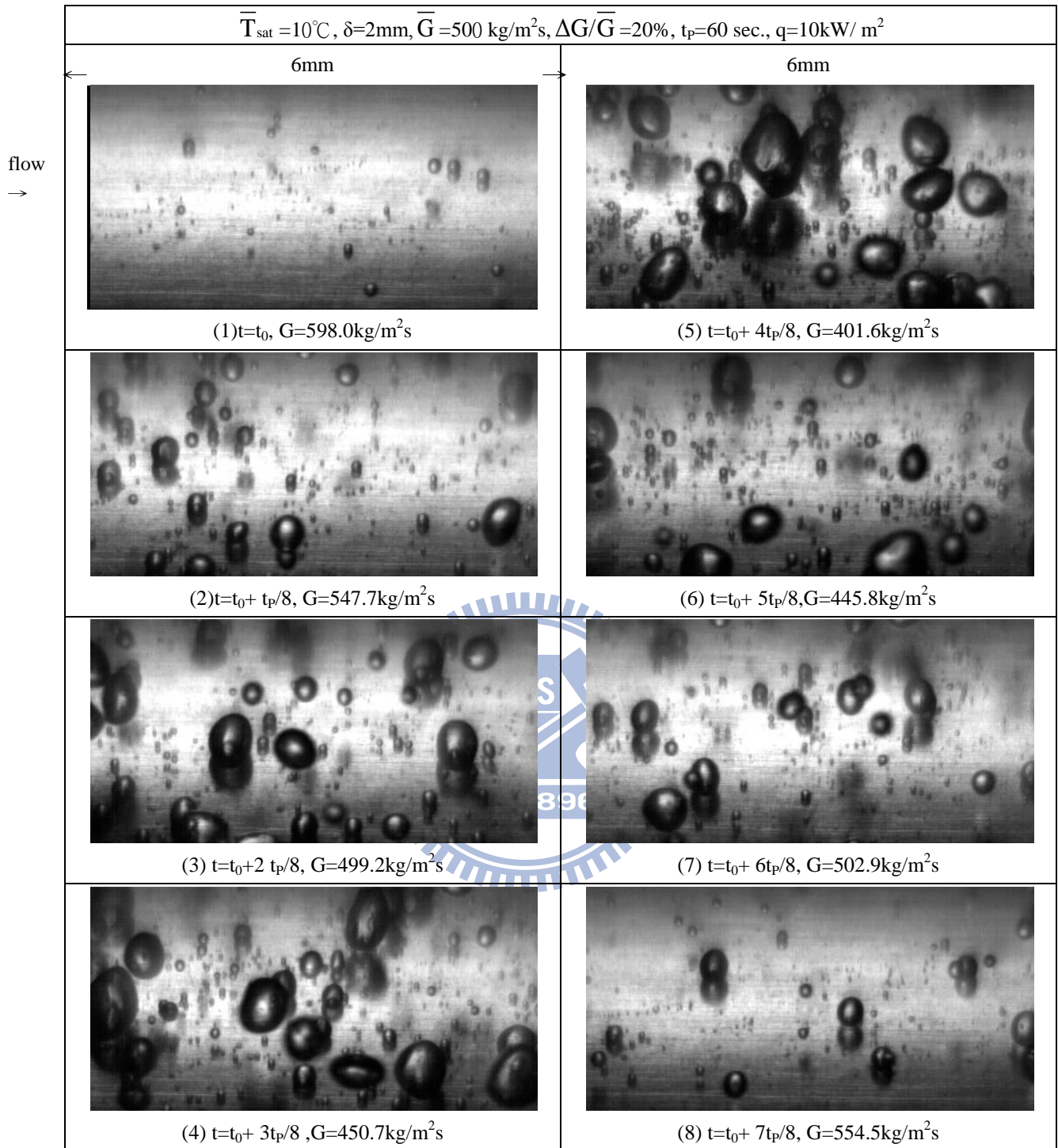


Fig. 4.46 Photos of time periodic saturated flow boiling of R-410A at selected time instants in a typical periodic cycle for  $q = 10 \text{ kW/m}^2$  at  $\bar{G} = 500 \text{ kg/m}^2\text{s}$ ,  $\Delta G/\bar{G} = 20\%$ ,  $\bar{T}_{\text{sat}} = 10^\circ\text{C}$ ,  $\delta = 2.0\text{mm}$  and  $t_p = 60\text{sec.}$



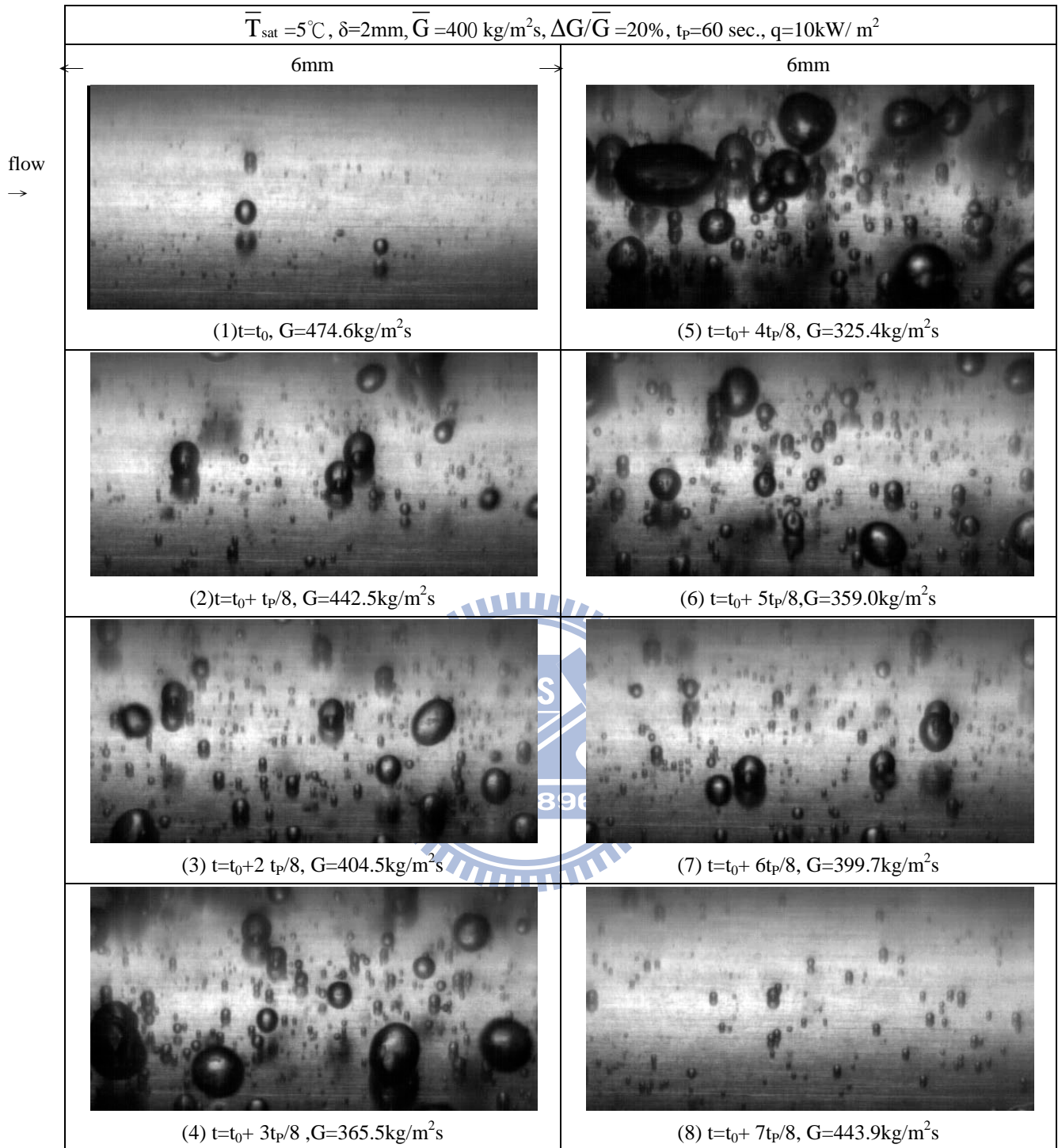


Fig. 4.47 Photos of time periodic saturated flow boiling of R-410A at selected time instants in a typical periodic cycle for  $q = 10 \text{ kW/m}^2$  at  $\bar{G} = 400 \text{ kg/m}^2\text{s}$ ,  $\Delta\bar{G}/\bar{G} = 20\%$ ,  $\bar{T}_{\text{sat}} = 5^\circ\text{C}$ ,  $\delta = 2.0\text{mm}$  and  $t_p = 60\text{sec.}$

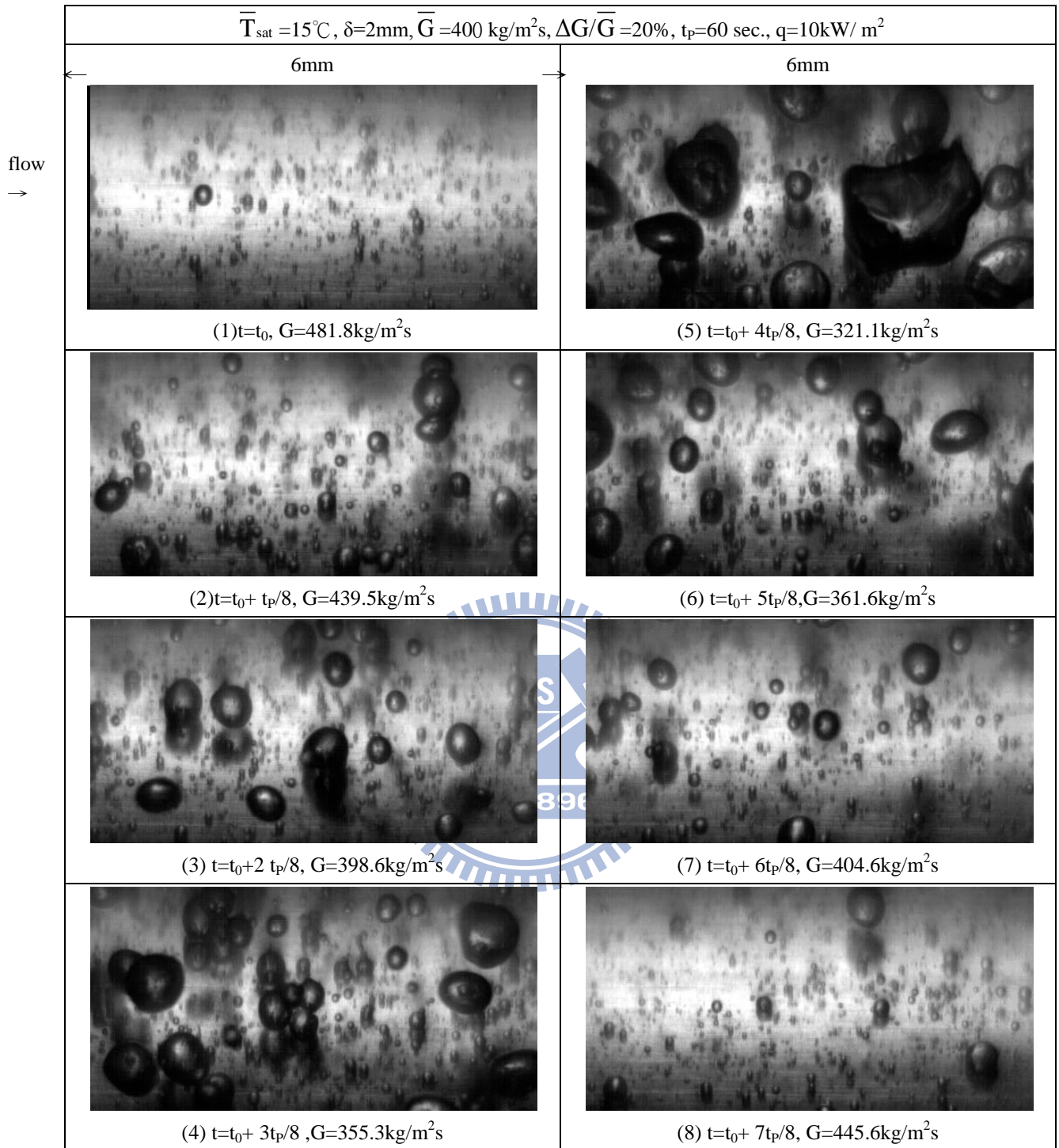


Fig. 4.48 Photos of time periodic saturated flow boiling of R-410A at selected time instants in a typical periodic cycle for  $q = 10 \text{ kW/m}^2$  at  $\bar{G} = 400 \text{ kg/m}^2\text{s}$ ,  $\Delta\bar{G}/\bar{G} = 20\%$ ,  $\bar{T}_{\text{sat}} = 15^\circ\text{C}$ ,  $\delta = 2.0\text{mm}$  and  $t_p = 60\text{sec.}$



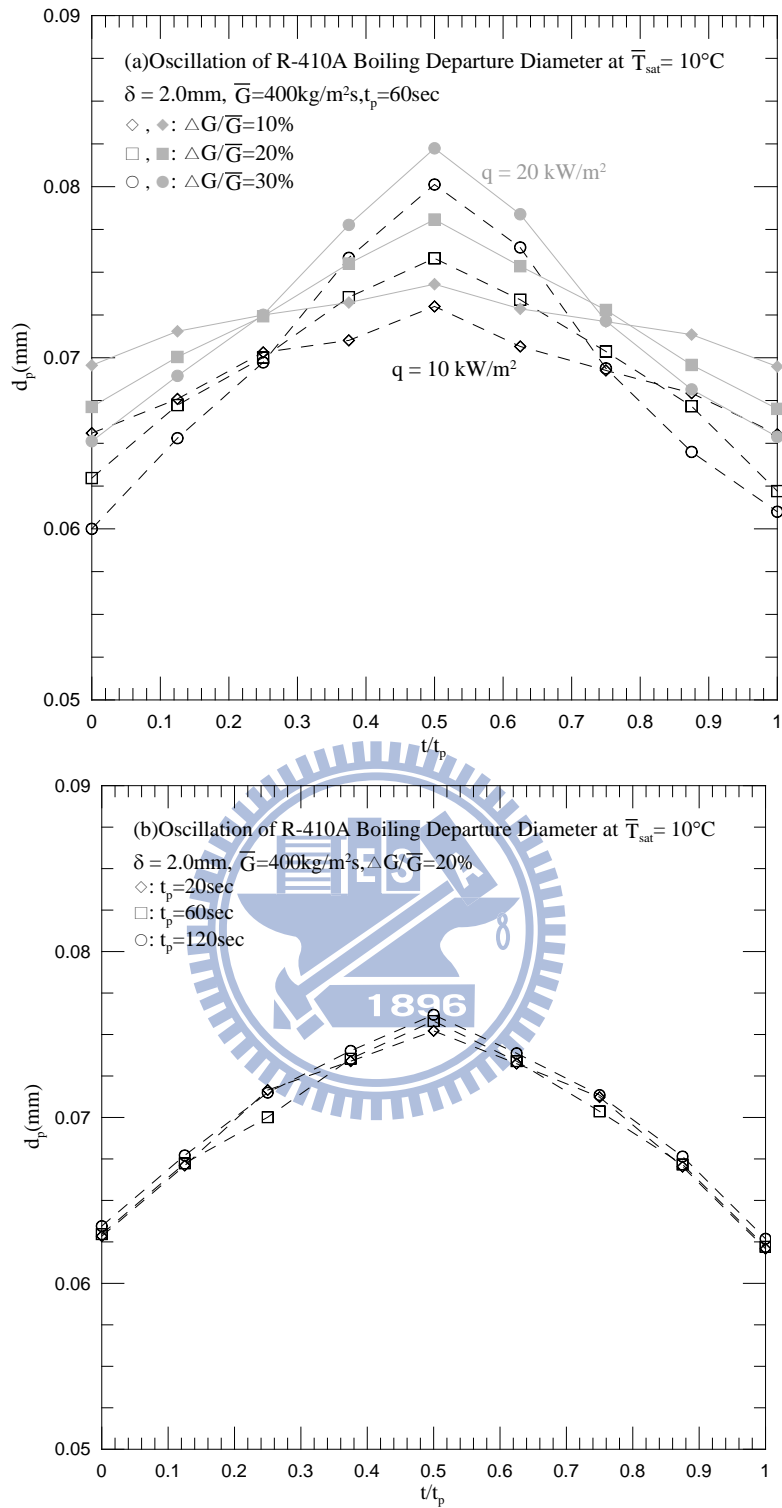


Fig. 4.49 Time variations of mean bubble departure diameter in time periodic saturated flow boiling of R-410A for  $q = 10\text{ kW/m}^2$  at  $\bar{T}_{sat} = 10^\circ\text{C}$ ,  $\bar{G} = 400\text{ kg/m}^2\text{s}$  and  $\delta = 2.0\text{mm}$  for (a) various oscillation amplitudes of  $G$  at  $t_p = 60\text{sec}$ , and (b) various periods of  $G$  oscillation at  $\Delta G/\bar{G} = 20\%$ .

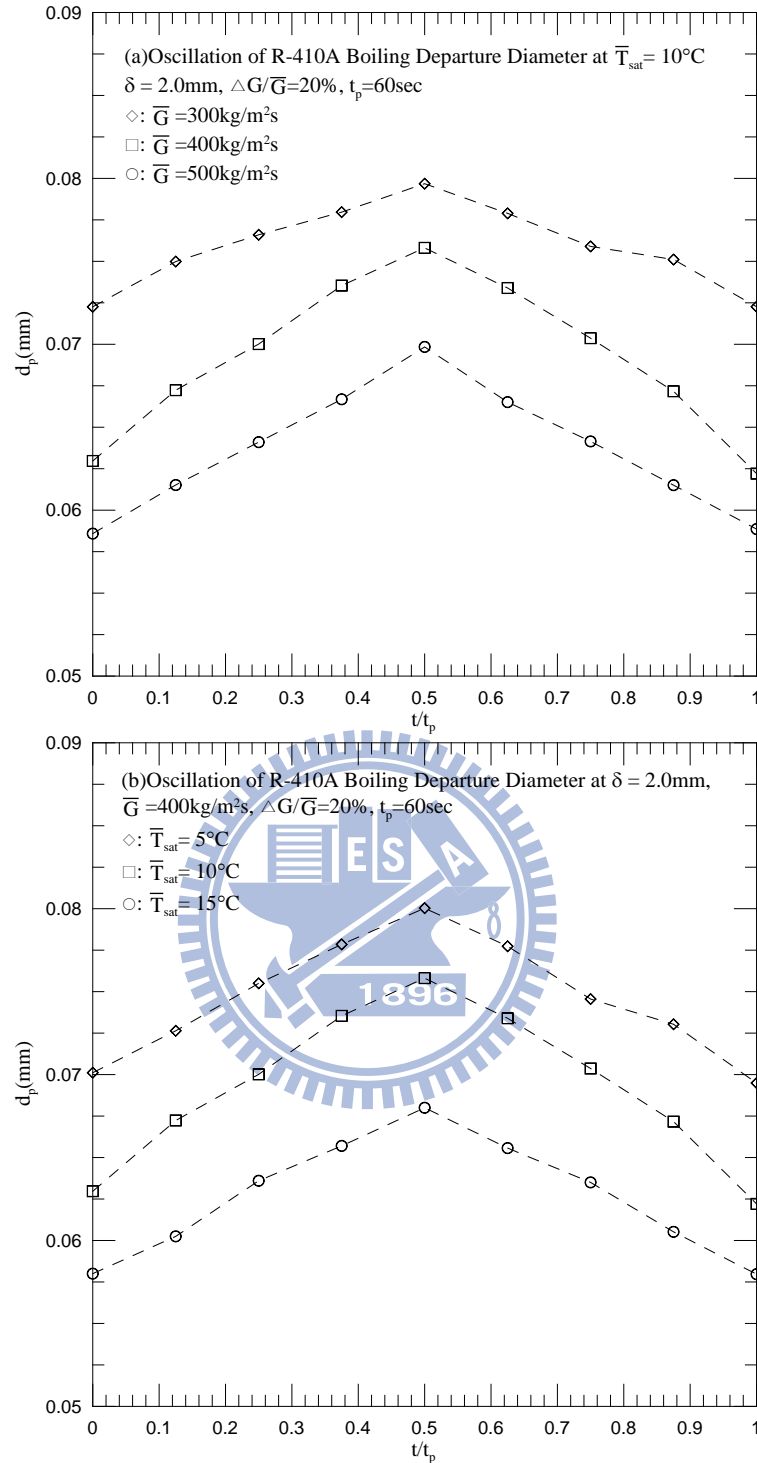


Fig. 4.50 Time variations of mean bubble departure diameter in time periodic saturated flow boiling of R-410A for  $q = 10\text{ kW/m}^2$  at  $t_p = 60\text{sec}$ ,  $\Delta G/\bar{G} = 20\%$ , and  $\delta = 2.0\text{mm}$  for (a) various mean mass fluxes at  $\bar{T}_{sat} = 10^\circ\text{C}$ , and (b) various mean saturated temperatures at  $\bar{G} = 400\text{kg/m}^2\text{s}$ .

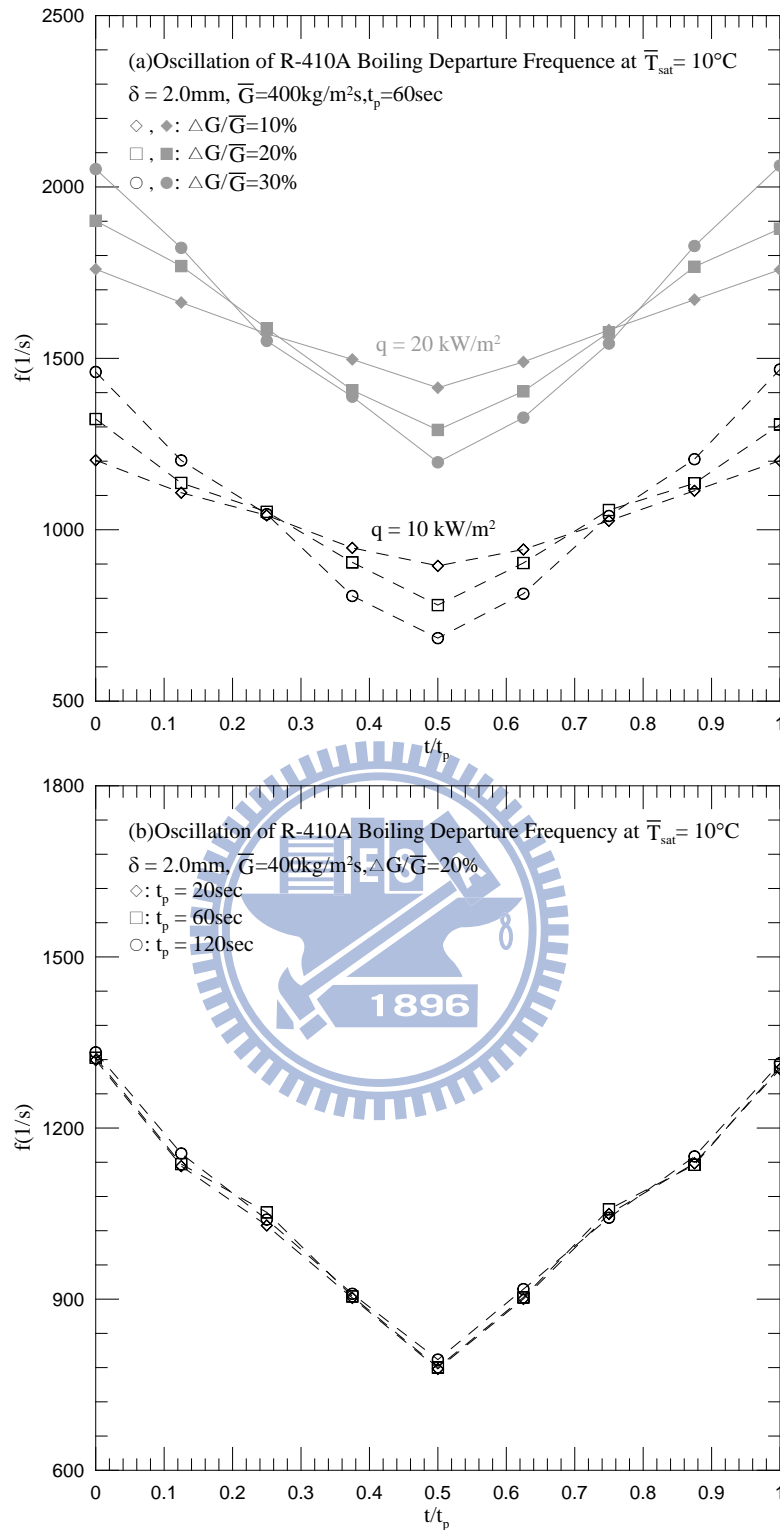


Fig. 4.51 Time variations of mean bubble departure frequency in time periodic saturated flow boiling of R-410A for  $q = 10\text{ kW/m}^2$  at  $\bar{T}_{sat} = 10^\circ\text{C}$ ,  $\bar{G} = 400\text{ kg/m}^2\text{s}$  and  $\delta = 2.0\text{mm}$  for (a) various oscillation amplitudes of  $G$  at  $t_p = 60\text{sec}$  and (b) various periods of  $G$  oscillation at  $\Delta G/\bar{G} = 20\%$ .

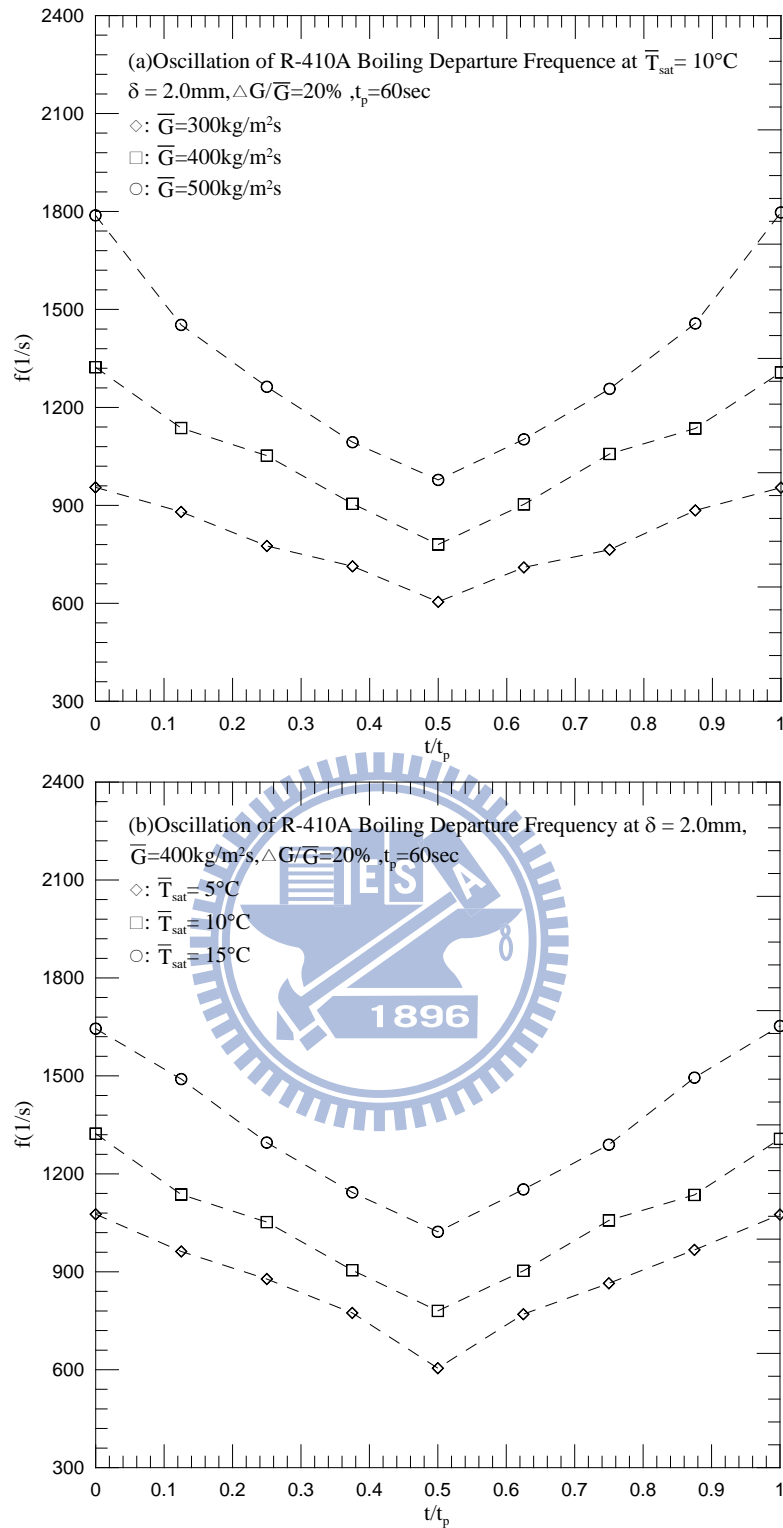


Fig. 4.52 Time variations of mean bubble departure frequency in time periodic saturated flow boiling of R-410A for  $q = 10\text{ kW/m}^2$  at  $\delta = 2.0\text{mm}$ ,  $\bar{G} = 400\text{ kg/m}^2\text{s}$ ,  $\Delta\bar{G}/\bar{G} = 20\%$  and  $t_p = 60\text{sec}$  for (a) various mean fluxes at  $\bar{T}_{\text{sat}} = 10^\circ\text{C}$  and (b) various mean saturated temperatures at  $\bar{G} = 400\text{kg/m}^2\text{s}$ .

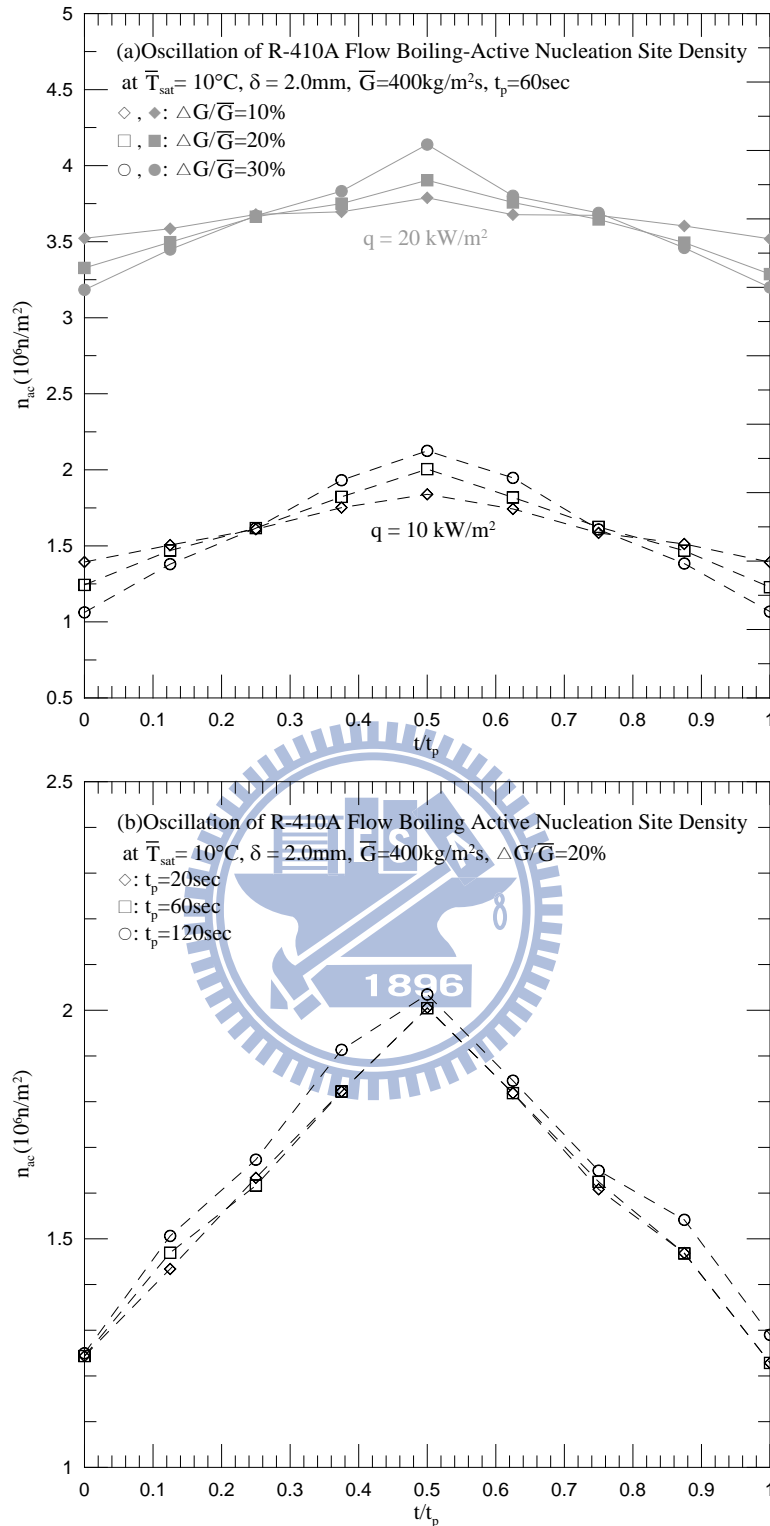


Fig. 4.53 Time variations of mean active nucleation site density in time periodic saturated flow boiling of R-410A for  $q = 10\text{ kW/m}^2$  at  $\delta = 2.0\text{mm}$ ,  $\bar{G} = 400\text{ kg/m}^2\text{s}$ ,  $\Delta G/\bar{G} = 20\%$  and  $t_p = 60\text{sec}$  for (a) various oscillation amplitudes of  $G$  at  $t_p = 60\text{sec}$  and (b) various periods of  $G$  oscillation at  $\Delta G/\bar{G} = 20\%$ .

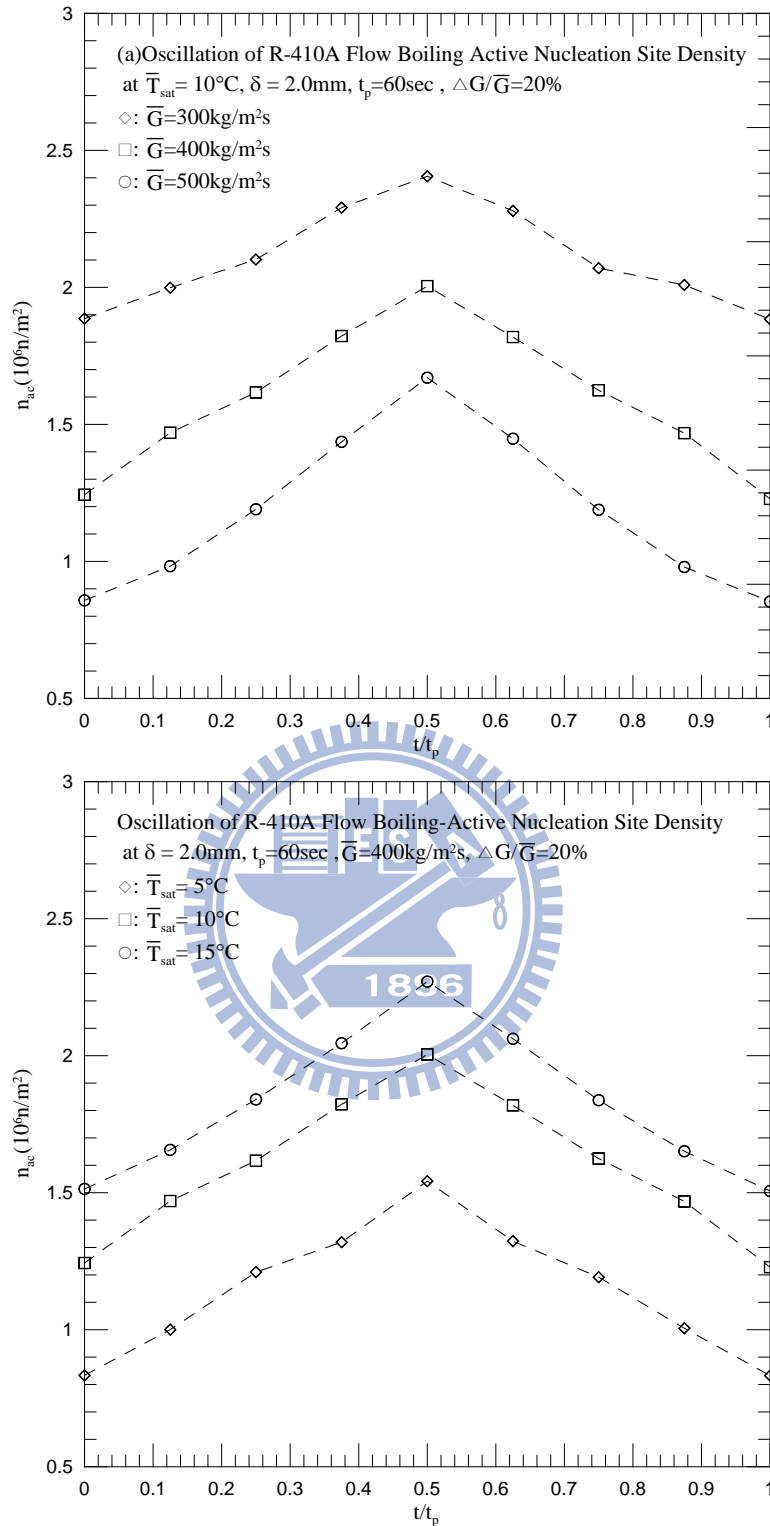


Fig. 4.54 Time variations of mean active nucleation site density in time periodic saturated flow boiling of R-410A for  $q = 10\text{kW/m}^2$  at  $\delta = 2.0\text{mm}$ ,  $\bar{G} = 400\text{kg/m}^2\text{s}$ ,  $\Delta G/\bar{G} = 20\%$  and  $t_p = 60\text{sec}$  for (a) various mean fluxes at  $\bar{T}_{sat} = 10^\circ\text{C}$ , and (b) various mean saturated temperatures at  $\bar{G} = 400\text{kg/m}^2\text{s}$ .

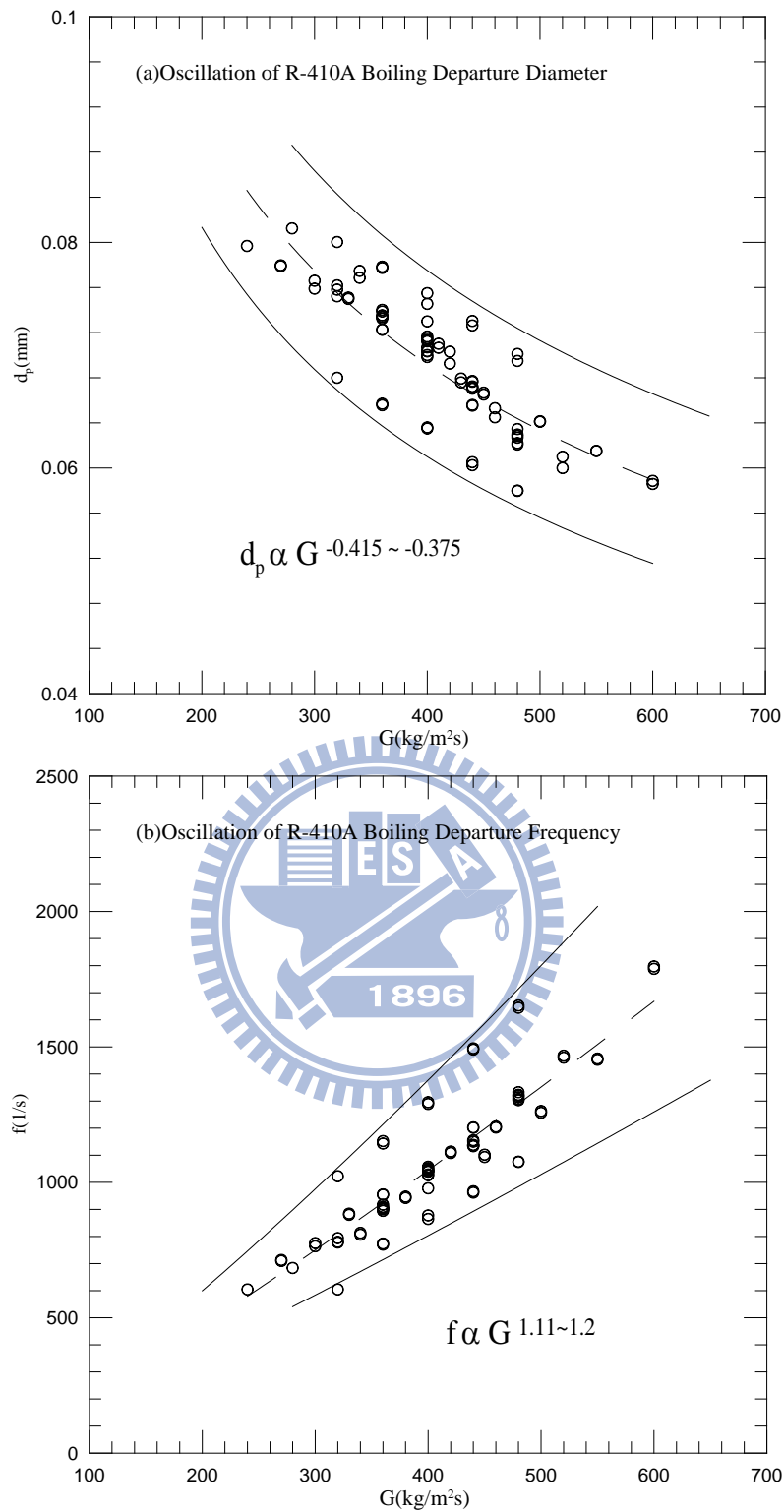


Fig. 4.55 Variations of bubble departure diameter (a), departure frequency (b), and active nucleation site density (c) with R-410A mass flux for time-periodic saturated flow boiling of R-410A.

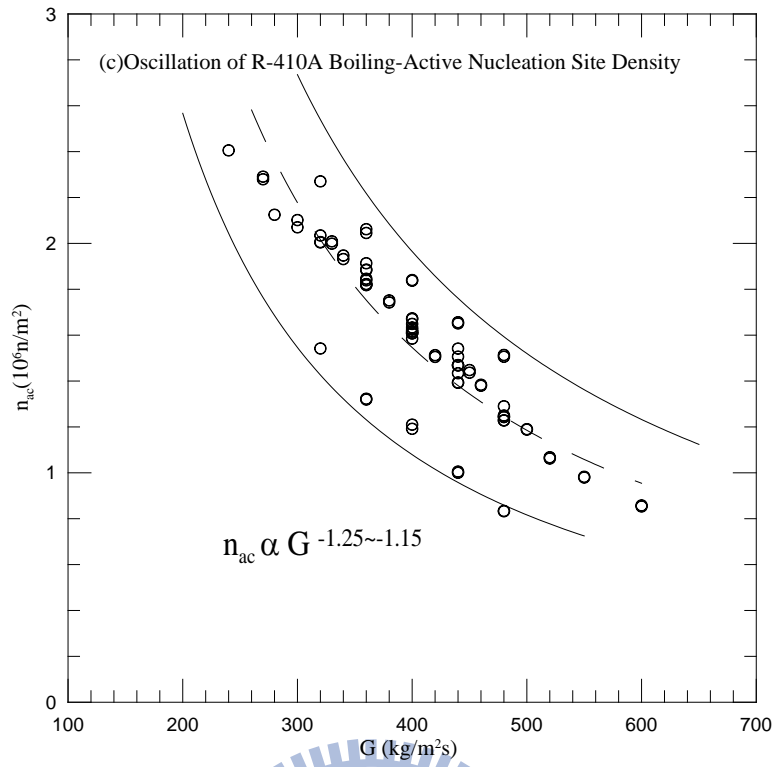


Fig. 4.55 continued







## CHAPTER 5

### TIME PERIODIC SATURATED FLOW BOILING OF R-410A IN A NARROW ANNULAR DUCT DUE TO HEAT FLUX OSCILLATION

The results obtained in the second part of the present study for the time periodic saturated flow boiling of R-410A in the duct due to the imposed heat flux oscillation are examined in this chapter. The present experiments are conducted for the refrigerant mass flux  $G$  varied from 300 to 500 kg/m<sup>2</sup>s, mean imposed heat flux  $\bar{q}$  from 0 to 45 kW/m<sup>2</sup>, and the amplitude of the heat flux oscillation  $\Delta q/\bar{q}$  fixed at 10, 30, 50% of  $\bar{q}$  with the period of the heat flux oscillation  $t_p$  fixed at 20, 60 and 120 seconds. The refrigerant saturation temperature  $T_{\text{sat}}$  is set at 5, 10 and 15°C. The gap between the inner and outer pipes  $\delta$  is fixed at 2.0 mm. Several time scales associated with the present saturated flow boiling over the heated inner pipe surface are given in Table 5.1. Specifically, there are four relevant time scales in the experiment. The conduction time scale  $t_1$  is estimated by considering a copper slab of the characteristic length  $L_c$  (thickness) subject to a step heat input at one of its surface at certain time instant and  $t_1$  is the duration for the other surface to begin to feel the heat input. According the thermal diffusion speed,  $t_1 \approx L_c^2/\alpha_w$ . The convection time scale  $t_2$  can be estimated by the equation  $t_2 = L/(G/\rho_1)$ . The time scale for the bubble growth or departure  $t_3$  is approximated by the empirical expression  $t_3 = \frac{d_p}{2000(\mu_1/(\rho_1 D_h))}$ . Finally, the time constant of the present flow boiling on the heated copper duct surface  $t_c$  is obtained by measuring  $T_w$  subject to a step input in the imposed heat flux for both single-phase and boiling conditions. The results in Table 5.1 for various time constants for selected cases clearly indicate that the values of  $t_c$  associated with the single-phase liquid flow and flow boiling over the heated surface are much larger than the other time constants and dominate the time response of the duct wall to the heat flux oscillation. Besides, the time lag of the heated surface temperature behind the imposed heat flux oscillation is expected to be significant. In the following, attention will be mainly paid to examining the effects of the amplitude and period of the heat flux oscillation on the time periodic R-410A saturated flow boiling heat transfer performance. Note that for the limiting case of  $\Delta q/\bar{q} = 0\%$  we have saturated flow boiling of R-410A at constant

refrigerant mass flow rate and imposed heat flux in the test section, which is designated as “stable flow boiling” here. The measured boiling heat transfer data are expressed in terms of the boiling curves and boiling heat transfer coefficients along with the time variations of the heated surface temperature. Besides, selected flow photos and data deduced from the images of the time periodic boiling processes are presented to show the temporal bubble characteristic in the boiling flow.

## 5.1 Time-average Saturated Flow Boiling Curves and Heat Transfer

### Coefficients

At first, Figs. 5.1 & 5.2 show the time-average boiling curves and heat transfer coefficients  $\bar{h}_r$  measured at the middle axial location ( $z = 80$  mm) of the narrow annular duct for various amplitudes and periods of the heat flux oscillation. The results in Figs. 5.1 & 5.2 reveal that the amplitudes and periods of the refrigerant mass flux oscillation have negligible influences on the time-average boiling curves and heat transfer coefficients. In fact, they are nearly the same as that for the stable flow boiling.

## 5.2 Time Periodic Flow Boiling Heat Transfer Characteristics

The time periodic saturated flow boiling heat transfer characteristics of R-410A in the annular duct resulting from the imposed heat flux oscillation are illustrated by presenting the time variations of the space-average heated surface temperature  $T_w$  and boiling heat transfer coefficient  $h_r$  at the middle axial location in the saturated state for various  $G$ ,  $T_{sat}$ ,  $\Delta q/\bar{q}$ ,  $t_p$  and  $q$  are shown in Figs. 5.3-5.20. For clarity, the measured data for the time variations of the actual imposed heat flux are also given here. The results manifest that when  $q$  oscillates periodically in time nearly like a triangular wave, significant temporal oscillations in  $T_w$  and  $h_r$  occur and they are also periodic in time and are at the same frequency as the heat flux. The results indicate that  $T_w$  and  $h_r$  oscillations get stronger for a higher amplitude and a longer period of the imposed heat flux oscillation, and  $T_w$  also oscillates stronger for a higher mean imposed heat flux. Note that single-phase forced convection prevails in the duct at a relatively low imposed heat flux. The data given in Figs. 5.3-5.20 further reveals that the  $T_w$  oscillation significantly lags the heat flux oscillation for both single-phase and boiling flows. The time lag apparently results from the thermal inertia of the heated pipe wall. Note that for given  $G$ ,  $T_{sat}$ , and  $\Delta q/\bar{q}$  the duration of time

lag relative to the oscillation period  $t_1/t_p$  is slightly longer at a lower time-average imposed heat flux and a shorter period of the imposed heat flux. Furthermore, the heat flux decreases with time in the first half of the periodic cycle for the single-phase convection, after the time lag the heating wall temperature is found to decrease with time. The opposite process occurs in the second half of the cycle. It is noted that at low mean imposed heat flux no bubble nucleates from the heating surface in the whole periodic cycle. Hence heat transfer in the flow results completely from the single-phase forced convection. As the mean imposed wall heat flux is raised gradually, the heating surface temperature increases correspondingly and the corresponding  $T_w$  oscillation amplitude can be significant. At a certain higher  $\bar{q}$  bubbles start to nucleate from the heating surface at certain instant of time but bubble nucleation is not seen in the whole cycle. Thus, we have intermittent boiling in the flow in which nucleate boiling only exists in a partial duration of the periodic cycle. The time instants for the start and termination of the nucleate boiling are marked on the curves for  $T_w$  for the cases with the presence of the intermittent boiling. Moreover, for a much higher  $\bar{q}$  nucleate boiling persists over the entire period of the cycle and we have persistent flow boiling in the duct. Note that after the time lag,  $T_w$  and  $h_r$  both decrease with time in the first half of the periodic cycle in which the imposed heat flux decreases with time for the single-phase flow, intermittent flow boiling and persistent flow boiling. The results in Figs. 5.10 and 5.11 also show that at a higher refrigerant saturated temperature, the amplitude of the  $T_w$  oscillation is larger in persistent flow boiling. This is because of the surface tension of R-410A is smaller at higher refrigerant saturated temperature, so more bubbles nucleate at the heating surface.

### 5.3 Intermittent Boiling

It is of interest to note in the visualization of the boiling flow over the heated inner pipe in the annular duct that over a certain intermediate range of the mean imposed heat flux the intermittent boiling appears, as already mentioned earlier. More specifically, in a typical periodic cycle of the imposed heat flux oscillation bubble nucleation in the heated annular duct disappears at a certain time instant after the heat flux decreases to a certain low level and the pipe wall temperature decreases to the level below that required for the onset of nucleate boiling. Single-phase flow prevails in the duct. At a certain later time instant in the second half of the cycle in which the imposed heat flux increases and  $T_w$  rises to exceed the wall superheat required for the onset of nucleate boiling, bubble nucleation is

seen on the heated surface and boiling appears. The above process of intermittent boiling is repeatedly seen on the heated surface. To be more clearer, we indicate the time instants at which boiling starts and stops in Figs. 5.3 – 5.11 for the cases with the presence of the intermittent boiling. Note that at a higher imposed heat flux the onset of boiling is earlier and the termination of boiling is later. A flow regime map to delineate the boundaries separating different flow boiling regimes in terms of the Boiling number versus the relative amplitude of the heat flux oscillation is given in Fig. 5.21. The results show that the intermittent boiling prevails over a significantly wider range of the boiling number for a higher amplitude of the imposed heat flux oscillation and a lower refrigerant mass flux. However, the effects of refrigerant saturated temperature are small. Based on the present data, the conditions leading to the appearance of the intermittent boiling can be empirically correlated as

$$\left(2.16 \times 10^{-7} + 3.47 \times 10^{-9} \overline{\text{Re}}^{0.5}\right) \leq \overline{\text{Bo}}^{1.2} \cdot (\Delta q / \bar{q})^{1.2} \cdot (t_p / t_c)^{1.2} \leq \left(2.21 \times 10^{-5} - 4.12 \times 10^{-8} \overline{\text{Re}}^{0.5}\right) \quad (5.1)$$

More than 97% of the present data falls within the above correlation.

#### 5.4 Effect of Heat Flux Oscillation at Extremely Short and Long Periods

How the period of the heat flux oscillation affects the time periodic flow boiling is further investigated by comparing the data for relatively short and long  $t_p$  in Figs. 5.22 – 5.24. Now when the oscillatory period is set to be much shorter than the time constant  $t_c$  at 2.0 seconds (Fig. 5.22), the heated surface temperature stays at a nearly constant level even for the case with the oscillation amplitude  $\Delta q$  being 50% of the mean imposed heat flux. In fact, for this case the amplitude of  $T_w$  oscillation is smaller than  $0.1^\circ\text{C}$  which is below the random thermal disturbances from the background and is close to that in the stable boiling. At this short  $t_p$  the heated copper duct is not able to quickly respond to the very rapid change in the imposed heat flux because of its heat capacity. This situation appears when the period of the imposed heat flux oscillation is significantly shorter than the dominated time constant of the flow boiling system.

On the other hand, when the oscillatory period is relatively long at 120 and 600 seconds, the data given in Figs. 5.23 & 5.24 manifest that the amplitude of the  $T_w$  oscillation is very large. Note that the  $T_w$  oscillation is slightly stronger for  $t_p$  raised from 120 to 600 seconds. The stronger  $T_w$  oscillation at a longer  $t_p$  can be attributed to the

longer period of time for the thermal energy storing in and releasing from the wall of the heated inner pipe. This in turn causes the heat pipe wall to accumulate and release thermal energy over a longer period of time and hence results in a larger amplitude of the  $T_w$  oscillation.

## 5.5 Effect of Heat Flux Oscillation Amplitude

The effect of the amplitude of the heat flux oscillation on the time periodic flow boiling of R-410A is examined further, too. The results in Fig. 5.25 for three different amplitudes of the imposed heat flux oscillation with  $\Delta q/\bar{q} = 10, 30$  and  $50\%$  at  $t_p = 60$  seconds show that the  $T_w$  oscillation is significantly stronger for a larger amplitude of the imposed heat flux oscillation. Note that the time lag in  $T_w$  oscillation increases substantially when the amplitude of the imposed heat flux oscillation is raised from  $10\%$  to  $30\%$ . But a further increase in the amplitude of the heat flux oscillation does not increase the time lag noticeably.

## 5.6 Time Periodic Bubble Characteristics in Saturated Flow Boiling

To elucidate the time periodic saturated flow boiling heat transfer characteristics resulting from the imposed heat flux oscillation, the data for the bubble characteristics of R-410A flow boiling obtained from the present flow visualization are examined in the following. The side views of the boiling flow in a small region around the middle axial location of the duct for various imposed heat fluxes are shown in Figs. 5.26-5.43 for selected cases for the time periodic saturated flow boiling. In these figures the symbol “  $t=t_0$  ” signifies the time instant at which the instantaneous heat flux is at the highest level and starts to decrease with time. The bubble behavior in the intermittent flow boiling for the cases with given intermediate imposed heat fluxes is manifested in Figs. 5.26-5.34. The results clearly indicates that initially in the beginning of the cycle the instantaneous heat flux decreases with time but is still well above  $\bar{q}_{ONB}$ , bubbles nucleation from the heated surface is clearly seen. Note that the number and size of the bubbles decrease noticeably with time in the first quarter of the periodic cycle for the continuing decrease of the heat flux. Then the bubble nucleation gradually disappears and finally boiling stops at certain time instant slightly after  $t_0+3t_p/8$  when the heat flux is slightly below  $\bar{q}_{ONB}$  and bubble nucleation stops completely. The flow is in single-phase state. But after a certain

time instant slightly after  $t_0+6t_p/8$  at which the imposed heat flux is raised to a certain high level,  $T_w$  rises to exceed the wall superheat required for the onset of nucleate boiling so that bubble nucleation on the heated surface is seen and more bubbles nucleate on the heated surface as time increases. Two-phase boiling flow again dominates in the duct. We have to wait until about the end of the first quarter of the next cycle to see the bubble nucleation gradually disappears on the heated surface. The above processes repeat in each cycle. The precise instants of time at which the onset and termination of nucleate boiling vary with the flow condition.

Then, we illustrate here how the time periodic bubble characteristics are affected by the amplitude and period of the heat flux oscillation for the persistent boiling in Figs. 5.35-5.43. The results indicate that for given  $G$ ,  $\bar{q}$ ,  $\Delta q/\bar{q}$  and  $t_p$  the departure bubbles get smaller in the duct in the first half of the cycle in which the heat flux decreases. The opposite processes take place in the second half of the cycle in which the heat flux increases with time. These changes of the bubble characteristics with the instantaneous heat flux become more significant for an increase in the amplitude of the heat flux oscillation, as shown from the results in the Figs. 5.35~5.37. Besides, the bubble coalescence occurs more frequently and more large bubbles appear in the duct for the cases with a longer period of the heat flux oscillation (Figs. 5.38&5.39). The results given in Figs. 5.42&5.43 indicate that for a higher refrigerant saturated temperature, more large bubbles appear in the duct. This is due to lower surface tension of R-410A at higher refrigerant saturated temperature.

To be more quantitative on the bubble characteristics in the time periodic flow boiling due to the heat flux oscillation, we estimate the bubble departure diameter and frequency and the number density of the active nucleation sites on the heating surface in a typical periodic cycle at the middle axial location for the persistent flow boiling. The results in Figs. 5.44 – 5.49 show the effects of the experimental parameters on  $d_p$ ,  $f$  and  $n_{ac}$ . In these plots time “ $t = 0$ ” denotes the instant of time the imposed heat flux is at the highest level and starts to decrease in a typical periodic cycle. The results in Figs. 5.44 and 5.45 indicate that as the imposed heat flux oscillates time periodically, the bubble departure diameter also varies time periodically and to some degree like a triangular wave as the imposed heat flux oscillation. Note that the effect of the time lag on the  $T_w$  oscillation is clearly seen. More specifically, the size of the departing bubbles does not decrease immediately with

time in the first half of the periodic cycle in which the heat flux decreases with time. In fact, the bubble size increases in the initial transient for  $t < t_1$  and then for  $t > t_1$  the bubble departure diameter decreases. While in the second half of the cycle an opposite process is noted when heat flux increases with time. The results in Fig. 5.44(a) show that at the larger amplitude of the heat flux oscillation and mean imposed head flux the time variation of bubble departure diameter is somewhat stronger. Moreover, the results in Fig. 5.44(b) indicate that to some degree the bubble departure diameter varies stronger with time for a longer period of the heat flux oscillation. Furthermore, the results in Figs. 5.45(a) and (b) show that increases in the refrigerant mass flux and saturated temperature cause the departing bubbles to become smaller but do not change the wave form of the  $d_p$  variation with time.

How the temporal variation of the bubble departure frequency is affected by the heat flux oscillation is shown in Figs. 5.46 and 5.47. Note that the bubble frequency also varies like a triangular wave. At first, for  $t < t_1$  the bubble departure frequency increases with time. Then, for an oscillation heat flux after the time lag for  $t > t_1$  the bubbles depart from the heated surface at a decreasing rate in the first half of the periodic cycle in which the heat flux decreases with time (Fig. 5.46(a)). Apparently, in the second half of the cycle in which the heat flux increases the opposite process takes place. Moreover, the results in Fig. 5.46(a) indicate that at the larger amplitude of the heat flux oscillation and mean imposed heat flux the bubble departure frequency exhibits a stronger variation with time. Then, the results in Fig. 5.46(b) indicate that the bubble departure frequency oscillates in a larger amplitude at a longer period of the heat flux oscillation. Finally, at higher  $G$  and  $T_{sat}$  the bubble departure frequency is higher (Figs. 5.47(a) and (b)).

The data given in Figs 5.48 and 5.49 show the time variations of the associated number density of the active nucleation sites on the heating surface affected by the heat flux oscillation. The results clearly indicate that in the time periodic flow boiling the active nucleation site density also varies like a triangular wave. Besides,  $n_{ac}$  decreases substantially with time after the time lag for  $t > t_1$  in the first half of the periodic cycle in which the heat flux decreases with time. The reverse process appears in the second half of the cycle in which the heat flux rises. At higher amplitude of the heat flux oscillation and mean imposed heat flux the temporal variation of  $n_{ac}$  is also stronger (Fig. 5.48(a)). Moreover, for a longer period of the heat flux oscillation the time variation of  $n_{ac}$  is also



stronger (Fig. 5.48(b)). Finally,  $n_{ac}$  is significantly higher at a lower  $G$  and higher  $T_{sat}$  (Figs. 5.49(a) and (b)).

It's worth mentioning that the time instants at which  $d_p$ ,  $f$  and  $n_{ac}$  attain their maximums and minimums are not exactly at the instants the imposed heat flux is at its highest and lowest levels respectively at  $t = 0$  and  $t = t_p/2$ . This is a direct consequence of the significant time lag in the time response of the heated surface temperature in the present time periodic flow boiling subject to the imposed heat flux oscillation.

Based on the data in Figs. 5.44 – 5.49, in the persistent boiling at a high  $q$  the dependence of the quantitative bubble characteristics on the R-410A heat flux oscillation can be approximately expressed as  $d_p \propto q^a$ ,  $f \propto q^b$ , and  $n_{ac} \propto q^c$  when the time lag in the  $T_w$  oscillation is neglected. Here the exponents  $a$ ,  $b$  and  $c$  range respectively from 0.02 to 0.13, 0.36 to 0.64 and 0.77 to 1.18, as shown in Fig. 5.50. Note that the latent heat transfer resulting from bubble nucleation in the persistent boiling  $q_b$  is proportional to  $d_p^3$ ,  $f$  and  $n_{ac}$ , as discussed in the previous study [8]. Thus,  $q_b \propto q^d$ , here  $d$  varies from 1.19 to 2.21. This result clearly indicates that flow boiling heat transfer gets better at increasing heat flux since  $q_b$  prevails in the boiling heat transfer. Besides, the dominant effect of the heat flux oscillation on the boiling heat transfer comes from the very strong influence of the heat flux on the active nucleation site density.

**Table 5.1 Time scales for transient R-410A saturated flow boiling ( $\delta = 2\text{mm}$ )**

Time scales		(sec)
Conduction time scale $t_1 = L_c^2 / \alpha_w$		$1.247 \times 10^{-11}$
Convection time scale $t_2 = L / (G / \rho_1)$	$T_{\text{sat}} = 10^\circ\text{C}, G = 300\text{kw/m}^2\text{s}$	0.6016
	$T_{\text{sat}} = 10^\circ\text{C}, G = 400\text{kw/m}^2\text{s}$	0.4512
	$T_{\text{sat}} = 10^\circ\text{C}, G = 500\text{kw/m}^2\text{s}$	0.3610
	$T_{\text{sat}} = 15^\circ\text{C}, G = 400\text{kw/m}^2\text{s}$	0.4436
Time scale of saturated flow boiling $t_3 = \frac{d_p}{2000(\mu_1 / (\rho_1 D_h))}$		0.00109
Time constant $t_4 = t_c$	$T_{\text{sat}} = 10^\circ\text{C}, G = 300\text{kw/m}^2\text{s}$	30 (Single-phase)
		24.4 (Saturated flow boiling)
	$T_{\text{sat}} = 10^\circ\text{C}, G = 400\text{kw/m}^2\text{s}$	29.4 (Single-phase)
		23.5 (Saturated flow boiling)
	$T_{\text{sat}} = 10^\circ\text{C}, G = 500\text{kw/m}^2\text{s}$	28.5 (Single-phase)
		22.7 (Saturated flow boiling)
	$T_{\text{sat}} = 15^\circ\text{C}, G = 400\text{kw/m}^2\text{s}$	27.9 (Single-phase)
		23.4 (Saturated flow boiling)

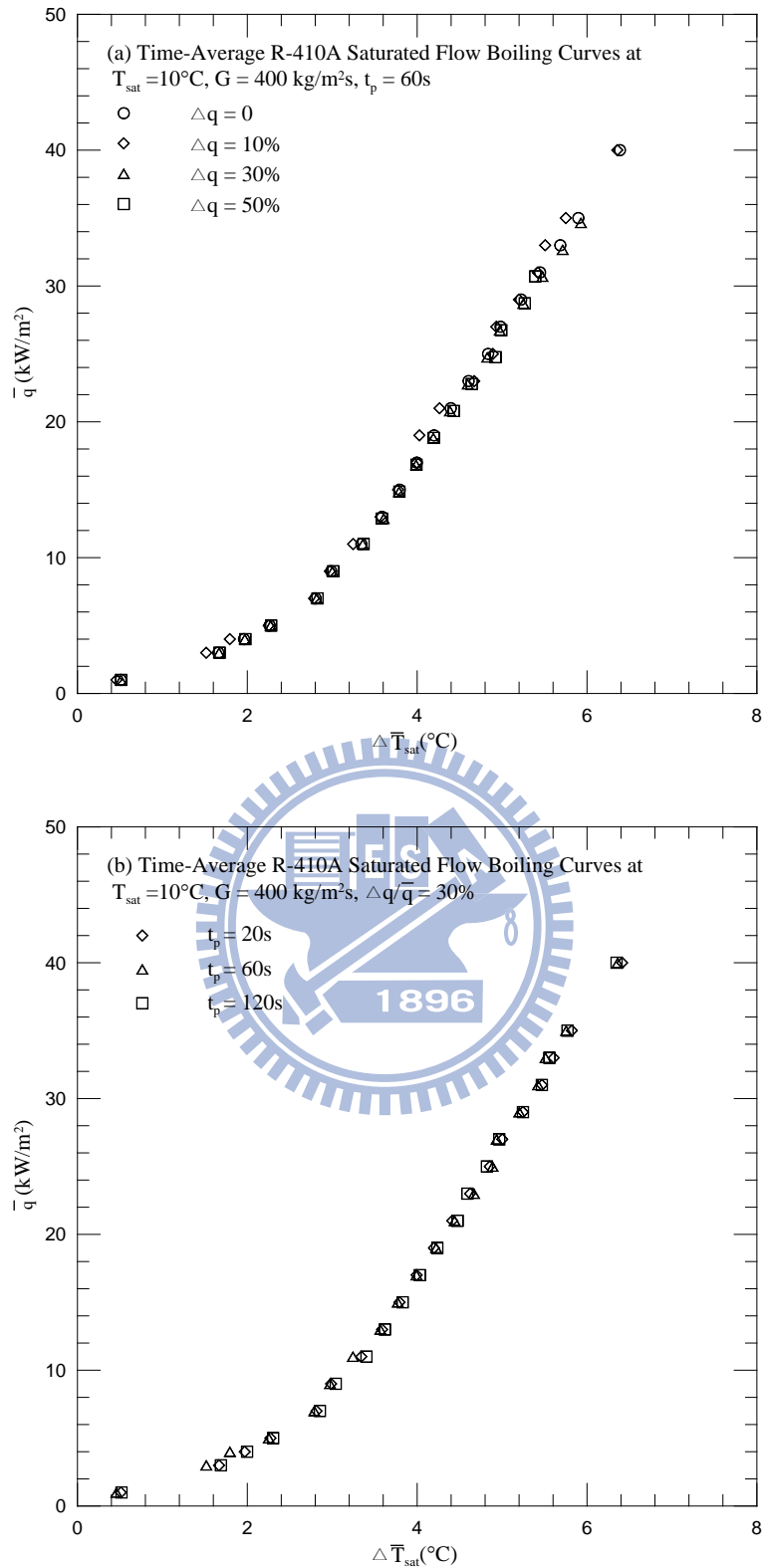


Fig. 5.1 Time-average flow boiling curves for R-410A for (a) various amplitudes of imposed heat flux oscillation at  $T_{\text{sat}} = 10^\circ\text{C}$ ,  $\delta = 2.0 \text{ mm}$ ,  $G = 400 \text{ kg/m}^2$  and  $t_p = 60 \text{ sec.}$  and (b) various periods of heat flux oscillation at  $T_{\text{sat}} = 10^\circ\text{C}$ ,  $\delta = 2.0 \text{ mm}$ ,  $G = 400 \text{ kg/m}^2$  and  $\Delta q/q = 30\%$ .

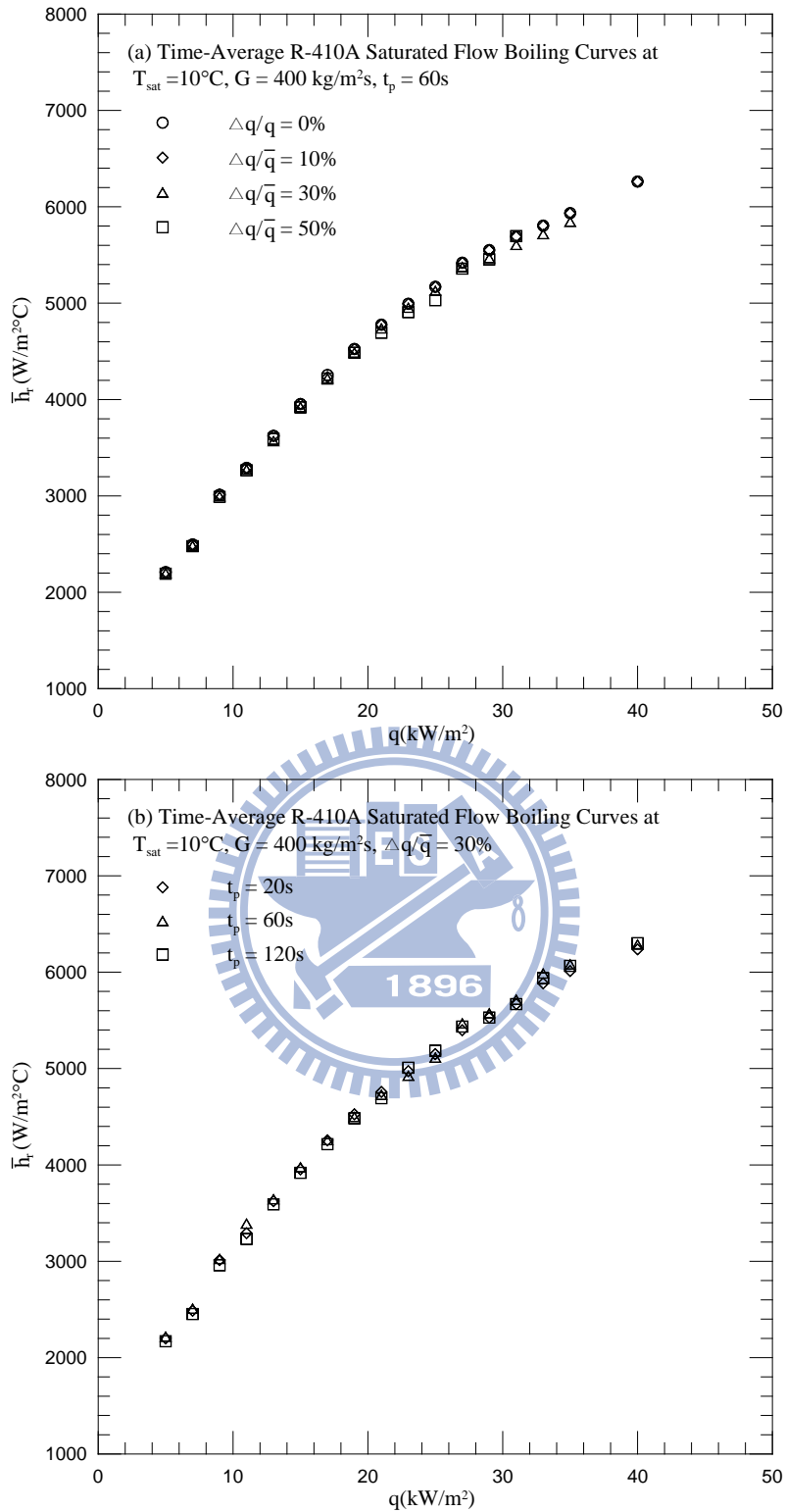


Fig. 5.2 Time-average flow boiling heat transfer coefficients for R-410A for (a) various amplitudes of imposed heat flux oscillation at  $T_{\text{sat}} = 10^\circ\text{C}$ ,  $\delta = 2.0 \text{ mm}$ ,  $G = 400 \text{ kg/m}^2$  and  $t_p = 60 \text{ sec}$ . and (b) various periods of heat flux oscillation at  $T_{\text{sat}} = 10^\circ\text{C}$ ,  $\delta = 2.0 \text{ mm}$ ,  $G = 400 \text{ kg/m}^2$  and  $\Delta q/\bar{q} = 30\%$ .

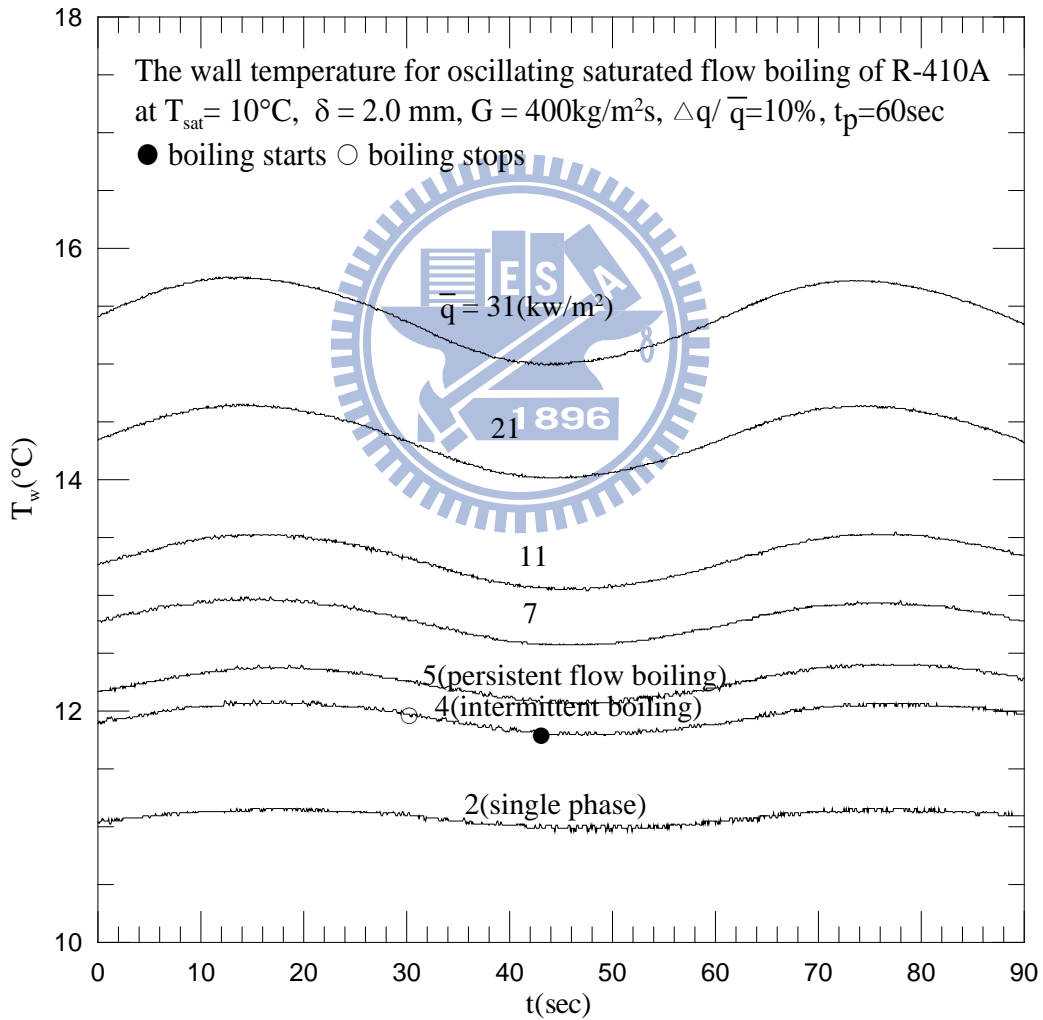
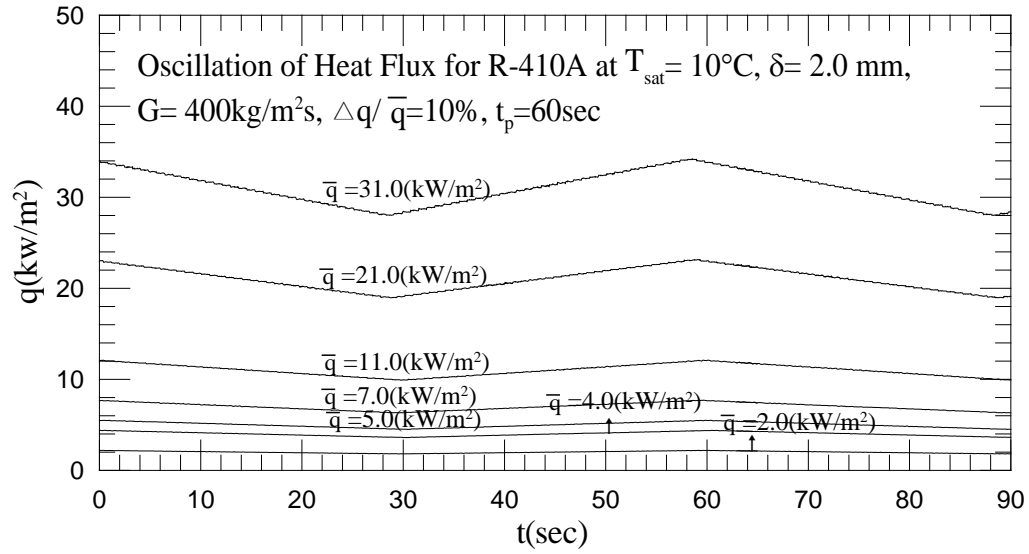


Fig. 5.3 Time variations of imposed heat flux and measured wall temperature in time periodic saturated flow boiling of R-410A at  $T_{\text{sat}} = 10^\circ\text{C}$ ,  $\delta = 2.0 \text{ mm}$ ,  $t_p = 60 \text{ sec}$  and  $G = 400 \text{ kg/m}^2\text{s}$  with  $\Delta q / \bar{q} = 10\%$ .

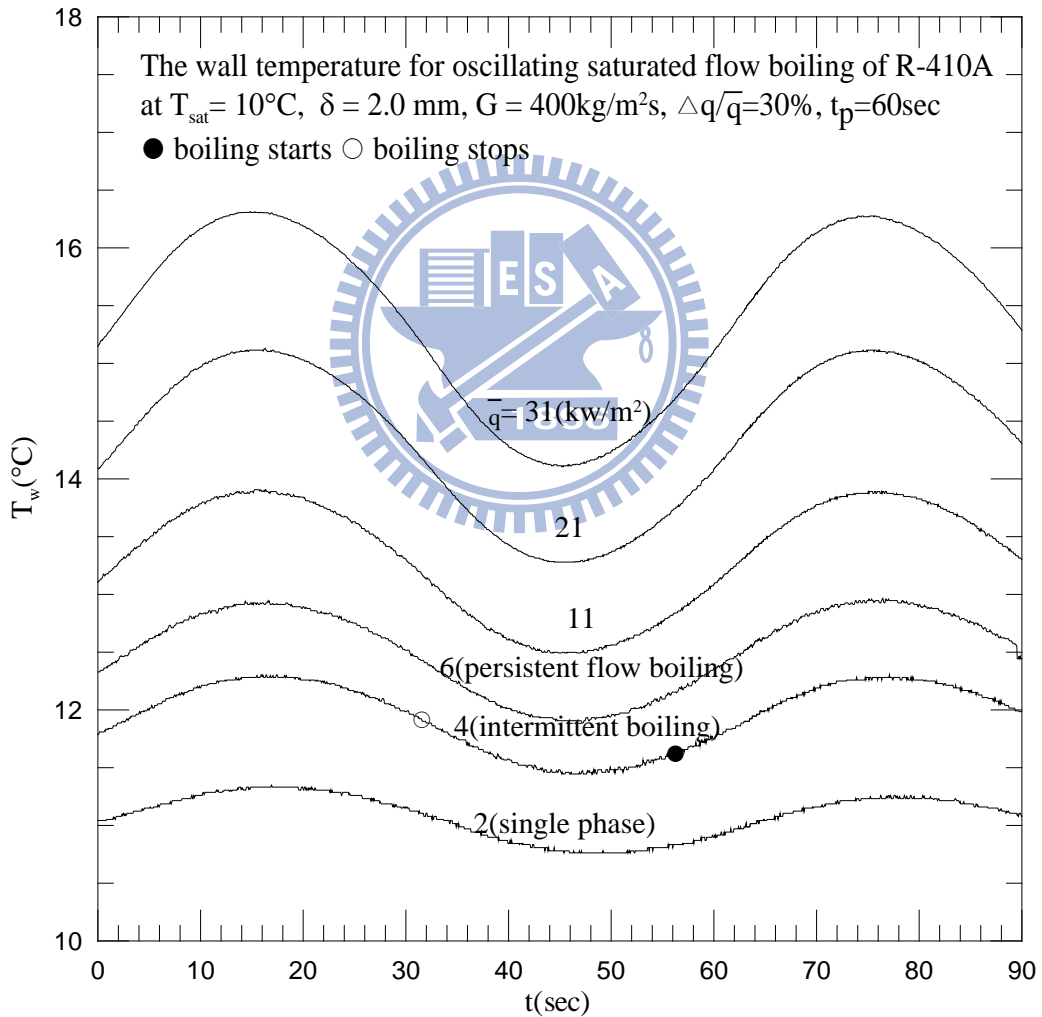
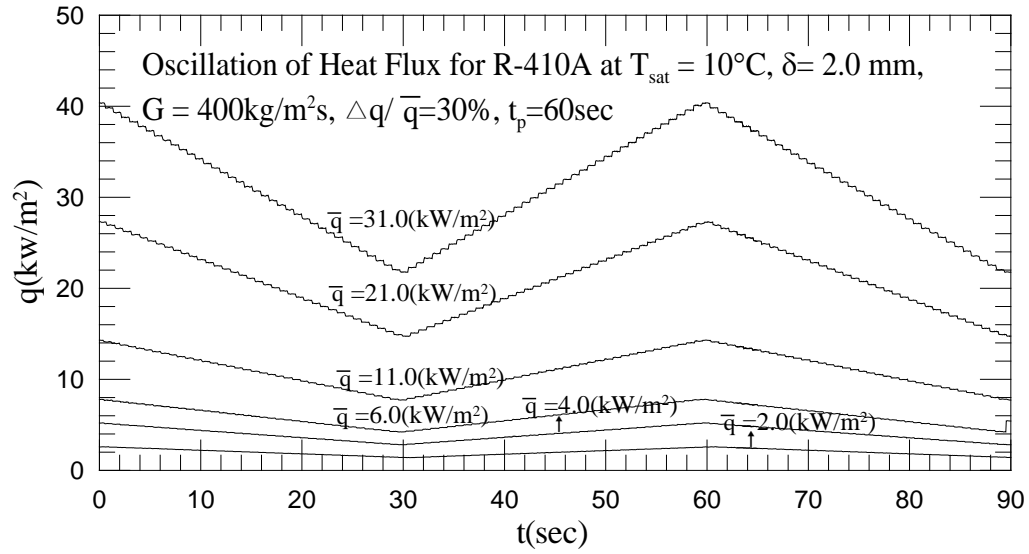


Fig. 5.4 Time variations of imposed heat flux and measured wall temperature in time periodic saturated flow boiling of R-410A at  $T_{\text{sat}} = 10^\circ\text{C}$ ,  $\delta = 2.0 \text{ mm}$ ,  $t_p = 60 \text{ sec}$  and  $G = 400 \text{ kg/m}^2\text{s}$  with  $\Delta q / \bar{q} = 30\%$ .

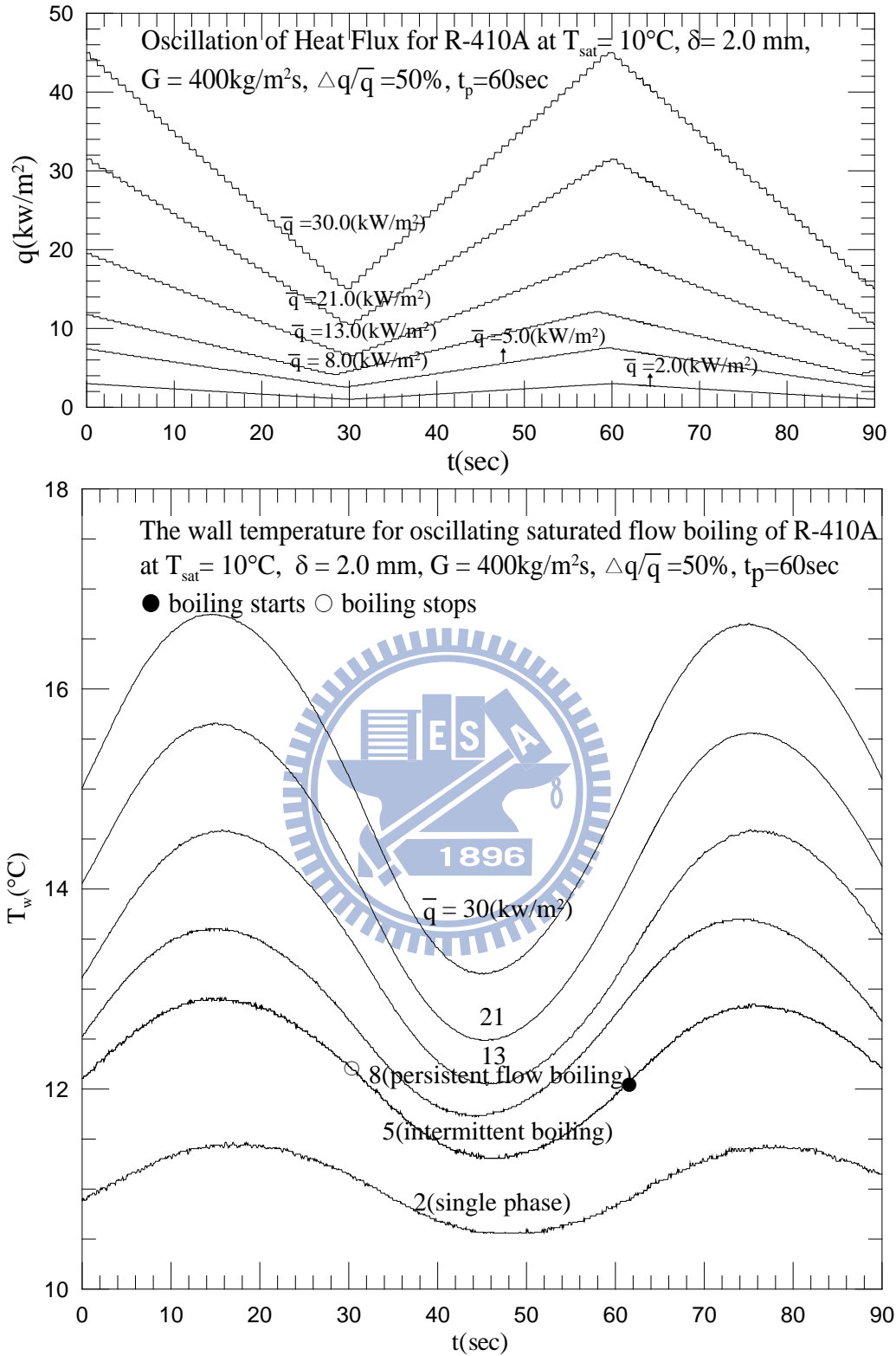


Fig. 5.5 Time variations of imposed heat flux and measured wall temperature in time periodic saturated flow boiling of R-410A at  $T_{sat} = 10^{\circ}\text{C}$ ,  $\delta = 2.0 \text{ mm}$ ,  $t_p = 60 \text{ sec}$  and  $G = 400 \text{ kg/m}^2\text{s}$  with  $\Delta q/\bar{q} = 50\%$ .

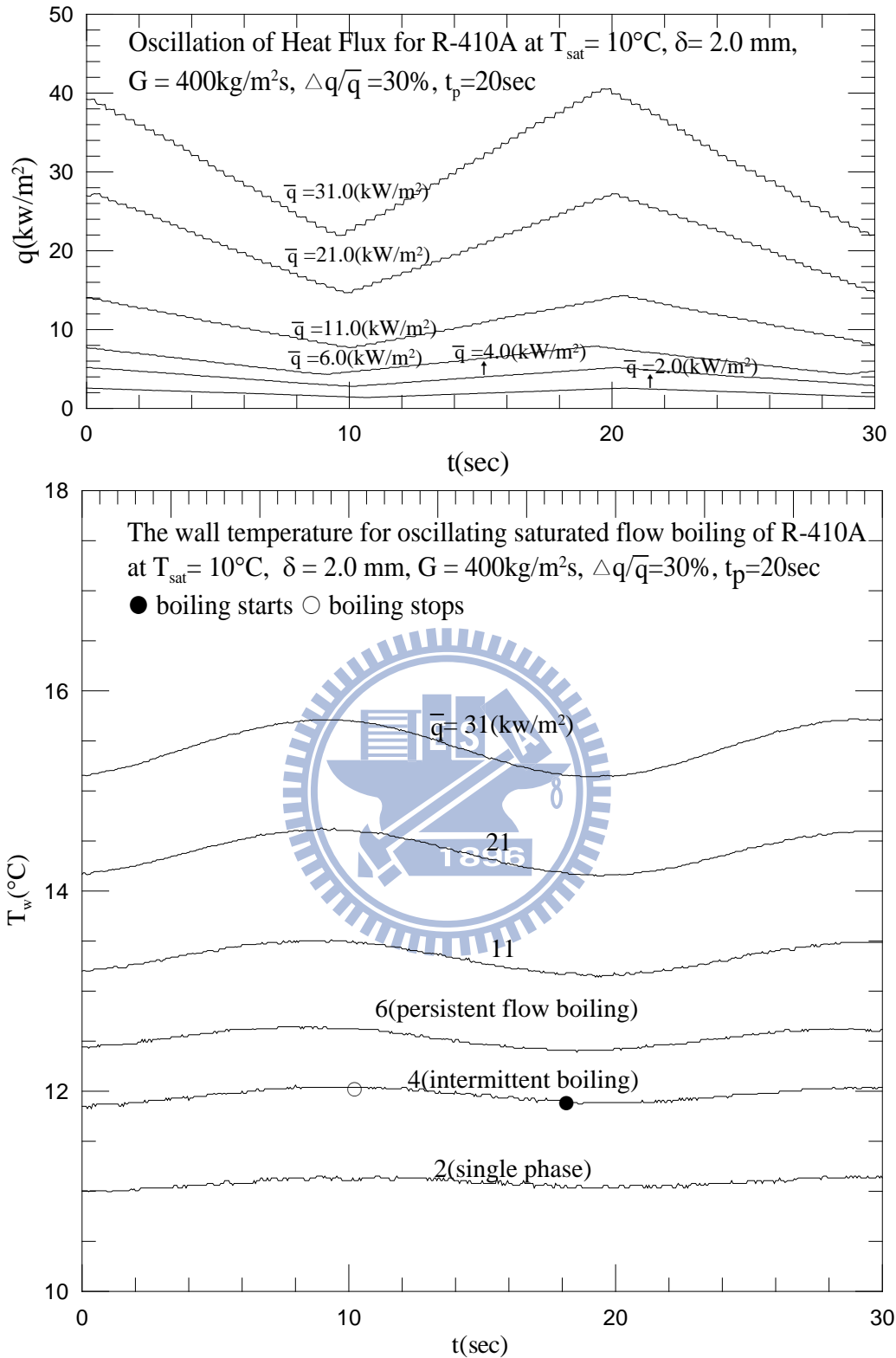


Fig. 5.6 Time variations of imposed heat flux and measured wall temperature in time periodic saturated flow boiling of R-410A at  $T_{\text{sat}} = 10^{\circ}\text{C}$ ,  $\delta = 2.0 \text{ mm}$ ,  $t_p = 20 \text{ sec}$  and  $G = 400 \text{ kg/m}^2\text{s}$  with  $\Delta q/\bar{q} = 30\%$ .



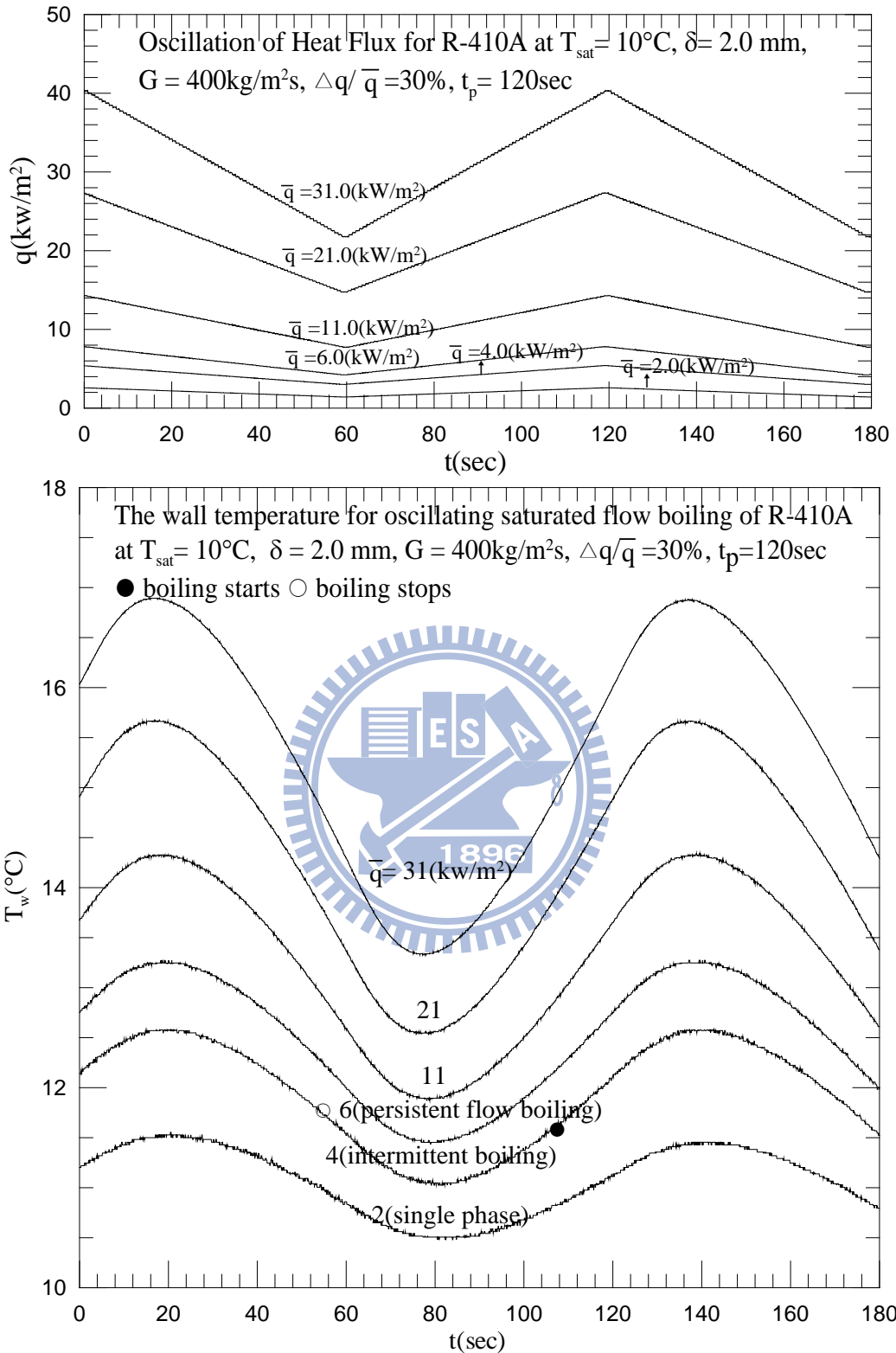


Fig. 5.7 Time variations of imposed heat flux and measured wall temperature in time periodic saturated flow boiling of R-410A at  $T_{\text{sat}} = 10^\circ\text{C}$ ,  $\delta = 2.0 \text{ mm}$ ,  $t_p = 120 \text{ sec}$  and  $G = 400 \text{ kg/m}^2\text{s}$  with  $\Delta q / \bar{q} = 30\%$ .

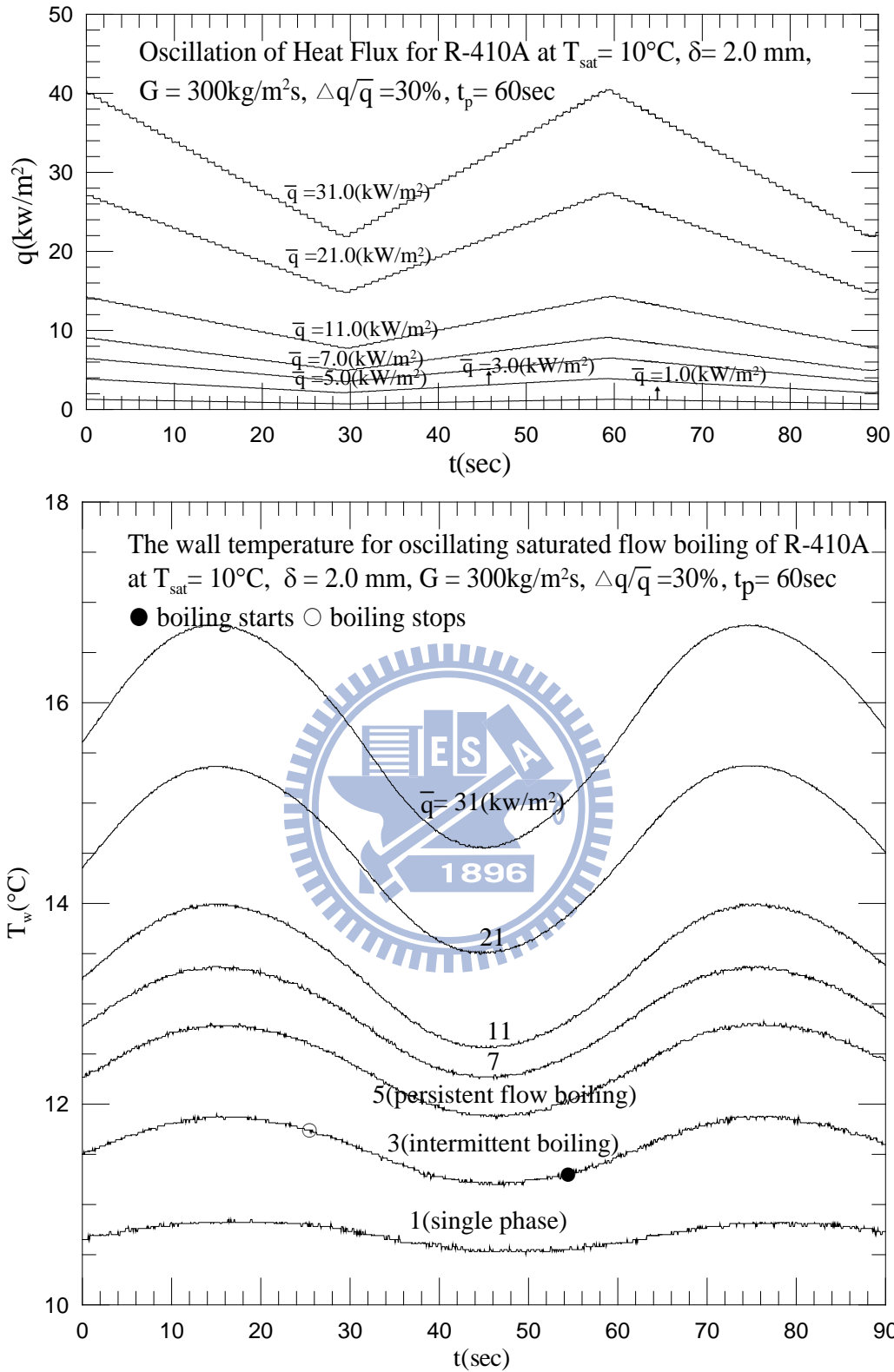


Fig. 5.8 Time variations of imposed heat flux and measured wall temperature in time periodic saturated flow boiling of R-410A at  $T_{sat} = 10^\circ\text{C}$ ,  $\delta = 2.0\text{mm}$ ,  $t_p = 60 \text{ sec}$  and  $G = 300\text{kg/m}^2\text{s}$  with  $\Delta q/\bar{q} = 30\%$ .

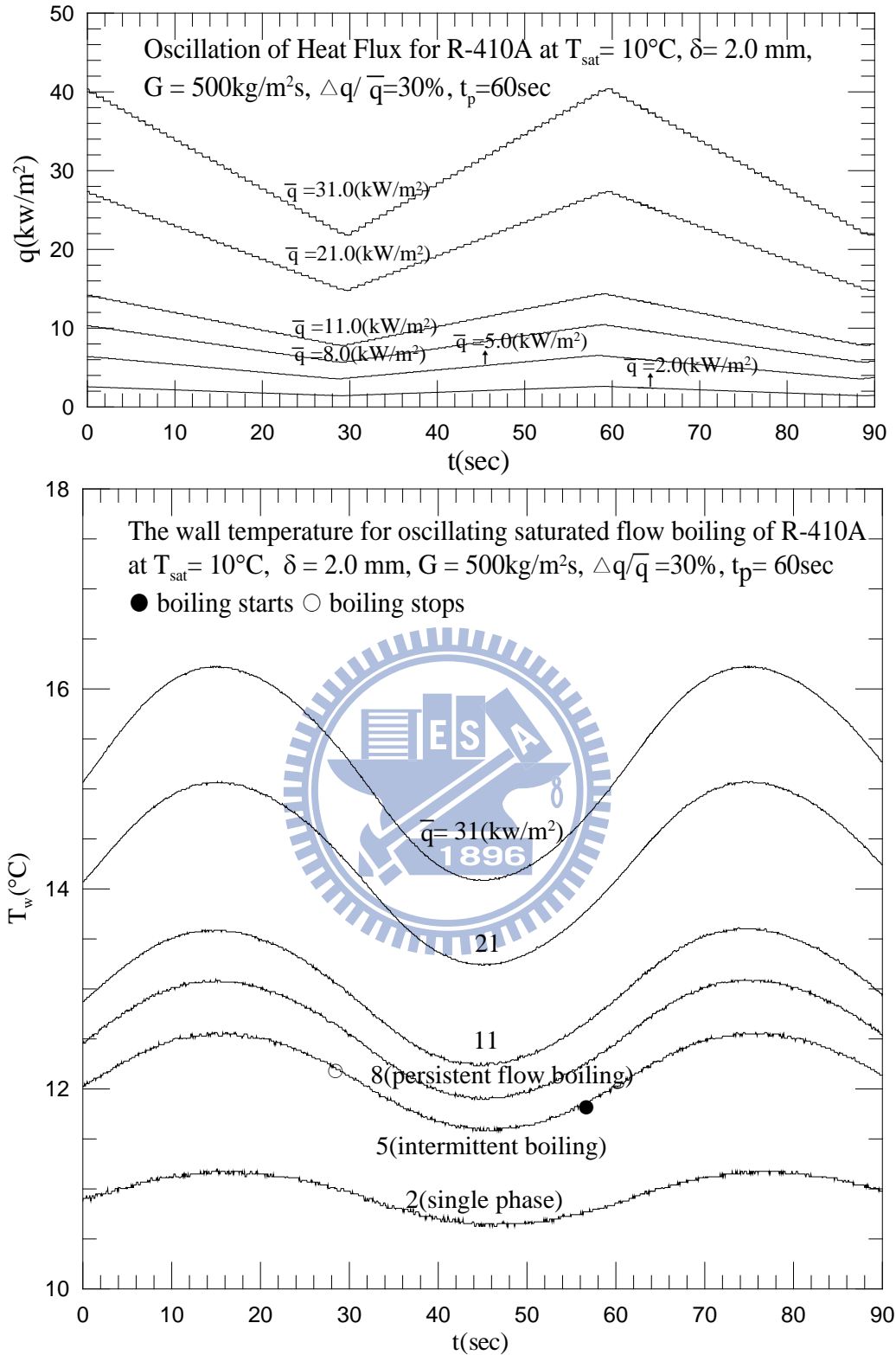


Fig. 5.9 Time variations of imposed heat flux and heat transfer coefficient in time periodic saturated flow boiling of R-410A at  $T_{\text{sat}} = 10^\circ\text{C}$ ,  $\delta = 2.0 \text{ mm}$ ,  $t_p = 60 \text{ sec}$  and  $G = 500 \text{ kg/m}^2\text{s}$  with  $\Delta q/\bar{q} = 30\%$ .

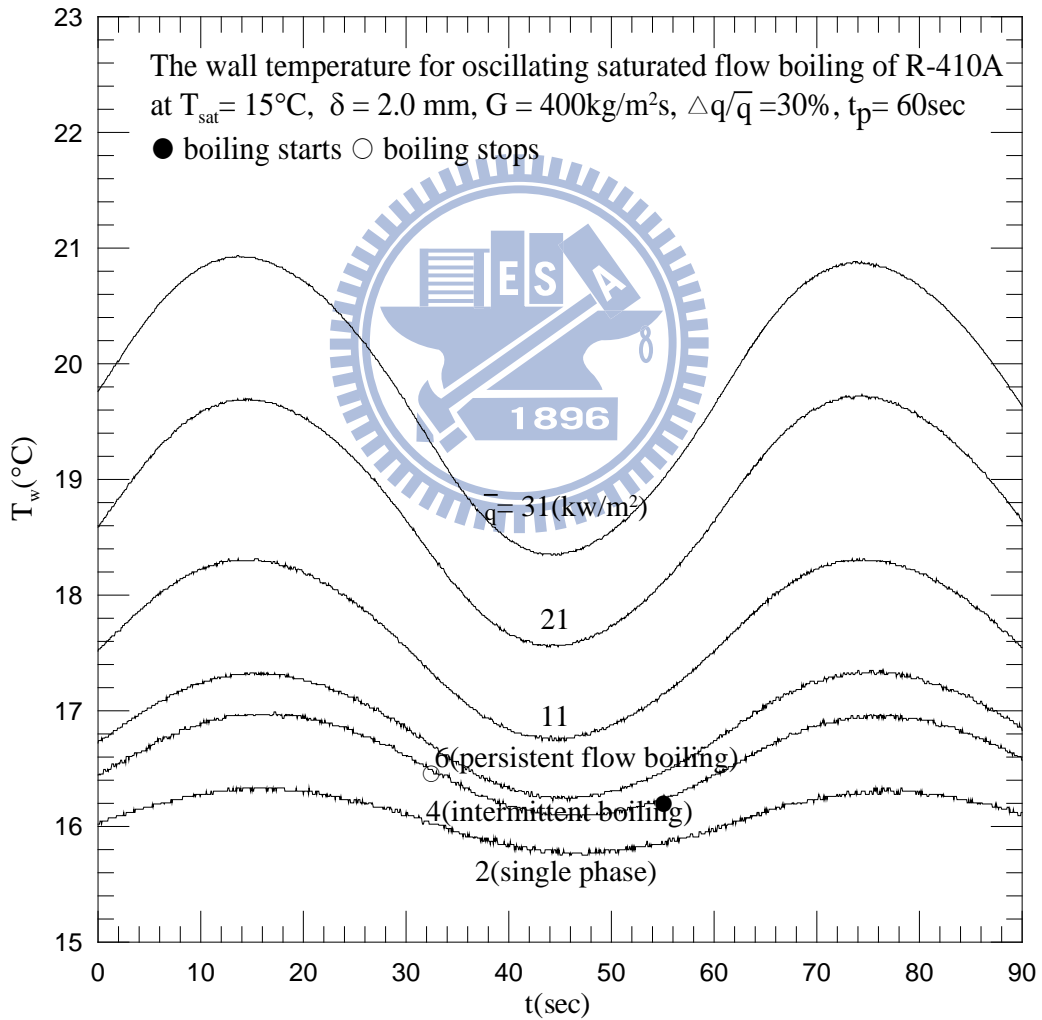
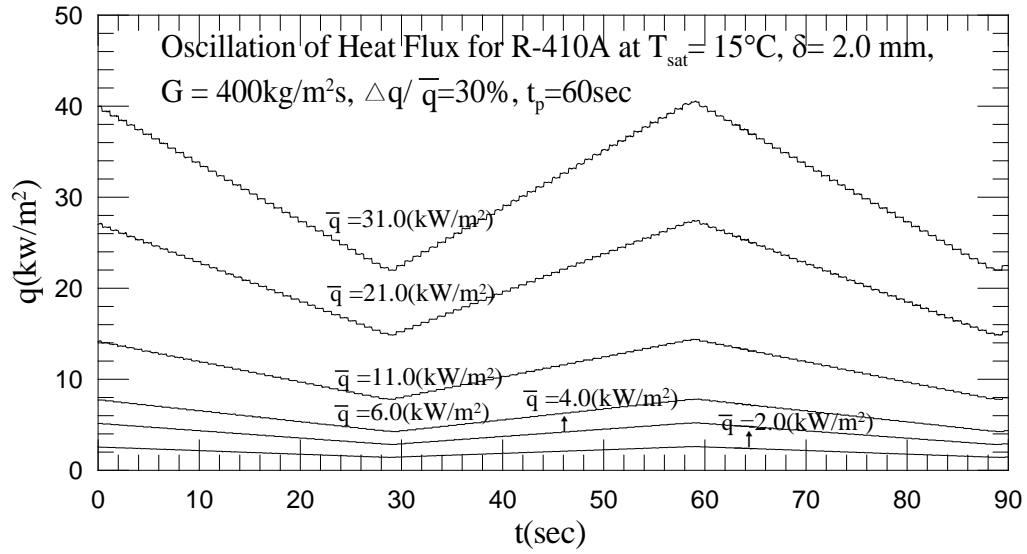


Fig. 5.10 Time variations of imposed heat flux and heat transfer coefficient in time periodic saturated flow boiling of R-410A at  $T_{\text{sat}} = 15^\circ\text{C}$ ,  $\delta = 2.0 \text{ mm}$ ,  $t_p = 60 \text{ sec}$  and  $G = 400 \text{ kg/m}^2\text{s}$  with  $\Delta q/\bar{q} = 30\%$ .

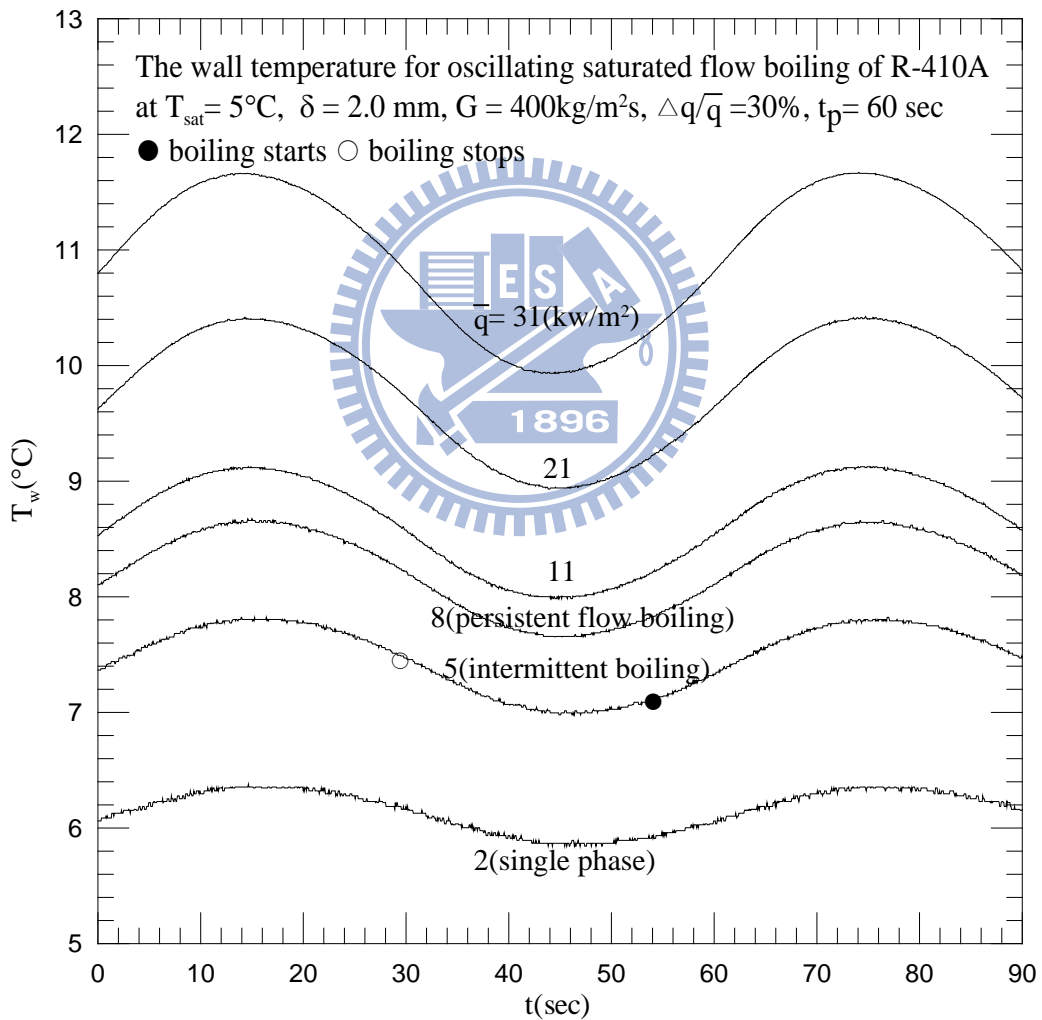
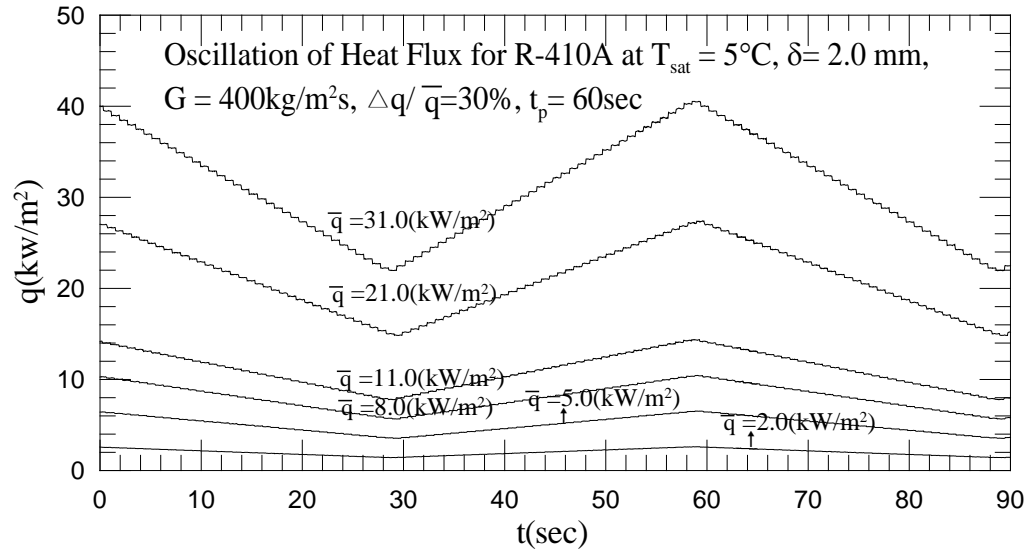


Fig. 5.11 Time variations of imposed heat flux and heat transfer coefficient in time periodic saturated flow boiling of R-410A at  $T_{\text{sat}} = 5^\circ\text{C}$ ,  $\delta = 2.0 \text{ mm}$ ,  $t_p = 60 \text{ sec}$  and  $G = 400 \text{ kg/m}^2\text{s}$  with  $\Delta q/\bar{q} = 30\%$ .

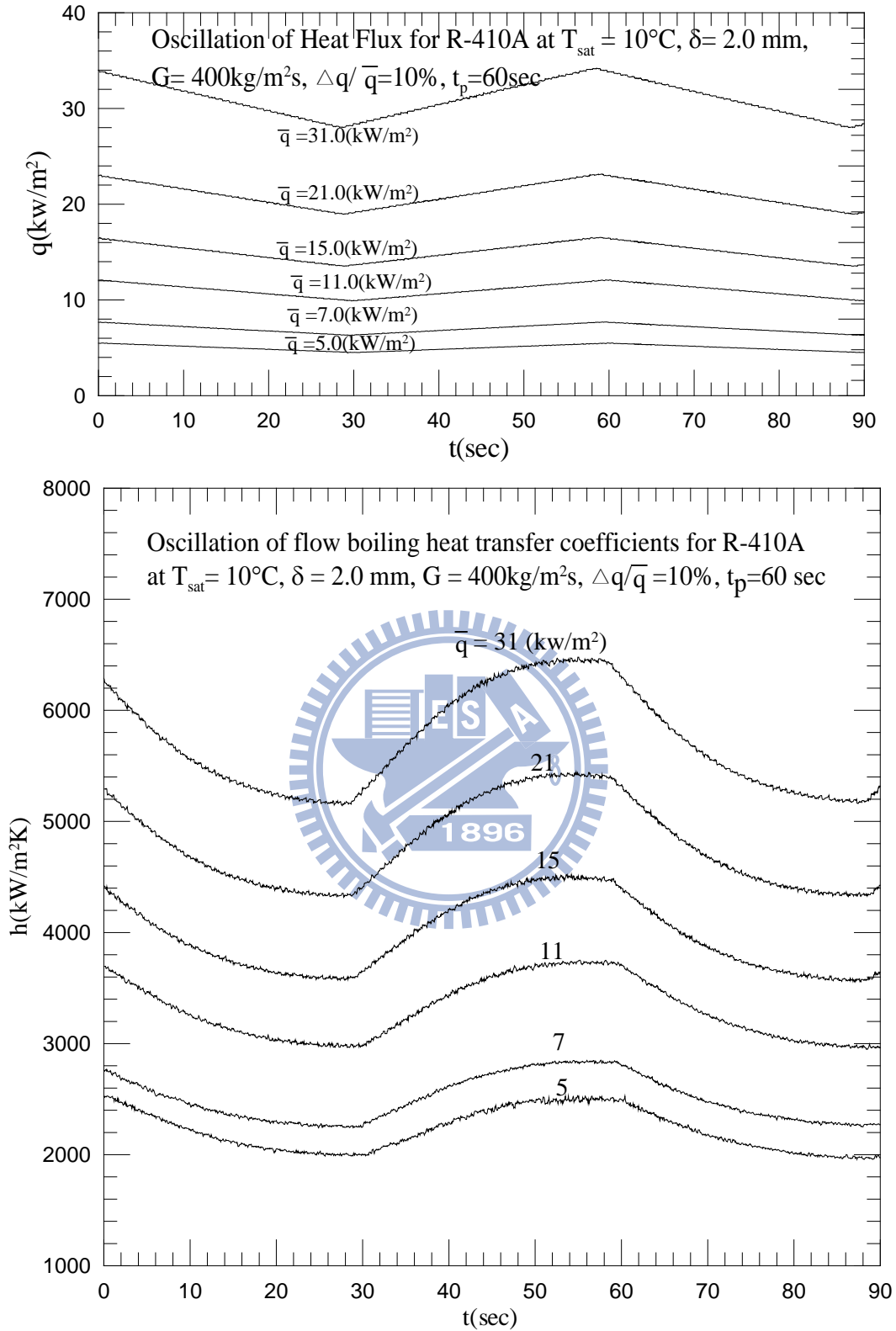


Fig. 5.12 Time variations of imposed heat flux and heat transfer coefficient in time periodic saturated flow boiling of R-410A at  $T_{sat} = 10^{\circ}\text{C}$ ,  $\delta = 2.0 \text{ mm}$ ,  $t_p = 60 \text{ sec}$  and  $G = 400 \text{ kg/m}^2\text{s}$  with  $\Delta q/\bar{q} = 10\%$ .

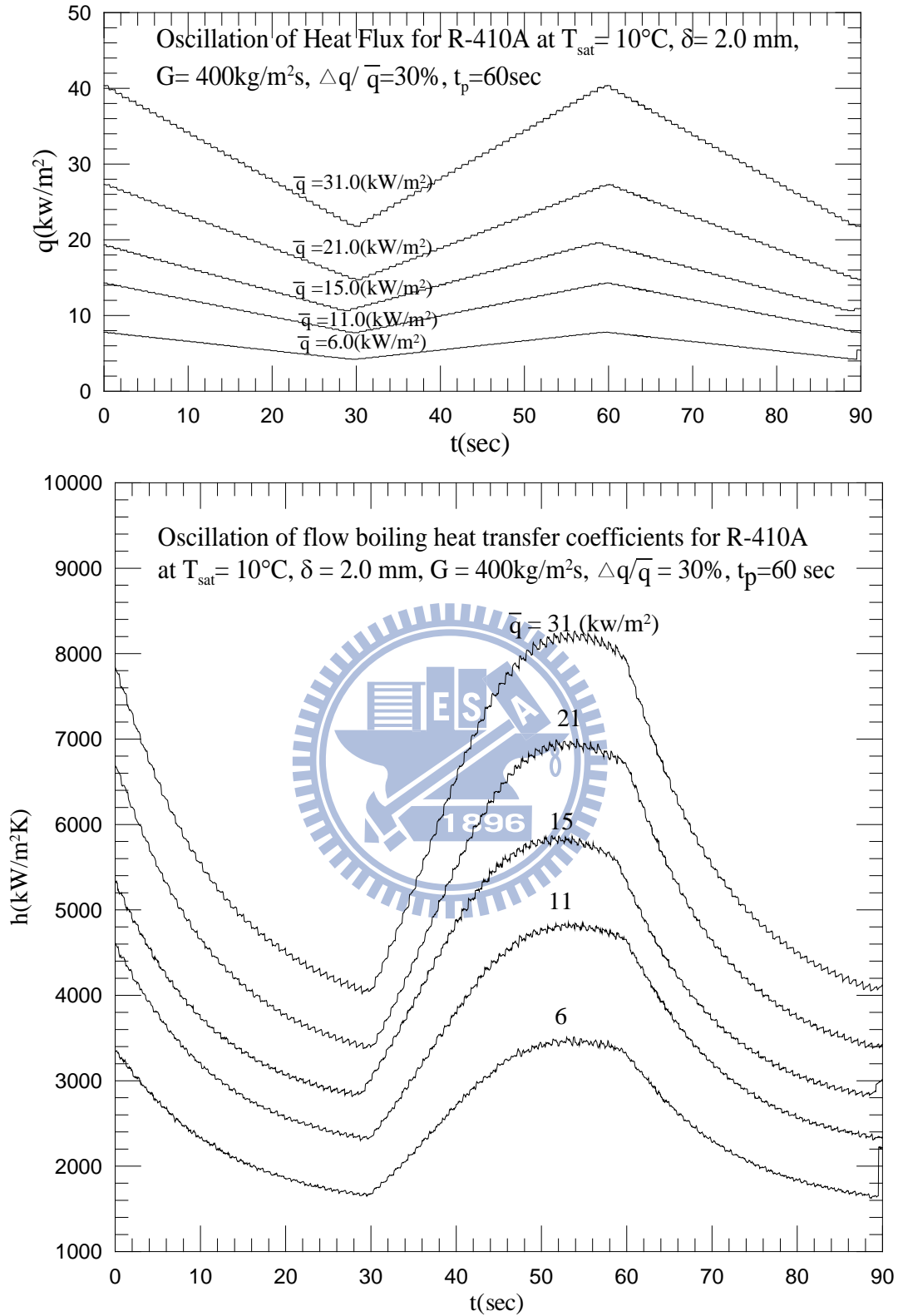


Fig. 5.13 Time variations of imposed heat flux and heat transfer coefficient in time periodic saturated flow boiling of R-410A at  $T_{\text{sat}} = 10^{\circ}\text{C}$ ,  $\delta = 2.0 \text{ mm}$ ,  $t_p = 60 \text{ sec}$  and  $G = 400 \text{ kg/m}^2\text{s}$  with  $\Delta q / \bar{q} = 30\%$ .

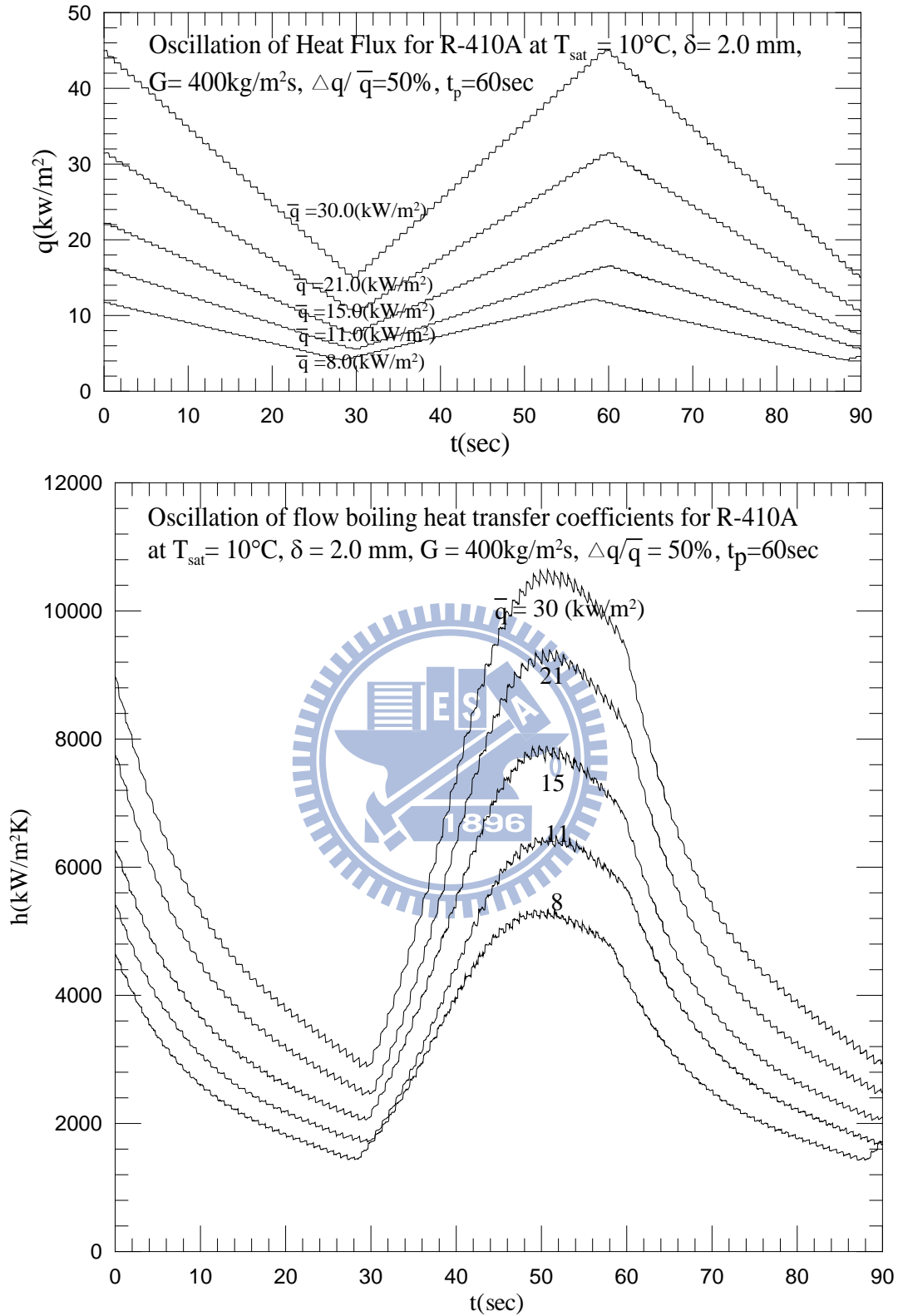


Fig. 5.14 Time variations of imposed heat flux and heat transfer coefficient in time periodic saturated flow boiling of R-410A at  $T_{\text{sat}} = 10^{\circ}\text{C}$ ,  $\delta = 2.0 \text{ mm}$ ,  $t_p = 60 \text{ sec}$  and  $G = 400 \text{ kg/m}^2\text{s}$  with  $\Delta q/\bar{q} = 50\%$ .



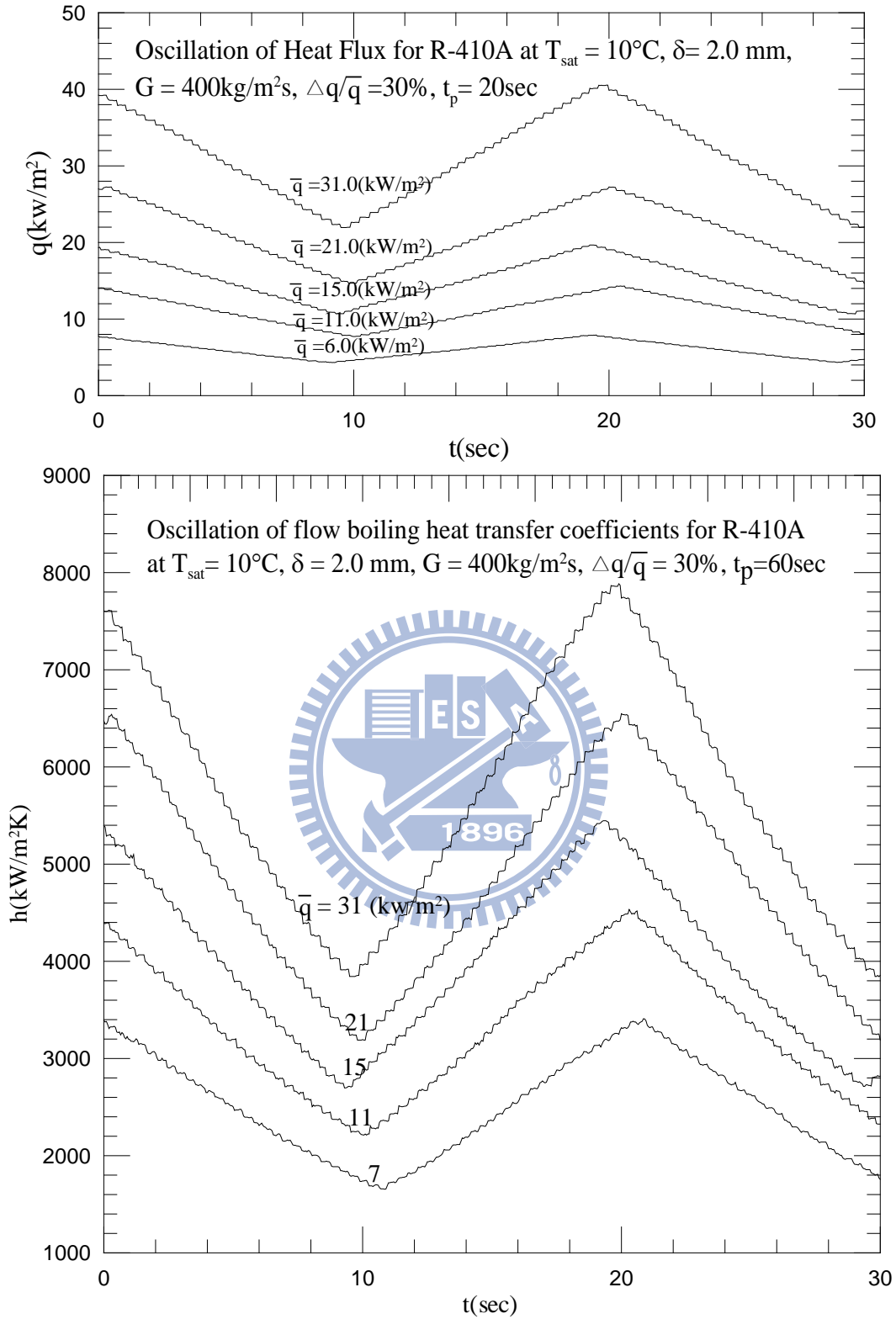


Fig. 5.15 Time variations of imposed heat flux and heat transfer coefficient in time periodic saturated flow boiling of R-410A at  $T_{\text{sat}} = 10^{\circ}\text{C}$ ,  $\delta = 2.0 \text{ mm}$ ,  $t_p = 20 \text{ sec}$  and  $G = 400 \text{ kg/m}^2\text{s}$  with  $\Delta q/\bar{q} = 30\%$ .

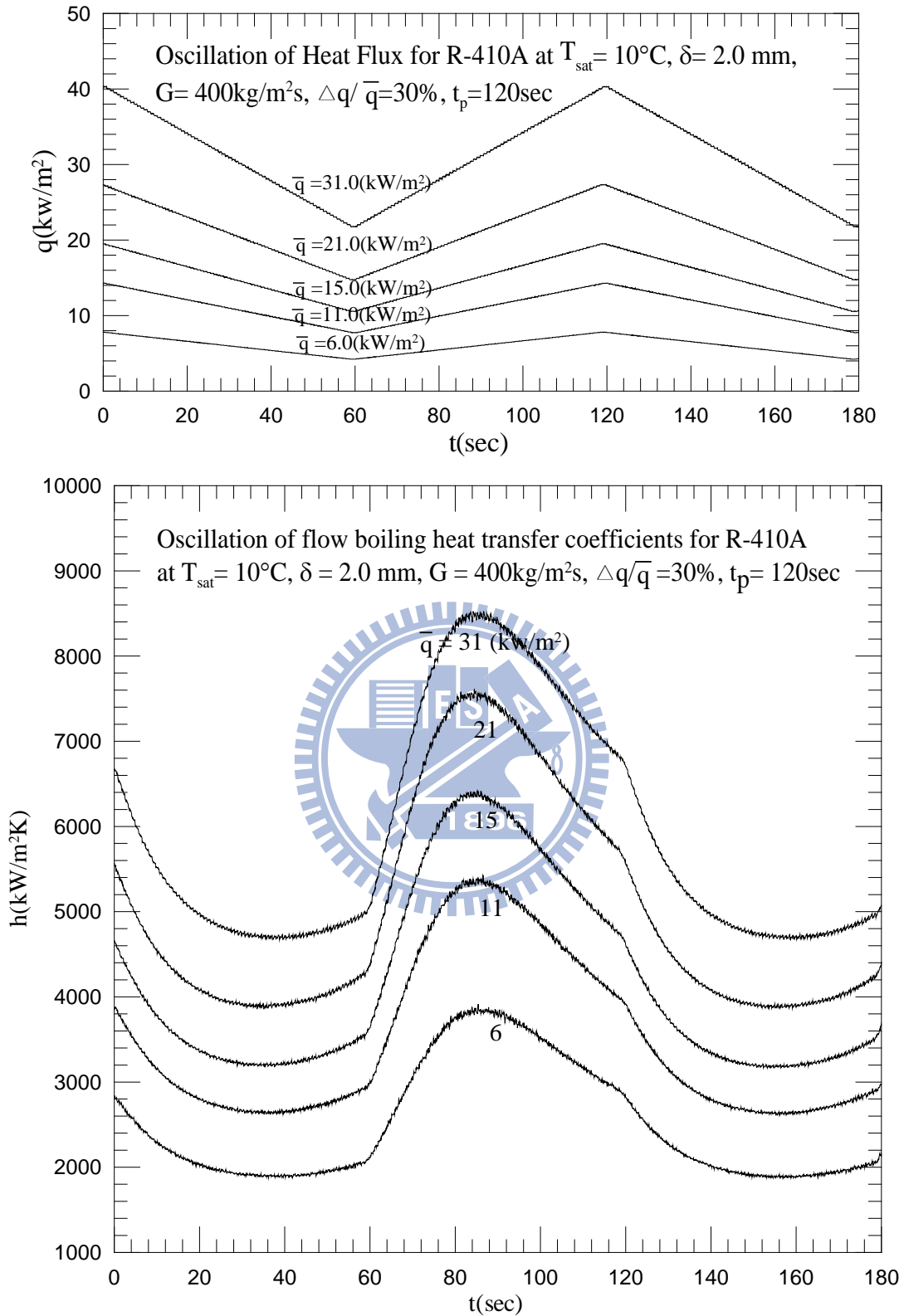


Fig. 5.16 Time variations of imposed heat flux and heat transfer coefficient in time periodic saturated flow boiling of R-410A at  $T_{\text{sat}} = 10^{\circ}\text{C}$ ,  $\delta = 2.0 \text{ mm}$ ,  $t_p = 120 \text{ sec}$  and  $G = 400 \text{ kg/m}^2\text{s}$  with  $\Delta q/\bar{q} = 30\%$ .

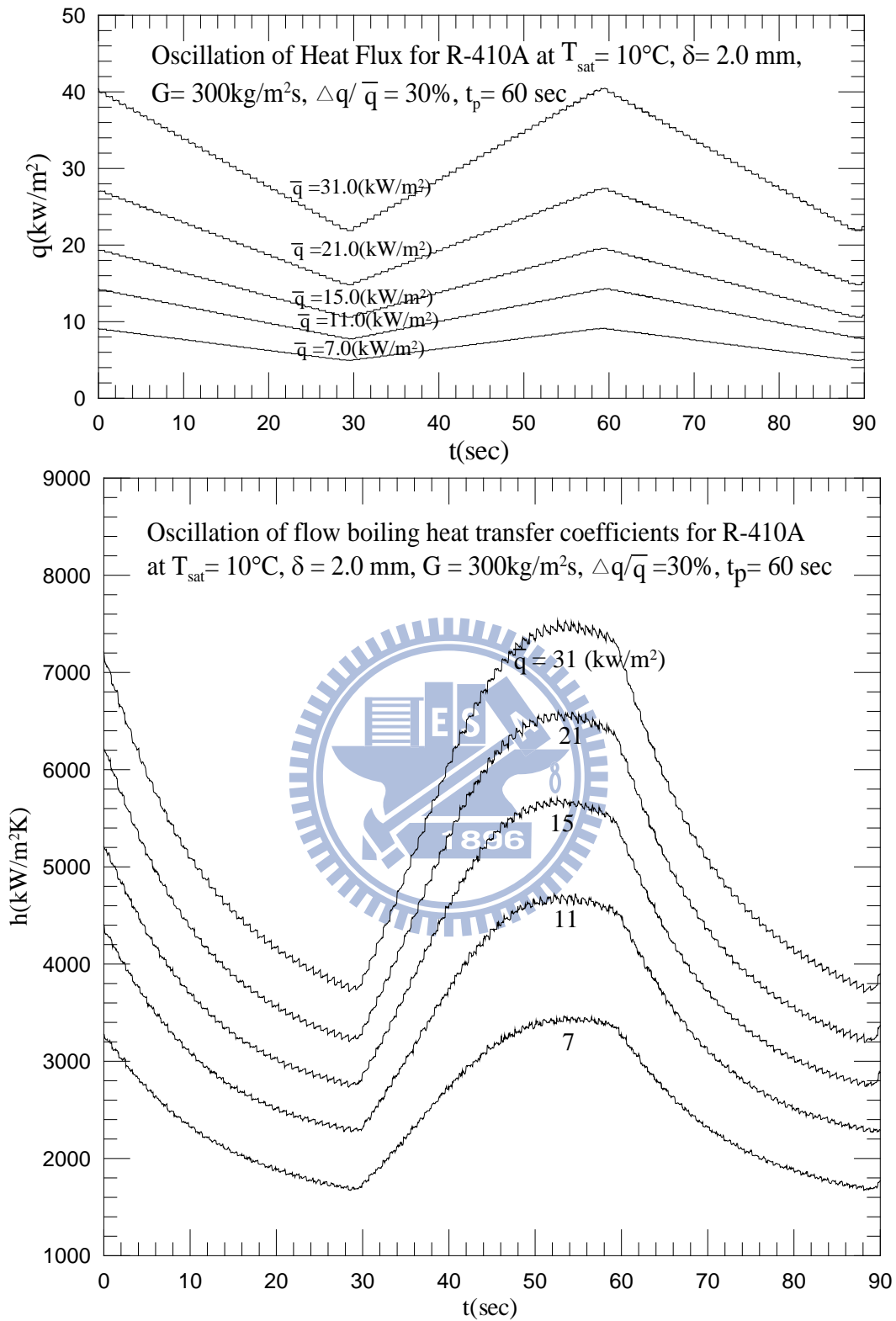


Fig. 5.17 Time variations of imposed heat flux and heat transfer coefficient in time periodic saturated flow boiling of R-410A at  $T_{\text{sat}} = 10^{\circ}\text{C}$ ,  $\delta = 2.0 \text{ mm}$ ,  $t_p = 60 \text{ sec}$  and  $G = 300 \text{ kg/m}^2\text{s}$  with  $\Delta q / \bar{q} = 30\%$ .

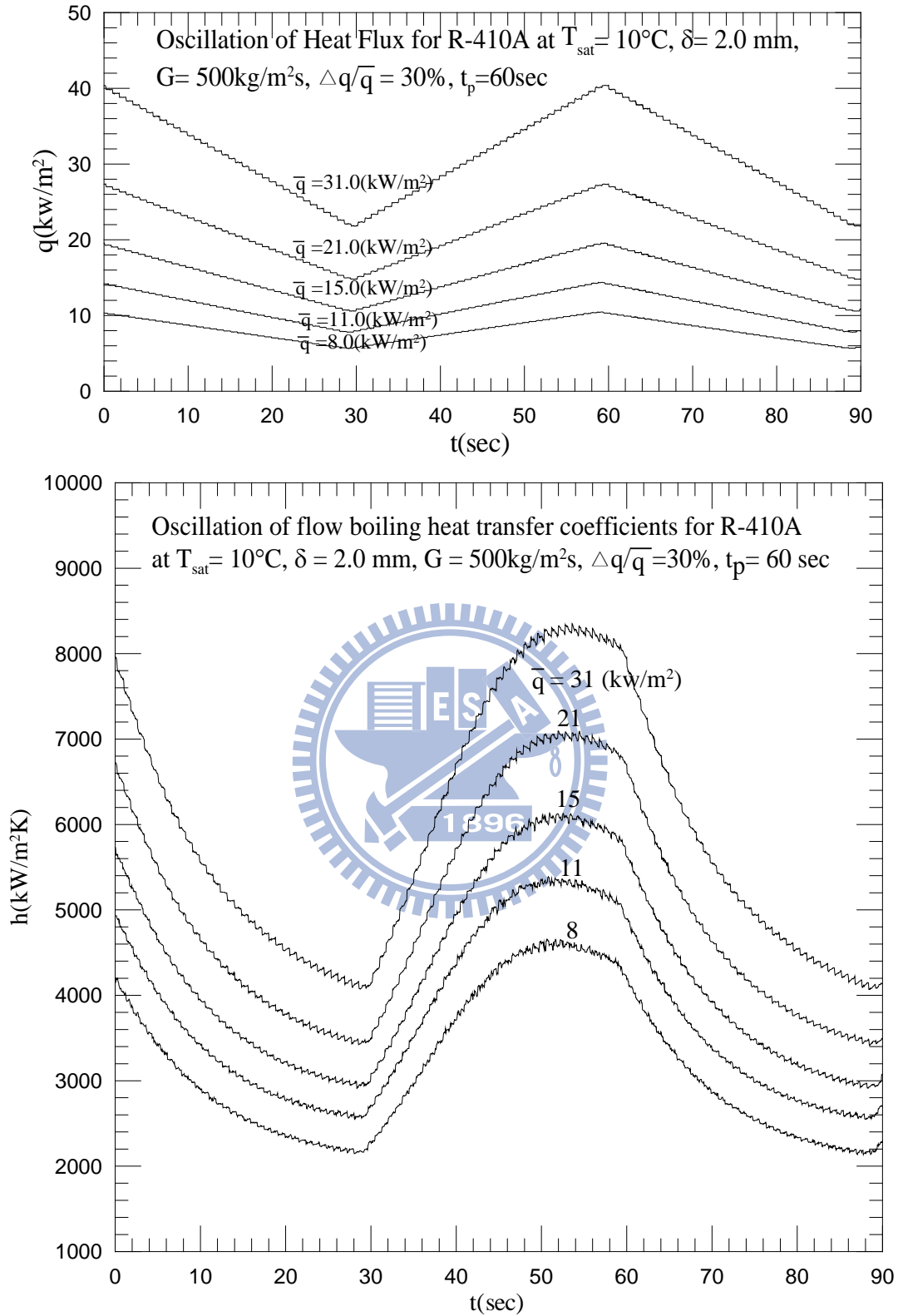


Fig. 5.18 Time variations of imposed heat flux and heat transfer coefficient in time periodic saturated flow boiling of R-410A at  $T_{\text{sat}} = 10^{\circ}\text{C}$ ,  $\delta = 2.0 \text{ mm}$ ,  $t_p = 60 \text{ sec}$  and  $G = 500 \text{ kg/m}^2\text{s}$  with  $\Delta q/\bar{q} = 30\%$ .

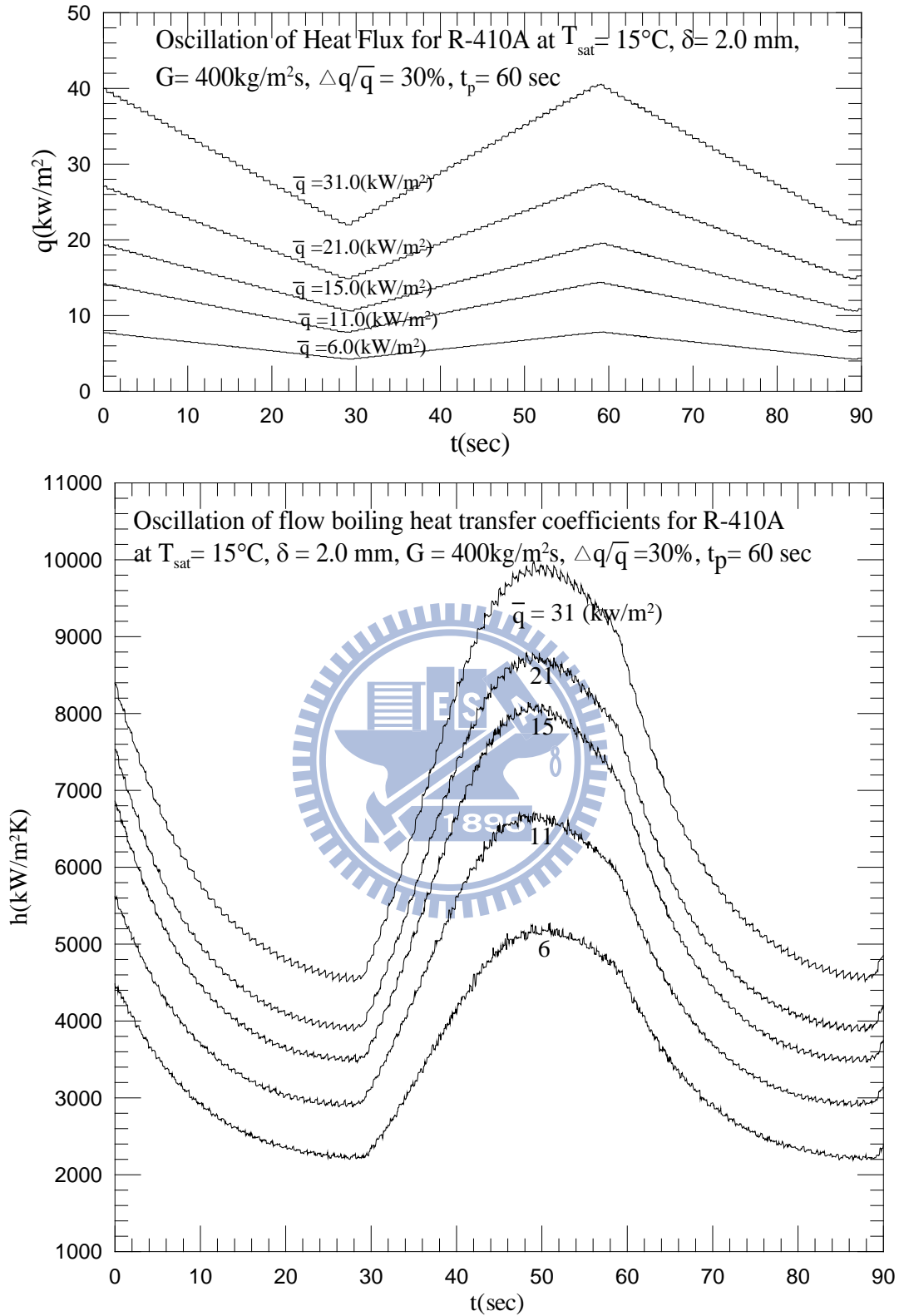


Fig. 5.19 Time variations of imposed heat flux and heat transfer coefficient in time periodic saturated flow boiling of R-410A at  $T_{\text{sat}} = 15^\circ\text{C}$ ,  $\delta = 2.0 \text{ mm}$ ,  $t_p = 60 \text{ sec}$  and  $G = 400 \text{ kg/m}^2\text{s}$  with  $\Delta q/\bar{q} = 30\%$ .

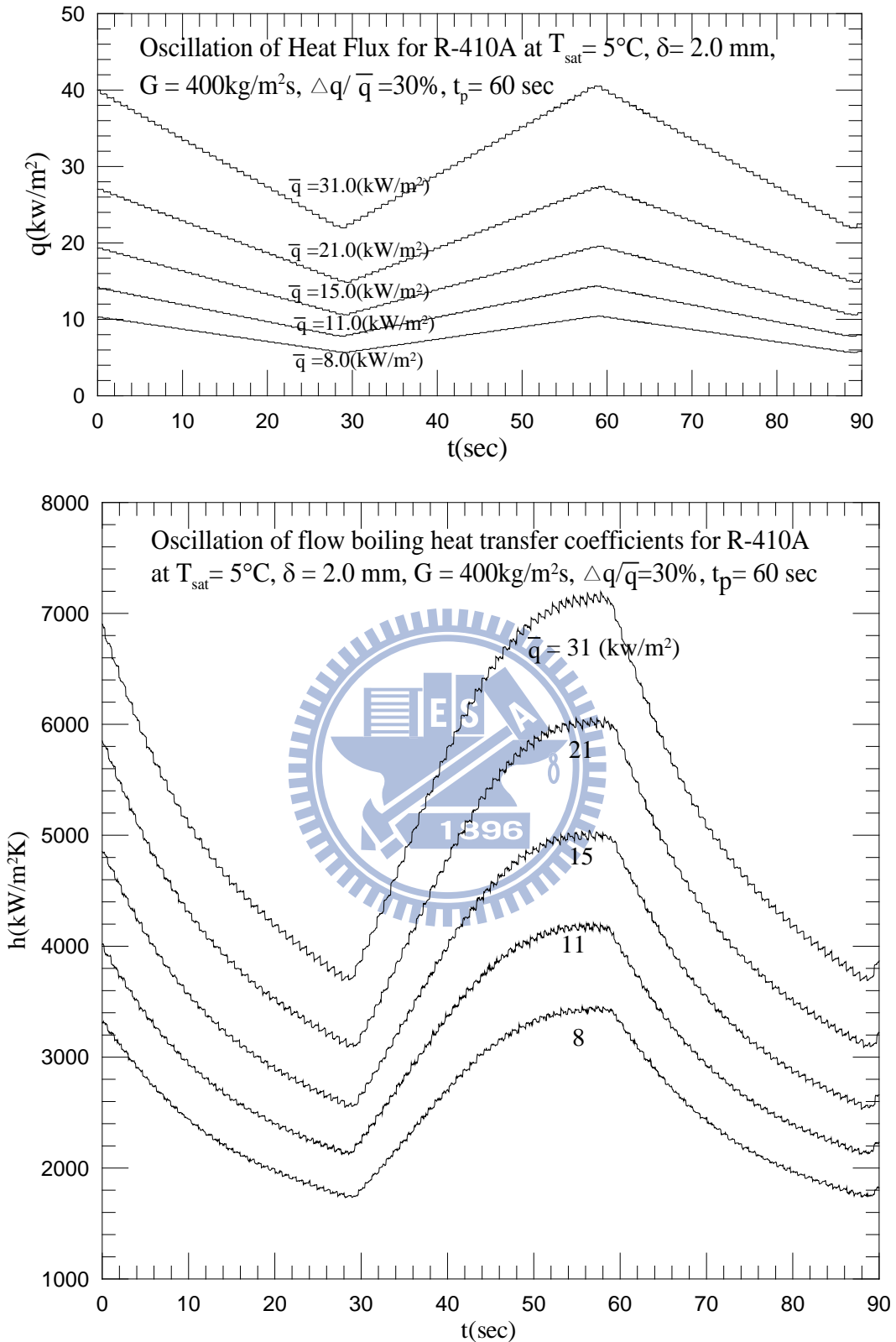


Fig. 5.20 Time variations of imposed heat flux and heat transfer coefficient in time periodic saturated flow boiling of R-410A at  $T_{\text{sat}} = 5^\circ\text{C}$ ,  $\delta = 2.0 \text{ mm}$ ,  $t_p = 60 \text{ sec}$  and  $G = 400 \text{ kg/m}^2\text{s}$  with  $\Delta q/\bar{q} = 30\%$ .

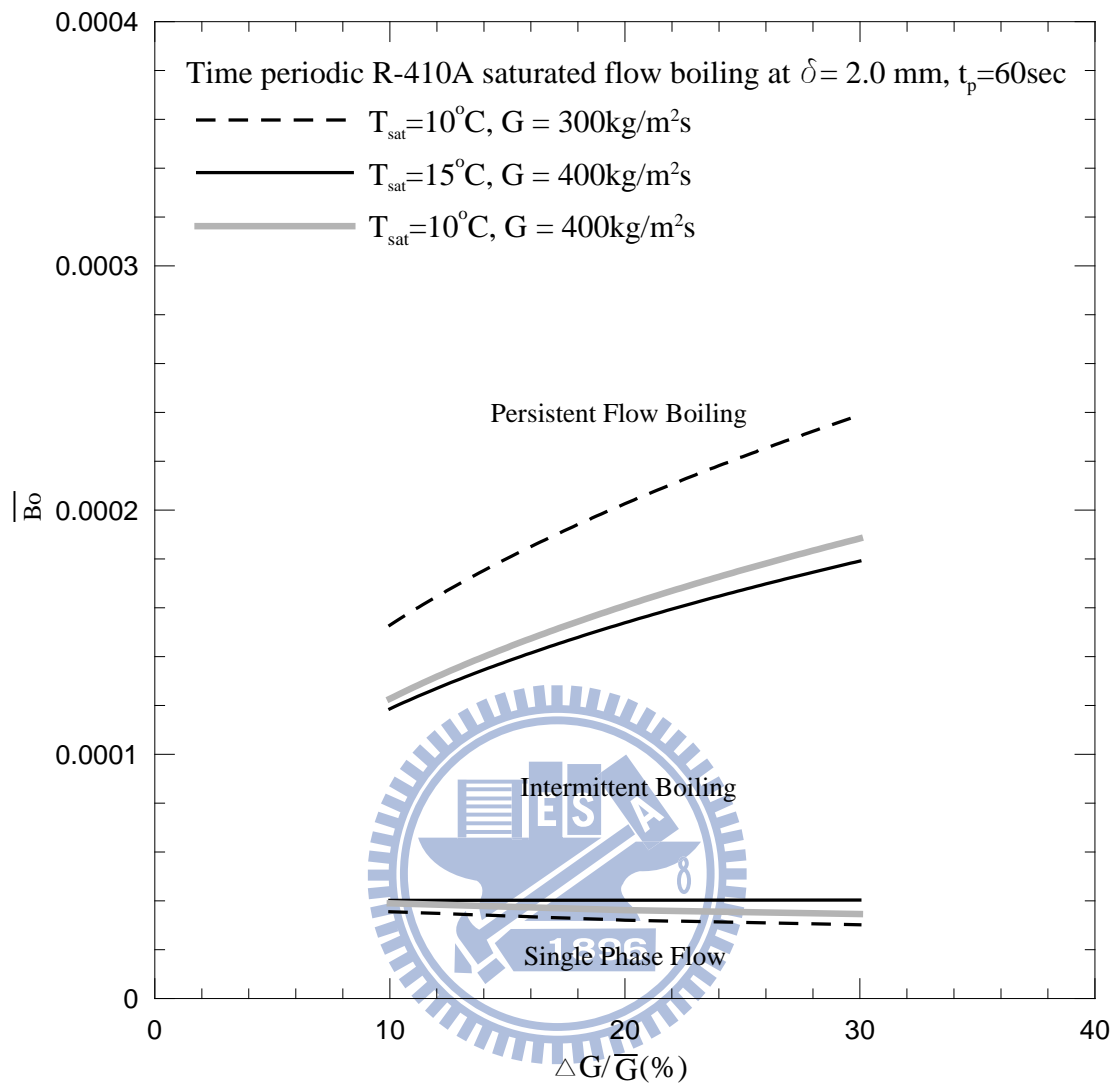


Fig. 5.21 Flow regime map for time periodic R-410A flow boiling regimes at  $\delta = 2\text{mm}$  and  $t_p = 60$  sec for various saturated temperatures and mass fluxes.

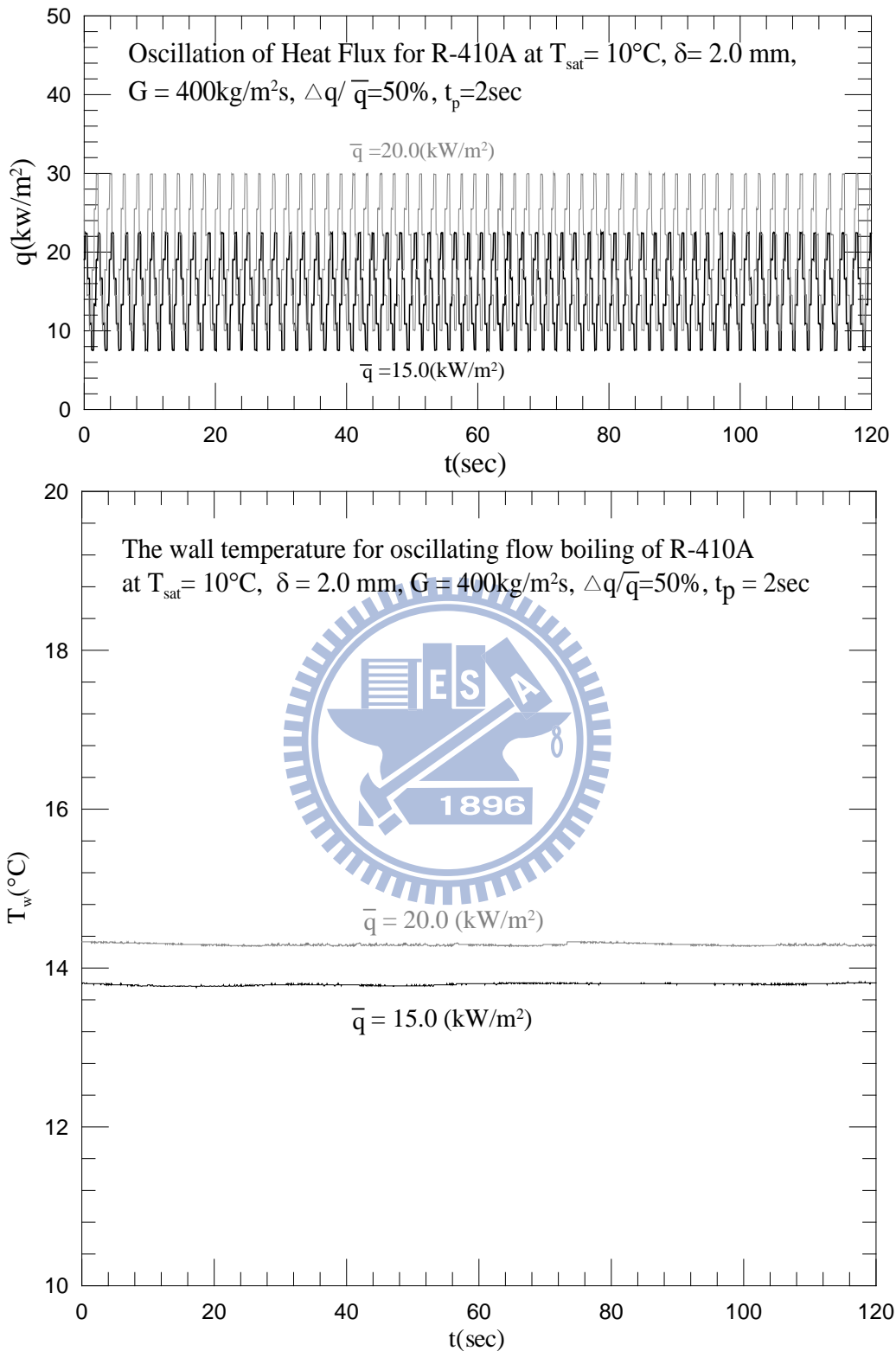


Fig. 5.22 Time variations of imposed heat flux and wall temperature at  $z = 80 \text{ mm}$  for  $t_p = 2 \text{ sec}$ .



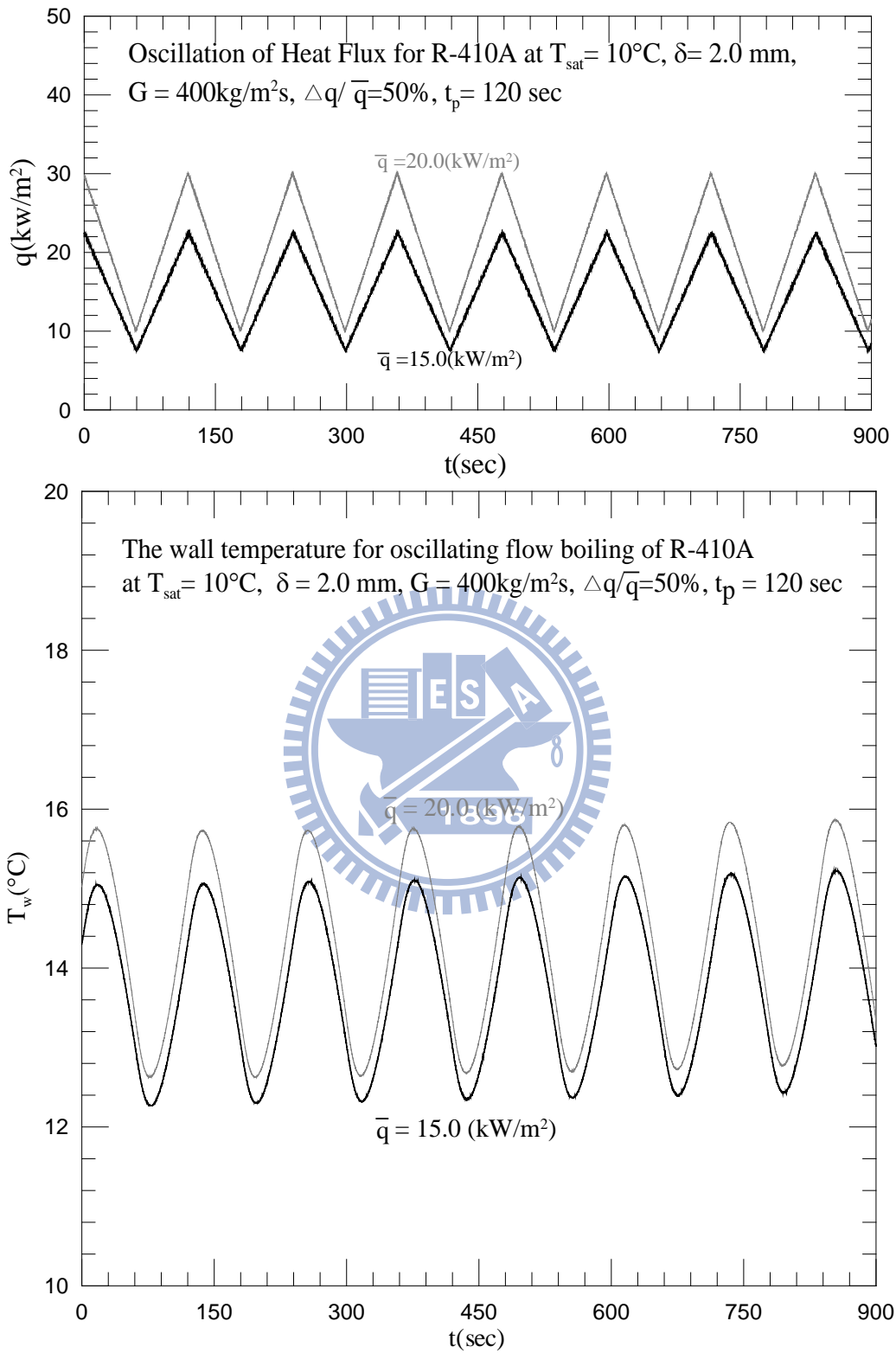


Fig. 5.23 Time variations of imposed heat flux and wall temperature at  $z = 80$  mm for  $t_p = 120$  sec.

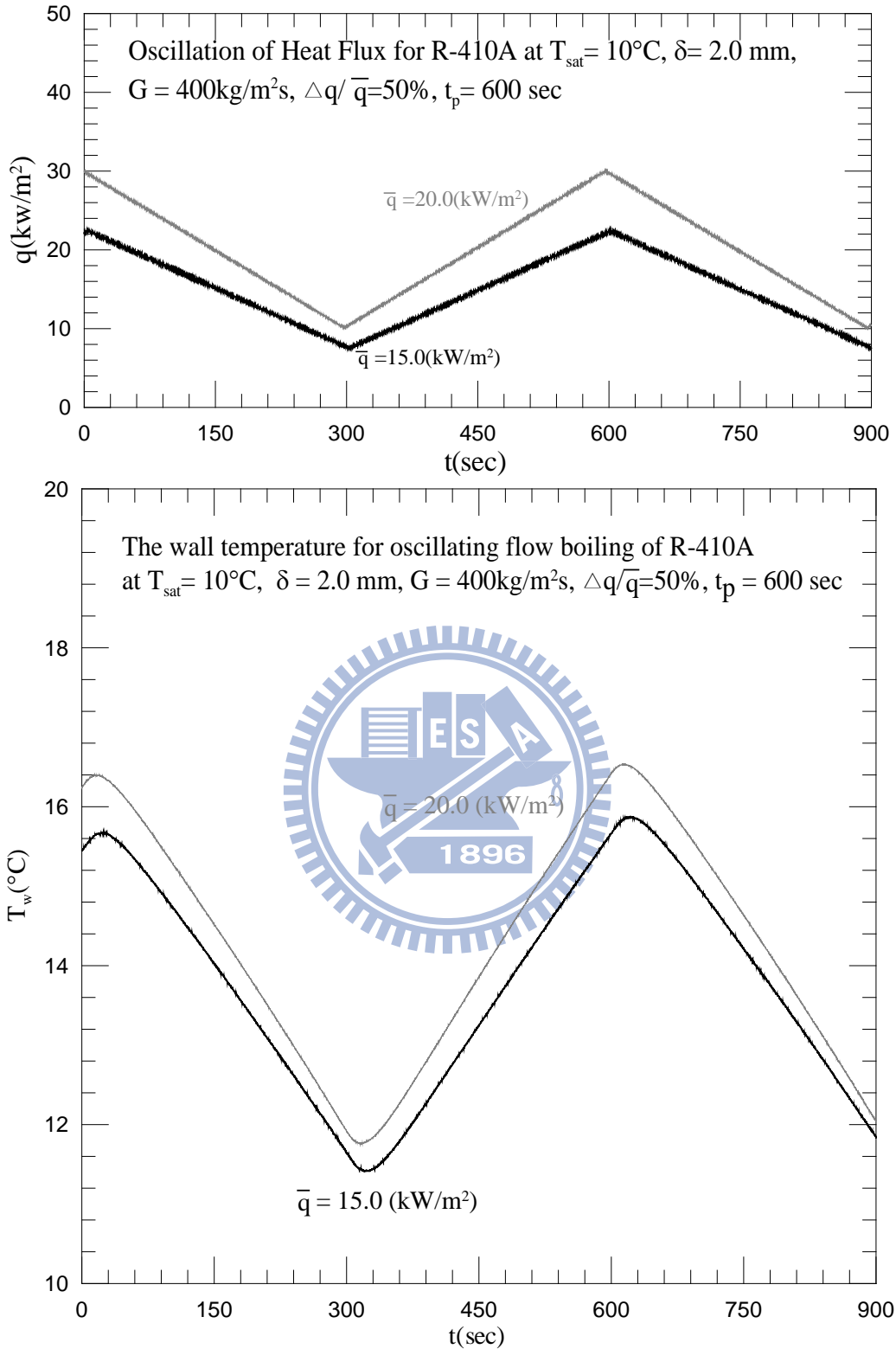


Fig. 5.24 Time variations of imposed heat flux and wall temperature at  $z = 80 \text{ mm}$  for  $t_p = 600 \text{ sec}$ .

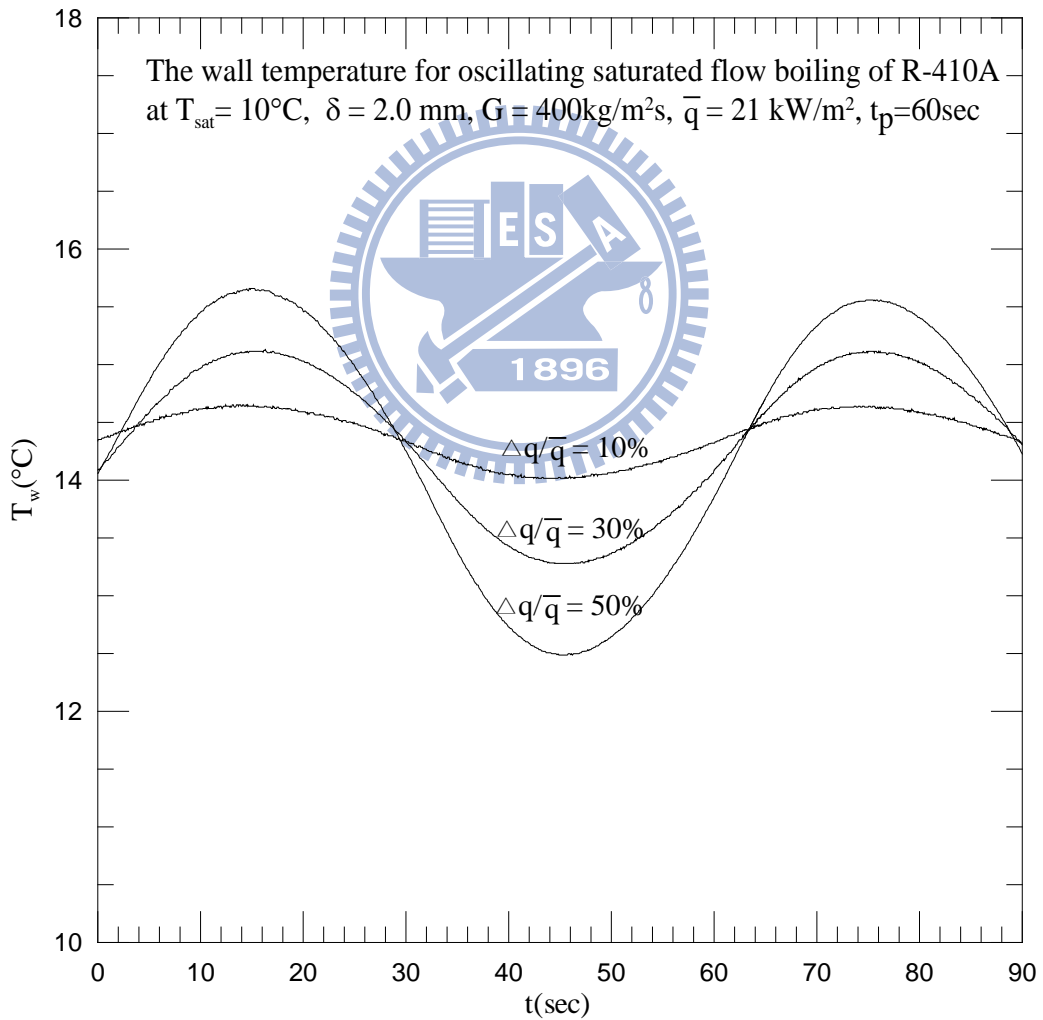
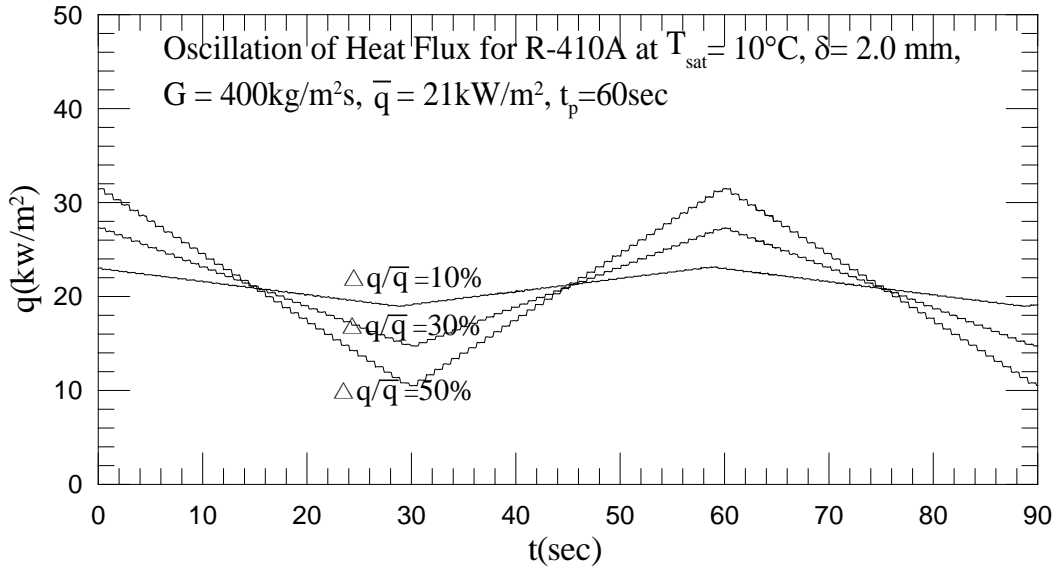


Fig. 5.25 Time variations of imposed heat flux and wall temperature at  $z = 80 \text{ mm}$  for various  $\Delta q/\bar{q}$ .

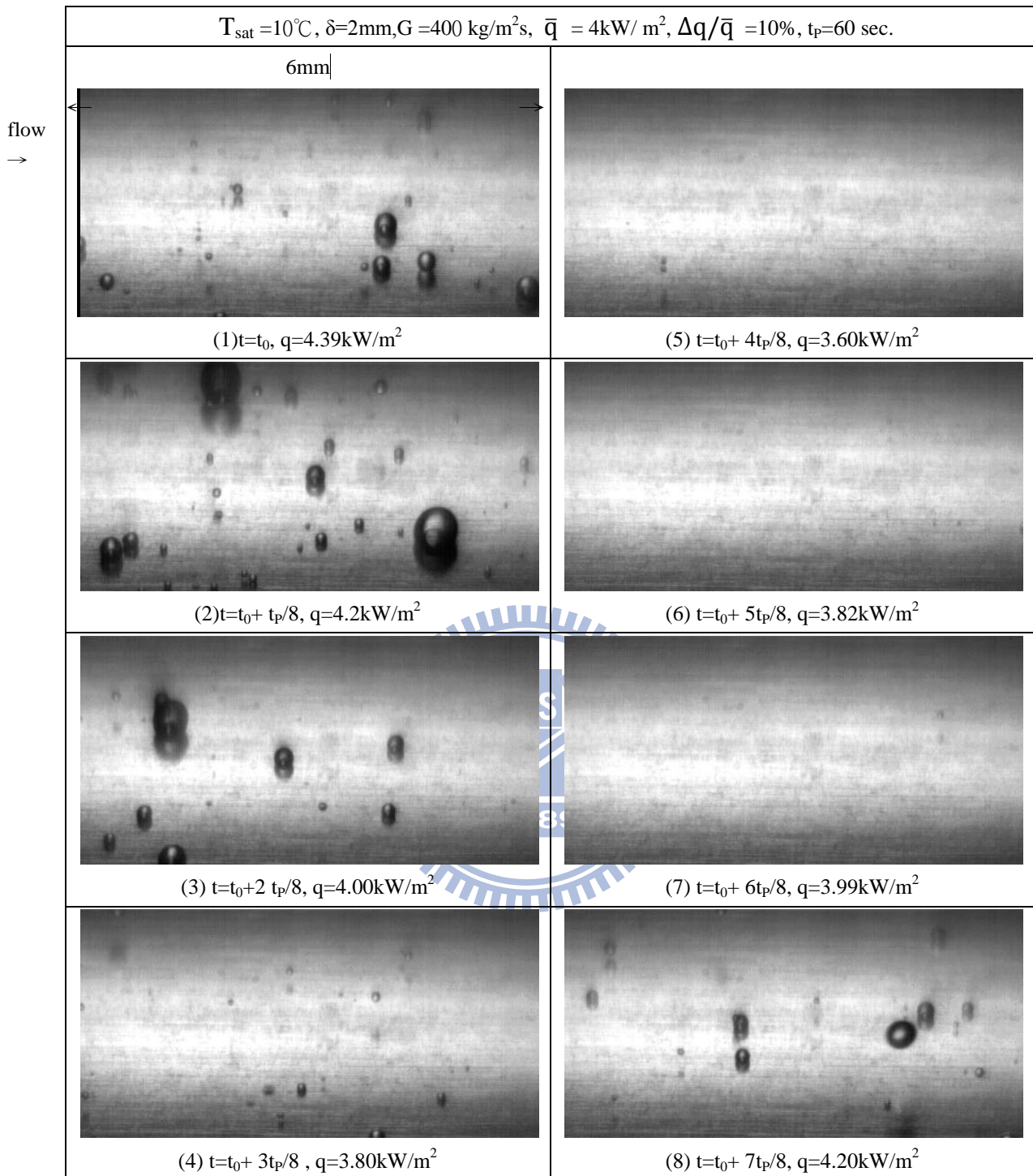


Fig. 5.26 Photos of time periodic intermittent flow boiling of R-410A at selected time instants in a typical periodic cycle at  $T_{\text{sat}} = 10^\circ\text{C}$ ,  $G = 400 \text{ kg/m}^2\text{s}$ ,  $\delta = 2.0\text{mm}$  and  $t_p = 60 \text{ sec}$  for  $\bar{q} = 4\text{kW/m}^2$ ,  $\Delta q/\bar{q} = 10\%$ .

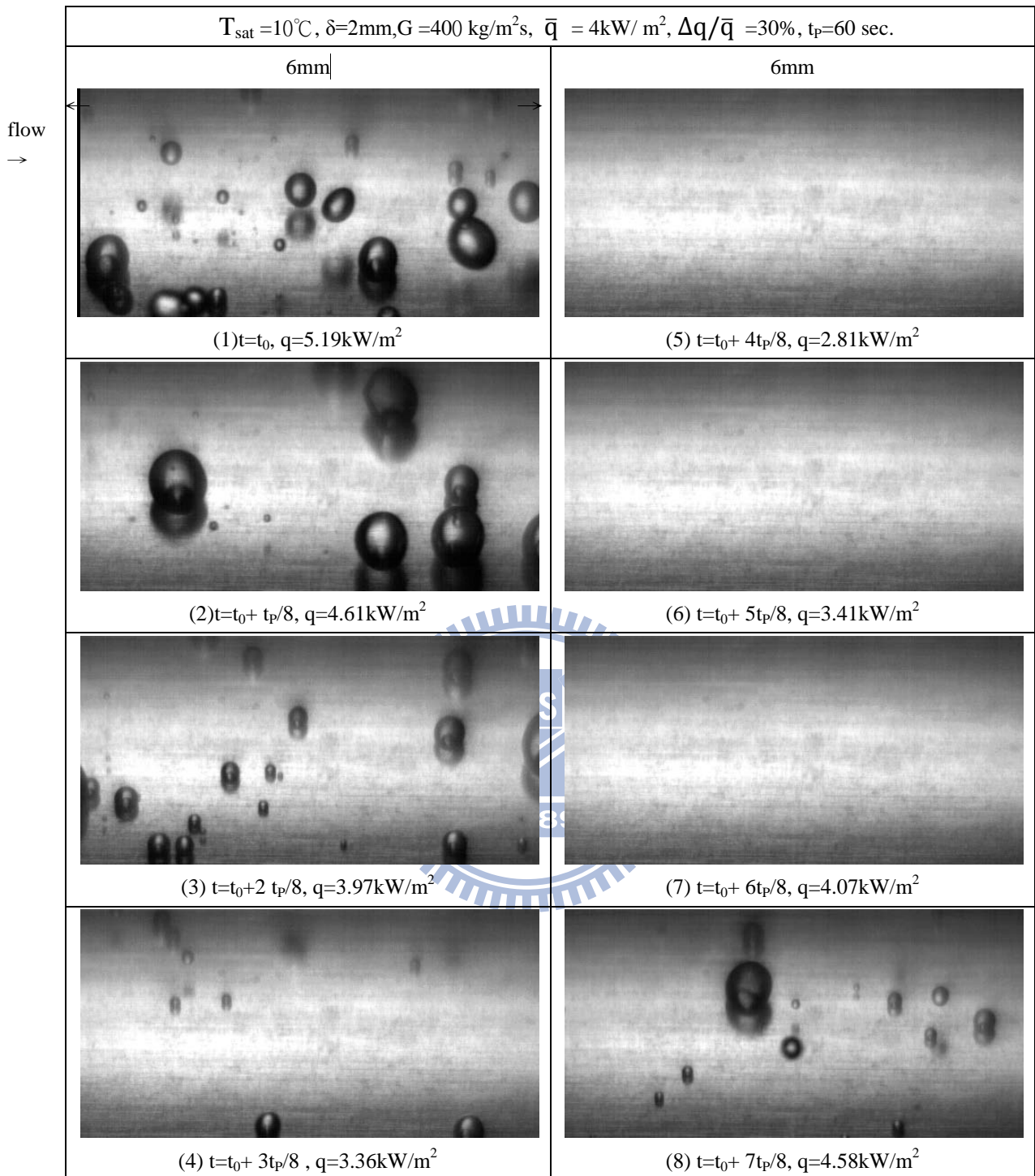


Fig. 5.27 Photos of time periodic intermittent flow boiling of R-410A at selected time instants in a typical periodic cycle at  $T_{\text{sat}} = 10^\circ\text{C}$ ,  $G = 400 \text{ kg/m}^2\text{s}$ ,  $\delta = 2.0\text{mm}$  and  $t_p = 60 \text{ sec}$  for  $\bar{q} = 4\text{kW/m}^2$ ,  $\Delta q/\bar{q} = 30\%$ .

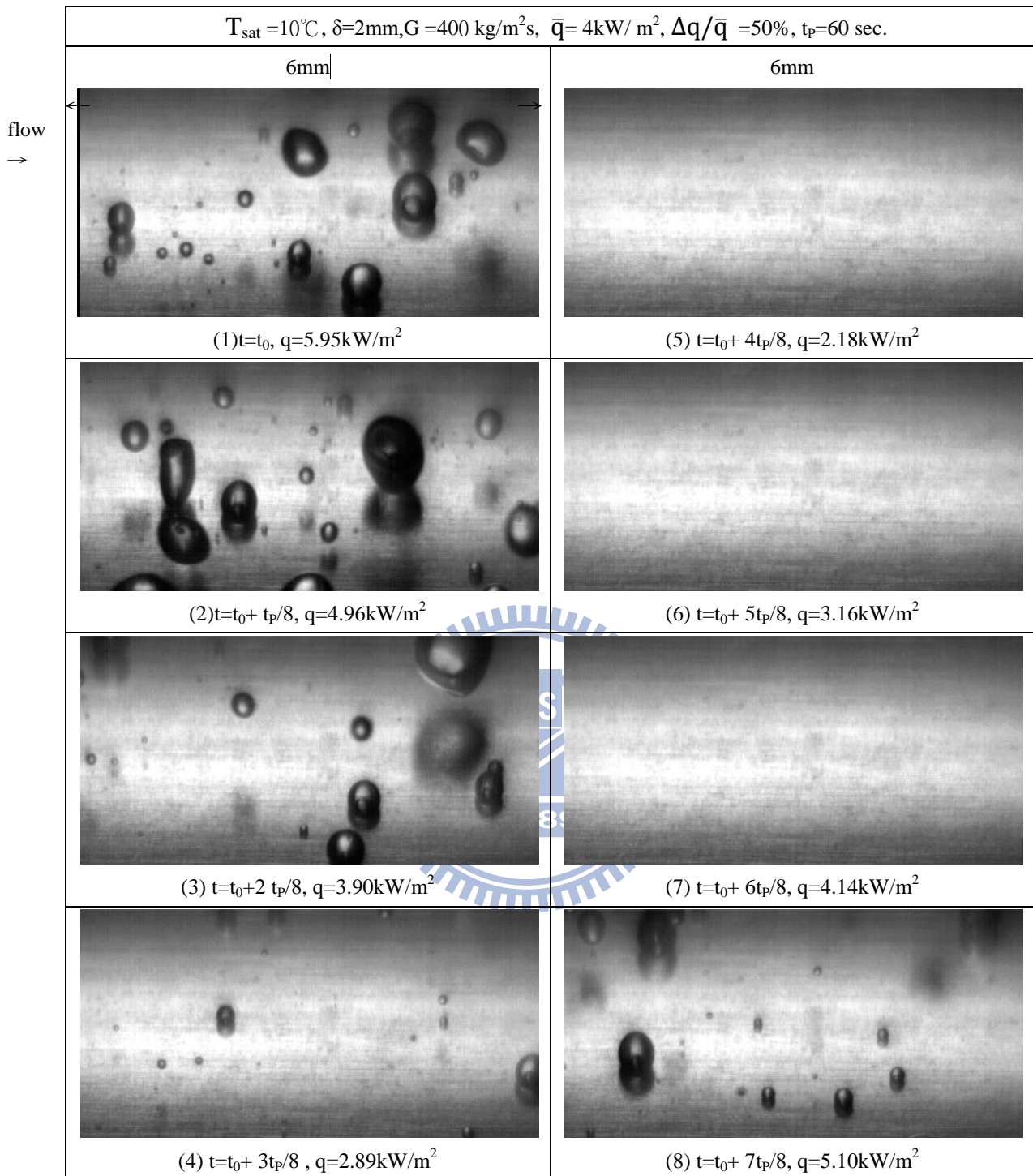


Fig. 5.28 Photos of time periodic intermittent flow boiling of R-410A at selected time instants in a typical periodic cycle at  $T_{\text{sat}} = 10^\circ\text{C}$ ,  $G = 400 \text{ kg/m}^2\text{s}$ ,  $\delta = 2.0\text{mm}$  and  $t_p = 60 \text{ sec}$  for  $\bar{q} = 4 \text{ kW/m}^2$ ,  $\Delta q/\bar{q} = 50\%$ .



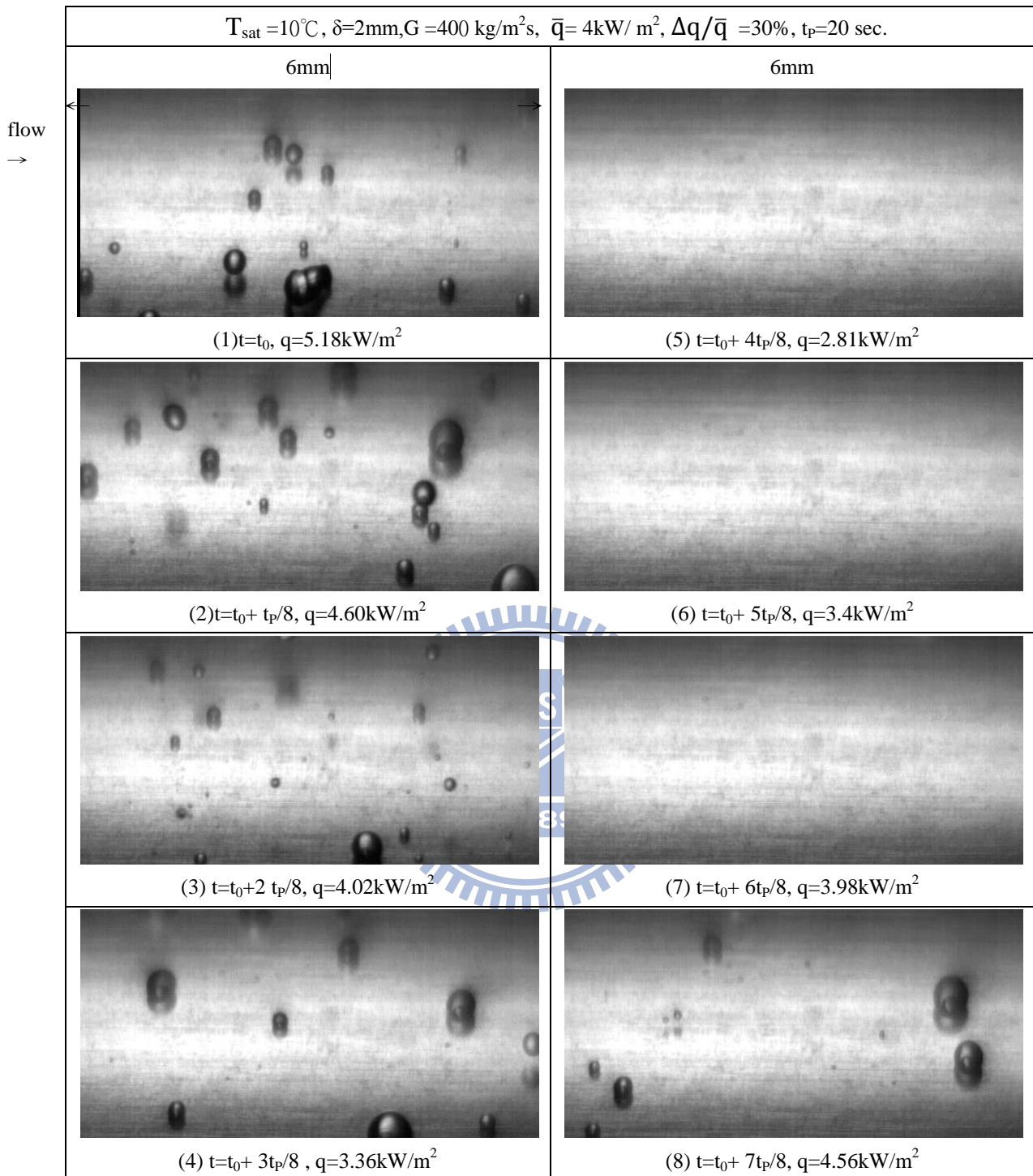


Fig. 5.29 Photos of time periodic intermittent flow boiling of R-410A at selected time instants in a typical periodic cycle at  $T_{\text{sat}} = 10^\circ\text{C}$ ,  $G = 400 \text{ kg/m}^2\text{s}$ ,  $\delta = 2.0\text{mm}$  and  $t_p = 20 \text{ sec}$  for  $\bar{q} = 4\text{kW/m}^2$ ,  $\Delta q/\bar{q} = 30\%$ .

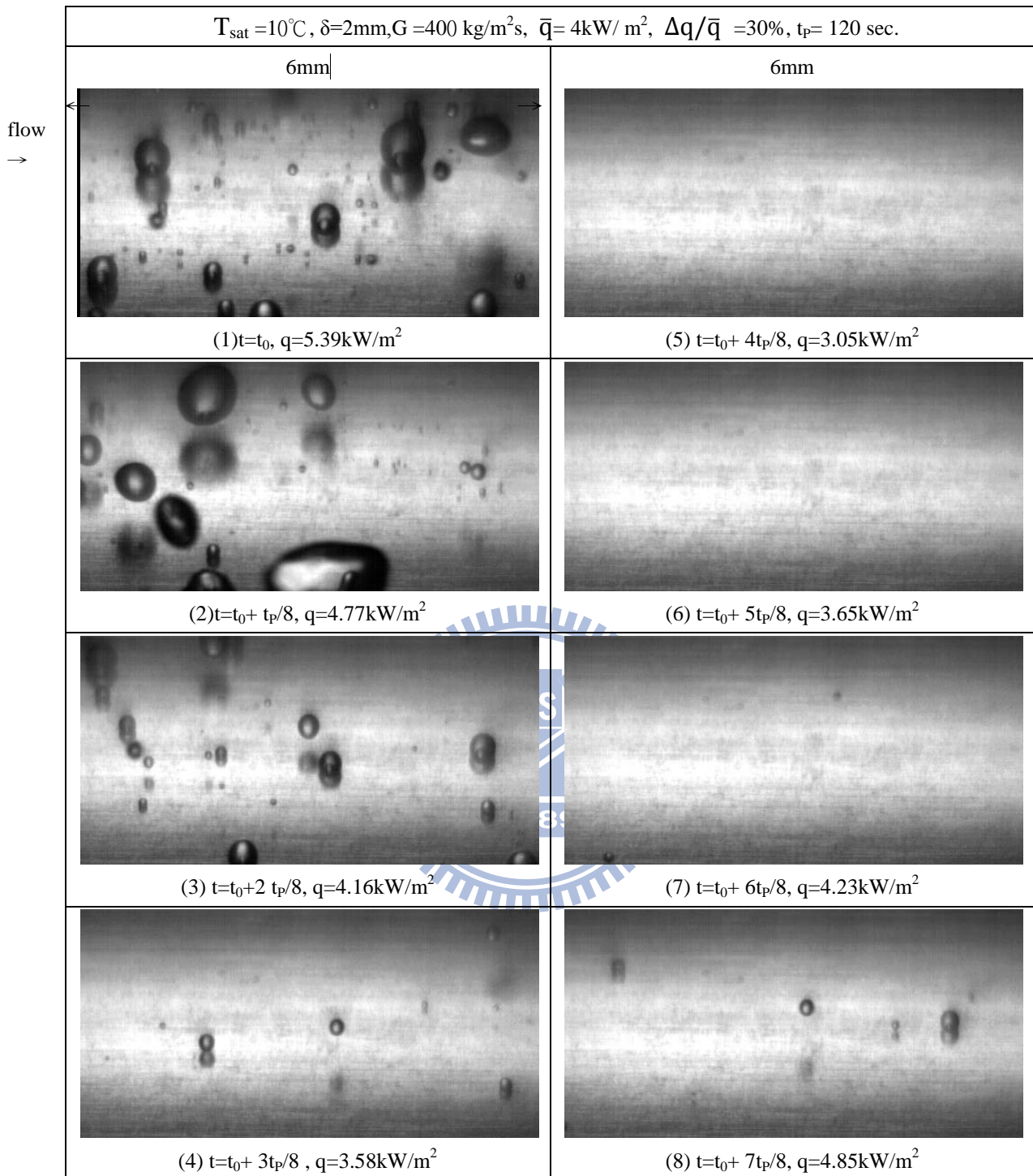


Fig. 5.30 Photos of time periodic intermittent flow boiling of R-410A at selected time instants in a typical periodic cycle at  $T_{\text{sat}} = 10^\circ\text{C}$ ,  $G = 400 \text{ kg/m}^2\text{s}$ ,  $\delta = 2.0\text{mm}$  and  $t_p = 120 \text{ sec}$  for  $\bar{q} = 4\text{kW/m}^2$ ,  $\Delta q/\bar{q} = 30\%$ .



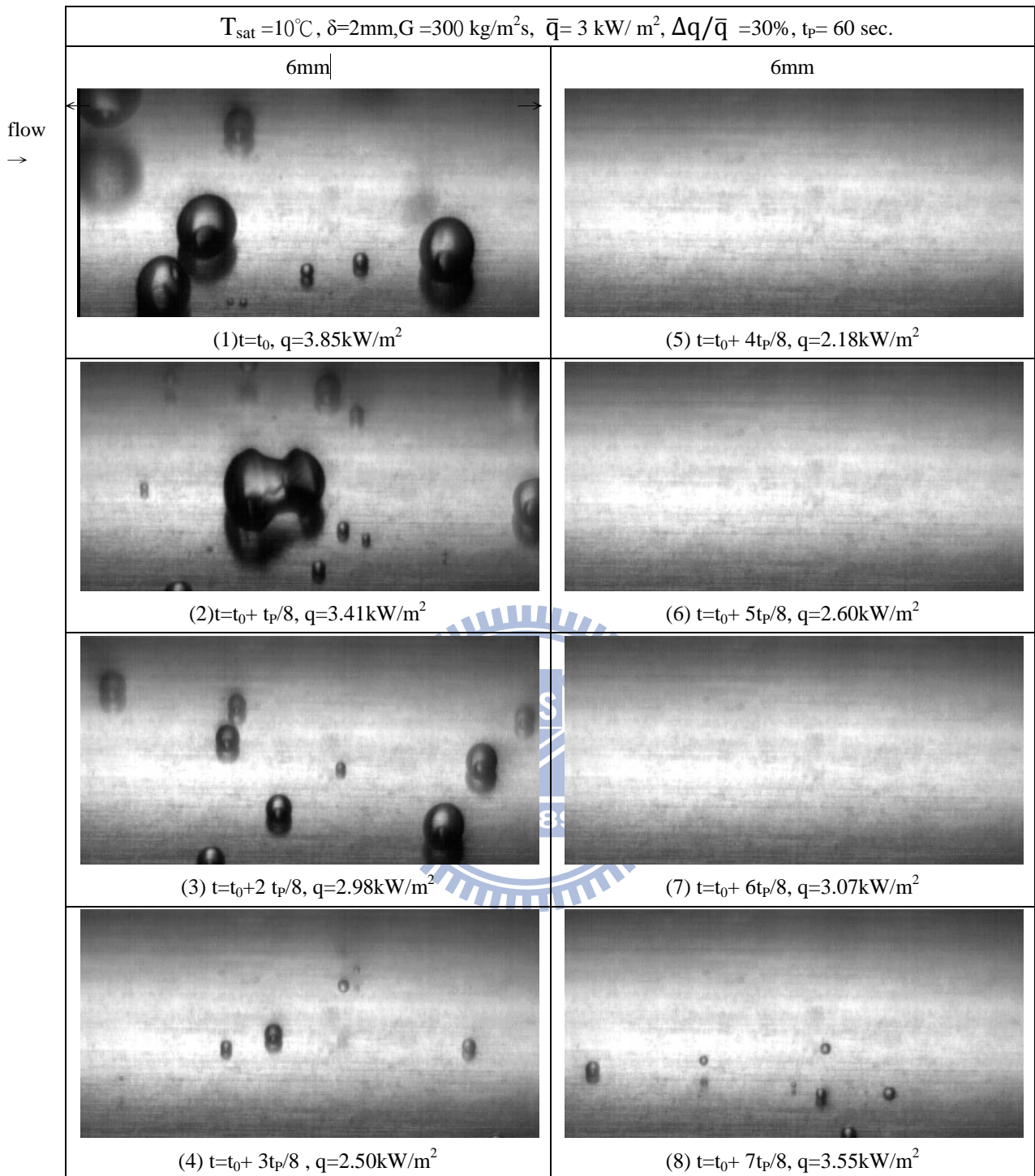


Fig. 5.31 Photos of time periodic intermittent flow boiling of R-410A at selected time instants in a typical periodic cycle at  $T_{\text{sat}} = 10^\circ\text{C}$ ,  $G = 400 \text{ kg/m}^2\text{s}$ ,  $\delta = 2.0\text{mm}$  and  $t_p = 60 \text{ sec}$  for  $\bar{q} = 3\text{kW/m}^2$ ,  $\Delta q/\bar{q} = 30\%$ .

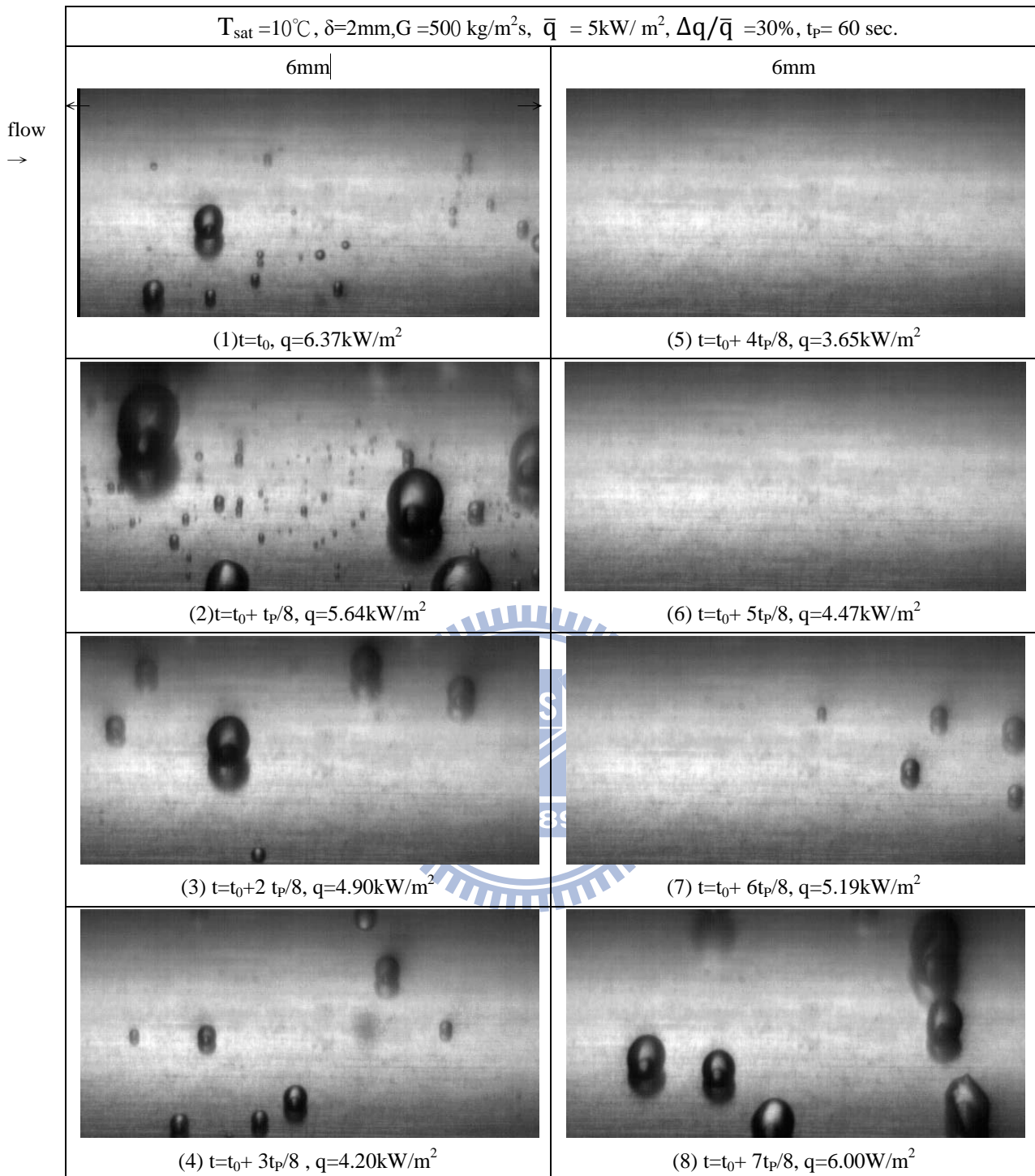


Fig. 5.32 Photos of time periodic intermittent flow boiling of R-410A at selected time instants in a typical periodic cycle at  $T_{\text{sat}} = 10^\circ\text{C}$ ,  $G = 400 \text{ kg/m}^2\text{s}$ ,  $\delta = 2.0\text{mm}$  and  $t_p = 60 \text{ sec}$  for  $\bar{q} = 5 \text{ kW/m}^2$ ,  $\Delta q/\bar{q} = 30\%$ .

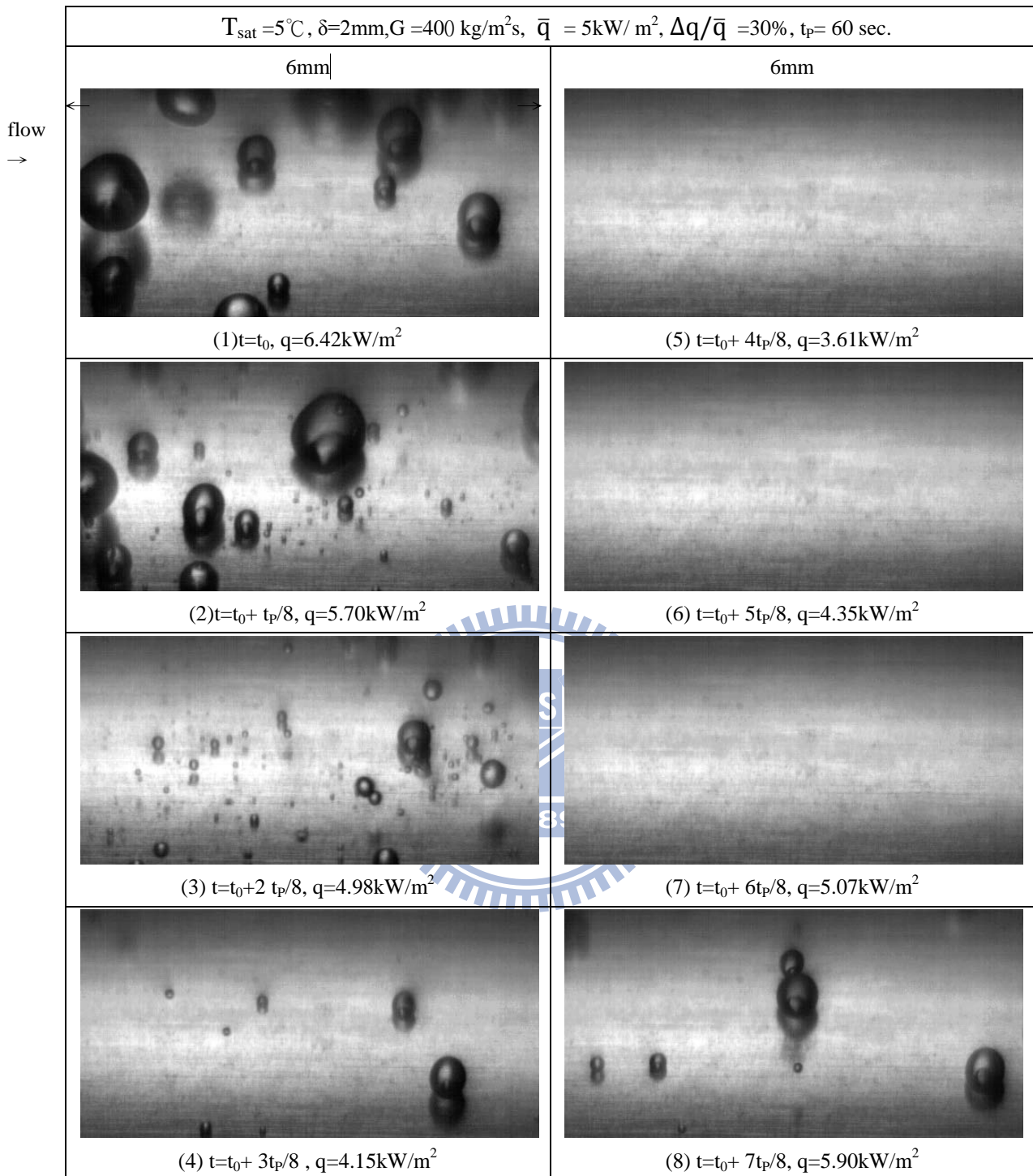


Fig. 5.33 Photos of time periodic intermittent flow boiling of R-410A at selected time instants in a typical periodic cycle at  $T_{\text{sat}} = 5^\circ\text{C}$ ,  $G = 400 \text{ kg/m}^2\text{s}$ ,  $\delta = 2.0\text{mm}$  and  $t_p = 60 \text{ sec}$  for  $\bar{q} = 5\text{kW/m}^2$ ,  $\Delta q/\bar{q} = 30\%$ .

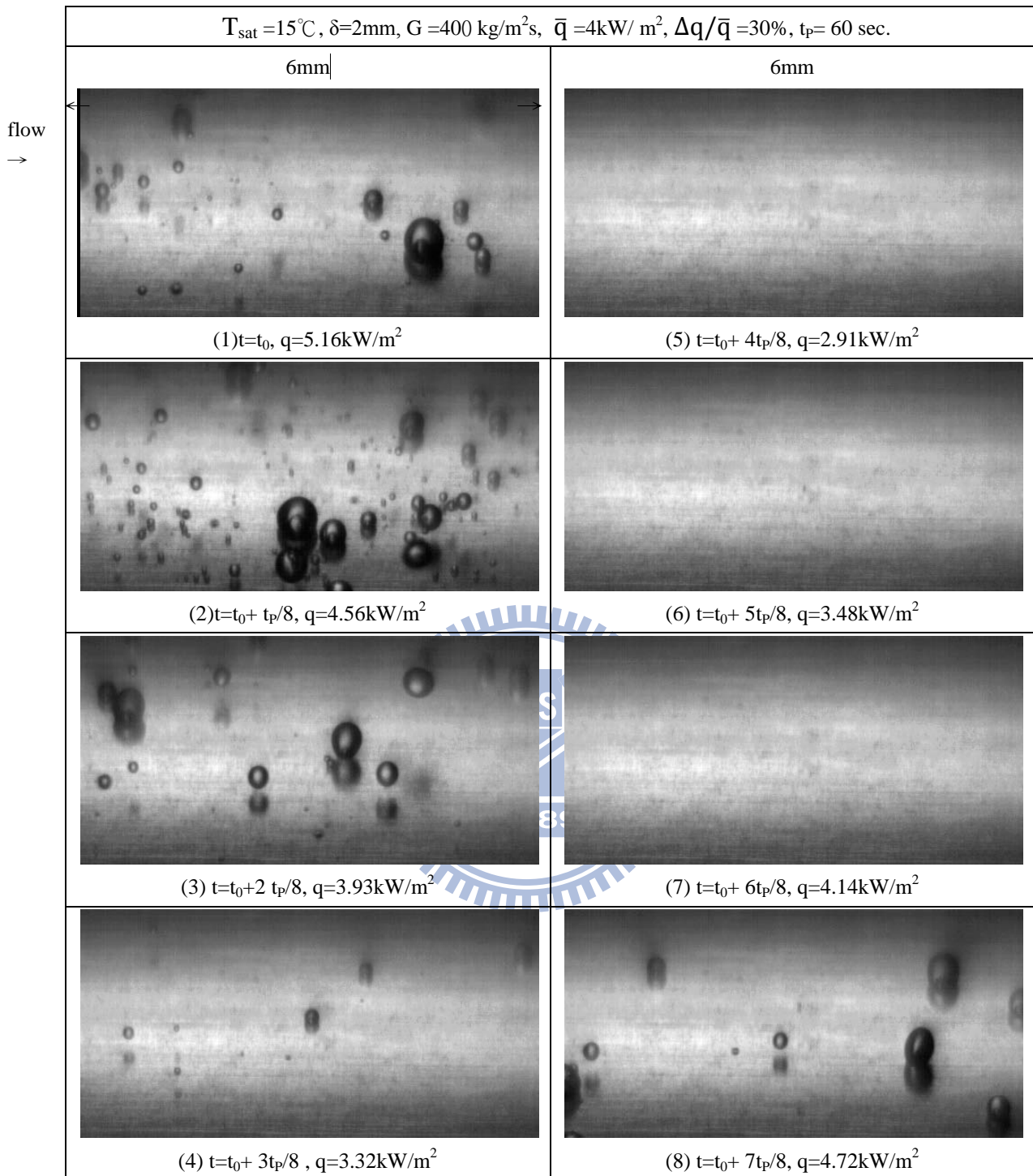


Fig. 5.34 Photos of time periodic intermittent flow boiling of R-410A at selected time instants in a typical periodic cycle at  $T_{\text{sat}} = 15^\circ\text{C}$ ,  $G = 400 \text{ kg/m}^2\text{s}$ ,  $\delta = 2.0\text{mm}$  and  $t_p = 60 \text{ sec}$  for  $\bar{q} = 4\text{kW/m}^2$ ,  $\Delta q/\bar{q} = 30\%$ .



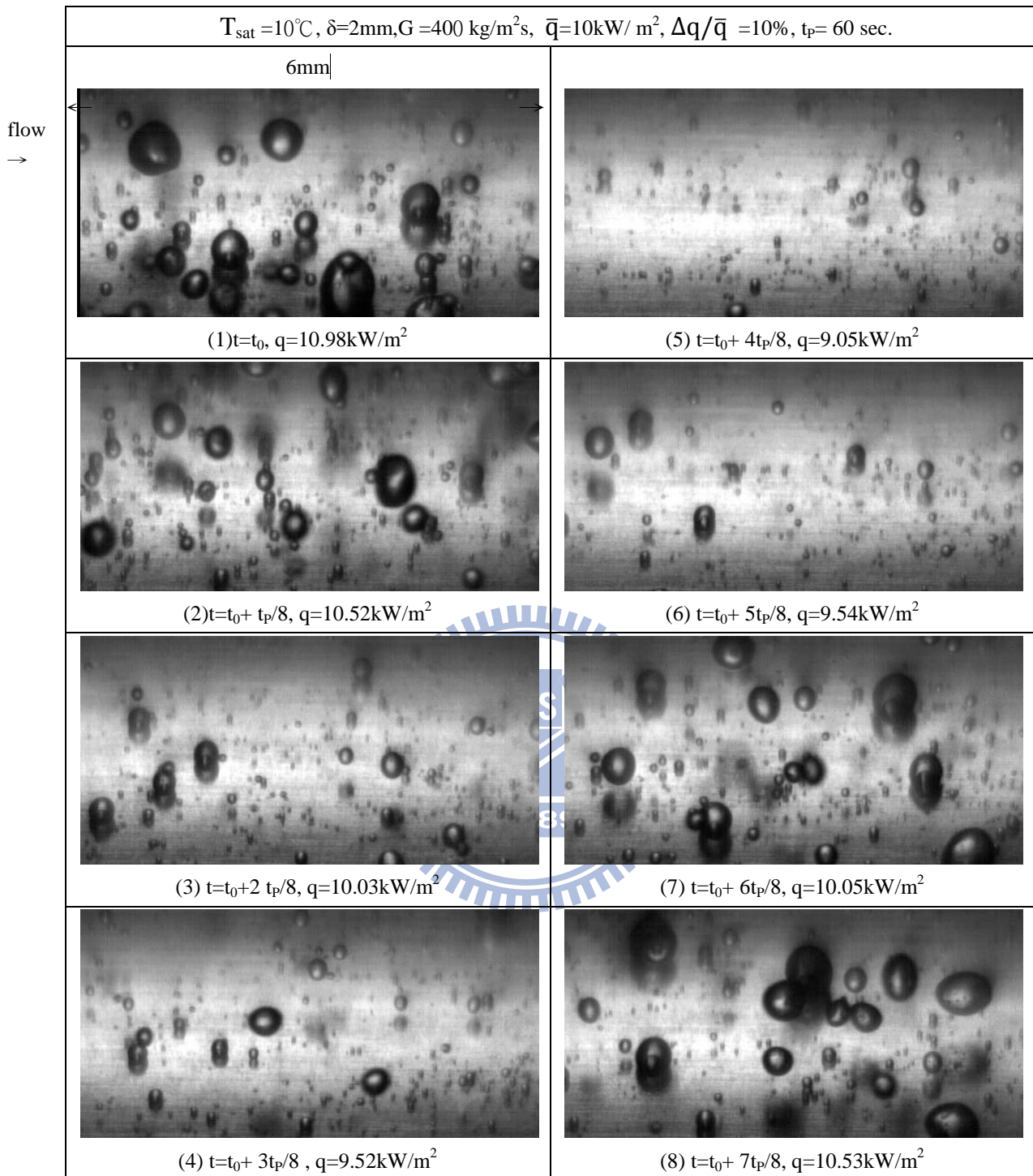


Fig. 5.35 Photos of time periodic saturated flow boiling of R-410A at selected time instants in a typical periodic cycle at  $T_{\text{sat}} = 10^\circ\text{C}$ ,  $G = 400 \text{ kg/m}^2\text{s}$ ,  $\delta = 2.0\text{mm}$  and  $t_p = 60 \text{ sec}$  for  $\bar{q} = 10\text{kW/m}^2$ ,  $\Delta q/\bar{q} = 10\%$ .

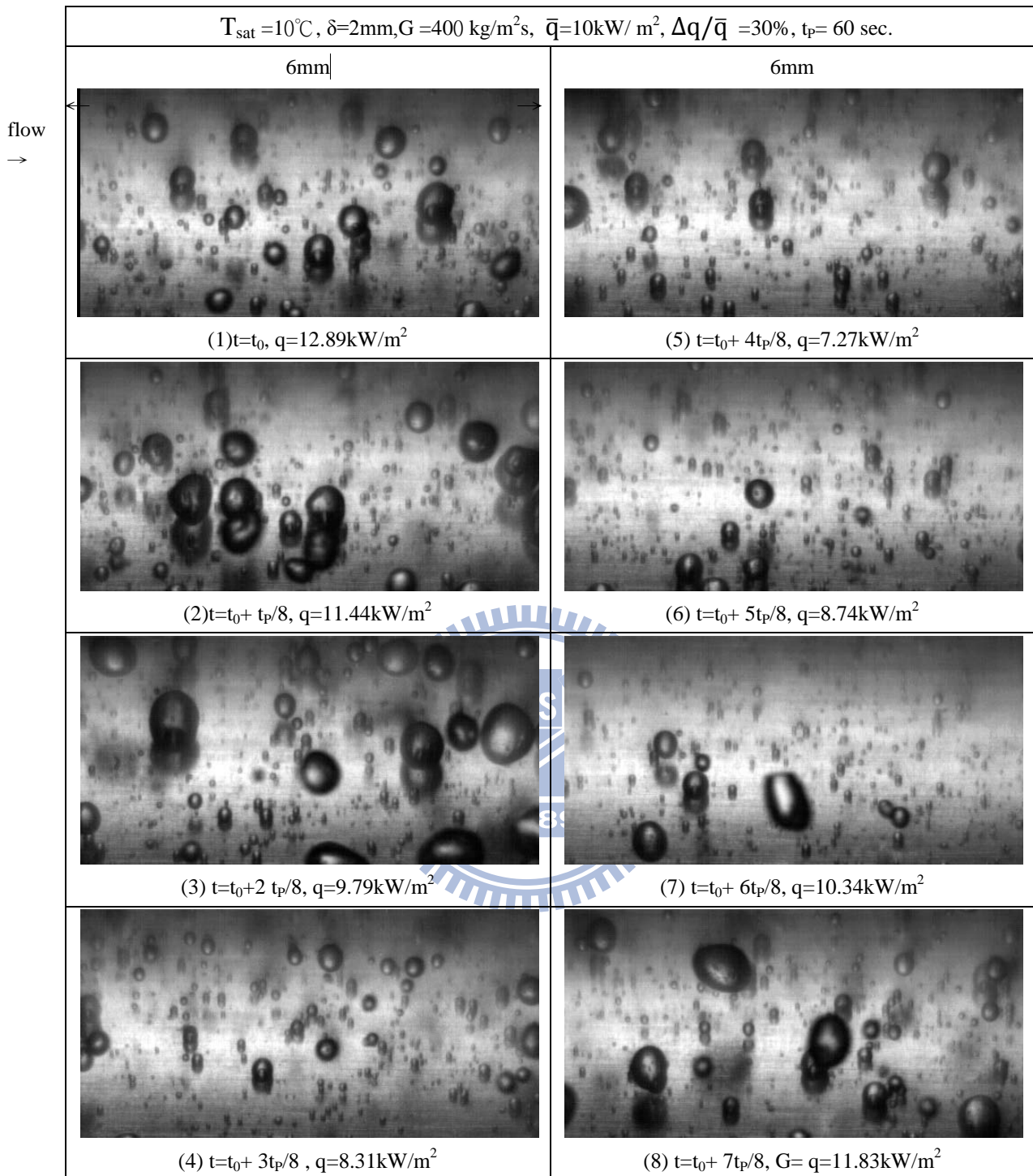


Fig. 5.36 Photos of time periodic saturated flow boiling of R-410A at selected time instants in a typical periodic cycle at  $T_{\text{sat}} = 10^\circ\text{C}$ ,  $G = 400 \text{ kg/m}^2\text{s}$ ,  $\delta = 2.0\text{mm}$  and  $t_p = 60 \text{ sec}$  for  $\bar{q} = 10\text{kW/m}^2$ ,  $\Delta q/\bar{q} = 30\%$ .

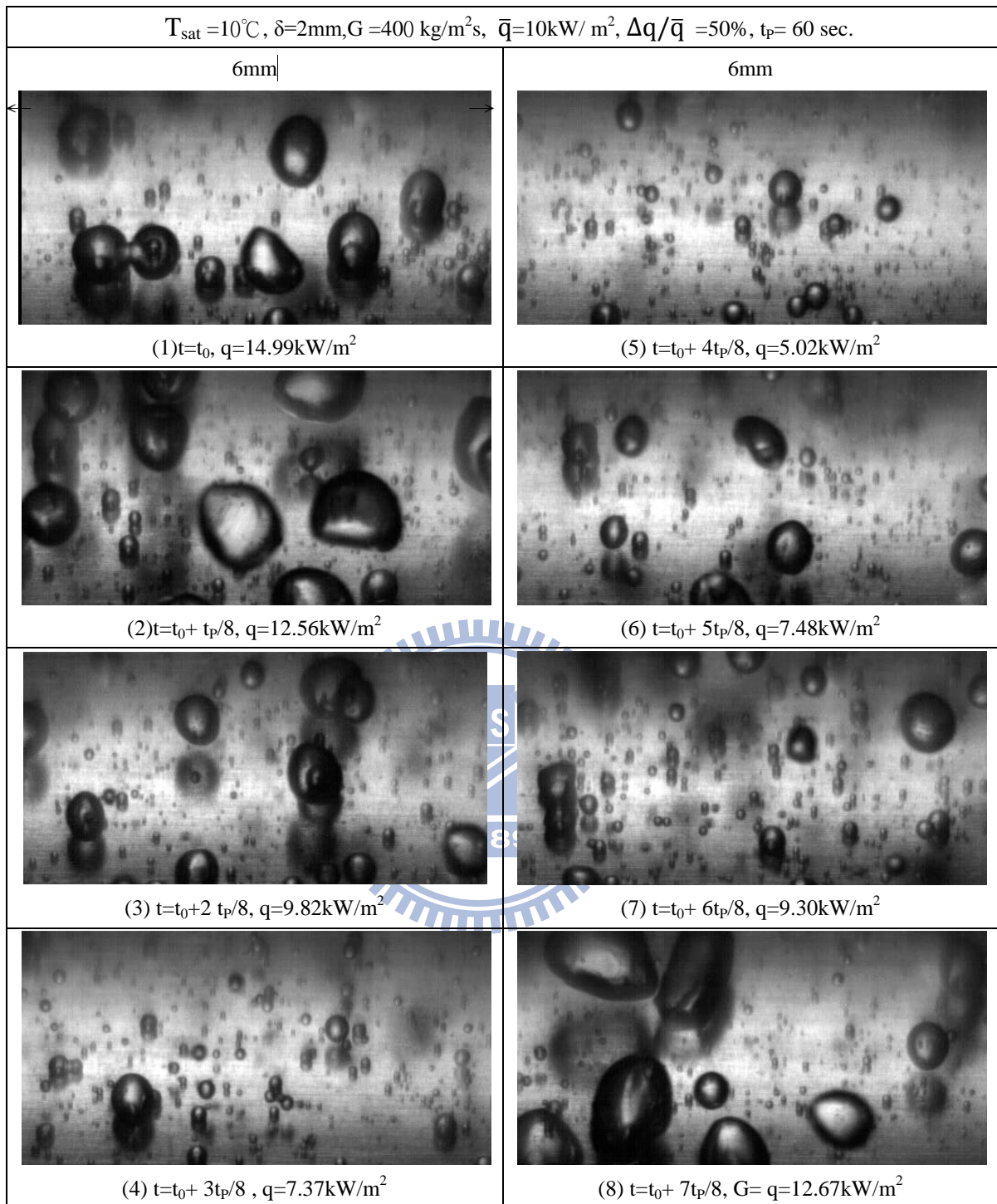


Fig. 5.37 Photos of time periodic saturated flow boiling of R-410A at selected time instants in a typical periodic cycle at  $T_{\text{sat}} = 10^\circ\text{C}$ ,  $G = 400 \text{ kg/m}^2\text{s}$ ,  $\delta = 2.0\text{mm}$  and  $t_p = 60 \text{ sec}$  for  $\bar{q} = 10\text{kW/m}^2$ ,  $\Delta q/\bar{q} = 30\%$ .



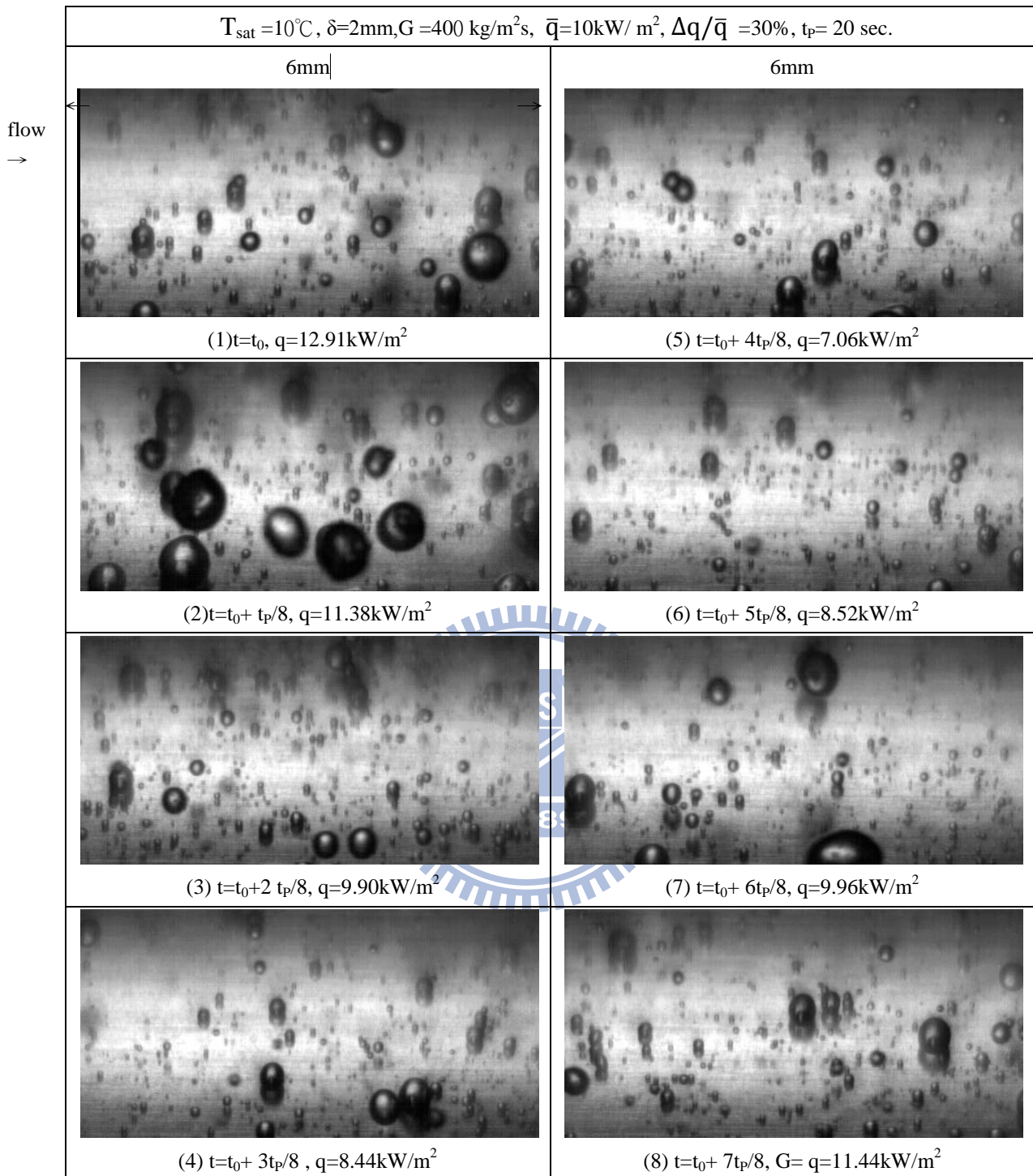


Fig. 5.38 Photos of time periodic saturated flow boiling of R-410A at selected time instants in a typical periodic cycle at  $T_{\text{sat}} = 10^\circ\text{C}$ ,  $G = 400 \text{ kg/m}^2\text{s}$ ,  $\delta = 2.0\text{mm}$  and  $t_p = 20 \text{ sec}$  for  $\bar{q} = 10\text{kW/m}^2$ ,  $\Delta q/\bar{q} = 30\%$ .



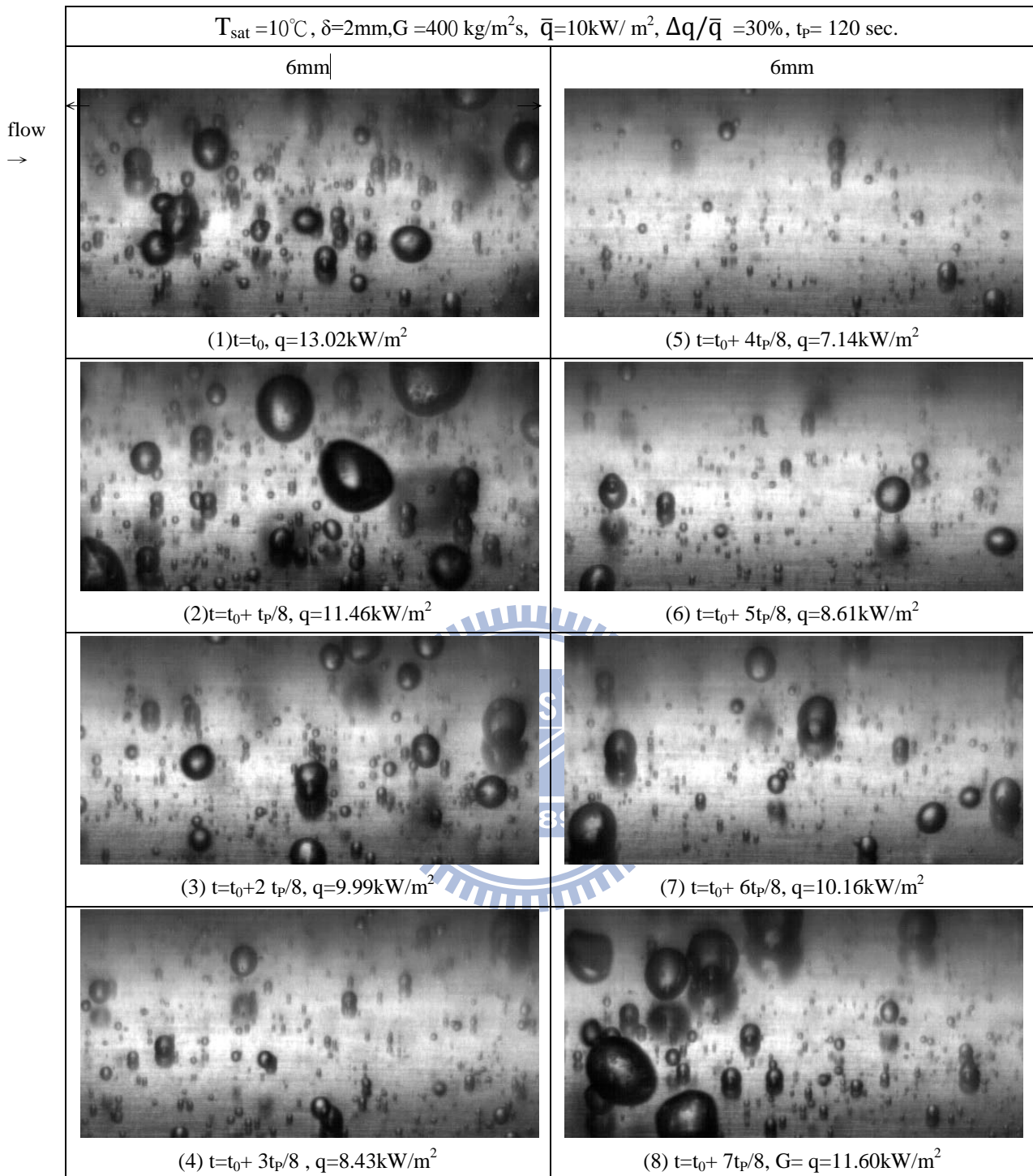


Fig. 5.39 Photos of time periodic saturated flow boiling of R-410A at selected time instants in a typical periodic cycle at  $T_{\text{sat}} = 10^\circ\text{C}$ ,  $G = 400 \text{ kg/m}^2\text{s}$ ,  $\delta = 2.0\text{mm}$  and  $t_p = 120 \text{ sec}$  for  $\bar{q} = 10\text{kW/m}^2$ ,  $\Delta q/\bar{q} = 30\%$ .

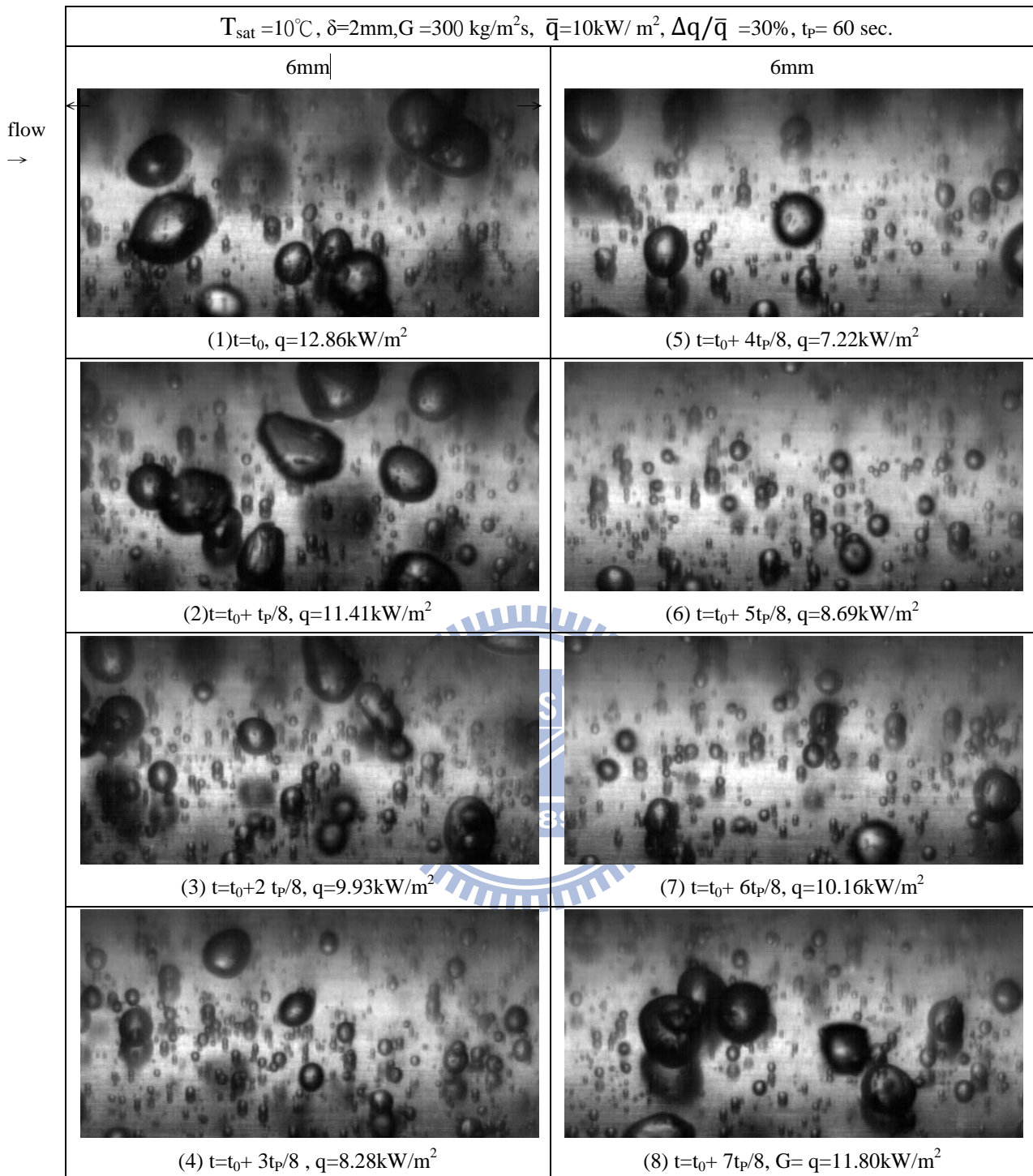


Fig. 5.40 Photos of time periodic saturated flow boiling of R-410A at selected time instants in a typical periodic cycle at  $T_{\text{sat}} = 10^\circ\text{C}$ ,  $G = 300 \text{ kg/m}^2\text{s}$ ,  $\delta = 2.0\text{mm}$  and  $t_p = 60\text{sec}$  for  $\bar{q} = 10\text{kW/m}^2$ ,  $\Delta q/\bar{q} = 30\%$ .

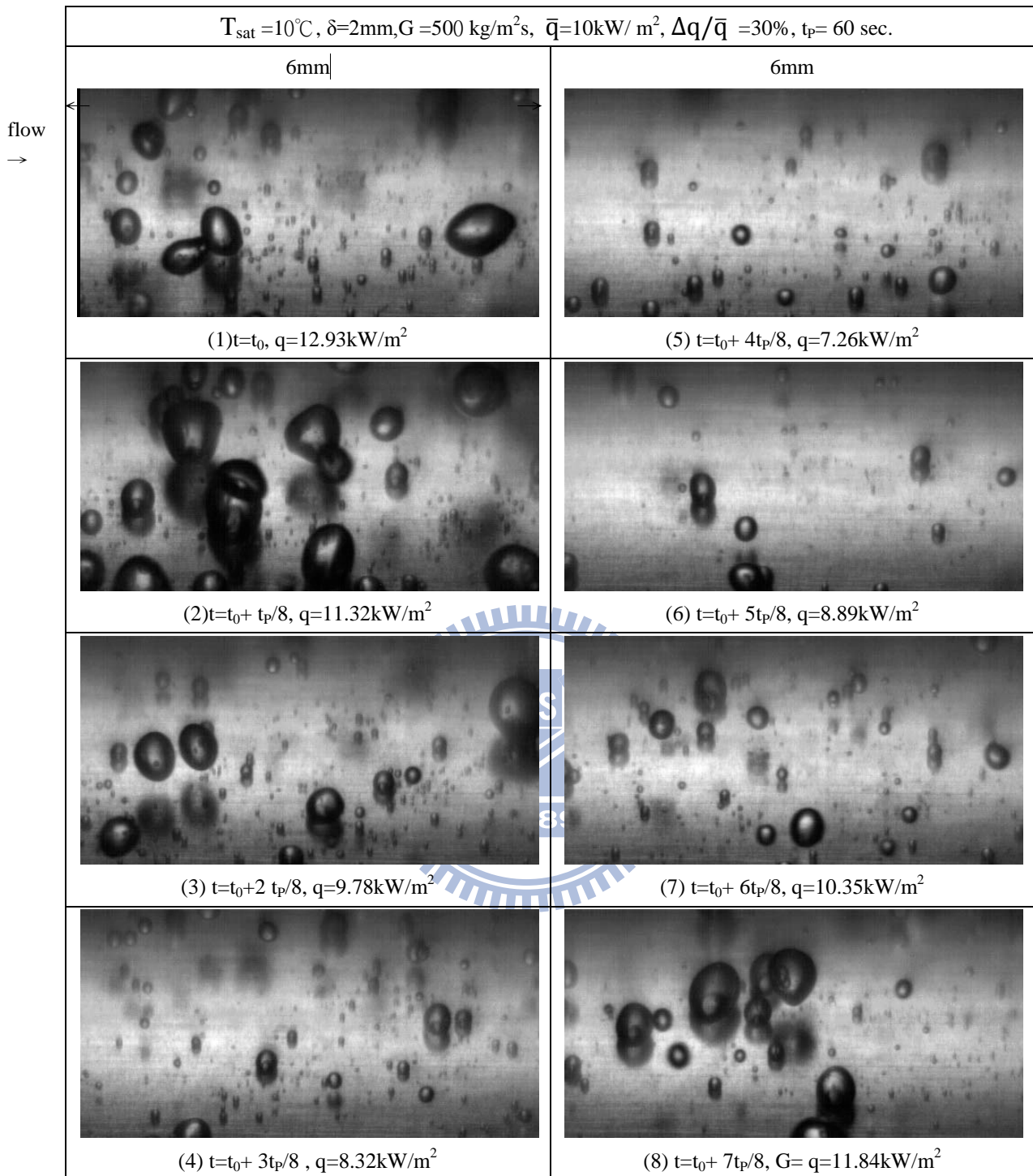


Fig. 5.41 Photos of time periodic saturated flow boiling of R-410A at selected time instants in a typical periodic cycle at  $T_{\text{sat}} = 10^\circ\text{C}$ ,  $G = 500 \text{ kg/m}^2\text{s}$ ,  $\delta = 2.0\text{mm}$  and  $t_p = 60\text{sec}$  for  $\bar{q} = 10\text{kW/m}^2$ ,  $\Delta q/\bar{q} = 30\%$ .



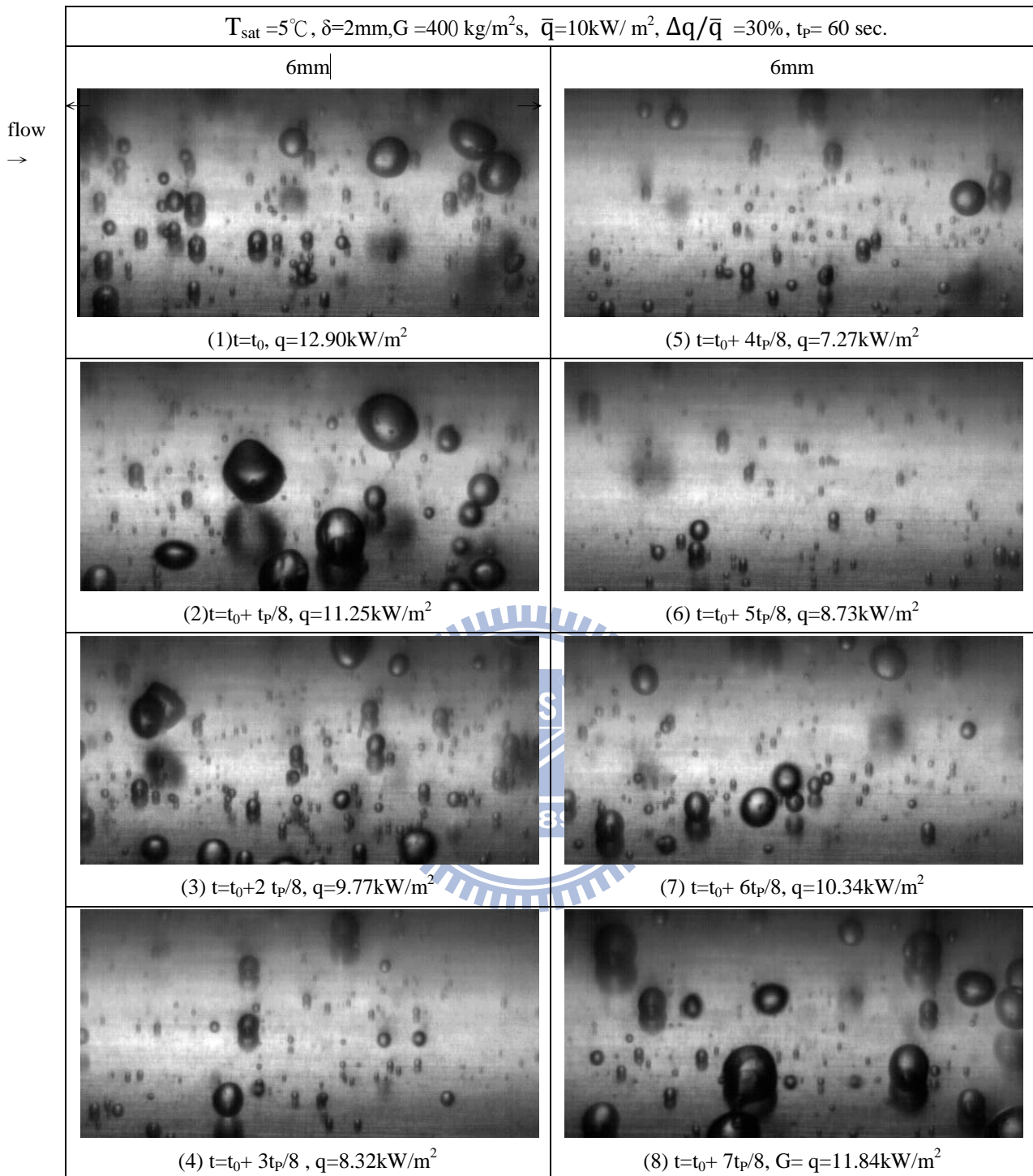


Fig. 5.42 Photos of time periodic saturated flow boiling of R-410A at selected time instants in a typical periodic cycle at  $T_{\text{sat}} = 5^\circ\text{C}$ ,  $G = 400 \text{ kg/m}^2\text{s}$ ,  $\delta = 2.0\text{mm}$  and  $t_p = 60\text{sec}$  for  $\bar{q} = 10\text{kW/m}^2$ ,  $\Delta q/\bar{q} = 30\%$ .

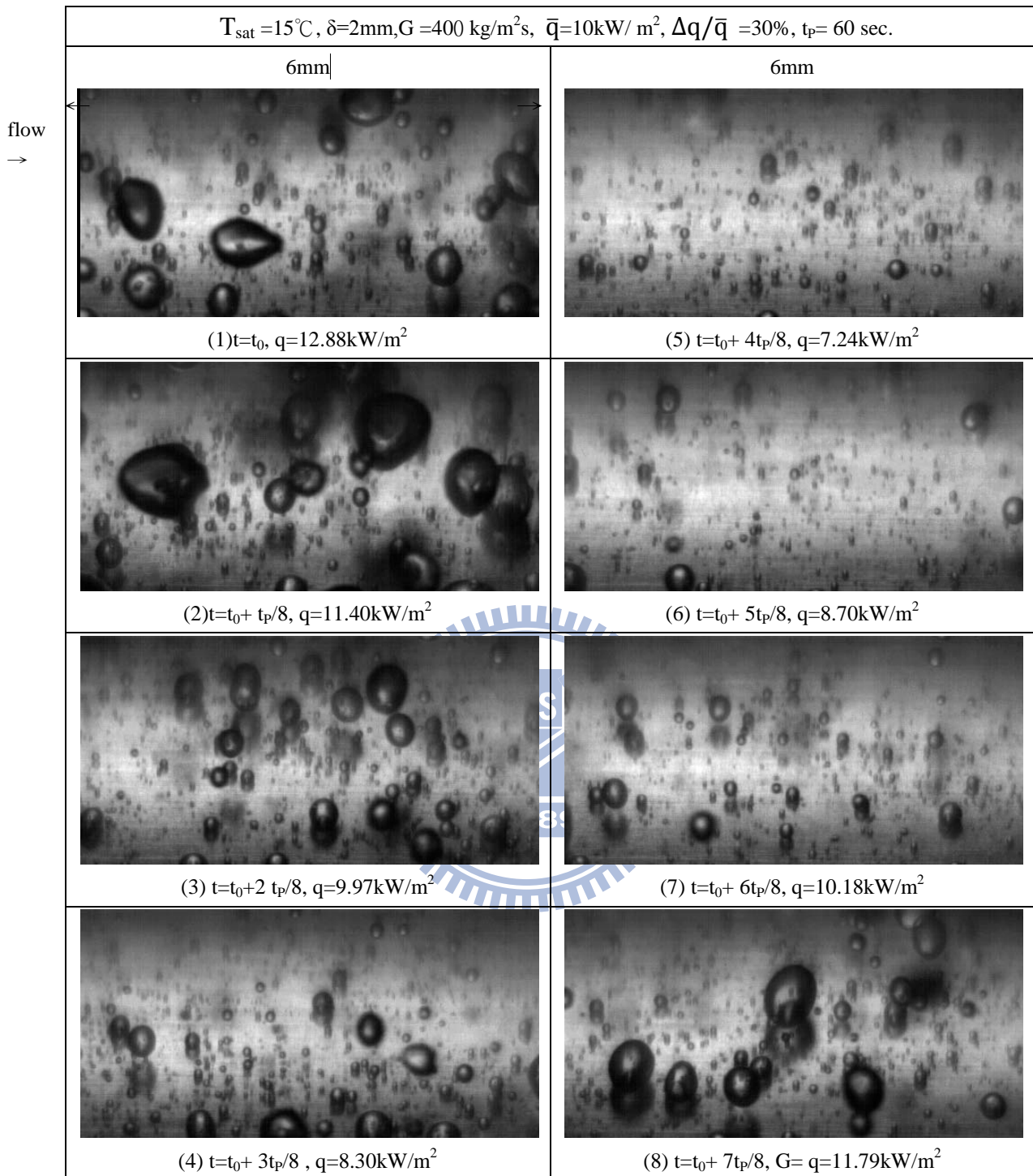


Fig. 5.43 Photos of time periodic saturated flow boiling of R-410A at selected time instants in a typical periodic cycle at  $T_{\text{sat}} = 15^\circ\text{C}$ ,  $G = 400 \text{ kg/m}^2\text{s}$ ,  $\delta = 2.0\text{mm}$  and  $t_p = 60\text{sec}$  for  $\bar{q} = 10\text{kW/m}^2$ ,  $\Delta q/\bar{q} = 30\%$ .

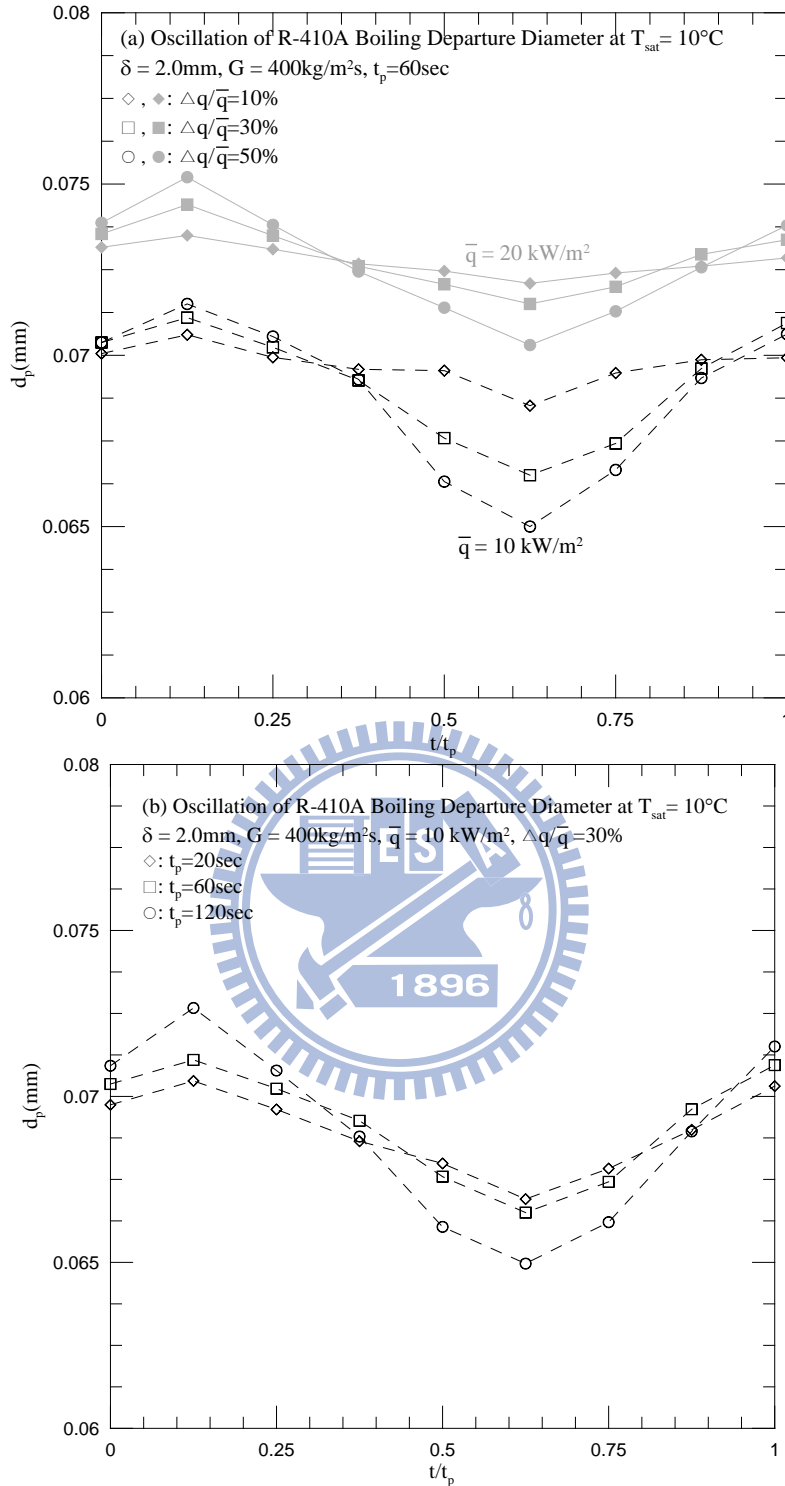


Fig. 5.44 Time variations of mean bubble departure diameter in time periodic saturated flow boiling of R-410A for  $\bar{q} = 10\text{ kW/m}^2$  at  $T_{sat} = 10^\circ\text{C}$ ,  $G = 400\text{ kg/m}^2\text{s}$  and  $\delta = 2.0\text{mm}$  for (a) various  $\Delta q/\bar{q}$  at  $t_p = 60\text{ sec}$  and (b) various  $t_p$  at  $\Delta q/\bar{q} = 30\%$ .

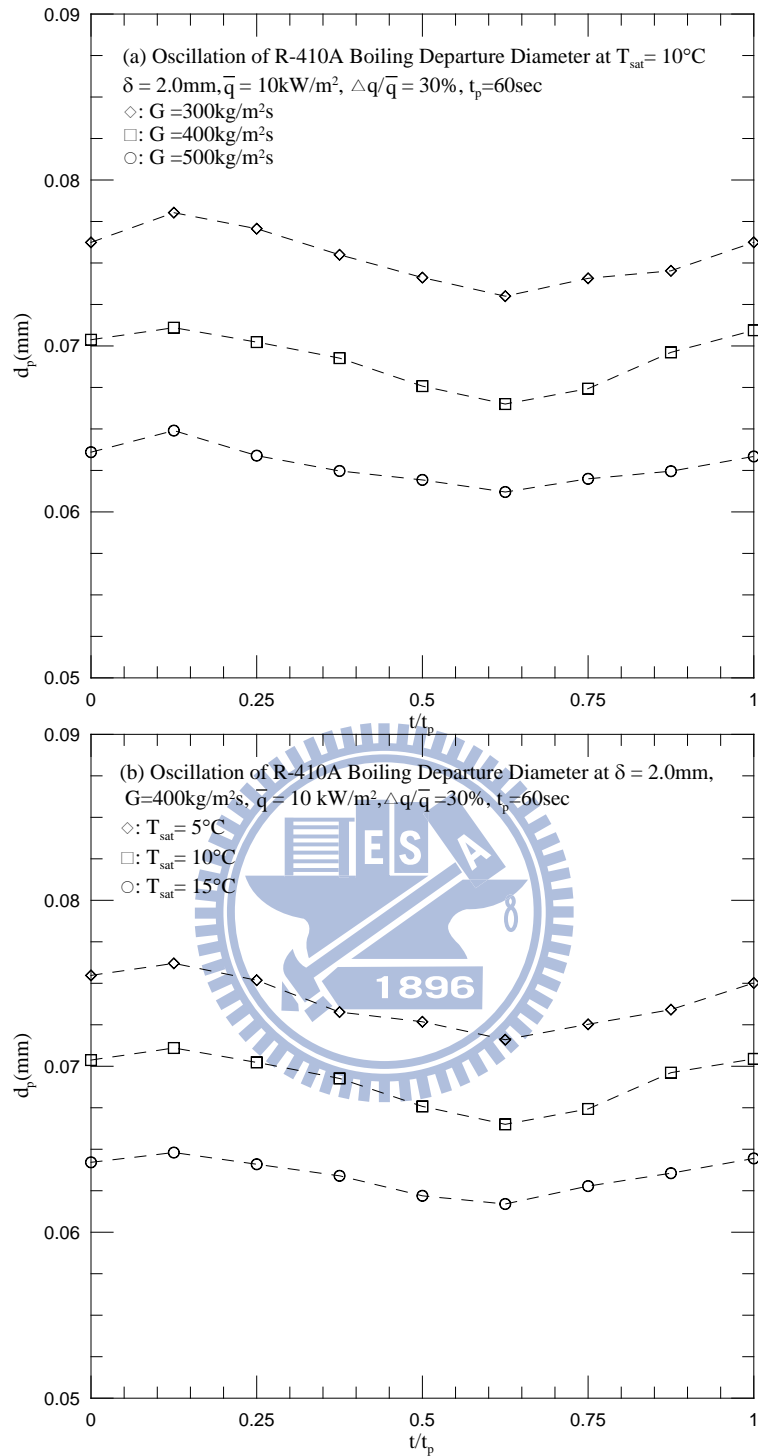


Fig. 5.45 Time variations of mean bubble departure diameter in time periodic saturated flow boiling of R-410A for  $\bar{q} = 10\text{kW/m}^2$  at  $\Delta q/\bar{q} = 30\%$ ,  $t_p = 60\text{ sec}$  and  $\delta = 2.0\text{mm}$  for (a) various  $G$  at  $T_{\text{sat}} = 10^\circ\text{C}$  and (b) various  $T_{\text{sat}}$  at  $G = 400\text{ kg/m}^2\text{s}$ .

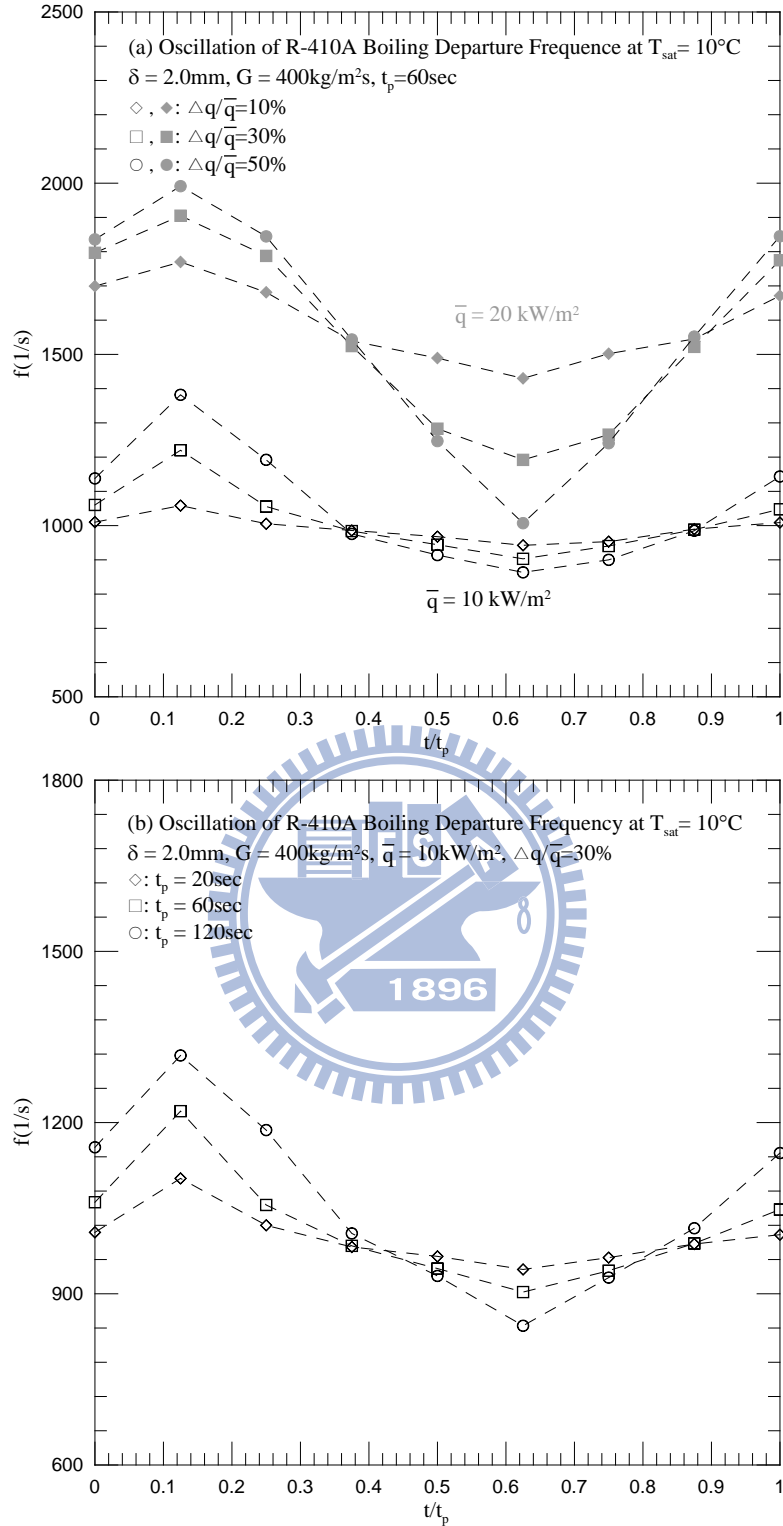


Fig. 5.46 Time variations of mean bubble departure frequency in time periodic saturated flow boiling of R-410A for  $\bar{q} = 10\text{kW/m}^2$  at  $T_{\text{sat}} = 10^\circ\text{C}$ ,  $G = 400\text{ kg/m}^2\text{s}$  and  $\delta = 2.0\text{mm}$  for (a) various  $\Delta q/\bar{q}$  at  $t_p = 60\text{ sec}$  and (b) various  $t_p$  at  $\Delta q/\bar{q} = 30\%$ .



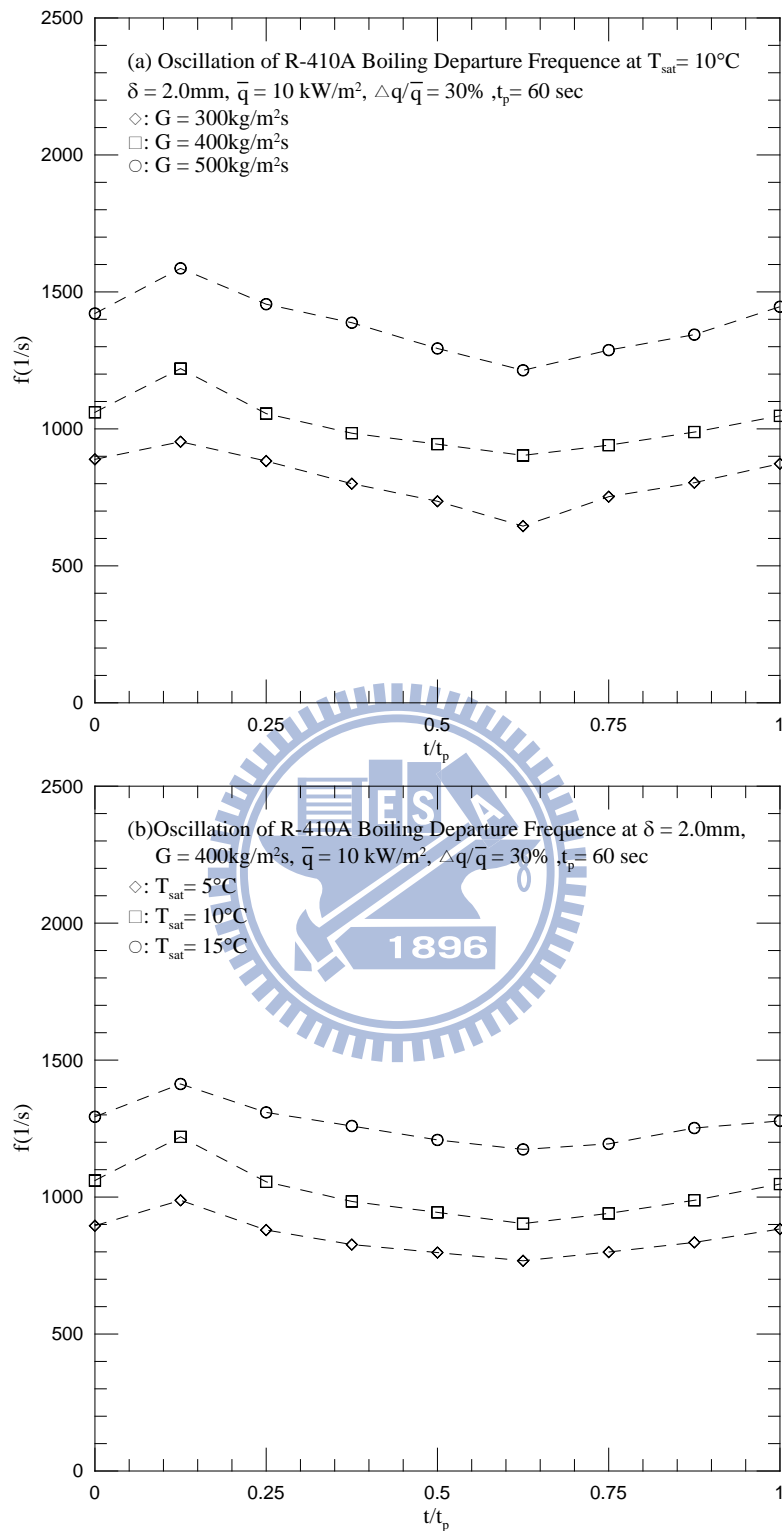


Fig. 5.47 Time variations of mean bubble departure frequency in time periodic saturated flow boiling of R-410A for  $\bar{q} = 10\text{ kW/m}^2$  at  $\Delta q/\bar{q} = 30\%$ ,  $t_p = 60\text{ sec}$  and  $\delta = 2.0\text{mm}$  for (a) various  $G$  at  $T_{\text{sat}} = 10^\circ\text{C}$  and (b) various  $T_{\text{sat}}$  at  $G = 400\text{ kg/m}^2\text{s}$ .

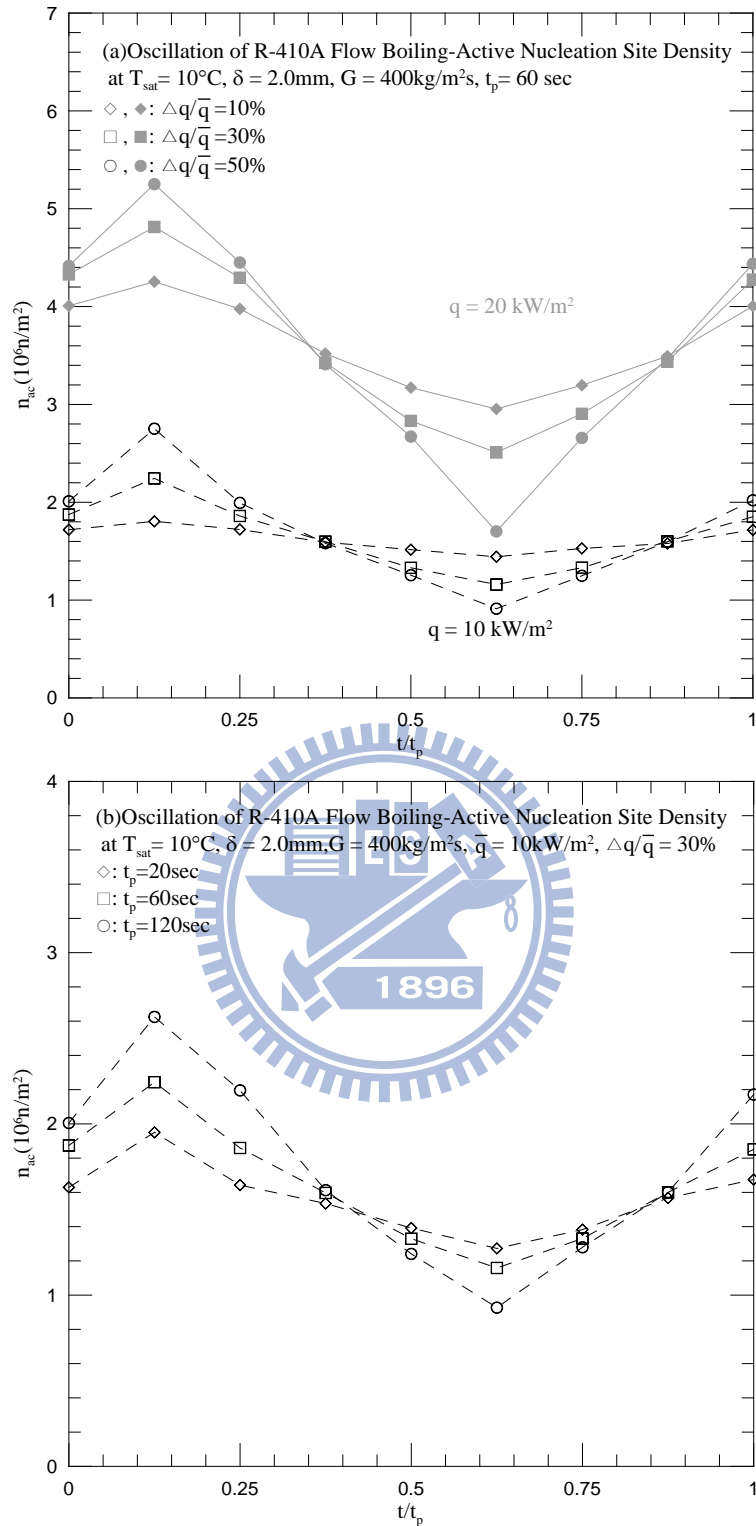


Fig. 5.48 Time variations of mean active nucleation site density in time periodic saturated flow boiling of R-410A for  $\bar{q} = 10\text{kW/m}^2$  at  $T_{\text{sat}} = 10^\circ\text{C}$ ,  $G = 400\text{ kg/m}^2\text{s}$  and  $\delta = 2.0\text{mm}$  for (a) various  $\Delta q/\bar{q}$  at  $t_p = 60\text{ sec}$  and (b) various  $t_p$  at  $\Delta q/\bar{q} = 30\%$ .

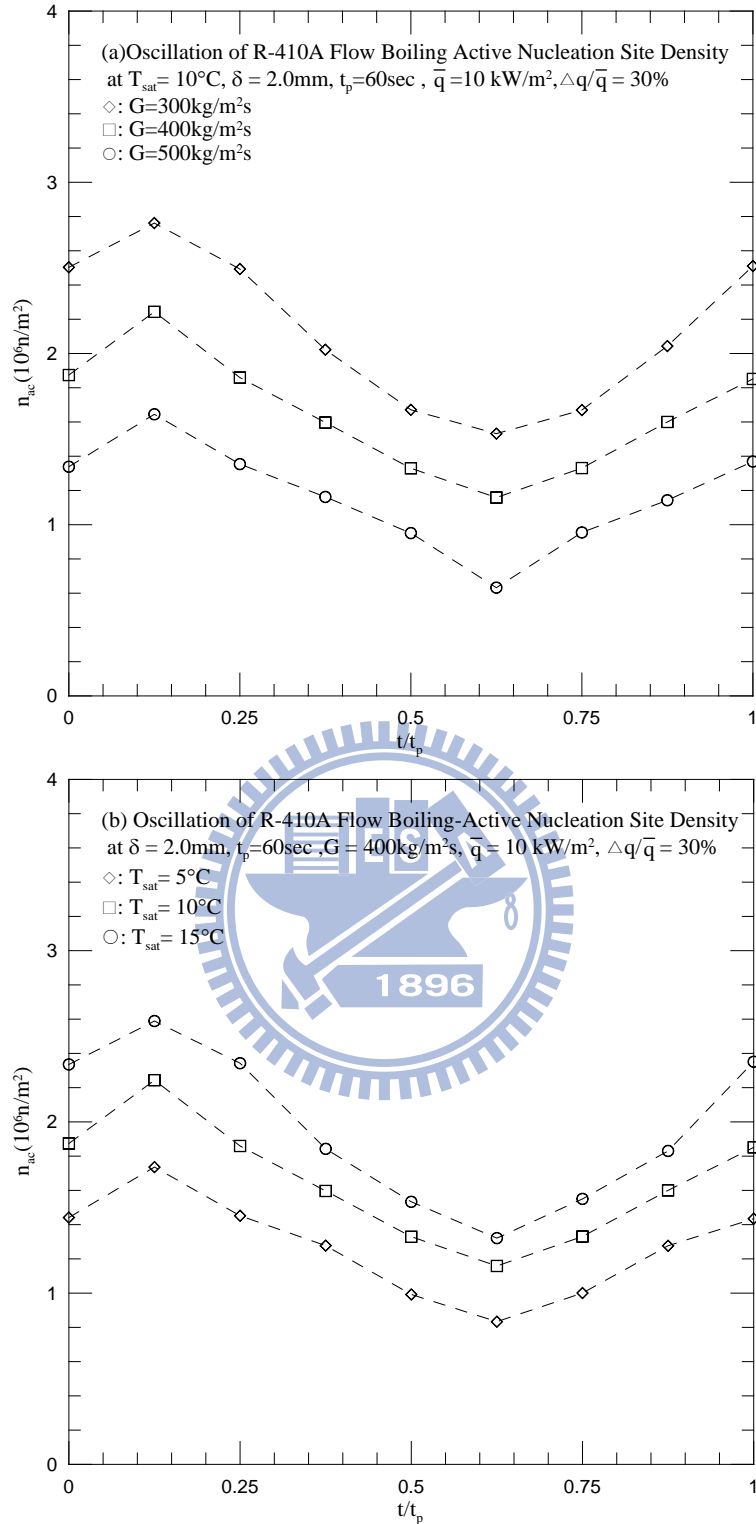


Fig. 5.49 Time variations of mean bubble departure frequency in time periodic saturated flow boiling of R-410A for  $\bar{q} = 10\text{ kW/m}^2$  at  $\Delta q/\bar{q} = 30\%$ ,  $t_p = 60\text{ sec}$  and  $\delta = 2.0\text{mm}$  for (a) various  $G$  at  $T_{\text{sat}} = 10^\circ\text{C}$  and (b) various  $T_{\text{sat}}$  at  $G = 400\text{ kg/m}^2\text{s}$ .

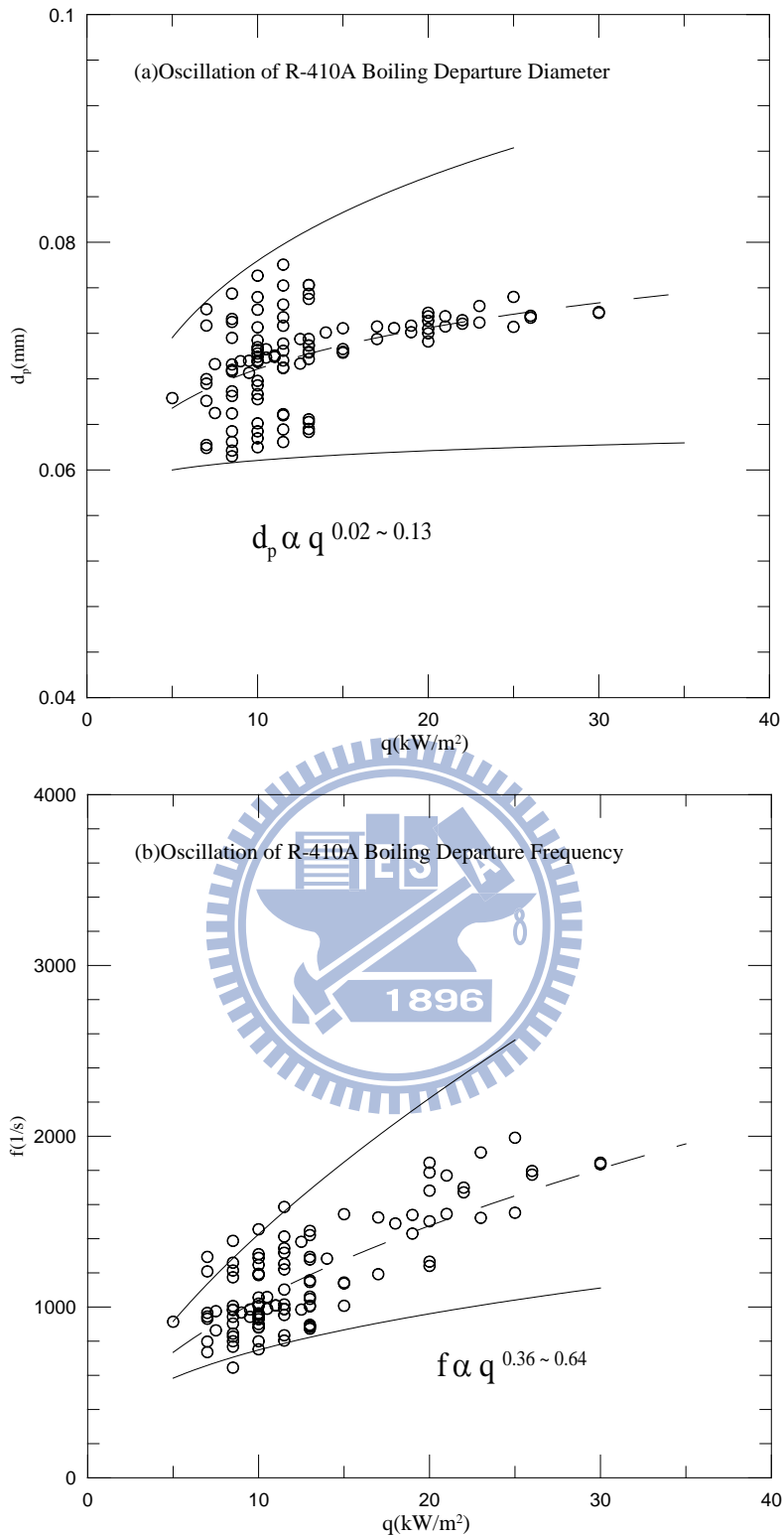


Fig. 5.50 Variations of bubble departure diameter (a), departure frequency (b), and active nucleation site density (c) with heat flux for time-periodic saturated flow boiling of R-410A.

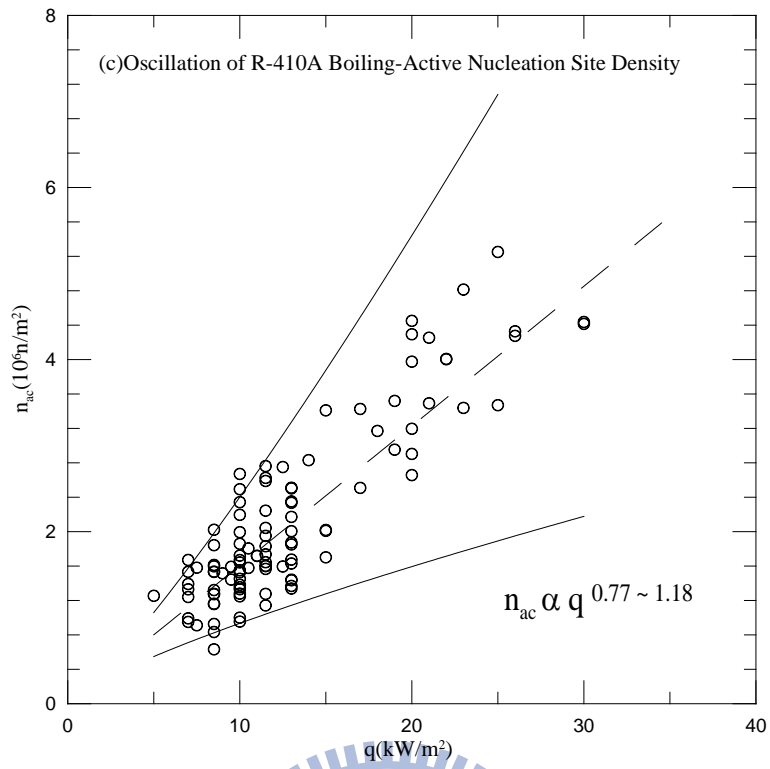
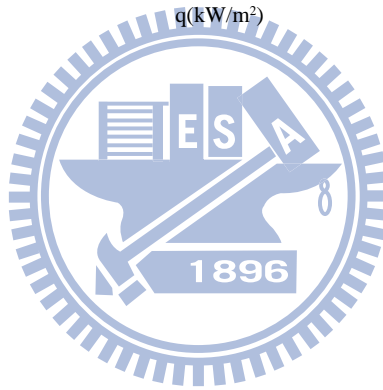


Fig. 5.50 continued



## CHAPTER 6

### Comparison of Flow Boiling in R-410A and R-134a

#### 6.1 Comparison of Stable Saturated Flow Boiling in R-410A and R-134a

We compare the present data for the stable saturated flow boiling of refrigerants R-410A and R-134a measured in the same narrow annular duct in Fig. 6.1. The results in Fig. 6.1(a) indicate that a much higher imposed heat flux is needed to initiate boiling for R-134a. This can be attributed to the lower surface tension for R-410A. Besides, the slopes of the boiling curves for R-410A are much steeper, suggesting the saturated flow boiling heat transfer for R-410A is much better than R-134a. Indeed, the data in Fig. 6.1(b) manifest that R-410A has a much higher saturated flow boiling heat transfer coefficient except at the low heat flux near ONB.

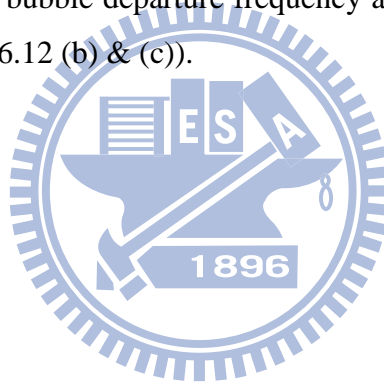
#### 6.2 Comparison of Time Periodic Flow Boiling in R-410A and R-134a

##### Due to Mass Flux Oscillation

Then the time variations of the space-average heated surface temperature  $T_w$  and boiling heat transfer coefficient  $h_r$  are shown in Figs. 6.2 & 6.3 for a given set of  $\bar{T}_{sat}$ ,  $t_p$ ,  $G$  and  $\Delta G/\bar{G}$  due to the imposed mass flux oscillation. The data in Figs 6.2 and 6.3 when compared with R-410A at the same set of the experimental parameters indicate that both in R-410A and R-134a we have the appearance of intermittent boiling. The comparison of the amplitudes of  $T_w$  oscillation for R-134a and R-410A is shown in Fig. 6.4. The  $T_w$  oscillation is much stronger for R-410A. Then the bubble characteristics for the persistent boiling in the narrow annular duct around the middle axial location at  $T_{sat} = 10^\circ\text{C}$ ,  $\bar{G} = 400 \text{ kg/m}^2\text{s}$ ,  $\Delta G/\bar{G} = 20\%$ , and  $\delta = 2.0 \text{ mm}$  for refrigerants R-410A & R-134a are illustrated by the photos in the Figs. 6.5 and 6.6. Because of the higher surface tension for R-134a, the mean bubble diameter is bigger in the R-410A boiling and the mean bubble departure frequency and active nucleation site density are lower in the R-134a boiling (Fig. 6.7).

### 6.3 Comparison of Time Periodic Flow Boiling in R-410A and R-134a Due to Heat Flux Oscillation

Finally, the time variations of the space-average heated surface temperature  $T_w$  and boiling heat transfer coefficient  $h_r$  for R-410A and R-134a are shown in Figs. 6.8 & 6.9 for a given set of the experimental parameters. The results indicate that when  $q$  oscillates periodically in time nearly like a triangular wave, significant temporal oscillations in  $T_w$  and  $h_r$  occur in both R-410A and R-134a boiling and they are also periodic in time and are at the same frequency as the heat flux. The  $T_w$  oscillation significantly lags the heat flux oscillation for both single-phase and boiling flows for R-134a and R-410A. In Figs. 6.10 and 6.11 we show the bubble characteristics for R-410A and R-134a in the narrow annular duct around the middle axial location at  $T_{\text{sat}} = 10^\circ\text{C}$ ,  $G = 400 \text{ kg/m}^2\text{s}$ ,  $\Delta q/\bar{q} = 30\%$ , and  $\delta = 2.0 \text{ mm}$ . The mean bubble departure diameter is smaller for R-410A than R-134a (Fig.6.12 (a)). However, the bubble departure frequency and active nucleation site density for R-410A are higher (Figs.6.12 (b) & (c)).





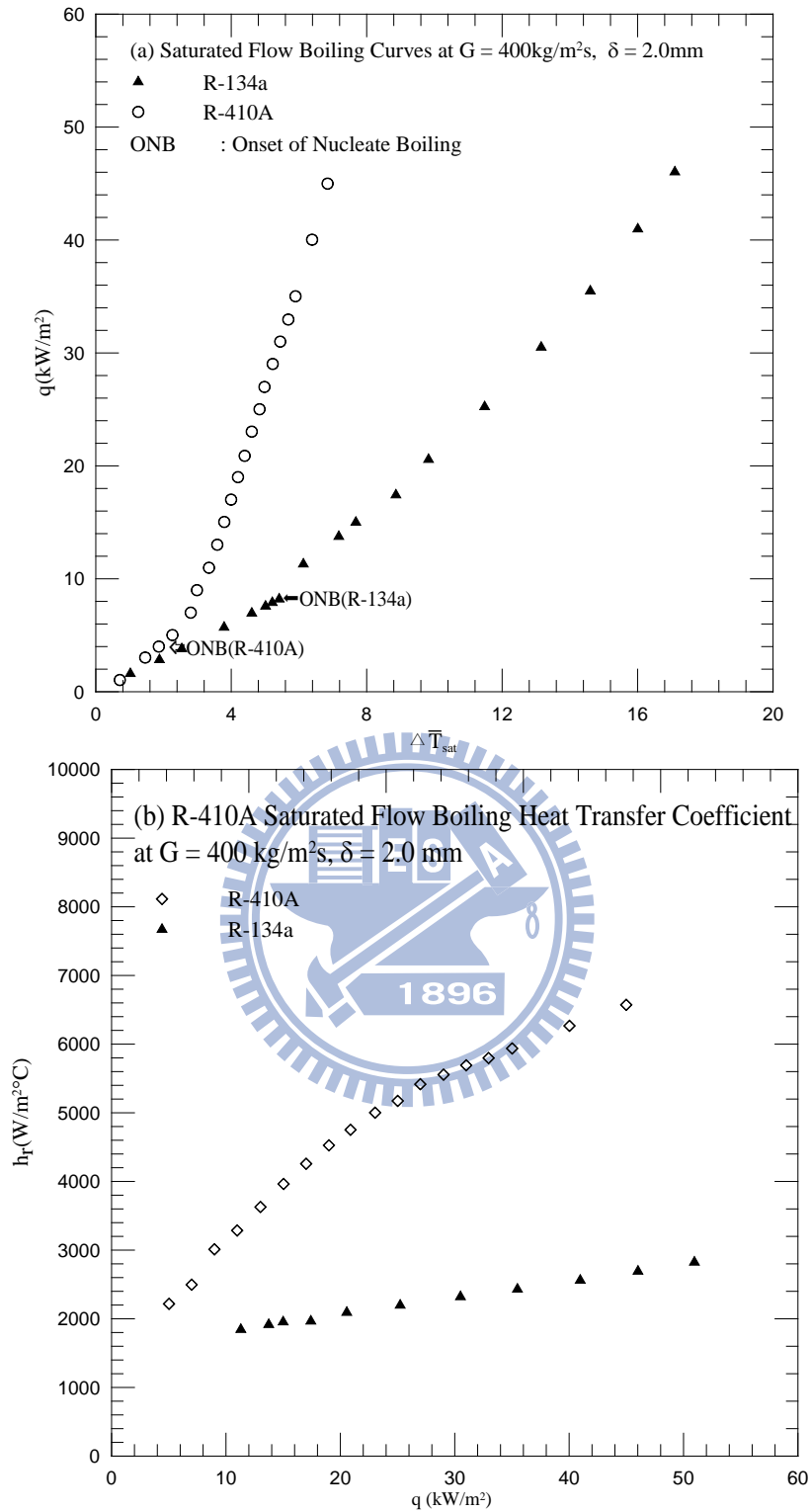


Fig. 6.1 Stable saturated flow boiling curves(a) and heat transfer coefficients for various refrigerant at  $T_{\text{sat}} = 10^\circ\text{C}$ ,  $G = 400 \text{ kg/m}^2\text{s}$  and  $\delta = 2.0 \text{ mm}$ .

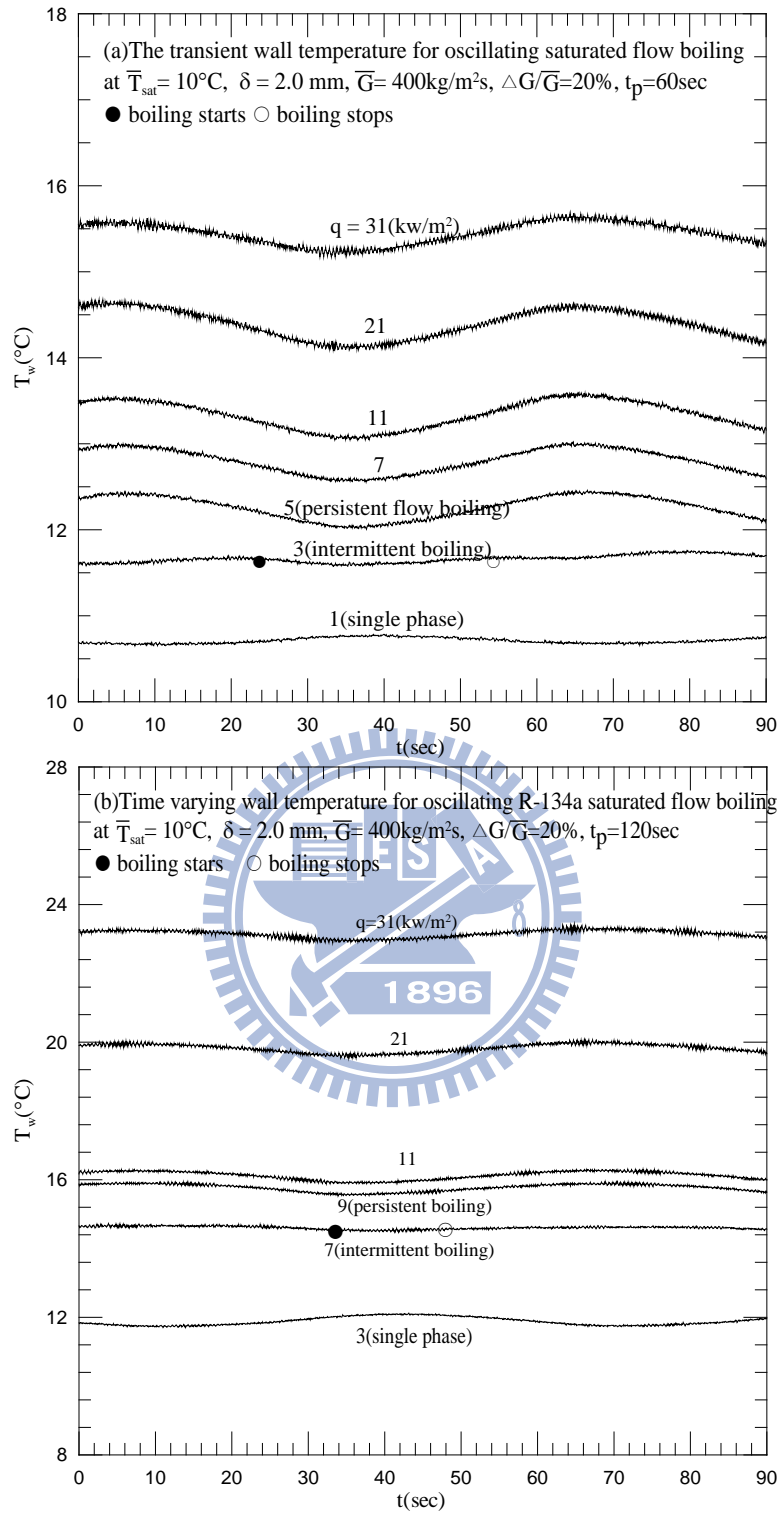


Fig. 6.2 Time variations of oscillating refrigerant mass flux and measured heated wall temperature in time periodic saturated flow boiling of R-410A (a) and R-134a (b) for various imposed heat fluxes at  $\bar{T}_{sat} = 10^\circ\text{C}$ ,  $\delta = 2.0\text{ mm}$ ,  $t_p = 60\text{ sec}$  and  $\bar{G} = 400\text{ kg/m}^2\text{s}$  with  $\Delta G/\bar{G} = 20\%$ .

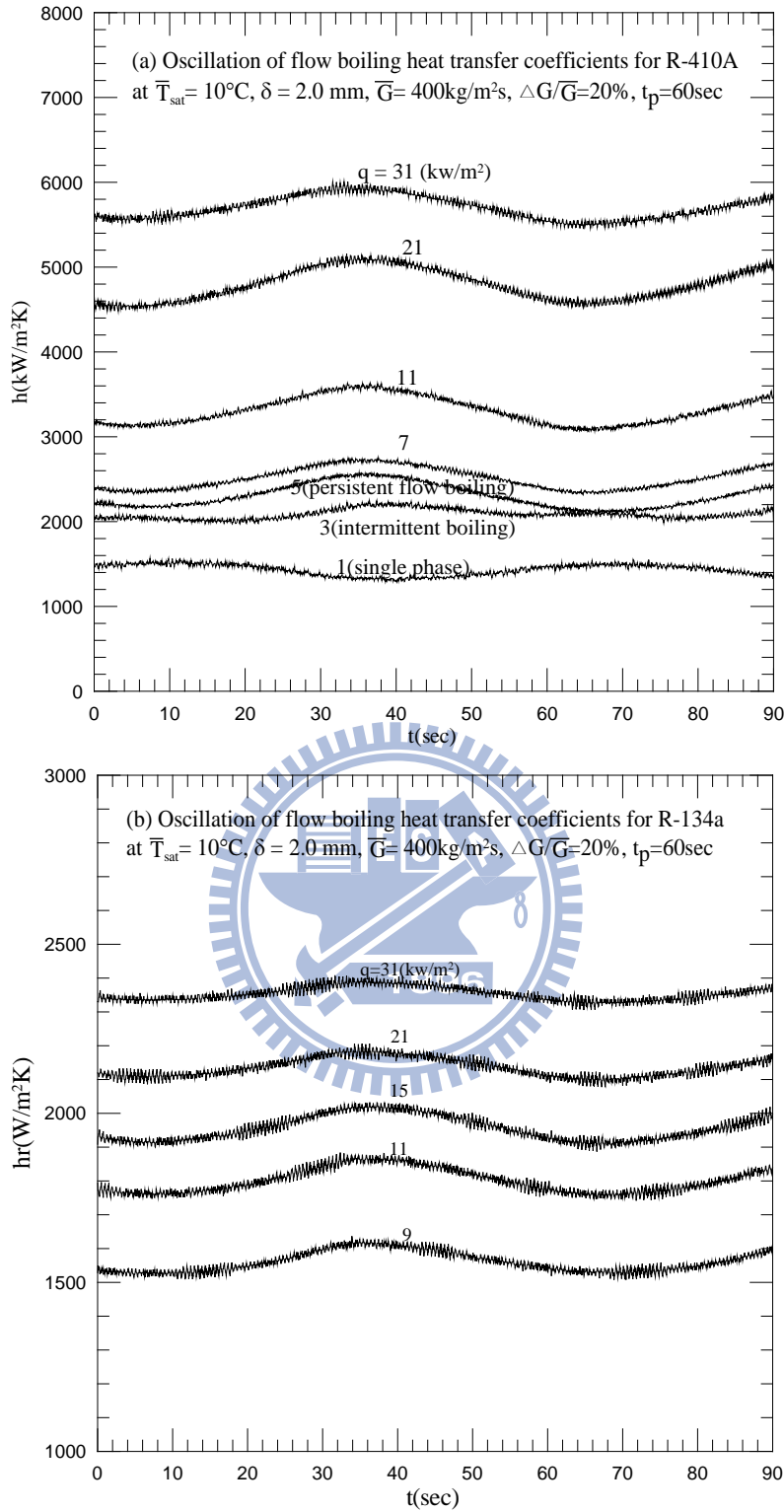


Fig. 6.3 Time variations of flow boiling heat transfer coefficients in time periodic saturated flow boiling of R-410A (a) and R-134a (b) for various imposed heat fluxes at  $\bar{T}_{\text{sat}} = 10^\circ\text{C}$ ,  $\delta = 2.0 \text{ mm}$ ,  $t_p = 60 \text{ sec}$  and  $\bar{G} = 400 \text{ kg/m}^2\text{s}$  with  $\Delta G/\bar{G} = 20\%$ .

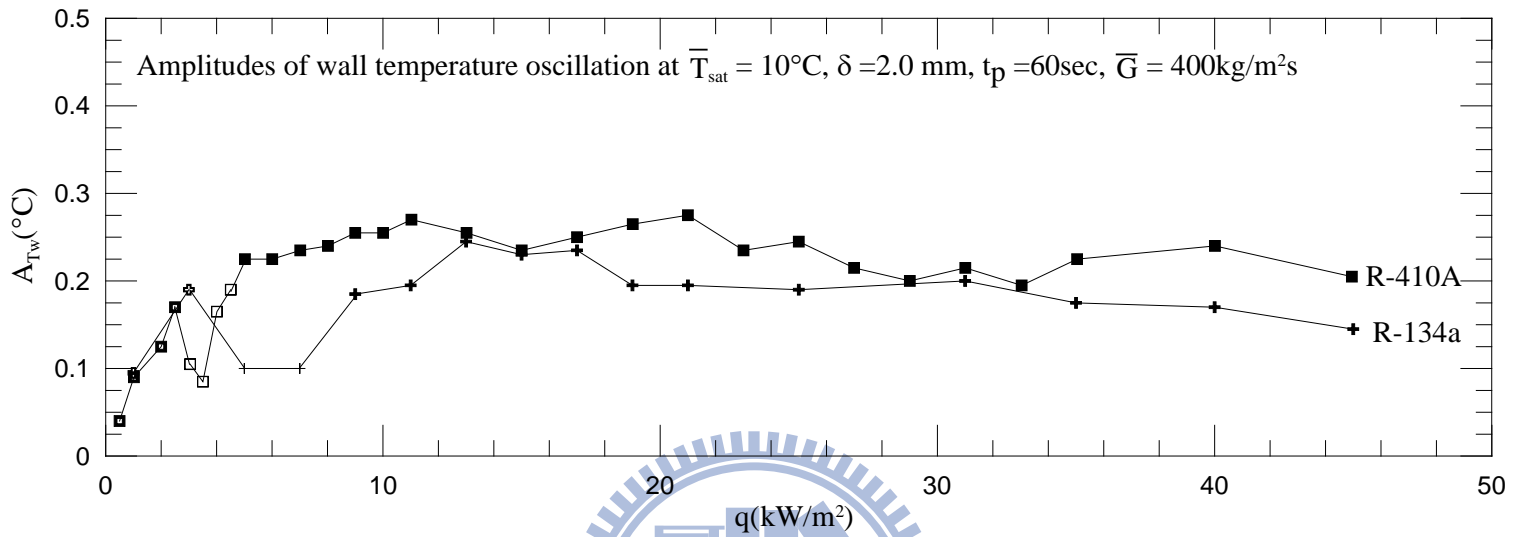


Fig. 6.4 Variations of amplitudes of heated wall temperature with imposed heat flux for various refrigerants R-410A & R-134a. (  $\oplus, \square$  Single Phase;  $+, \square$  Intermittent Boiling;  $+, \blacksquare$  Persistent Flow Boiling )

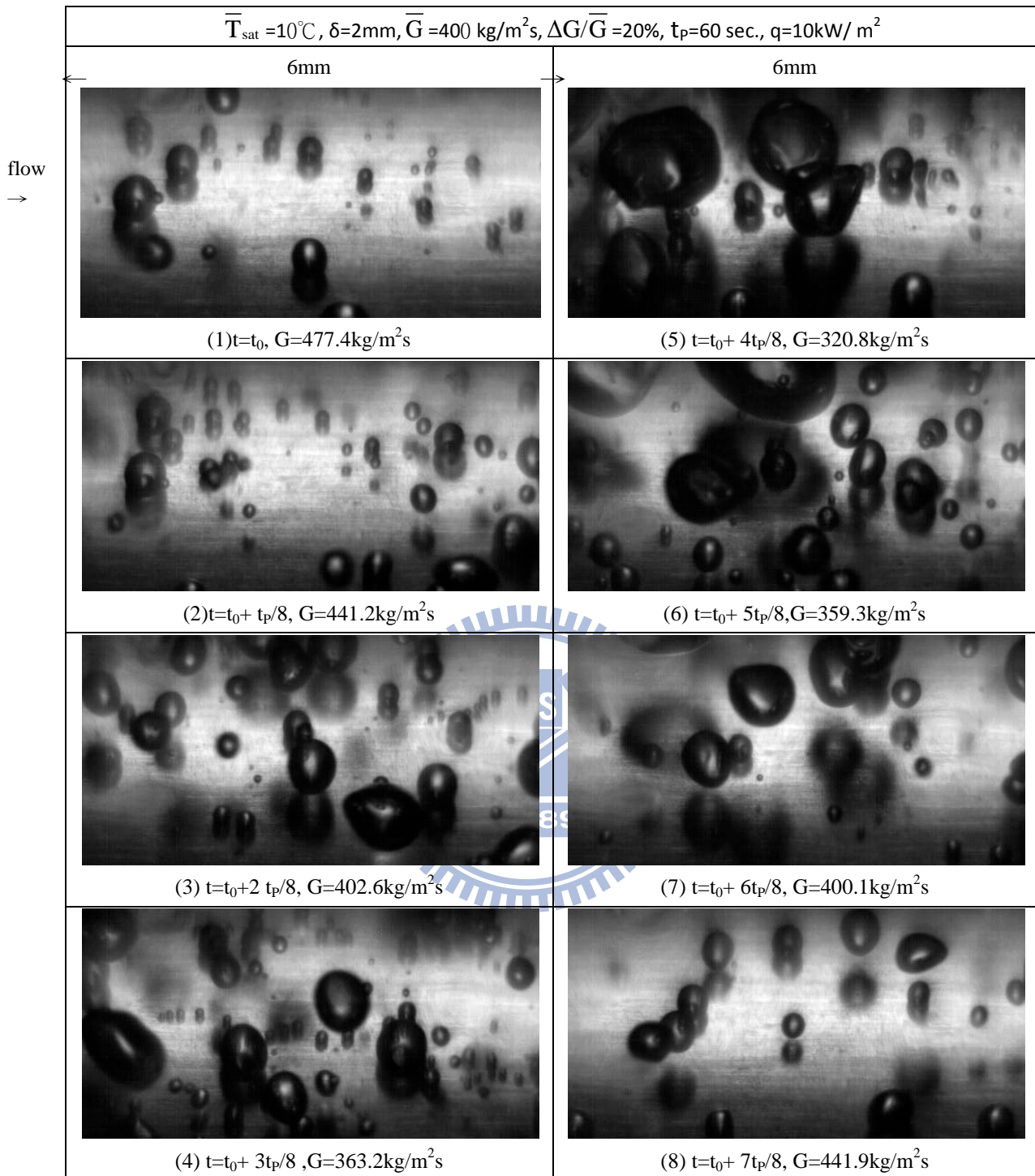


Fig. 6.5 Photos of time periodic saturated flow boiling of R-134a at selected time instants in a typical periodic cycle for  $q = 10 \text{ kW/m}^2$  at  $\bar{G} = 400 \text{ kg/m}^2\text{s}$ ,  $\Delta\bar{G}/\bar{G} = 20\%$ ,  $\bar{T}_{\text{sat}} = 10^\circ\text{C}$ ,  $\delta = 2.0\text{mm}$  and  $t_p = 60\text{sec}$ .

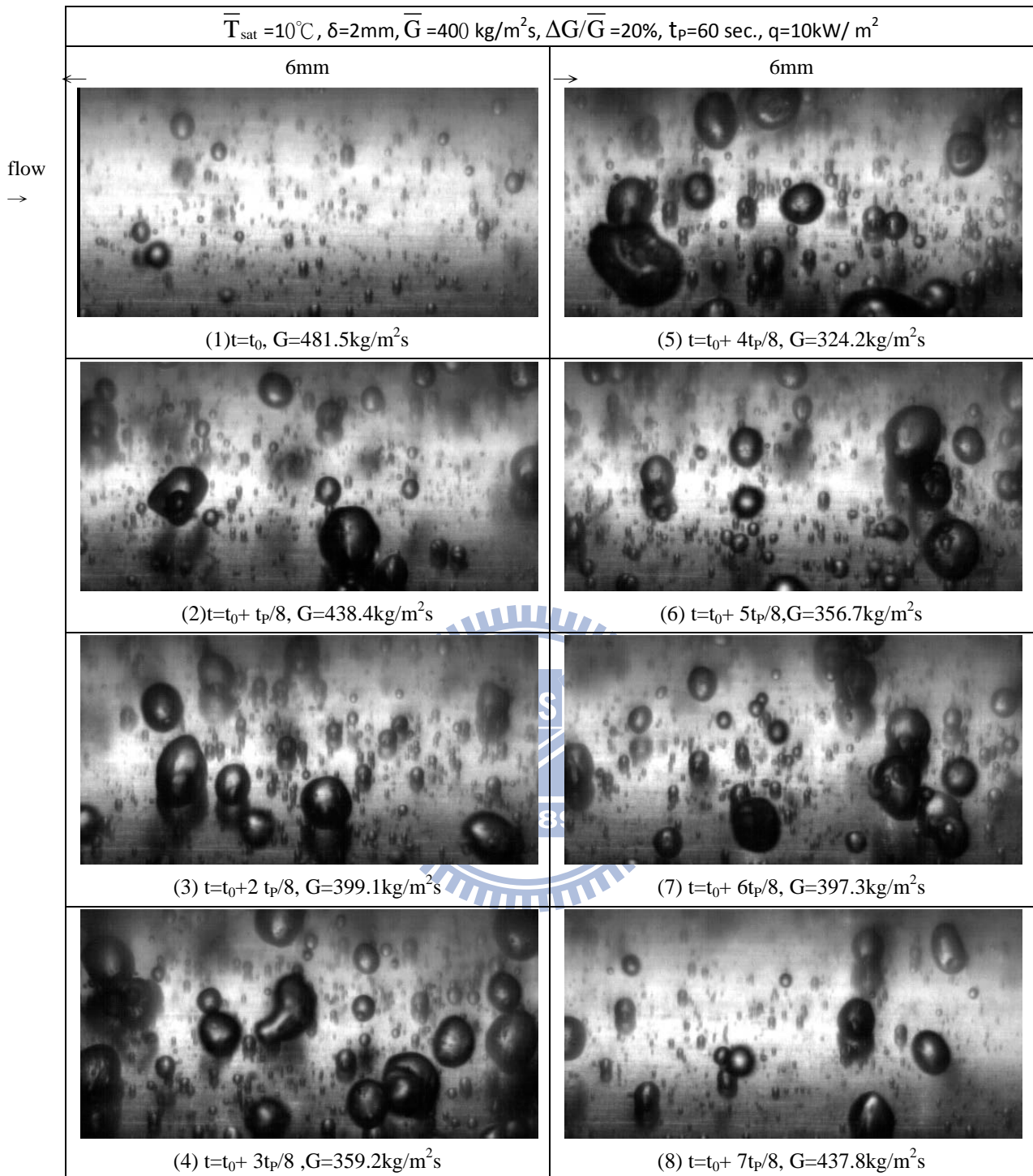


Fig. 6.6 Photos of time periodic saturated flow boiling of R-410A at selected time instants in a typical periodic cycle for  $q = 10 \text{ kW/m}^2$  at  $\bar{G} = 400 \text{ kg/m}^2\text{s}$ ,  $\Delta\bar{G}/\bar{G} = 20\%$ ,  $\bar{T}_{\text{sat}} = 10^\circ\text{C}$ ,  $\delta = 2.0\text{mm}$  and  $t_p = 60\text{sec}$ .

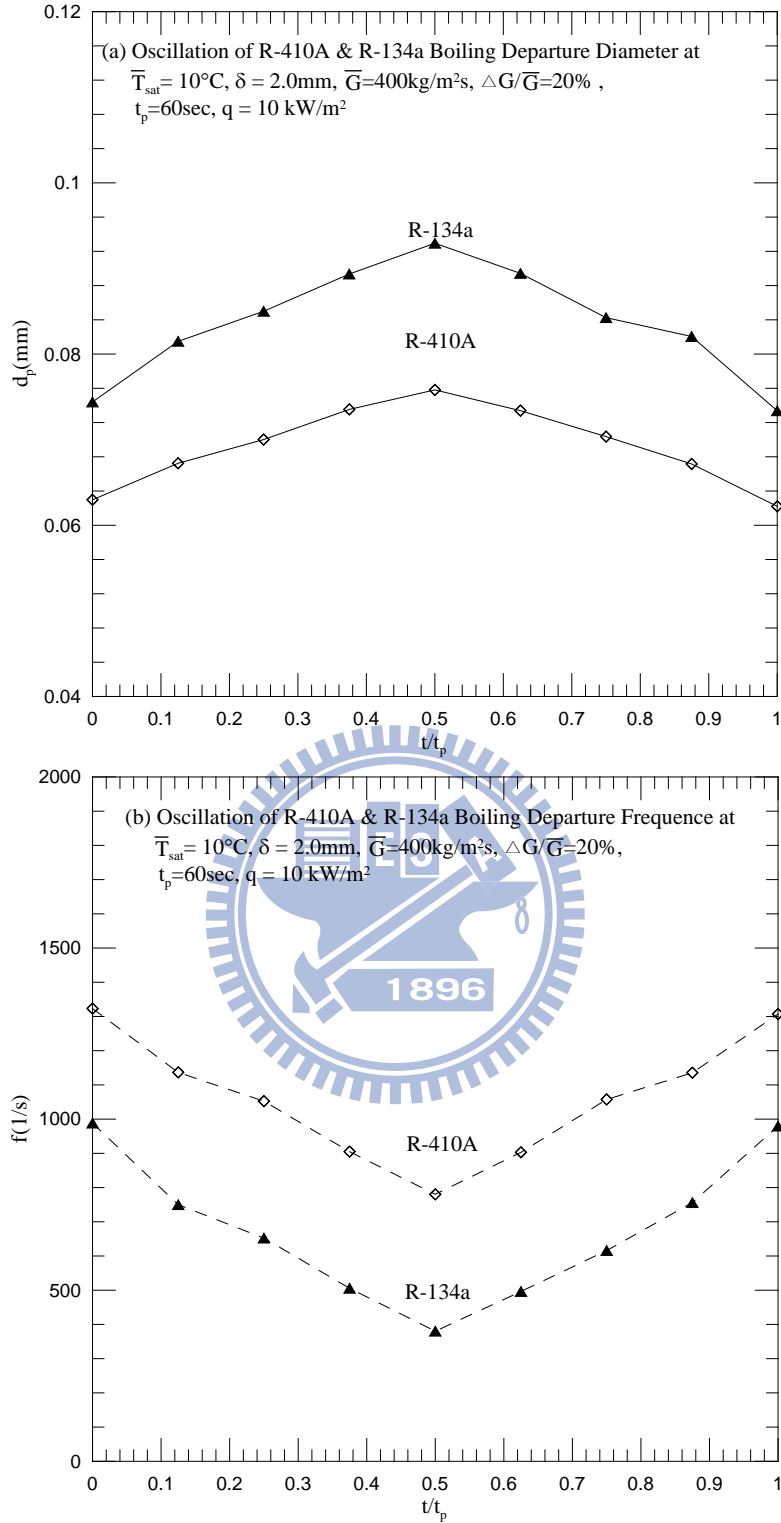


Fig. 6.7 Time variations of mean bubble departure diameter(a), bubble departure frequency(b), and active nucleation site density(c) in time periodic saturated flow boiling of R-410A & R-134a.



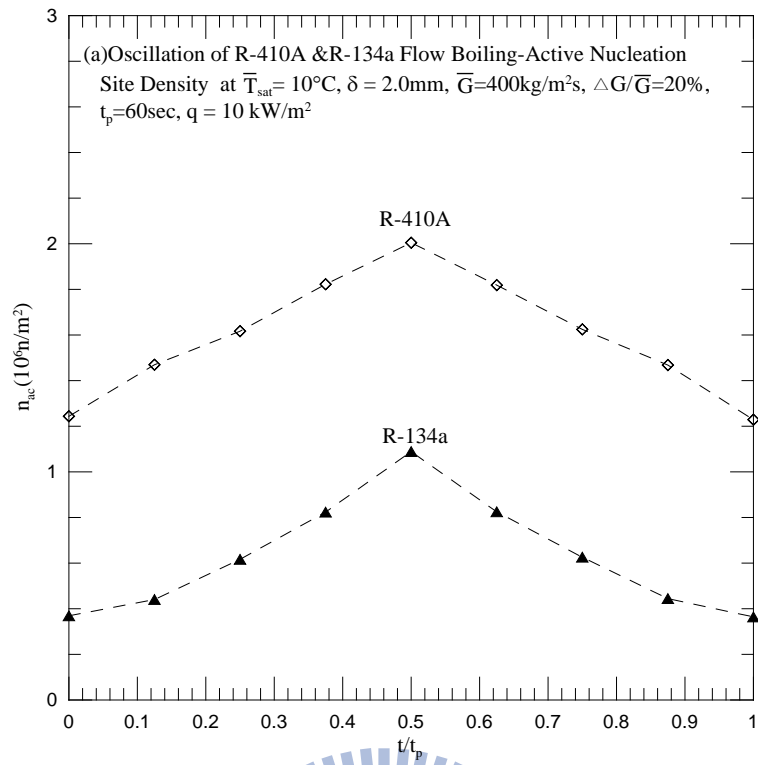
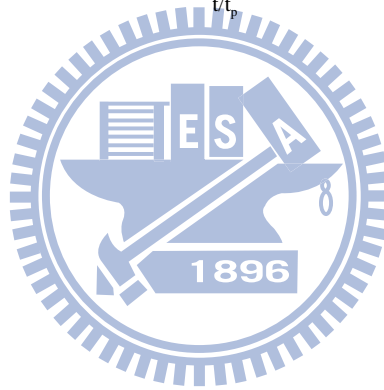


Fig. 6.7 continued.



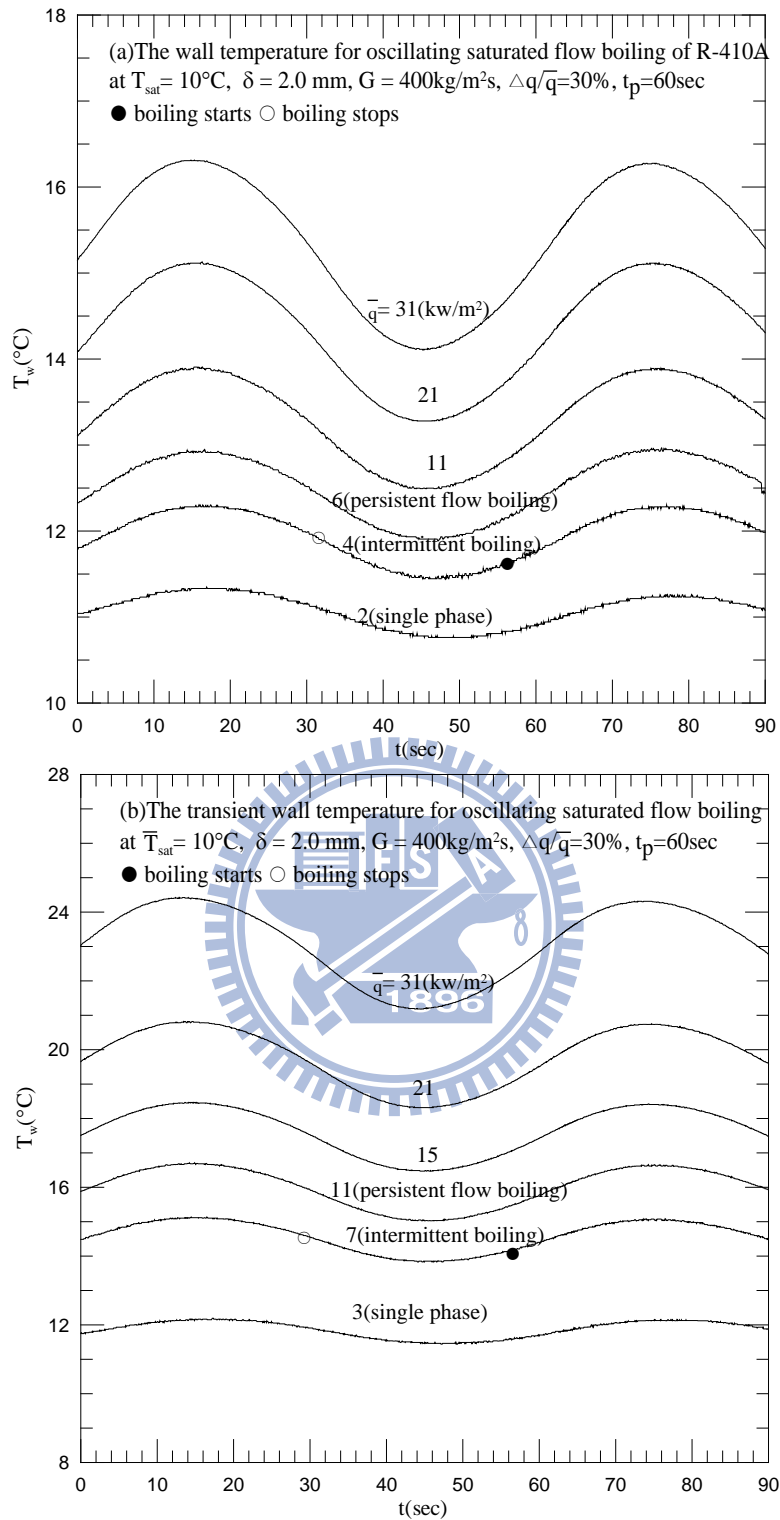


Fig. 6.8 Time variations of imposed heat flux and measured wall temperature in time periodic saturated flow boiling of R-410A (a) and R-134a (b) for various imposed heat fluxes at  $T_{sat} = 10^\circ\text{C}$ ,  $\delta = 2.0\text{ mm}$ ,  $t_p = 60\text{ sec}$  and  $G = 400\text{ kg/m}^2\text{ s}$  with  $\Delta q/\bar{q} = 30\%$ .

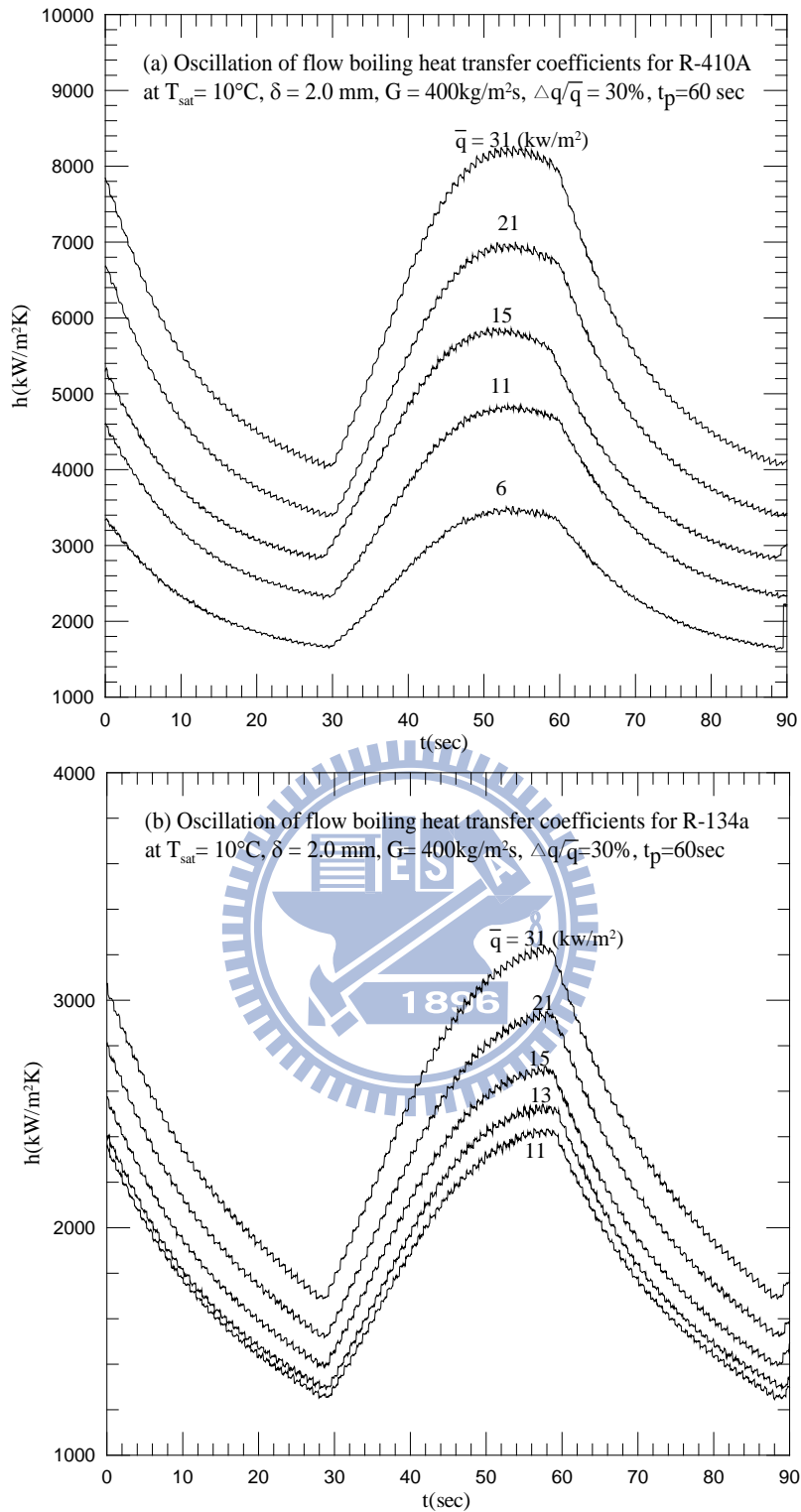


Fig. 6.9 Time variations of imposed heat flux and heat transfer coefficients in time periodic saturated flow boiling of R-410A (a) and R-134a (b) at  $T_{\text{sat}} = 10^\circ\text{C}$ ,  $\delta = 2.0 \text{ mm}$ ,  $t_p = 60 \text{ sec}$  and  $G = 400 \text{ kg/m}^2\text{s}$  with  $\Delta q/\bar{q} = 30\%$ .

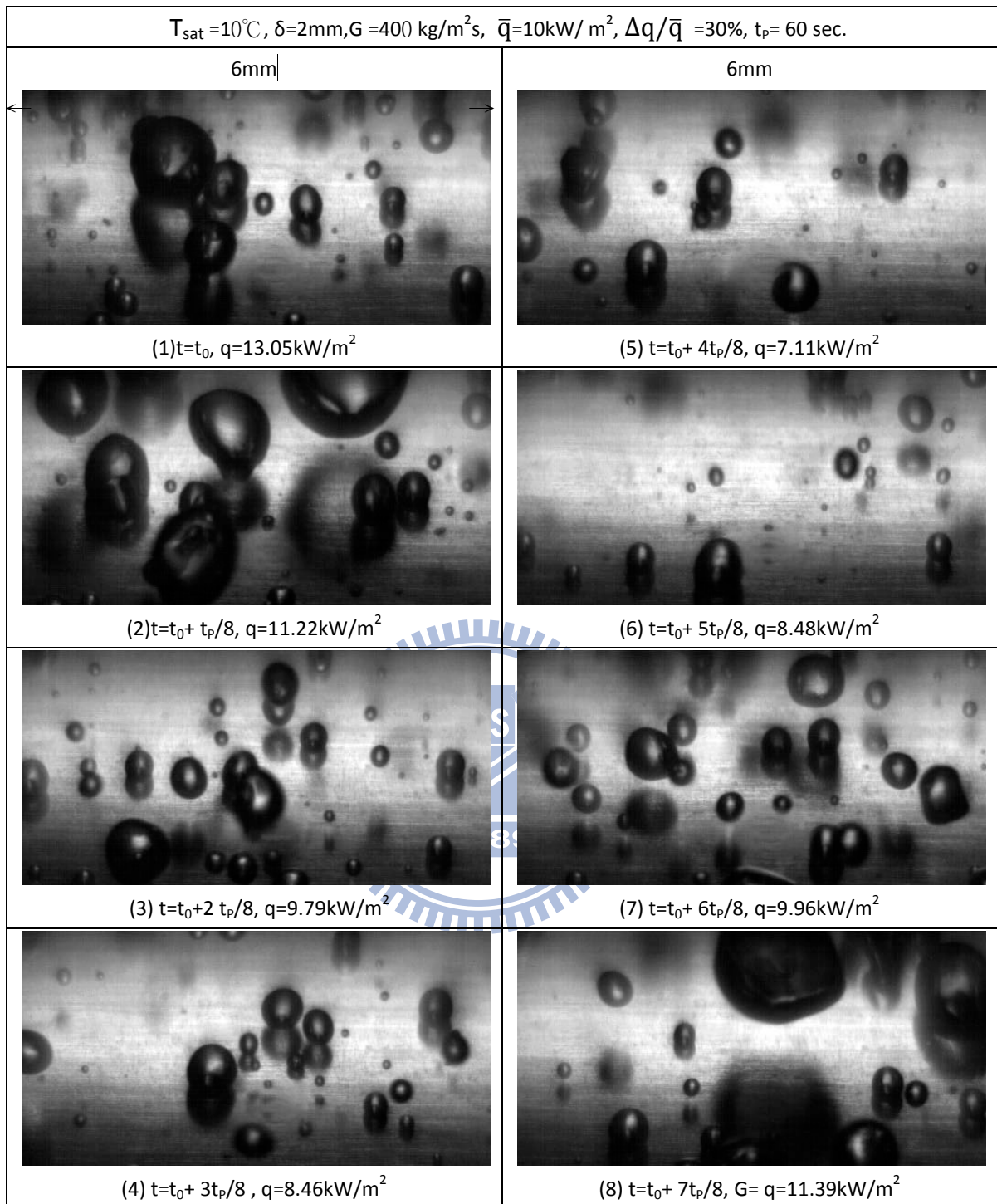


Fig. 6.10 Photos of time periodic saturated flow boiling of R-134a at selected time instants in a typical periodic cycle for  $q = 10 \text{ kW/m}^2$  at  $T_{\text{sat}} = 10^\circ\text{C}$ ,  $\delta = 2.0\text{mm}$ ,  $t_p = 60 \text{ sec}$  and  $G = 400\text{kg/m}^2\text{s}$  with  $\Delta q/\bar{q} = 30\%$ .

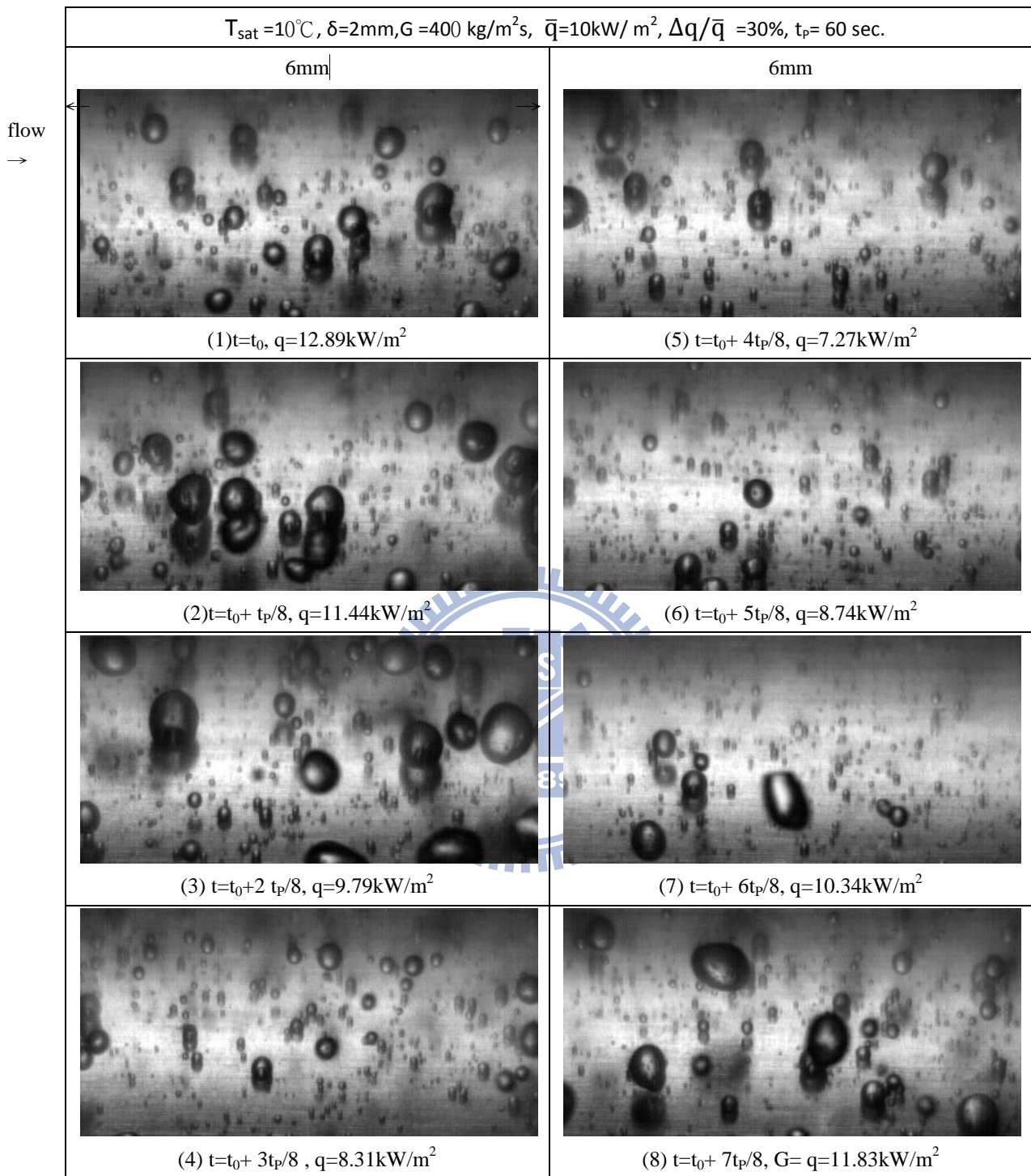


Fig. 6.11 Photos of time periodic saturated flow boiling of R-410A at selected time instants in a typical periodic cycle for  $q = 10 \text{ kW/m}^2$  at  $T_{\text{sat}} = 10^\circ\text{C}$ ,  $\delta = 2.0\text{mm}$ ,  $t_p = 60 \text{ sec}$  and  $G = 400\text{kg/m}^2\text{s}$  with  $\Delta q/\bar{q} = 30\%$ .

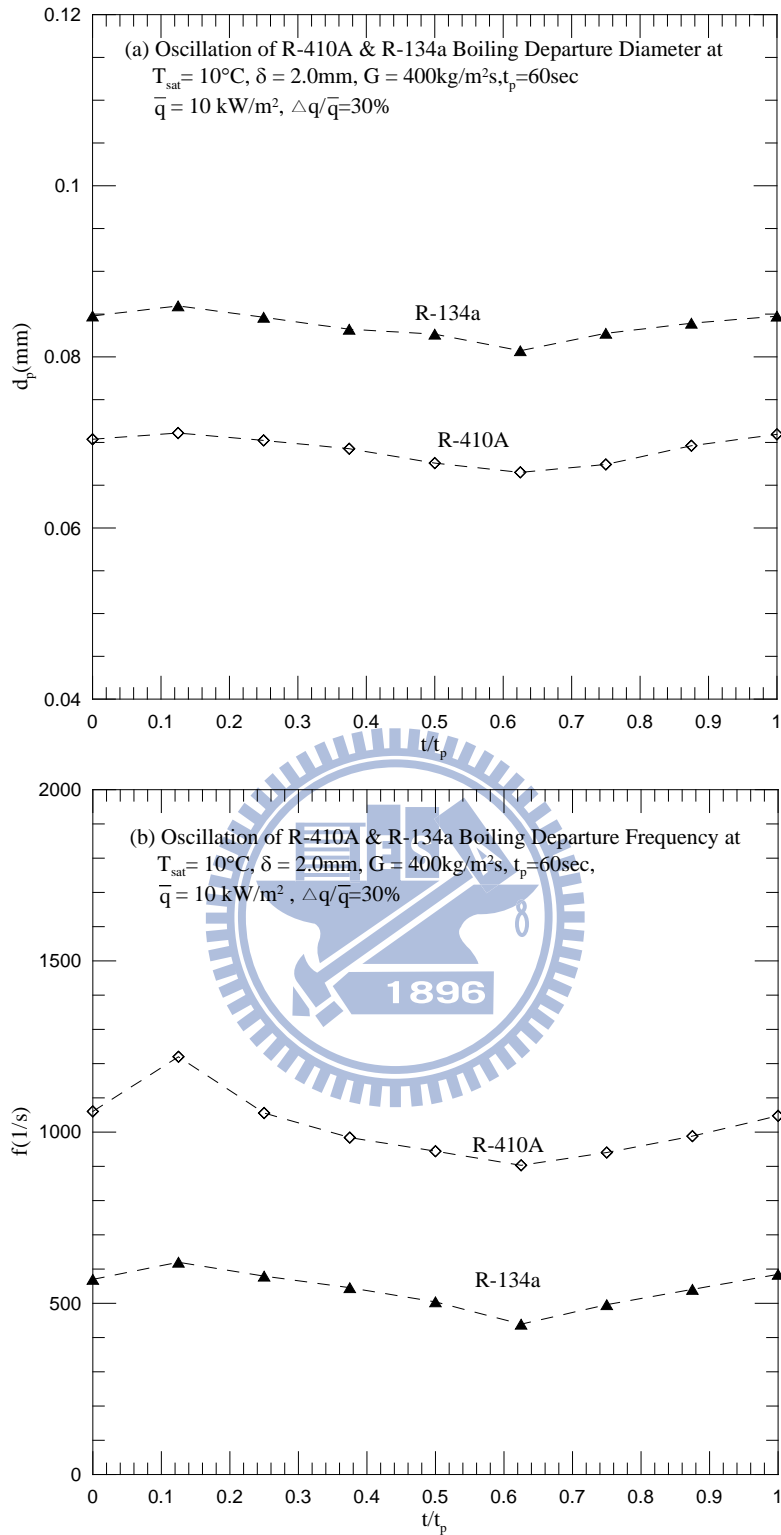


Fig. 6.12 Time variations of mean bubble departure diameter(a), bubble departure frequency(b), and active nucleation site density(c) in time periodic saturated flow boiling of R-410A & R-134a.

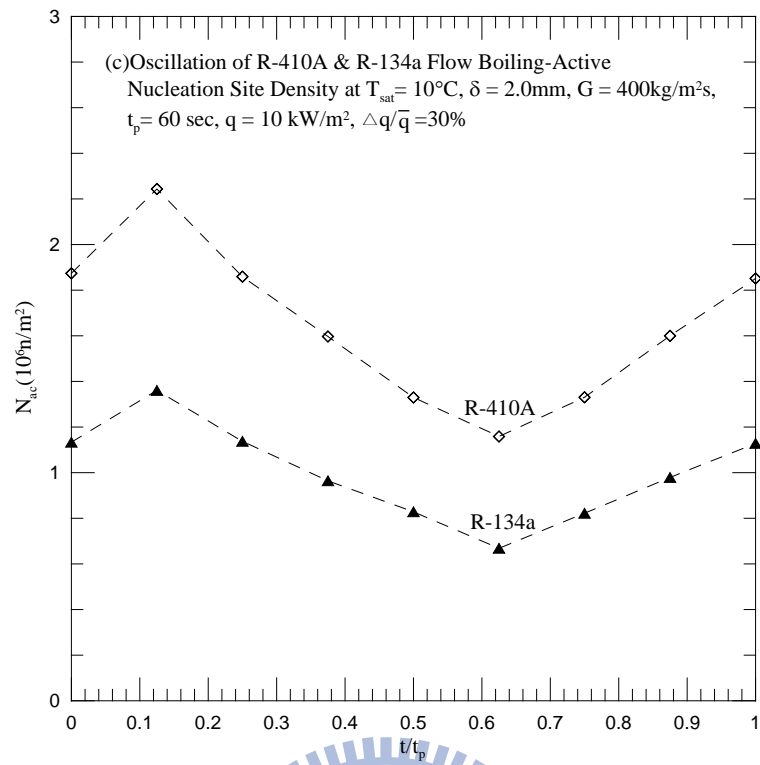
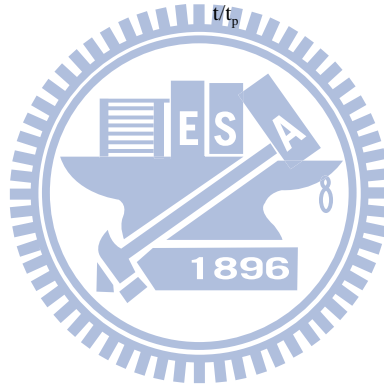


Fig. 6.12 continued.





## CHAPTER 7

### CONCLUDING REMARKS

The R-410A time periodic saturated flow boiling heat transfer and associated bubble characteristics in a narrow annular duct for an imposed time periodic mass flux oscillation or heat flux oscillation have been experimentally investigated. The effects of the mean level and oscillation amplitude and period of the refrigerant mass flux or heat flux, and refrigerant saturated temperature on the time periodic R-410A flow boiling heat transfer coefficients and associated bubble characteristics such as the mean bubble departure diameter and frequency, and active nucleation site density have been examined in detail. Major results presented in Chapters 4 and 5 can be summarized as follows:

- (1) The time-average boiling curves and heat transfer coefficients for the time periodic flow boiling of R-410A are not affected to a noticeable degree by the amplitude and periodic of the imposed mass flux oscillation or heat flux oscillation. In fact, they resemble that for the stable flow boiling.
- (2) In the flow boiling subject to the mass flux oscillation, the heated pipe wall temperature, bubble departure diameter and frequency and active nucleation site density also oscillate periodically in time and at same frequency as the mass flux oscillation. Experiments also show that the resulting oscillation amplitudes of the wall temperature get larger for a larger amplitude and a longer period of the mass flux oscillation. Besides for a larger amplitude of the mass flux oscillation, stronger oscillations in the bubble characteristics, such as  $d_p$ ,  $f$  and  $n_{ac}$ , are noted. A short time lag in the wall temperature oscillation is also noted. Moreover, the bubbles become smaller and more dispersed in the flow when the refrigerant mass flux increases with time. The opposite processes take place for a decreasing refrigerant mass flux.
- (3) In the visualization of the boiling flow in the heated annular duct with the mass flux oscillation we noted that for the imposed heat flux close to that needed for ONB of the stable boiling, intermittent boiling appears. A flow regime map and an

empirical correlation are given to delineate the boundaries separating different flow regimes in the annular duct. In the persistent flow boiling, the heated wall temperature decreases with the decrease in the mass flux, opposite to that in the single-phase flow. This is due to increases in the bubble departure size and active nucleation site density at decreasing refrigerant mass flux overwhelm the decrease in the bubble frequency, so an increase in the latent heat transfer and a drop in the heated wall temperature at decreasing  $G$ .

- (4) For the flow boiling subject to the heat flux oscillation, the heated pipe wall temperature, bubble departure diameter and frequency and active nucleation site density also oscillate periodically in time and at same frequency as the heat flux oscillation. Experiments also show that the resulting oscillation amplitudes of the heated surface temperature, heat transfer coefficient and bubble parameters, such as  $d_p$ ,  $f$  and  $n_{ac}$ , get larger for a longer period and a larger amplitude of the imposed heat flux oscillation and for a higher mean imposed heat flux. Moreover, a significant time lag in the heated surface temperature oscillation is also noted, which apparently results from the thermal inertia of the copper inner pipe. Furthermore, the bubbles become smaller and more dispersed after the time lag when the imposed heat flux decreases with time. The opposite process processes take place at increasing heat flux. Finally, reductions in the size of the departing bubbles, the bubble departure frequency and active nucleation site density with time result in the time duration in which the heat flux is sinking. When the heat flux is rising, the opposite processes occur.
- (5) The effects of the heat flux oscillation at extremely short and long periods have been explored. Due to the existence of the thermal inertia of the heated copper duct, the resulting heated surface temperature does not oscillate with time at an extremely short period of the imposed heat flux oscillation. But the oscillation amplitude of the heated surface temperature gets noticeably stronger for an extremely long period of the imposed heat flux oscillation.
- (6) When the imposed heat flux over the heated surface is close to that for the onset of the stable flow boiling, intermittent flow boiling appears. A flow regime map and an empirical correlation are given to delineate the boundaries separating different boiling flow regimes in the annular duct with the imposed mass flux oscillation or heat flux oscillation.

## REFERENCES

1. S. G. Kandlikar, and W. J. Grande, Evolution of microchannel flow passages-thermohydraulic performance and fabrication technology, *Heat Transfer Engineering*, 24(1)(2003)3-17.
2. P. A. Kew and K. Cornwell, Correlations for the prediction of boiling heat transfer in small-diameter channels, *Applied Thermal Engineering* 17(1997)705-715.
3. Y. Y. Hsieh, Y. M. Lie and T. F. Lin, Saturated flow boiling heat transfer of refrigerant R-410A in a horizontal annular finned duct, *International Journal of Heat and Mass Transfer*, 50(2007)1442-1454
4. C. C. Wang, W. T. Shieh, Y. J. Chang, An experimental study of convective boiling of refrigerants R-22 and R-410A, *ASHRAE Trans.* 121 (1998) 1144-1150.
5. T. Ebisu, K. Torikoshi, Heat transfer characteristics and correlations for R-410A flowing inside a horizontal smooth tube, *ASHRAE Trans.* 121 (1998) 556-561.
6. Y. Fujita, Y. Yang and N. Fujita, Flow boiling heat transfer and pressure drop in uniformly heated small tubes, *Proceedings of the Twelfth International Heat Transfer Conference* 3(2002)743-748.
7. F. C. Hsieh, K. W. Lin, Y. M. Lie, C. A. Chen, and T. F. Lin, Saturated flow boiling heat transfer of R-407C and associated bubble characteristics in narrow annular duct, *International Journal of Heat and Mass Transfer*, 51 (2008) 3763-3775.
8. Y. M. Lie and T. F. Lin, Saturated flow boiling heat transfer and associated bubble characteristics of R-134a in a narrow annular duct, *International Journal of Heat and Mass Transfer* 48(25-26)(2005)5602-5615.
9. Y. M. Lie and T. F. Lin, Subcooled flow boiling heat transfer and associated bubble characteristics of R-134a in a narrow annular duct, *International Journal of Heat and Mass Transfer*, 49 (2006) 2077-2089.
10. Z. Y. Bao, D. F. Fletcher and B. S. Haynes, Flow boiling heat transfer of Freon R11 and HCFC123 in narrow passages, *International Journal of Heat and Mass Transfer* 43(18)(2000)3347-3358.

11. T. N. Tran, M. W. Wambsganss and D. M. France, Small circular- and rectangular-channel boiling with two refrigerants, *International Journal of Multiphase Flow* 22(1996)485-498.
12. S. G. Kandlikar and M. E. Steinke, Flow boiling heat transfer coefficient in minichannels – correlation and trends, *Proceedings of the Twelfth International Heat Transfer Conference*, vol.3(2002)785-790.
13. H. Oh, M. Katsuta and K. Shibata, Heat transfer characteristics of R134a in a capillary tube heat exchanger, *Proceedings of 11<sup>th</sup> International Heat Transfer Conference*, Vol. 6,1998, pp.131-136.
14. C. P. Yin, Y. Y. Yan, T. F. Lin, and B. C. Yang, Subcooled flow boiling heat transfer of R-134a and bubble characteristics in a horizontal annular duct, *International Journal of Heat and Mass Transfer*, 43 (2000) 1885-1896.
15. C. A. Chen, W. R. Chang, K. W. Li, Y. M. Lin, and T. F. Lin, Subcooled flow boiling heat transfer of R-407C and associated bubble characteristics in a narrow annular duct, *International Journal of Heat and Mass Transfer*, 52 (2009) 3147-3158.
16. O. Comakli, S. Karsli, and M. Yilmaz, “Experimental investigation of two phase flow instabilities in a horizontal in-tube boiling system,” *Energy Conversion and Management* 43 (2002) 249-268
17. S. Kakac, T. N. Veziroglu, M. M. Padki, L. Q. Fu, and X. J. Chen, “Investigation of Thermal Instabilities in a Forced Convection Upward Boiling System,” *Experimental Thermal and Fluid Science* 3 (1990) 191-201.
18. Y. Ding, S. Kakac, and X. J. Chen, “Dynamic Instabilities of Boiling Two-Phase Flow in a Single Horizontal Channel,” *Experimental Thermal and Fluid Science* 11 (1995) 327-342.
19. Q. Wang, X. J. Chen, S. Kakac, and Y. Ding, “Boiling Onset Oscillation : a new type of Dynamic Instability in a Forced-Convection Upflow Boiling System,” *International Journal of Heat and Fluid Flow* 17( 1996) 418-423s
20. M. Ozawa, H. Umekawa, Y. Yoshioka and A. Tomiyama, Dryout under oscillatory flow condition in vertical and horizontal tubes : experiments at low velocity and pressure conditions, *International journal of heat and mass transfer*, 36 (1983) 4076-4078.
21. I. Kataoka, A. Serizawa and A. Sakurai, “Transient Boiling Heat Transfer

- Under Forced Convection,” *International Journal of Heat and Mass Transfer* 26 (1983) 583-595.
22. S. Lin, P.A. Kew and K. Cornwell, “Two-Phase Heat Transfer to a Refrigerant in a 1mm Diameter Tube,” *International Journal of Refrigeration* 24 (2001) 51-56.
  23. P. R. Mawasha and R. J. Gross, “Periodic Oscillations in a Horizontal Single Boiling Channel with Thermal Wall Capacity,” *International Journal of Heat and Fluid Flow* 22 (2001) 643-649.
  24. P. R. Mawasha, R. J. Gross, and D. D. Quinn, “Pressure-Drop Oscillations in a Horizontal Single Boiling Channel,” *Heat Transfer Engineering* 22 (2001) 26-34.
  25. K. Cornwell and P. A. Kew, *Boiling in small parallel channels, Energy Efficiency in Process Technology*, P.A. Pilavachi, Elsevier Applied Science, London, 1993, pp. 624-638.
  26. R. Situ, Y. Mi, M. Ishii and M. Mori, Photographic study of bubble behaviors in forced convection subcooled boiling, *International Journal of Heat and Mass Transfer* 47(2004)3659-3667.
  27. G. E. Thorncroft, J. F. Klausner and R. Mei, An experimental investigation of bubble growth and detachment in vertical upflow and downflow boiling, *International Journal of Heat and Mass Transfer* 41 (1998) 3857-3871
  28. S. G. Kandlikar, “Bubble Nucleation and Growth Characteristics in Subcooled Flow Boiling of Water,” *National Heat Transfer Conference HTD-Vol. 342* 4 (1997) 11-18
  29. S. H. Chang, I. C. Bang and W. P. Baek, A photographic study on the near-wall bubble behavior in subcooled flow boiling, *International Journal of Thermal Science* 41(2002)609-618.
  30. Victor H. Del Balle M. and D. B. R. Kenning, Subcooled flow boiling at high heat flux, *International Journal of Heat and Mass Transfer* 28(10)(1985)1907-1920
  31. R. Maurus, V. Ilchenko and T. Sattelmayer, Automated high-speed video analysis of the bubble dynamics in subcooled flow boiling, *International Journal of Heat and Fluid Flow* 25(2004)149-158.

32. T. Okawa, T. Ishida, I. Kataoka and M. Mori, An experimental study on bubble rise path after the departure from a nucleation site in vertical upflow boiling, *Experimental Thermal and Fluid Science* 29(2005)287-294.
33. J. C. Chen, A correlation for boiling heat transfer to saturated fluids in convective flow, *Ind. Engng. Chem. Proc. Des. Dev.* 5(1966)322-329.
34. F. W. Dittus and L. M. K. Boelter, Heat transfer in automobile radiator of the tube type, Publication in Engineering, University of California, Berkley, 2(1930)250.
35. K. E. Gungor and R. H. S. Winterton, A general correlation for flow boiling in tubes and annuli, *International Journal of Heat and Mass Transfer* 29(1986)351-358.
36. Z. Liu and R. H. S. Winterton, A general correlation for saturated and subcooled flow boiling in tubes and annuli, based on a nucleate pool boiling equation, *International Journal of Heat and Mass Transfer* 34(1991)2759-2766.
37. W. Zhang, T. Hibiki and K. Mishima, Correlation for flow boiling heat transfer in mini-channels, *International Journal of Heat and Mass Transfer* 47(2004)5749-5763.
38. G. M. Lazarek and S. H. Black, Evaporative heat transfer, pressure drop and critical heat flux in a small vertical tube with R-113, *International Journal of Heat and Mass Transfer*, 25(7)(1982)945-960.
39. S. G. Kandlikar, A general correlation for two-phase flow boiling heat transfer coefficient inside horizontal and vertical tubes, *Journal of Heat Transfer* 102(1990)219-228.
40. S. G. Kandlikar, A model for predicting the two-phase flow boiling heat transfer coefficient in augmented tube and compact heat exchanger geometries, *Journal of Heat Transfer* 113(1991)966-972.
41. S. G. Kandlikar and P. Balasubramanian, An extension of the flow boiling correlation to transition, laminar, and deep laminar flows in minichannels and microchannels, *Heat Transfer Engineering* 25(2004)86-93.
42. S. W. Churchill and H. H. S. Chu, Correlating equations for laminar and turbulent free convection from a horizontal cylinder, *International Journal of Heat and Mass Transfer* 18(1975)1049-1053.

43. S. J. Kline and F. A. McClintock, Describing uncertainties in single-sample experiments, *Mech. Eng.* 75(1)(1953)3-12.
44. V. Gnielinski, New equations for heat and mass transfer in turbulent pipe and channel flow, *International Chemical Engineering* 16(2)(1976)359-368.
45. C. A. Chen, Time periodic flow boiling heat transfer of refrigerant R-134a in a horizontal annular duct due to flow rate or heat flux oscillation, Ph.D thesis, National Chiao Tung University, Hsinchu, Taiwan (2010).

